Fall 12-1-2017

A measurement of the *Wγ* cross section at √S = 8 TEV in *PP* collisions with the CMS detector

Ekaterina Avdeeva
University of Nebraska-Lincoln, tsukanovaeg@gmail.com

A MEASUREMENT OF THE $W\gamma$ CROSS SECTION AT $\sqrt{S} = 8$ TEV IN PP COLLISIONS WITH THE CMS DETECTOR

by

Ekaterina Avdeeva

A DISSERTATION

Presented to the Faculty of

The Graduate College at the University of Nebraska

In Partial Fulfilment of Requirements

For the Degree of Doctor of Philosophy

Major: Physics & Astronomy

Under the Supervision of Professor Ilya Kravchenko

Lincoln, Nebraska

September, 2017

A MEASUREMENT OF THE $W\gamma$ CROSS SECTION AT $\sqrt{S} = 8$ TEV IN PP COLLISIONS WITH THE CMS DETECTOR

Ekaterina Avdeeva, Ph.D.

University of Nebraska, 2017

Adviser: Ilya Kravchenko

A measurement of cross section of the $W\gamma \rightarrow l\nu\gamma$ production in proton-proton collisions using 19.6 fb^{-1} of LHC data collected by CMS detector at the center-of-mass collision energy of $\sqrt{s} = 8$ TeV is reported. The W bosons are identified in their electron and muon decay modes. The process of $W\gamma$ production in the Standard Model (SM) involves a pure gauge boson coupling, a $WW\gamma$ vertex, which allows one to test the electroweak sector of the SM in a unique way not achievable by studies of other processes. In addition to the total cross section, we measure the differential cross section of $W\gamma$ production as a function of a photon transverse momentum. The measurement of the differential cross section is a sensitive probe for new physics originating from an anomalous gauge coupling because possible effects of its presence increase with the photon transverse momentum and, thus, are more likely to be observed in the differential than in the total cross section. The results of this measurement agree with the Standard Model prediction at NLO in QCD, and no evidence of an anomalous triple gauge coupling has been observed. The reported total cross section measurement is the first measurement of this quantity at the 8 TeV collision energy with CMS data. The differential cross section measurement discussed in this dissertation is the first ever measurement of this process performed by CMS since the start of the LHC.

ACKNOWLEDGMENTS

This dissertation represents a work that required effort from a lot of different people in many different ways. The list of people includes but is not limited to CMS and UNL colleagues from all over the world, family, and friends.

Specifically, I first would like to thank my advisor Ilya Kravchenko for his help and support throughout my whole experience as a PhD student at UNL, from the admission process and to the writing this dissertation. We discussed every single step of the $W\gamma$ measurement, and I could always rely on getting a guidance and valuable advice whether I came with a physical, technical, or organizational question.

Overall, the list of CMS colleagues who made a direct contribution to the $W\gamma$ measurement and/or provided a good number meaningful recommendations starts from Yurii Maravin, Lovedeep Saini, Joshua Kunkle, Senka Duric, Dmytro Kovalskyi, Kuo Chia-Ming, Sachiko Toda McBride, Yutaro Iiyama, and never ends.

Additionally, I would like to express my gratitude to Frank Meier for supervising another part of my work, the alignment of the CMS tracking system. We spent hours discussing alignment algorithms, various technical tools, results, and effective ways to collaborate with other colleagues.

The work in the tracker alignment group is a very integrated team work, where it is impossible to separate your contribution from the contributions of others. The list of colleagues who made our collaboration so fruitful, besides Frank, includes Marco Musich, Matthias Schröder, Tapio Lampen, Patrick Connor, Nazar Stephaniuk, Candice You and many others.

I would like to thank UNL professors Ken Bloom, Brad Schadwick and Glenn Ledder for their time spent on serving as my graduate committee and providing a set of questions and comments regarding the dissertation. Ken Bloom also, alongside with other UNLHEP professors, postdocs and students, participated in tricky discussions regarding various aspects of my research work during our group meetings as well as during individual meetings and over e-mails.

Finally, special thanks to my parents Elena Tsukanova and Grigory Tsukanov, to my husband Sergey Avdeev, and to my daughters Oksana and Yana Avdeeva for being a source of support in my life and research career, for their patience and understanding. Family support has meant a lot to me, and these people's effect on any aspect of my personality cannot be overestimated.

Table of Contents

List of Figures

List of Tables

1 Introduction

Elementary particle physics describes fundamental particles and their interactions. Fundamental particles are the smallest constituents of our Universe. When examined at smaller scales, the substances around us consist of molecules, and molecules consist of atoms. In an atom there is a nucleus made of neutrons and protons and some number of electrons occupying orbits around the nucleus. Protons and neutrons have a structure while an electron is not known to have any internal structure, therefore an electron is an example of a particle which is considered to be fundamental.

Interactions of elementary particles are described by quantum field theories which incorporate principles of the quantum mechanics and the special theory of relativity. The set of such theories, including quantum elecrtrodynamics (QED), quantum chromodynamics (QCD) and the theory of weak interactions, is called the Standard Model (SM). Current observations have proved the SM to be an accurate description of elementary particle interactions.

However, there are several experimental observations that are not described by the SM such as effects of gravity, dark matter, dark energy, matter/antimatter asymmetry and others. Therefore, the SM is not a complete theory of particle interactions. There are several SM extensions offered by theorists as well as radically new theories waiting for experimental confirmation or exclusion.

Some SM extensions and new theories predict the existence of heavy particles with masses lying beyond experimentally reachable energies. The search of these particles is a priority in particle physics. One source of highly energetic elementary particles is cosmic rays. The most energetic particles ever observed have come from this source. However, cosmic rays are totally uncontrollable and such highly energetic particles are rare. If we want to produce a large number of particles in a given energy range, we need to use a particle accelerator. A large amount of data allows experimentalists to perform a statistical analysis and increase the probability of finding a new particle if it exists.

Symmetric colliding beams is the most effective way to produce as heavy particles as possible given the energies of the colliding particles. Compared to experiments colliding a single beam at a fixed target, in the case of a symmetric collision the total momentum of two colliding particles is zero and, therefore, a much larger fraction of energy can be transferred to a mass of a new particle. The Large Hadron Collider (LHC) is one such collider. It has the highest energy in the world, and can produce the most massive particles to probe physics beyond the SM (BSM).

The Compact Muon Solenoid (CMS) is one of two general-purpose detectors at the LHC. It is placed at one of four collision points. CMS has a broad physics program including searches for the BSM physics as well as the precision measurements of the parameters of the SM itself. The measurement of this dissertation is a SM measurement with CMS data collected in 2012 in proton-proton (pp) collisions of LHC with beam energies of 4 TeV. The result can be compared to the SM prediction. Certain BSM theories predict a deviation of the result of this measurement from its SM value, therefore, with this measurement, in addition to testing the SM, we also search for a new physics.

The rest of this chapter gives general introductory information about the SM while Ch. 2 concentrates on the theory of the SM and BSM $W\gamma$ production and also discusses previous measurements of this process. Chapter 3 describes LHC and CMS in more detail. Chapter 4 explains one specific detail of the CMS operation that is the spatial alignment of the charge particle tracking detector. Finally, Ch. 5 describes the details of the measurement of this dissertation and reports the results.

1.1 Fundamental Particles and Interactions

The SM describes interactions of elementary particles. There are four fundamental interactions: electromagnetic, strong, weak and gravitational. Gravity is not included in the SM but its effect on particles is negligible compared to the other forces which makes it possible to develop a theory of the particle physics and conduct experiments even without having the gravity included in the model.

All fundamental elementary particles in the SM can be split into three categories by their spins. There are fermions which possess spin s=1/2, there are gauge bosons which are vector particles (s=1) and there is the Higgs boson which is a scalar particle (s=0).

The fermions are arranged into three generations, each generation consisting of a quark with charge Q=+2/3 (up, charm, and top quarks), a quark with Q=$-$1/3 (down, strange, and bottom quarks), a charged lepton with Q=$-$1 (electron, muon, and tau-lepton) and a neutrino (electron, muon, and tau neutrinos) which is electrically neutral. Each quark can carry any of three colors: red, blue, or green. Additionally, each fermion has its antiparticle. Therefore, the total number of fundamental fermions is $(6(\text{leptons}) + 6(\text{quarks}) \cdot 3(\text{colors})) \cdot 2(\text{to include antiparticles}) = 48$.

Corresponding particles in different generations have the same charges, spins and interaction properties but masses of particles increase with generation. These mass differences lead to different decay properties because a particle A can decay to particles B and C only if their masses relate as $m_A > m_B + m_C$. Thus, an electron is a stable particle, a muon decays as $\mu^- \rightarrow e^- + \bar{\nu_e} + \nu_\mu$, a tau-lepton, as the heaviest charged lepton, has the largest number of decay channels amongst the charged leptons: $\tau^- \rightarrow \mu^- + \bar{\nu_\mu} + \nu_\tau$, $\tau^- \rightarrow e^- + \bar{\nu_e} + \nu_\tau$, $\tau^- \rightarrow \nu_\tau +$ quarks.

In addition to fermions, the SM includes gauge bosons which are interaction mediators. They are called mediators because fermions interact with each other by exchanging them. For example, two charged fermions can interact with each other by exchanging a photon. Such interaction is called electromagnetic interaction and a photon is a mediator for the electromagnetic interaction. Similarly, a gluon is a mediator for strong interactions, and $W^{\pm}$ and Z^0 bosons are mediators for weak interactions. $W^{\pm}$ and Z^0 bosons are massive while a photon and a gluon are massless particles.

The last SM particle is the Higgs boson. The Higgs boson is a scalar neutral particle which plays a critical role in the electroweak symmetry breaking. The Higgs mechanism explains how W and Z bosons become massive particles.

All the particles are summarized in Fig. 1.1. These and only these fundamental particles and their antiparticles have been discovered by now. However, there are many composite particles which are called hadrons. Hadrons can consist of three quarks (baryons), quark and antiquark (meson), or three antiquarks (antibaryons). Hadrons always possess an integer electric charge.

Most of the particles are short-lived and decay within microseconds. The only stable particles are protons and antiprotons, electrons and positrons, neutrinos and antineutrinos, photons, and, in some sense, gluons. However, if a particle cannot decay, it does not mean that it would live forever. There are many different kinds of reactions in which particles can disappear. Antiprotons and positrons would immediately annihilate with protons and electrons, photons can be absorbed by charged particles, electrons and protons can scatter to produce neutrons and neutrinos and many other reactions are possible.

In this dissertation, a study of $pp \rightarrow W\gamma + X \rightarrow l\nu\gamma$ process where $\ell = e, \mu$ is presented. $W\gamma$ production with leptonic W decays proceeds through one of the following three processes: initial state radiation where a photon is emitted from one of the incoming partons, final state radiation where a photon is radiated off the charged lepton from the W boson decay, and, finally, triple gauge coupling (TGC) where a photon is emitted from the W boson. Many BSM theories predict an enhancement of TGC production over the SM value and, therefore, the experimental search for such an enhancement is a good test for such theories.

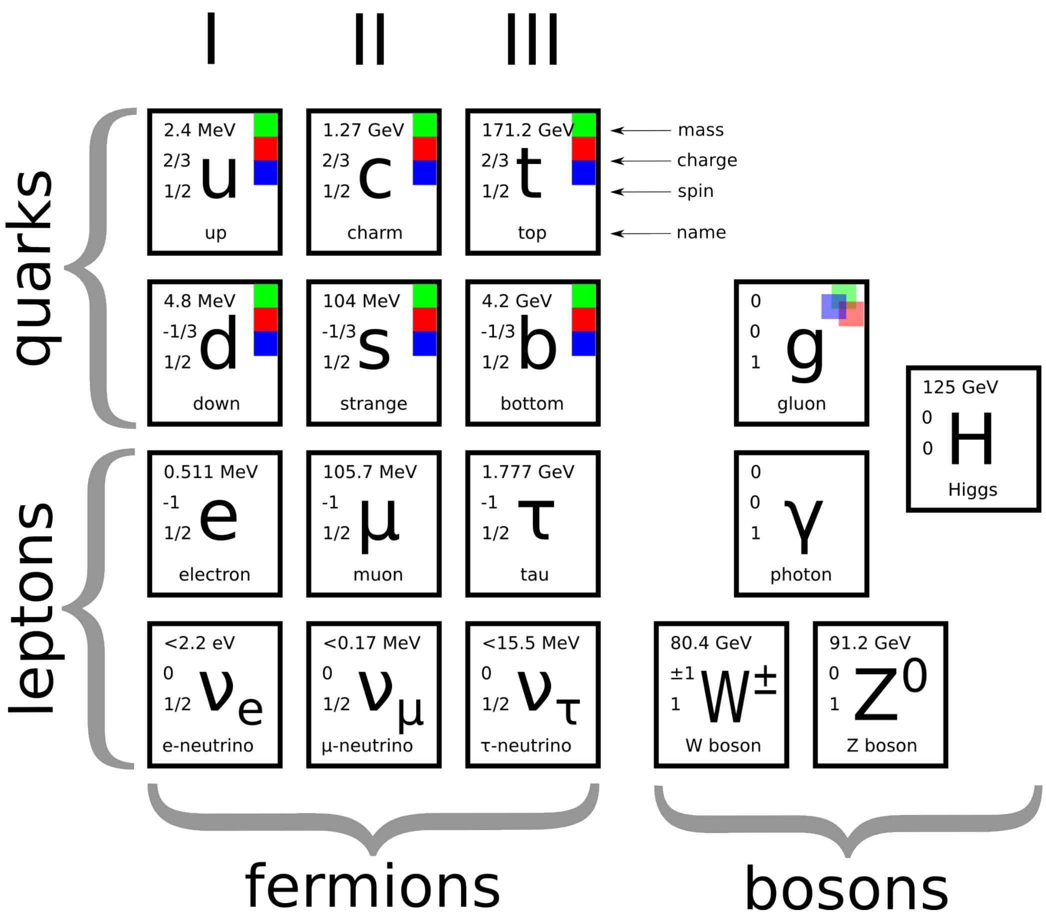

Figure 1.1: Standard Model Particles.

1.2 Electroweak Interactions

All electrically charged particles participate in electromagnetic interactions. The theory of electromagnetic interactions is called quantum electrodynamics (QED). All electromagnetic interactions are mediated by a photon, a spin-one electrically neutral massless particle, and can be reduced to one elementary process (Fig. 1.2, left). This process represents a charged fermion radiating or absorbing a photon. Such elementary process itself is forbidden by the energy and momentum conservation laws but this element is a base of an actual process. For example, the Bhabha scattering, $e^+e^- \to e^+e^-$, occures through e^+e^- annihilation with further production of a new e^+e^- pair (Fig. 1.2, middle) or through exchange of a photon between the positron and the electron (Fig. 1.2, right). Both cases involve nothing except the electromagnetic elementary process (Fig. 1.2, left). Such graphical representations of the particle physics processes are called Feynman diagrams.

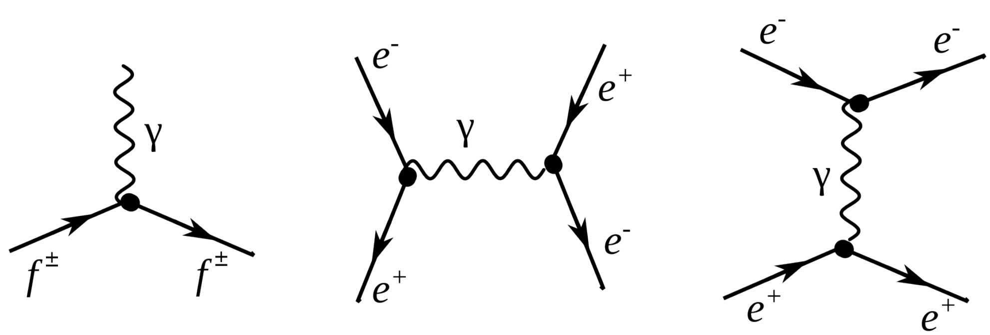

Figure 1.2: Electromagnetic interactions. Left: a photon radiation off a charged fermion, middle and right: Bhabha scattering.

As for the weak interactions, they can be either neutral (mediated by a Z boson) or charged (mediated by a $W^{\pm}$ boson). Elementary processes with W and Z bosons

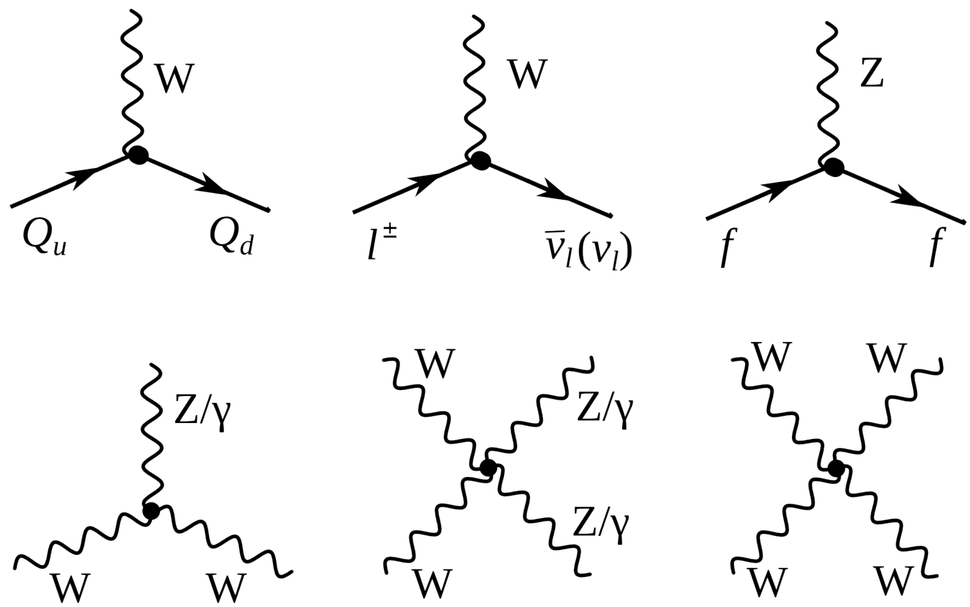

Figure 1.3: Weak elementary processes and gauge couplings. Top left: a quark with charge Q=+2/3 enters, emits a W boson, and a quark with charge Q=−1/3 escapes. Top middle: a charged lepton enters, emits a W boson, and a neutrino or antineutrino escapes conserving a lepton flavor number. Top right: a fermion enters, emits a Z boson and escapes. Bottom left: TGC $WW\gamma$ and WWZ. Bottom middle: QGC (quartic gauge couplings) $WW\gamma\gamma$, $WWZ\gamma$ and $WWZZ$. Bottom right: QGC $WWWW$.

are shown in Fig. 1.3. Because the electric charge must be conserved at any vertex, a particle radiating or absorbing a W boson converts to a different particle. Thus, a charged lepton converts to a neutrino (or vice versa) as shown in Fig. 1.3, top middle. Each lepton carries a lepton flavor number (Tab. 1.1). Lepton flavor is conserved in any interaction, thus an electron radiating a W boson always converts to an electron neutrino, a muon converts to a muon neutrino etc.

From top left diagram in Fig. 1.3 we see that if a quark with Q=+2/3 enters, then a quark with Q=−1/3 escapes and, therefore, the flavor of the quark is changed. The charged weak interaction is the only interaction which changes a

Table 1.1: Lepton Flavor Number

particles	L_e	L_μ	L_τ
e^-, ν_e	+1	0	0
$e^+, \bar{\nu_e}$	-1	0	0
μ^-, ν_μ	0	+1	0
$\mu^+, \bar{\nu_\mu}$	0	-1	0
τ^-, ν_τ	0	0	+1
$\tau^+, \bar{\nu_\tau}$	0	0	-1

quark flavor. The probability of each of three quarks with Q=$-1/3$ to be born is determined by the Cabibbo-Kobayashi-Maskawa matrix which relates mass eigenstates d, c and b to weak eigenstates d', c' and b' (Eq. 1.1). Absolute values of the matrix elements are all known, either have been measured or inferred through matrix unitarity (Eq. 1.2) and are the highest for the quark of the same generation as the initial state quark. In the particular case shown in the top left diagram in Fig. 1.3, u is the initial state quark and d has the highest probability to be produced after an interaction with a W boson but s and b can also be produced if there is enough energy.

$$\begin{pmatrix} d' \\ s' \\ b' \end{pmatrix} = \begin{pmatrix} V_{ud} & V_{us} & V_{ub} \\ V_{cd} & V_{cs} & V_{cb} \\ V_{td} & V_{ts} & V_{tb} \end{pmatrix} \begin{pmatrix} d \\ s \\ b \end{pmatrix} \tag{1.1}$$

$$\begin{pmatrix} |V_{ud}| & |V_{us}| & |V_{ub}| \\ |V_{cd}| & |V_{cs}| & |V_{cb}| \\ |V_{td}| & |V_{ts}| & |V_{tb}| \end{pmatrix} = \begin{pmatrix} 0.97 & 0.23 & 0.00 \\ 0.23 & 0.97 & 0.04 \\ 0.01 & 0.04 & 1.00 \end{pmatrix} \tag{1.2}$$

An elementary process of a neutral weak interaction is an emission a Z boson off a fermion line (right top diagram in Fig. 1.3). Diagrams with a Z boson are very similar to ones with a photon except a photon can only be radiated off a charged particle but a Z boson can also be radiated off a neutrino or antineutrino.

The bottom diagrams in Fig. 1.3 are gauge bosons coupling diagrams including self-coupling of a W boson, its interaction with a Z boson and its electromagnetic radiation of a photon. Charge-conserving TGC and quartic gauge couplings (QGC) containing two or four W bosons are all possible in the SM: WWZ, $WW\gamma$, $WWZZ$, $WWZ\gamma$, $WW\gamma\gamma$, and $WWWW$.

Electromagnetic and weak interactions are unified by the electroweak Glashow-Weinberg-Salam (GWS) theory which is based on $SU(2) \times U(1)$ symmetry. $SU(2)$ is the symmetry of weak isospin which generates three bosons: W^1, W^2 and W^3. $U(1)$ is the symmetry of the weak hypercharge and generate one neutral boson B. W^1 and W^2 are mixed to create W^+ and W^- mediators while W^3 and B are mixed to create a Z boson and a photon. Therefore, the GWS theory considers electromagnetic and weak forces as different manifestations of the electroweak force. The electroweak theory is discussed in greater details in Ch. 2.

Weak interactions are mediated by heavy bosons ($M_W = 80$ GeV, $M_Z = 91$ GeV) while electromagnetic interactions are mediated by a massless photon, thus the electroweak symmetry is broken. To explain this phenomenon, the Higgs mechanism was introduced. The mechanism predicted an existence of an additional boson: the Higgs boson. The Higgs boson was a missing piece of the SM for many years and was finally discovered in 2012 at LHC by ATLAS and CMS collaborations through the processes shown in Fig. 1.4 [13], [14].

The measurement in this dissertation is an electroweak measurement because the process involves a W boson. It includes an interaction of a W boson with leptons and quarks as well as the TGC $WW\gamma$. Thus, the measurement is a test of the SM electroweak theory.

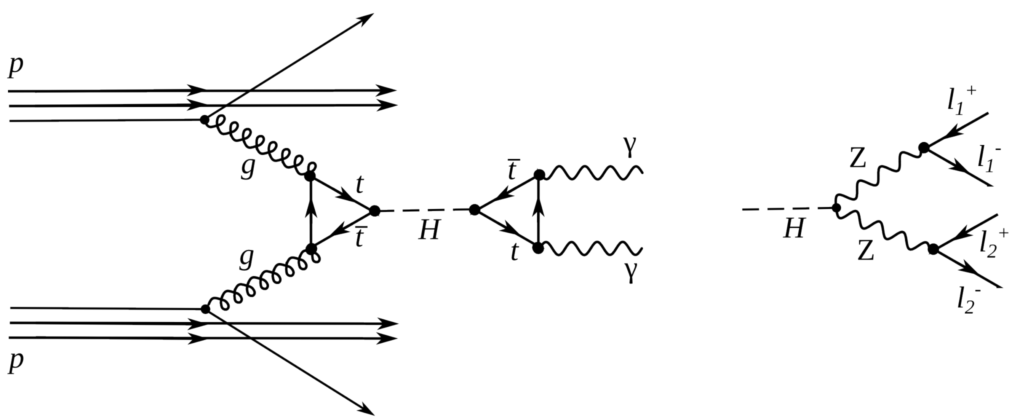

Figure 1.4: The Higgs boson production and decay. Left: $H \rightarrow \gamma\gamma$, right: $H \rightarrow ZZ \rightarrow 4l$.

1.3 Strong Interactions

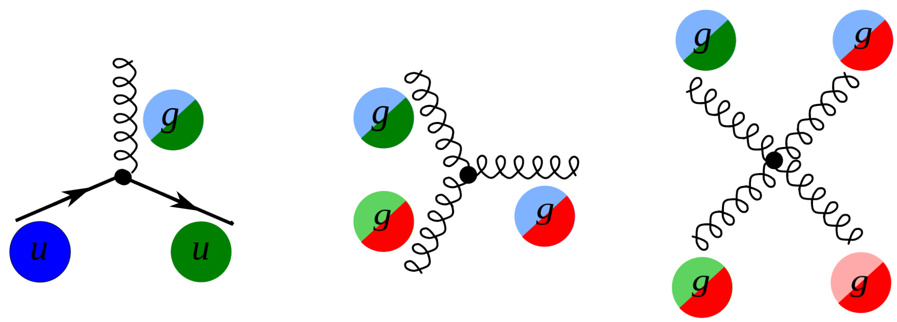

Figure 1.5: Elementary processes of strong interations

The third fundamental force after the electromagnetic and weak ones is the strong force. The strong force is responsible for gluing protons and neutrons together in the nuclei as well as for forming protons and neutrons themselves. The strong interactions occur by exchanging gluons which are spin-one massless electrically neutral particles.

The elementary strong processes are shown in Fig. 1.5. There are three elementary processes: qqg, ggg and $gggg$, all are involving particles with color charges. Thus, gluons couple to quarks and self-couple. Color charges must be conserved at each elementary vertex of the strong interaction. Each quark possesses one of three colors at a time, and there are eight types of gluons to cover all possible color exchanges.

The coupling constant of the strong interaction depends on the distance between interacting particles: it becomes larger as the distance becomes larger and smaller as the distance becomes smaller. As the distance approaches zero, the coupling constant approaches zero too, and, thus, in the asymptotic limit two quarks located at the same place do not interact. This property is called asymptotic freedom.

On the other hand, when the distance between quarks becomes larger, the coupling constant also becomes larger. This property confines quarks to always stay in the color neutral combinations (hadrons); it forbids the existence of free quarks. A combination becomes color neutral when there is the same amount of color and anticolor or if there is the same amount of each of the three colors. Thus, mesons are comprised of a quark and an antiquark with the opposite color charges, and baryons are composed of three quarks: red, green and blue. Examples of baryons include such well-known particles as a proton and a neutron.

The asymptotic freedom and the confinement are properties that are specific to strong interactions. The theory of strong interactions is called the quantum chromodymanics (QCD) which is a quantum field theory invariant under $SU(3)$ color transformations. When the coupling constant is much less than one, $\alpha_s \ll 1$, the perturbative approach can be used to compute observables.

The Wγ process being measured in this dissertation is not intended to test QCD, but a good understanding of QCD is essential for performing this measurement because the QCD corrections to the Feynman diagrams of the process are large. In addition, QCD describes the dynamics of quarks and gluons within colliding protons and predicts probabilities of one or another quark-antiquark pair to interact. Physics of proton-proton collisions is discussed in Ch. 1.4.

1.4 Physics of Proton-Proton Collisions

A proton is a baryon; it consists of three quarks: uud. These three quarks are called valence quarks. They interact with each other by exchanging gluons which produce virtual $q\bar{q}$ pairs (Fig. 1.6). Such virtual quarks are also called sea quarks.

Consider a pp collision at LHC. The proton energies are so high that we can probe the proton substructure. Any parton, which can be a quark, an antiquark or a gluon, from one proton can interact with any parton from another proton. Probabilities $f_i(x, Q^2)$ of any particular constituent i to interact are described partially by QCD and partially by experimental measurements and depend on the momentum transfer Q and the momentum fraction of a specific parton x. These probabilities are called parton distribution functions (PDFs).

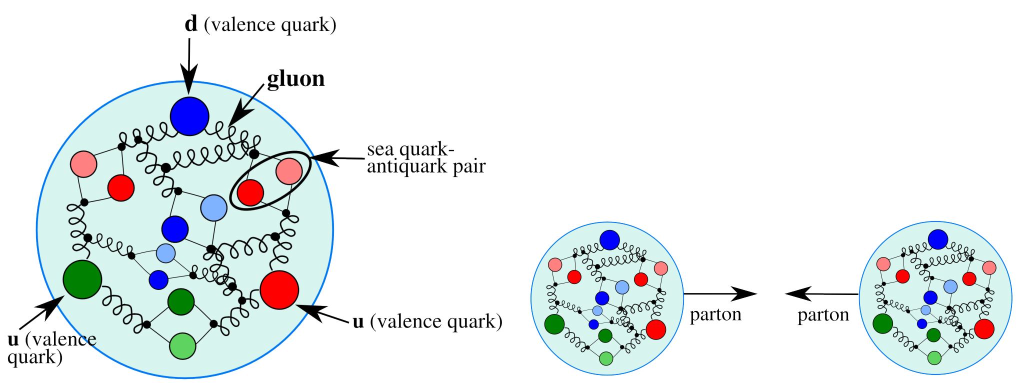

Figure 1.6: The proton structure (left) and the proton-proton collision (right).

For large Q^2 and x, gluon-gluon interactions have the largest probabilities to occur (Fig. 1.7). However, gluons do not couple directly to a W boson, thus in the $W\gamma$ measurement we are mostly interested in quark-antiquark pairs which would have a total charge corresponding to the charge of a W boson (± 1). Since we have u and d as valence quarks and we know that the probability to couple to

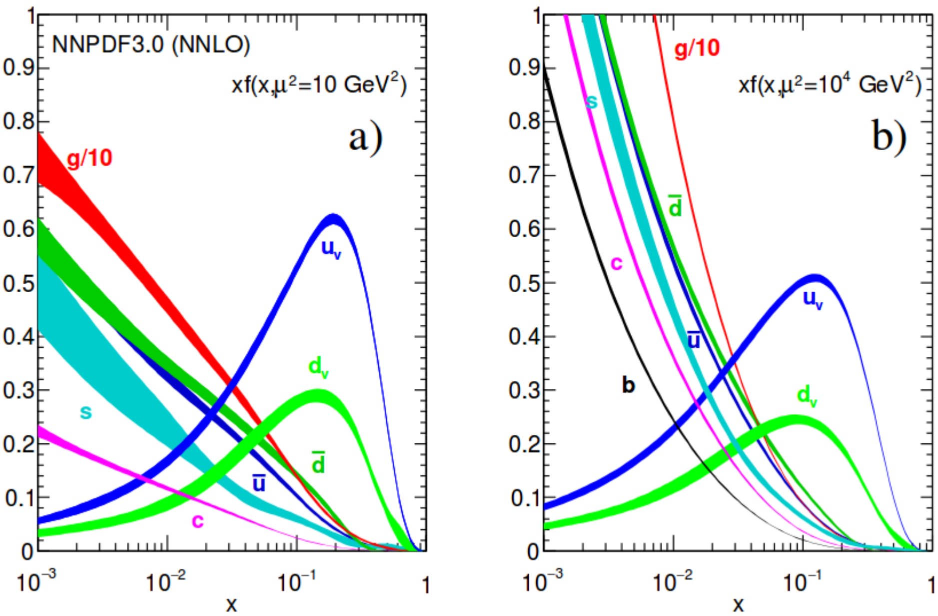

Figure 1.7: Parton distribution functions [1].

the same generation quark in charged weak interactions is the highest, most of the W bosons are created by $u\bar{d}$ and $d\bar{u}$ pairs however other $q\bar{q}'$ combinations with the total charges of ± 1 are also possible.

1.5 Open Questions of the Standard Model

While the SM is an accurate description of all particle physics experimental results, there are certain phenomena which are not included into the SM. In this subsection we discuss some of them.

The gravitational interactions do not fit into the SM. It is an open question whether the quantum theory of gravity is possible and whether there is a mediator of the gravitational interactions. Also, it is not known why the gravitational force is so much weaker than the other forces. One possible explanation comes from a theory which predicts extra spatial dimensions beyond the three we experience (e.g. string theory). In this case, it is possible that the gravitational force is shared with other dimensions and only a fraction is available in our three dimensions.

Another mystery of the universe is its composition: it is known from studies of the gravitational effects that our universe consists of dark energy by 68%, of dark matter by 27% and of baryon matter only by 5% [15]. The dark energy resists the gravitational attraction and accelerates the expansion of the universe, and is not detectable by any effects except gravitational. The understanding of dark energy is a question of general relativity rather than particle physics. Dark matter, however, likely consists of particles and therefore is a subject of particle physics. It does not radiate and that is why it cannot be detected by telescopes. The nature of the dark matter is not known but its constituents must be very stable to remain since the Big Bang. The theory of the supersymmetry which unifies fundamental particles and mediators predicts many new heavy particles and the lightest supersymmetric particle, the neutralino, is a good candidate for dark matter.

One more open question is the reason for the matter/antimatter asymmetry. Matter and antimatter should have been created in the same amount at the moment of the Big Bang. Most of it has annihilated but because of asymmetry, there was more matter than antimatter which led to the state of the Universe we observe now. There is a phenomenon of CP-violation in weak interactions observed and described which predicts the asymmetry at a certain level. However, the effect of CP-violation is not large enough to account for the observed amount of the matter and, therefore, the total matter/antimatter asymmetry remains unexplained.

The measurement of the $W\gamma$ production in pp collisions has a goal to both test the SM and search for the BSM physics. We measure a cross section differential in the component of the photon momentum, transverse to the beamline (referred as photon transverse momentum, or P_T^γ). The low P_T^γ region is not expected to be affected by any new physics and must agree well with the SM predictions while the high P_T^γ region may indicate an existence of new physics if there is an enhancement over the SM predictions. An excess would be indirect evidence of the BSM particles like supersymmetric particles or additional gauge bosons which could be part of the explanation of the dark matter presence or difference in magnitudes of different interactions. More theoretical details about the SM description of Wγ process as well as possible BSM physics are given in Ch. 2.

2 $W\gamma$ Production Theory and Previous Experimental Results

Chapter 2 provides deeper theoretical background for the measurement of this dissertation and discusses previous experimental results. The derivation of the electroweak Lagrangian is described in Ch. 2.1, including the appearance of triple gauge coupling (TGC) and quartic gauge coupling (QGC) terms. Then concepts of the cross section and the luminosity are discussed in Ch. 2.2. More specific details regarding the SM cross section of $W\gamma$ are summarized in Ch. 2.3. Possible causes and potential effects of anomalous TGC (aTGC) are explained in Ch. 2.4. Finally, Ch. 2.5 lists previous physics experiments which probed the same aTGC vertex which is probed in the measurement of this dissertation including measurments of exactly the same process at lower LHC beam energy.

2.1 Electroweak Theory of the Standard Model

To develop a quantum field theory, we start with the Lagrangian of free fermions. In order to describe a system with a conserved physical quantity, the Lagrangian is required to satisfy a local invariance with respect to a certain transformation. For instance, a conservation of electric charge requires local invariance under a $U(1)$ transformation for the QED Lagrangian [16]. The requirement of local invariance introduces an interaction between one or more new vector fields and our free fermions. The new vector fields are mediators of an interaction conserving the physical quantity. To provide a full description for a new boson field, in addition to the interaction term we introduce an invariant term for the kinetic energy of the boson. Such an approach allows us to derive a Lagrangian which is locally invariant with respect to a certain gauge transformation and contains interacting fermions as well as interaction mediators.

The SM is a quantum field theory invariant under the local $SU(3)_C \times SU(2)_L \times U(1)_Y$ transformation [16]. The SM Lagrangian includes all observed quantum fields and their interactions.

The part of the SM Lagrangian based on the $SU(3)_C$ symmetry is called QCD or the theory of strong interactions. QCD has three types of charges which are called colors: red, blue, and green. To be a subject of the strong interaction, a fermion must posses a color charge. Quarks and antiquarks are such fermions. The requirement to satisfy the gauge invariance with respect to $SU(3)_C$ transformations generates eight massless gluons, and the non-abelian nature of the $SU(3)$ group generates self-interactions of gluons including three-gluon and four-gluon vertices.

The part of the SM Lagrangian based on the $SU(2)_L \times U(1)_Y$ symmetry is the foundation of the unified theory of electroweak interactions. $SU(2)_L$ reflects transformations in the weak isospin space of left-handed fermions ([17], Ch. 9) while $U(1)_Y$ reflects transformations in a weak hypercharge space of all fermions. The requirement of the local gauge invariance generates four massless vector bosons which are mediators of electromagnetic and weak interactions. The non-abelian structure of the $SU(2)$ group generates gauge boson self-couplings the same way as self-interactions of gluons appear in QCD.

Mass terms for the vector bosons would violate the gauge invariance of the electroweak Lagrangian, however it is experimentally known that the mediators of weak interactions are heavy particles with masses $M_W = 80$ GeV and $M_Z = 91$ GeV. A possible solution of this discrepancy is the mechanism of spontateous symmetry breaking.

The mechanism of Spontaneous Symmetry Breaking and the appearance of the mass terms for W and Z bosons is realized by introducing an additional doublet of scalar fields. After that, the Lagrangian is transformed in such a way that W and Z bosons acquire masses through their interactions with a new particle: the Higgs boson (H). A photon does not couple to the Higgs boson remaining a massless particle and leaving QED symmetry group $U(1)$ to be unbroken.

The measurement in this dissertation provides a test for the electroweak sector of the SM. We will retrace the steps of the derivation of the electroweak part of the SM Lagrangian starting from the terms for free fermions. The resulting Lagrangian accommodates electroweak gauge bosons and their self-couplings. One of these self-couplings, $WW\gamma$, is the primary focus of our measurement.

It is experimentally known that the dynamics of weak interactions depend on particle chirality ([17], chapter 4.4.1). In particular, a W boson couples to left-handed fermions and right-handed antifermions only. Given different properties of left-handed and right-handed fermions, they are treated differently by the electroweak theory. $SU(2)$ doublets are introduced for the wave functions of left-handed fermions while $SU(2)$ singlets are introduced for the wave functions of right-handed fermions. Equations 2.1 and 2.2 show wave functions for the first generation fermions. Wave functions for the other two generations are constructed the same way.

$$\psi_1(x) = \begin{pmatrix} u \\ d' \end{pmatrix}_L, \psi_2(x) = u_R, \psi_3(x) = d'_R. \tag{2.1}$$

$$\psi_1(x) = \begin{pmatrix} \nu_e \\ e^- \end{pmatrix}_L, \psi_2(x) = \nu_{eR}, \psi_3(x) = e^-_R. \tag{2.2}$$

The state d' in Eq. 2.1 is a weak eigenstate which is a linear combination of the mass eigenstates of the d, c and b quark wave functions and is determined by the quark mixing matrix, V, which is also called Cabibbo-Kobayashi-Maskawa matrix [16]:

$$\begin{pmatrix} d' \\ c' \\ b' \end{pmatrix} = V \begin{pmatrix} d \\ c \\ b \end{pmatrix} \tag{2.3}$$

To derive the unified electroweak Lagrangian, we start with the free fermion terms:

$$L_0 = \sum_{j=1}^{3} i\bar{\psi}_j(x)\gamma^\mu \partial_\mu \psi_j(x), \tag{2.4}$$

where γ^μ are Dirac matrices ([17], chapter 7.1) and $\psi_j(x)$ are wave functions determined by Eqs. 2.1 and 2.2.

The wave function ψ_1 changes under the $SU(2)_L \times U(1)_Y$ transformations in the following way:

$$\psi_1(x) \rightarrow e^{iy_1\beta} U_L \psi_1(x), \tag{2.5}$$

while the wave functions $\psi_{(2,3)}(x)$ are singlets of $SU(2)_L$ and are affected only by $U(1)$ transformations:

$$\psi_{(2,3)}(x) \rightarrow e^{iy_{(2,3)}\beta} \psi_{(2,3)}(x). \tag{2.6}$$

The transformation in the weak isospin space is defined as $U_L \equiv e^{i\sigma_i \alpha_i/2}$ where σ_i are Pauli matrices ([17], chapter 4.2.2). Phases $\alpha_i(x)$ and $\beta(x)$ in Eqs. 2.5 and 2.6 are arbitrary functions of x, and $y_{(1,2,3)}$ are weak hypercharges which are named analogous to electric charges in QED.

In order for the Lagrangian to satisfy the local $SU(2)_L \times U(1)_Y$ invariance, partial derivatives in Eq. 2.4 have to be substituted with covariant derivatives:

$$D_\mu \psi_1(x) = [\partial_\mu - ig\tilde{W}_\mu(x) - ig' y_1 B_\mu(x)]\psi_1(x) \tag{2.7}$$

$$D_\mu \psi_{(2,3)}(x) = [\partial_\mu - ig' y_{(2,3)} B_\mu(x)]\psi_{(2,3)}(x) \tag{2.8}$$

where g, g' are arbitrary constants,

$$\tilde{W}_\mu(x) \equiv \frac{\sigma_i}{2} W_\mu^i(x) = \frac{1}{\sqrt{2}} \begin{pmatrix} \sqrt{2} W_\mu^3 & (W_\mu^1 - iW_\mu^2)/\sqrt{2} \\ (W_\mu^1 + iW_\mu^2)/\sqrt{2} & -W_\mu^3 \end{pmatrix}, \tag{2.9}$$

B_μ, W_μ^1, W_μ^2, W_μ^3 are four vector bosons that arise from the requirement that the Lagrangian is invariant under local $SU(2)_L \times U(1)$ transformations.

The Lagrangian becomes:

$$L_0 \to L = \sum_{j=1}^{3} i\bar{\psi}_j(x)\gamma^\mu D_\mu \psi_j(x) \tag{2.10}$$

To make new vector bosons physical fields it is necessary to add terms for their kinetic energies:

$$L_{KIN} = -\frac{1}{4}B_{\mu\nu}B^{\mu\nu} - \frac{1}{4}W^i_{\mu\nu}W_i^{\mu\nu} \tag{2.11}$$

where $B_{\mu\nu} \equiv \partial_\mu B_\nu - \partial_\nu B_\mu$, $W^i_{\mu\nu} \equiv \partial_\mu W^i_\nu - \partial_\nu W^i_\mu + g\epsilon^{ijk}W^j_\mu W^k_\nu$

Off-diagonal terms of $\tilde{W}_\mu$ are wave functions of charged vector bosons

$$W^\pm = (W^1_\mu \mp iW^2_\mu)/\sqrt{2} \tag{2.12}$$

while W^3_μ and B_μ are neutral fields which are mixtures of a Z boson and a photon determined by:

$$\begin{pmatrix} W^3_\mu \\ B_\mu \end{pmatrix} \equiv \begin{pmatrix} \cos\theta_W & \sin\theta_W \\ -\sin\theta_W & \cos\theta_W \end{pmatrix} \begin{pmatrix} Z_\mu \\ A_\mu \end{pmatrix} \tag{2.13}$$

where θ_W is the electroweak mixing angle and A_μ is a photon field.

In order to be consistent with QED, terms involving A_μ in the electroweak Lagrangian must be equal to the corresponding terms in the QED Lagrangian [16]:

$$L_{QED} = i\bar{\psi}(x)\gamma^\mu\partial_\mu\psi(x) - m\bar{\psi}(x)\psi(x) + qA_\mu(x)\bar{\psi}(x)\gamma^\mu\psi(x) - \frac{1}{4}F_{\mu\nu}(x)F^{\mu\nu}(x), \tag{2.14}$$

where q is electric charge of the $\psi(x)$ field, $F_{\mu\nu} \equiv \partial_\mu A_\nu - \partial_\nu A_\mu$.

This requirement relates g, g', θ_W and q as $g\sin\theta_W = g'\cos\theta_W = e$ and provides an expression for weak hypercharges: $y = q - t_3$, where q is the electric charge and t_3 is the z-component of the weak isospin. This results in $y_1 = 1/6$, $y_2 = 2/3$, and $y_3 = -1/3$ for quarks and $y_1 = -1/2$, $y_2 = 0$, and $y_3 = -1$ for leptons. A right-handed neutrino has a weak hypercharge of $y_2 = 0$. It also does not have an electric charge, and as a right-handed fermion has $t_3 = 0$, therefore, it does not couple to a W boson. Thus, a right-handed neutrino does not participate in any SM interaction.

Writing $\tilde{W}_\mu$ in Eq. 2.11 explicitly, we obtain triple gauge coupling (TGC) and quartic gauge coupling (QGC) terms:

$$L_{TGC} = -\frac{g}{4}(\partial_\mu W_\nu^i - \partial_\nu W_\mu^i)\epsilon^{ijk}W^{\mu j}W^{\nu k} - \frac{g}{4}\epsilon^{ijk}W_\mu^j W_\nu^k(\partial^\mu W^{\nu i} - \partial^\nu W^{\mu i}) \qquad (2.15)$$

$$L_{QGC} = -\frac{g^2}{4}\epsilon^{ijk}\epsilon^{ilm}W_\mu^j W_\nu^k W^{\mu l}W^{\nu m} \qquad (2.16)$$

Substituting expressions for W_μ^i and B_μ determined by Eqs. 2.12 and 2.13 into Eqs. 2.15 and 2.16 we receive charged TGC and QGC terms in the Lagrangian (those involving two or four W bosons) in the forms of Eqs. 2.17 and 2.20, but all neutral TGC and QGC terms (those not involving any W bosons) cancel out.

Equation 2.17 involves WWZ (Eq. 2.18) and $WW\gamma$ (Eq. 2.19) interactions:

$$L_{TGC} = L_{TGC}^{(1)} + L_{TGC}^{(2)}, \qquad (2.17)$$

$$L_{TGC}^{(1)} = -ie\cot\theta_W(W^{-\mu\nu}W_\mu^+Z_\nu - W^{+\mu\nu}W_\mu^-Z_\nu + W_\mu^-W_\nu^+Z^{\mu\nu}), \tag{2.18}$$

$$L_{TGC}^{(2)} = -ie(W^{-\mu\nu}W_\mu^+A_\nu - W^{+\mu\nu}W_\mu^-A_\nu + W_\mu^-W_\nu^+F^{\mu\nu}). \tag{2.19}$$

Equation 2.20 involves $WWWW$ (Eq. 2.21), $WWZZ$ (Eq. 2.22), $WWZ\gamma$ (Eq. 2.23), and $WW\gamma\gamma$ (Eq. 2.24) interactions:

$$L_{QGC} = L_{QGC}^{(1)} + L_{QGC}^{(2)} + L_{QGC}^{(3)} + L_{QGC}^{(4)}, \tag{2.20}$$

$$L_{QGC}^{(1)} = -\frac{e^2}{2\sin^2\theta_W}(W_\mu^+W^{-\mu}W_\nu^+W^{-\nu} - W_\mu^+W^{\mu+}W_\nu^-W^{-\nu}), \tag{2.21}$$

$$L_{QGC}^{(2)} = -e^2\cot^2\theta_W(W_\mu^+W^{-\mu}Z_\nu Z^\nu - W_\mu^+Z^\mu W_\nu^-Z^\nu), \tag{2.22}$$

$$L_{QGC}^{(3)} = -e^2\cot\theta_W(2W_\mu^+W^{-\mu}Z_\nu A^\nu - W_\mu^+Z^\mu W_\nu^-A^\nu - W_\mu^+A^\mu W_\nu^-Z^\nu), \tag{2.23}$$

$$L_{QGC}^{(4)} = -e^2(W_\mu^+W^{-\mu}A_\nu A^\nu - W_\mu^+A^\mu W_\nu^-A^\nu). \tag{2.24}$$

In the measurement of this dissertation we probe the $WW\gamma$ coupling (Eq. 2.19).

The unified electroweak Lagrangian discussed above involves kinetic energy terms for fermions and gauge bosons as well as interactions of fermions with gauge bosons, TGC, and QGC. However, this Lagrangian does not contain any mass terms. Because left-handed and right-handed wave functions transform differently under the electroweak symmetry, adding fermion mass terms of $\frac{1}{2}m_f^2\bar{\psi}\psi$ would violate the Lagrangian invariance and, therefore, fermion mass terms are forbidden by the $SU(2) \times U(1)$ symmetry requirement. Mass terms for gauge bosons also would violate the Lagrangian invariance just as a photon mass term $\frac{1}{2}m^2 A^\mu A_\mu$ would violate $U(1)$ invariance of L_{QED} [17]. Therefore, Lagrangian L in Eq. 2.10 contains massless particles only.

However, it is known from experiments that the Z and W bosons as well as fermions are massive particles and, therefore, our theory should accommodate their masses. To introduce masses into the electroweak Lagrangian, an $SU(2)_L$ doublet of complex scalar fields $\phi(x)$ is added to the Lagrangian:

$$\phi(x) \equiv \begin{pmatrix} \phi^{(+)}(x) \\ \phi^{(0)}(x) \end{pmatrix} \tag{2.25}$$

By selecting a special gauge for $\phi(x)$ it is possible to spontaneously break electroweak symmetry, generate a new scalar particle, the Higgs boson [16], and introduce mass terms for W and Z bosons and the charged fermions through their couplings to the Higgs boson. The strength of the coupling constant is proportional to the square of the particle's mass, therefore, heavier particles are more likely to interact with H, and massless particles do not couple to H.

The mechanism of generating a fermion's mass involves both left-handed and right-handed components of the fermion. If our hypothesis that right-handed neutrinos do not exist is right, then the Higgs mechanism does not generate neutrino masses. However, from the experiments of neutrino oscillations, neutrinos are known to have masses even though they are orders of magnitude smaller than those of other fermions. Several hypotheses have been offered to resolve this contradiction however at the moment the mechanism for neutrinos to acquire masses remain unknown [1].

In this dissertation, we study an electroweak process $W\gamma \rightarrow l\nu_l\gamma$ and probe the TGC vertex $WW\gamma$ (Eq. 2.19). To do that, we measure the differential cross section of $W\gamma \rightarrow l\nu_l\gamma$ with respect to the photon transverse momentum. The concept of the cross section in particle physics is discussed in the next section.

2.2 Cross Section and Luminosity

In this dissertation we measure the total cross section of the process $pp \rightarrow l\nu_l\gamma + X$ and its differential cross section in transverse momentum of the photon. A cross section in particle physics is an interaction probability per unit flux of incident particles [18]. It can be interpreted as an area which must be crossed by an incident particle in order to interact with a scattering center, or, in case of a differential cross section, area $d\sigma$ within which an incident particle must appear to be scattered off by an angle $d\theta$ (Fig. 2.1). The relationship between $d\sigma$ and $d\theta$ gives us the expression for a differential cross section $d\sigma/d\theta$. Integrating over $d\theta$, we obtain the total cross section σ. The cross section concept illustrated in Fig. 2.1 is generalized to be an effective area, and is generalized for two (or more) particle interactions rather than a light particle scattering off a stationary center.

The angle θ here is used only as an illustration of a concept of differential cross section. In particle physics we measure a differential cross section with respect to a parameter X which can be a parameter of one of the final state particles or of a system of final state particles. For example, a cross section could be measured as a function of the transverse momentum of a final state photon P_T^γ, the invariant mass of two final state leptons m_{ll}, or even of discrete observables such as the number of jets associated with the process N_{jets}.

In the scenario illustrated in Fig. 2.1, the number of particles passing through the area σ per unit time is

$$N = L \cdot \sigma, \tag{2.26}$$

where L is the flux of incident particles and is called luminosity. For colliding

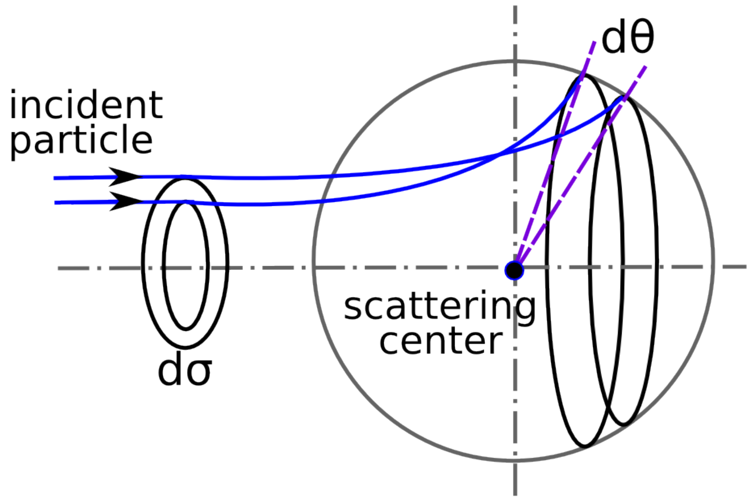

Figure 2.1: Illustration of the differential cross section concept in the classical case.

beams, the luminosity is determined by collisions frequency, the number of colliding particles in each beam, and beams cross sections. The cross section σ of a specific process can be determined from an experiment as $\sigma = N/L$.

A cross section can be computed theoretically using the following expression:

$$\sigma = \frac{W_{fi}}{F} N_{fs}, \tag{2.27}$$

where W_{fi} is a transition probability between final and initial states of the system per unit spatial volume, F is the initial flux, and N_{fs} is the density of final states ([19], chapter 4.3). The initial flux in this expression is determined as number of incident particles per unit volume multiplied by their velocity and by the number of target particles per unit volume.

The formula for the cross section relevant for our measurement, two particles to three final state particles scattering $1 + 2 \rightarrow 3 + 4 + 5$, is determined by the Fermi's Golden Rule [17]:

$$\sigma = \frac{1}{4\sqrt{(p_1p_2)^2 - (m_1m_2)^2}} \int |M|^2 (2\pi)^4 \delta^4 (p_1 + p_2 - p_3 - p_4 - p_5) \prod_{j=3}^{5} \frac{1}{2\sqrt{\bar{p}_j^2 + m_j^2}} \frac{d^3\bar{p}_j}{(2\pi)^3}, \tag{2.28}$$

where p_i are four-momenta and $\bar{p}_i$ are three momenta of the initial state and the final state particles, m_i are masses of particles, M is the process amplitude determined by the dynamics of the particles interaction. All possible momenta of the final state particles is called the phase space.

During proton-proton collisions at high energy, the hard scattering process occurs between partons in the protons, as discussed in Ch. 1.4. Therefore, the cross section of a process $pp \to X + Y$ has two ingredients: PDFs and a partonic cross section $\sigma_{ab \to X}$. The partonic cross section is described by perturbative QCD while PDFs require non-perturbative computations and are determined, in part, from experiments (Fig. 1.7). According to the QCD factorization theorem [20]:

$$\sigma(pp \to X + Y) = \sum_{a,b} \int dx_a dx_b f_a(x_a, Q^2) f_b(x_b, Q^2) \sigma(ab \to X). \tag{2.29}$$

In the case of a $W\gamma$ process, X is $l\nu\gamma$, ab are $q_i\bar{q}_j$ or $q_j\bar{q}_i$. Q^2 is the large momentum scale that characterizes hard scattering, f_a and f_b are PDFs, x_a and x_b are fractions of momenta of the partons. In the next sections we will discuss the computation of partonic cross sections of the $W\gamma$ process and possible BSM effects.

2.3 Standard Model $W\gamma$ Production

A W boson in proton-proton collisions can be produced in the processes $q\bar{q}' \rightarrow W$ where q and $\bar{q}'$ are a quark and an antiquark which have a total charge of $+1$ if producing a W^+ boson or -1 if producing a W^- boson. The processes $u\bar{d} \rightarrow W^+$ and $d\bar{u} \rightarrow W^-$ are the most likely to occur because u and d are valence quarks in a proton. There are twice as many u quarks in a proton as d quarks, therefore, W^+ is produced twice more frequently than W^-. Antiquarks $\bar{d}$ and $\bar{u}$ come from the sea $q\bar{q}$ pairs of the other proton.

Once created, a W boson decays immediately; its lifetime is $\simeq 10^{-25}$ s. In an experiment one detects its decay products rather than the W boson itself. Decay modes of a W boson include $W^\pm \rightarrow l^\pm \nu_l(\bar{\nu_l})$ where $l^\pm = e^\pm$, $\mu^\pm$ or $\tau^\pm$ with branching fractions of 11% per a leptonic channel [1]. The remaining 67% account for various $W \rightarrow q\bar{q}'$ decays. In this dissertation we only consider $W^\pm \rightarrow \mu^\pm \nu_\mu(\bar{\nu_\mu})$ and $W^\pm \rightarrow e^\pm \nu_e(\bar{\nu_e})$ channels.

A photon can be emitted from any charged particle of the process: a quark, an antiquark, a charged lepton or a W boson (Fig. 2.2, top). A quark and an antiquark are initial state particles and, therefore, if one of them radiates a photon, we refer to the process as initial state radiation (ISR). A muon or an electron is a final state particle and if it radiates a photon, we call such a process final state radiation (FSR). Finally, a W boson is a gauge boson and if it radiates a photon, the process has a vertex with three gauge bosons: $WW\gamma$, and we call such process the triple gauge coupling (TGC). We cannot distinguish between these processes experimentally because we detect final state particles only.

The electroweak Lagrangian is described in Chapter 2.1. It is possible to derive equations of motion from the Lagrangian for any fields involved [17]. However, in

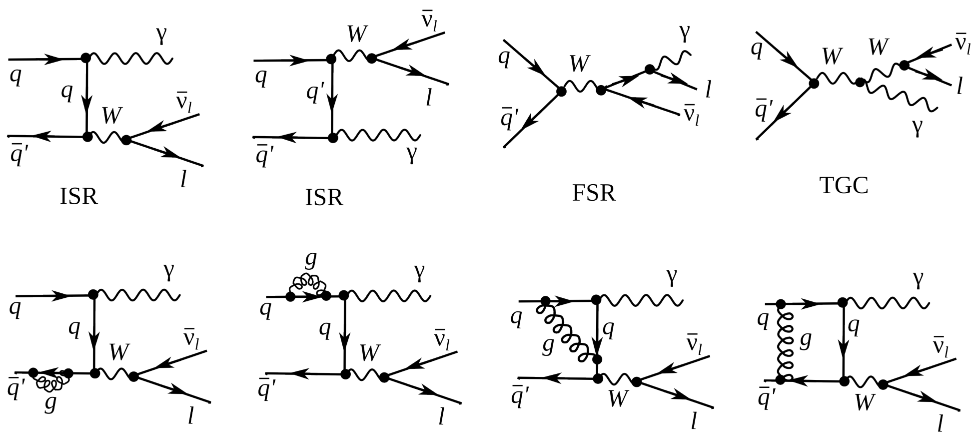

Figure 2.2: Feynman diagrams of Wγ production. Top: LO diagrams, bottom: several examples of NLO in QCD.

a quantum field theory equations of motion cannot be solved exactly and, therefore, the perturbative approach is used if a coupling constants is $g \ll 1$.

To represent the process graphically Feynman diagrams were invented. Also the diagrams can be used to calculate the process amplitude M in Eq. 2.28 because they are determined by Lagrangian terms relevant to the process. There are an infinite number of Feynman diagrams corresponding to any specific process and the total amplitude of the process is a sum of individual amplitudes of each diagram and it is not technically possible to take into account all of them. Each vertex introduces a factor in the amplitude of the process that is proportional to the coupling constant. If the coupling constant is $g \ll 1$, the perturbative approach arranges all the diagrams by orders of contribution, and, therefore, the Feynman diagrams with fewer vertices would give a significantly larger contribution to the amplitude. In Fig. 2.2 examples of the Leading Order (LO) and the Next-to-Leading Order (NLO) Feynman diagrams are shown (top and bottom diagrams respectively).

At LO, the $W\gamma$ process is represented by four Feynman diagrams including one FSR, one TGC and two ISR diagrams. Each LO diagram has three vertices. The first calculation of the $W\gamma$ process with necessary expressions can be found in [21].

The NLO corrections to the amplitude of the $W\gamma$ process that are shown in Fig. 2.2 are QCD corrections only, which include gluon loops at the same quark line and exchange of a gluon between two different quark lines, however, QED and weak NLO diagrams are also possible. QED corrections involve radiations of extra photons by charged particles, exchange of photons between different charged particles or a photon can be radiated and absorbed by the same charged particle forming a loop. Similarly, weak corrections involve extra virtual W or Z bosons. The QCD corrections are the largest among the discussed correction types because the QCD coupling constant is the largest [22].

A theoretical cross section in particle physics is compared to a measurement result to test the predictions of the model. Also the theoretical cross section is used for producing simulated data. In a simulation (often referred as Monte Carlo or MC), a large set of pp collisions resulting in a physics process of interest is modeled to create a data set that mimics real data. A typical simulation consists of two parts: the generation of the process and the simulation of particles paths through the detector. The first stage contains a collection of events with final state particles with kinematic quantities distributed according to theoretical predictions for a given process. This stage relies on the theory including the cross section and also all dynamics of the process. The second stage simulates the interaction with media during propagation of particles through the model of the detector as well as the response of detector electronics. In its final form, a simulated dataset has the same format and content of detector signals for each event as real data, and can undergo the same reconstruction and analysis procedure as real data would.

The most precise theoretical $W\gamma$ cross section available is the Next-to-Next-to-Leading Order (NNLO) cross section in QCD [23]. The effects of the NNLO correction over the NLO correction and over the LO result are shown in Fig. 2.3 for the transverse mass of the final state particles $m_T^{l\nu\gamma}$ and for the rapidity difference between a charged lepton and a photon $\Delta_{l\gamma}$. Rapidity is defined as $y = \frac{1}{2} \ln \left(\frac{E+p_L}{E-p_L} \right)$, where E and p_L are particle's energy and a momentum component along the beam axis respectively. The NNLO and NLO theoretical predictions for the photon transverse momentum p_T^{γ} are overlaid with the 7 TeV ATLAS result. The contribution from higher order corrections is estimated to be $\pm 4\%$. However, the NNLO theoretical result was published only recently, in 2015, and no NNLO $W\gamma$ simulation is available at this time. The simulation used in this analysis is LO + up to two hadronic jets simulation which was found to give the same predictions as the NLO result.

Certain BSM theories predict an enhancement of the contribution from the TGC diagram over the SM prediction. The discussion of these BSM effects and how they affect the $W\gamma$ process takes place in Ch. 2.4.

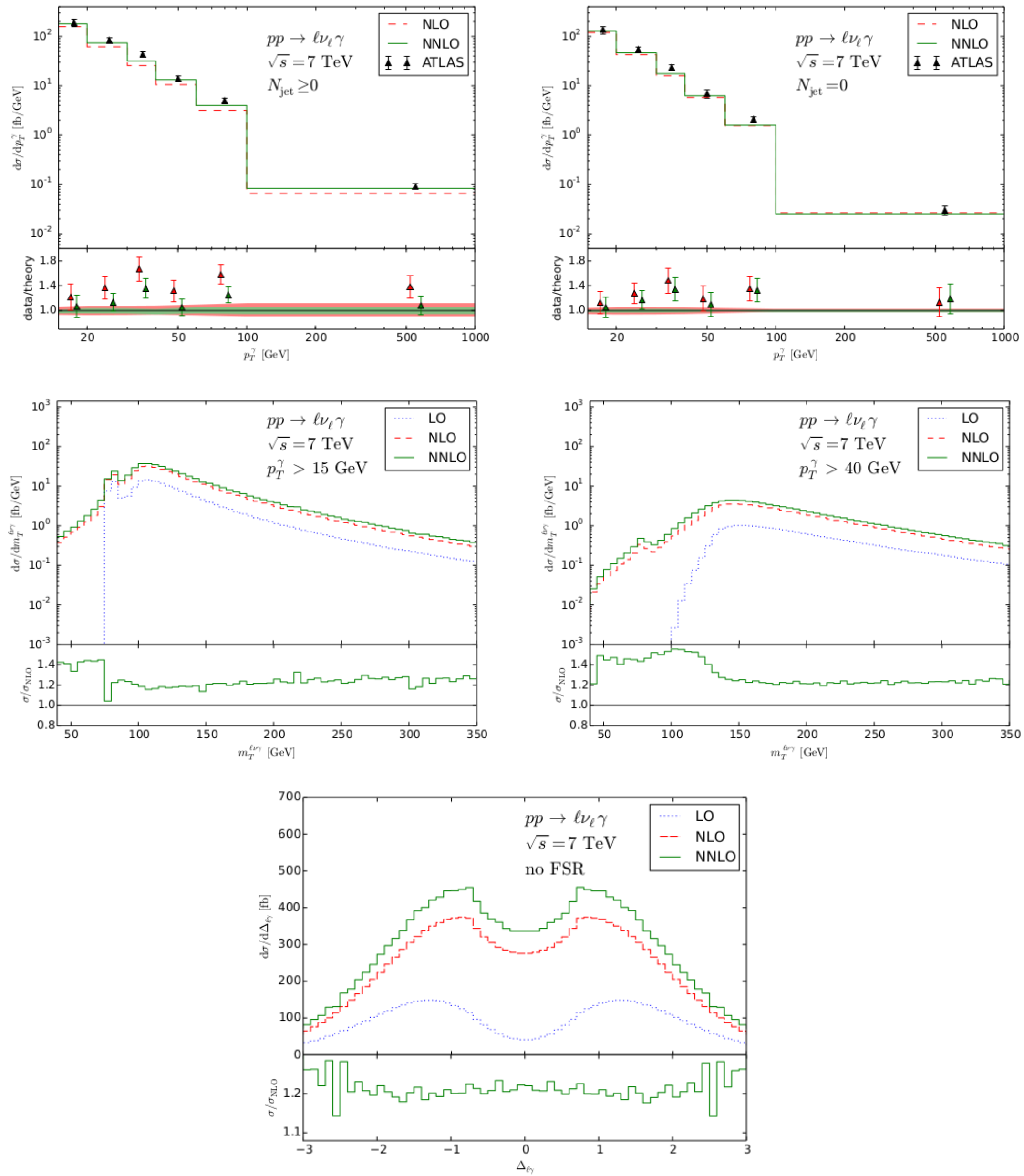

Figure 2.3: Theory spectra. Top: NLO and NNLO p_T^γ spectra of $W\gamma \to l\nu\gamma$ at $\sqrt{s} = 7$ TeV overlaid with ATLAS data for $N_{jet} \geq 0$ (left) and $N_{jet} = 0$ (right). Middle: LO, NLO and NNLO $m_T^{l\nu\gamma}$ spectra of $W\gamma \to l\nu\gamma$ at $\sqrt{s} = 7$ TeV for $P_T^\gamma > 15$ GeV (left) and $P_T^\gamma > 40$ GeV (right). Bottom: LO, NLO and NNLO $\Delta_{l\gamma}$ spectra of $W\gamma \to l\nu\gamma$ at $\sqrt{s} = 7$ TeV.

2.4 Anomalous $W\gamma$ Production

Most BSM physics theories predict the existence of particles with masses larger than those of particles already observed. If their masses are not accessible even at the accelerators with the highest energies, the direct detection of such particles is not possible. However, loops of heavy particles can affect diagrams of production of lighter particles. They would give additional contributions to TGC and QGC couplings and, therefore, to the amplitudes to the processes involving TGC and QGC production. There would be a different number of events produced in the process than one would expect based on SM predictions as shown in Fig. 2.5.

TGC and QGC couplings can be probed by precision measurements of SM processes of diboson and triboson productions because these processes can occur through TGC and QGC. TGC and QGC are represented by vertices with three and four bosons (Fig. 2.4). As discussed in Ch. 2.1, charged TGC and QGC are possible at tree level in the SM while neutral TGC and QGC are not.

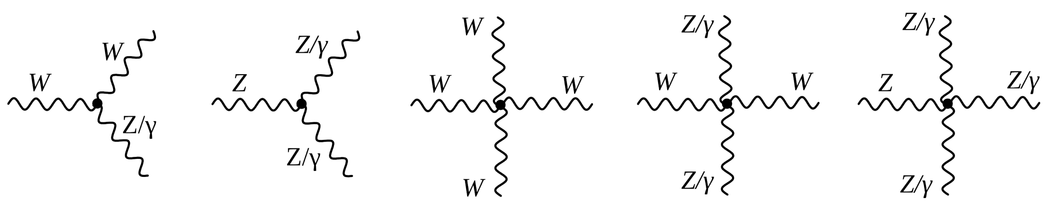

Figure 2.4: Charged TGC (first), neutral TGC (second), charged QGC (third and fourth), and neutral QGC (fifth) vertices. Charged TGC and QGC are SM and neutral TGC and QGC are not.

To account for the effects from the potential loops of heavy particles, we introduce an effective Lagrangian with arbitrary values of coupling constants which can be reduced to the SM Lagrangian if these constants would have their SM values. Introducing the effective Lagrangian makes searches model-independent because we do not specify particles that form the loops but instead just check whether there is a deviation from the SM prediction in measured observables.

In a $W\gamma$ measurement we can probe the $WW\gamma$ vertex. The most general Lorentz invariant Lagrangian terms for $WW\gamma$ interaction takes the following form [24]:

$$iL_{eff}^{WW\gamma} = iL_{eff(1)}^{WW\gamma} + iL_{eff(2)}^{WW\gamma} + iL_{eff(3)}^{WW\gamma}, \tag{2.30}$$

where

$$iL_{eff(1)}^{WW\gamma} = e[g_1^\gamma A^\mu (W_{\mu\nu}^- W^{+\nu} - W_{\mu\nu}^+ W^{-\nu}) + \kappa_\gamma W_\mu^+ W_\nu^- F^{\mu\nu} + \frac{\lambda_\gamma}{m_W^2} F^{\mu\nu} W_\nu^{+\rho} W_{\rho\mu}^-], \tag{2.31}$$

$$iL_{eff(2)}^{WW\gamma} = e[ig_5^\gamma \epsilon_{\mu\nu\rho\sigma}((\partial^\rho W^{-\mu})W^{+\nu} - W^{-\mu}(\partial^\rho W^{+\nu}))A^\sigma + ig_4^\gamma W_\mu^- W_\nu^+ (\partial^\mu A^\nu + \partial^\nu A^\mu)], \tag{2.32}$$

$$iL_{eff(3)}^{WW\gamma} = e[\frac{\tilde{\kappa_\gamma}}{2} W_\mu^- W_\nu^+ \epsilon^{\mu\nu\rho\sigma} F_{\rho\sigma} - \frac{\tilde{\lambda_\gamma}}{2m_W^2} W_{\rho\mu}^- W_\nu^{+\mu} \epsilon^{\nu\rho\alpha\beta} F_{\alpha\beta}], \tag{2.33}$$

where e is the absolute value of the electron charge, A^μ is the photon field, $W^{\pm\mu}$ are the fields of the $W^\pm$ bosons, $W_{\mu\nu} = \partial_\mu W_\nu - \partial_\nu W_\mu$, $F_{\mu\nu} = \partial_\mu A_\nu - \partial_\nu A_\mu$, m_W is the mass of the W boson, g_1^γ, κ_γ, λ_γ, g_5^γ, g_4^γ, $\tilde{\kappa_\gamma}$, and $\tilde{\lambda_\gamma}$ are constants. The $L_{eff(1)}$ of this Lagrangian is the SM piece, and the other pieces are non-SM.

Despite seven constants in the extended Lagrangian, only λ_γ and κ_γ are considered in the aTGC searches. The rest of the constants are fixed to their SM values based on the following considerations. The constants $g_1^\gamma = 1$ and $g_5^\gamma = 0$ are fixed to make the Lagrangian obey the electromagnetic gauge invariance for the on-shell photons. Non-zero values of g_4^γ, $\tilde{\kappa_\gamma}$, $\tilde{\lambda_\gamma}$ violate the CP conservation law. Such violation parametrizations are not considered in charged TGC measurements, thus, constants g_4^γ, $\tilde{\kappa_\gamma}$, and $\tilde{\lambda_\gamma}$ are fixed to zero.

The SM values of λ_γ and κ_γ are $\lambda_\gamma = 0$ and $\kappa_\gamma = 1$. For convenience, the deviation from the SM value is introduced $\Delta\kappa_\gamma \equiv \kappa_\gamma - 1$. These two parameters are tested in $WW\gamma$ aTGC searches because non-zero values of these parameters would not violate any fundamental law.

The most significant effects of aTGC would appear at high energy scales. Figure 2.5 shows this effect in P_T^γ spectrum of 7 TeV $W\gamma \to \mu\nu\gamma$ measurement. As seen in Fig. 2.5, the spectrum with non-zero values of aTGC constants at low P_T^γ coincides with the SM prediction but for higher P_T^γ the disagreement appears.

A common approach to aTGC searches is to measure the spectrum of a kinematic parameter highly correlated with the energy of a final state particle or a system of final state particles. For $W\gamma$ process, the most sensitive variable is P_T^γ. Examining this spectrum allows us to probe and constrain aTGC coupling constants. Chapter 2.5 reviews the experimental results to date on constraining aTGC coupling constants of the $WW\gamma$ vertex.

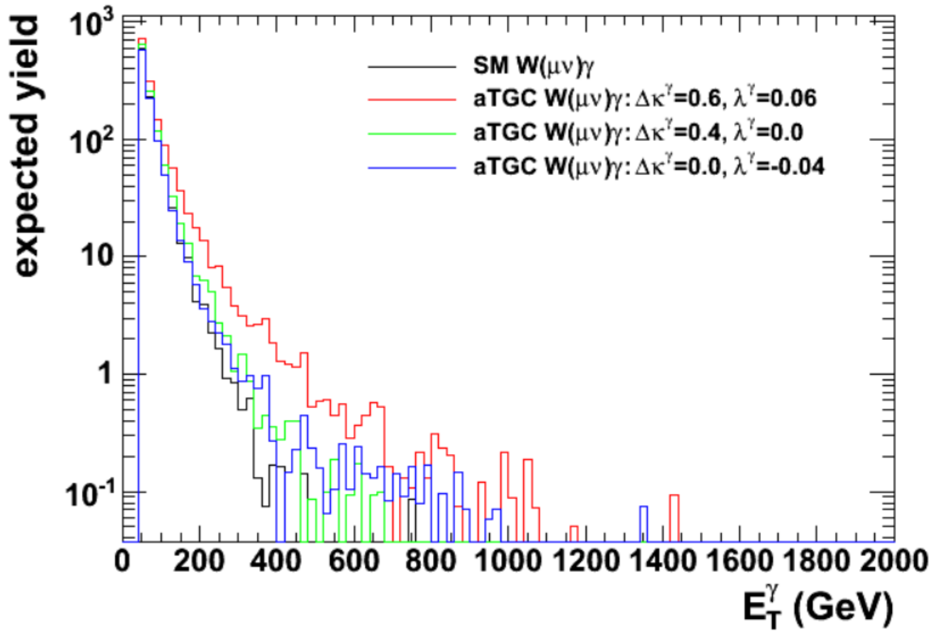

Figure 2.5: Distributions of E_T^γ in simulated $W\gamma \rightarrow \mu\nu\gamma$ events with different values of aTGC constants at LHC energy of $\sqrt{s} = 7$ TeV. For a photon, $P_T^\gamma = E_T^\gamma$. Source of figure: [2].

2.5 A brief history of $W\gamma$ measurements

aTGC parameters of the $WW\gamma$ vertex can be probed in measurements of $W\gamma$, WW, and WZ processes. Limits on the $\Delta\kappa_\gamma$ and λ_γ constants obtained by different experiments are summarized in Fig. 2.6. The summary includes the combination results from D0 [25] and LEP [26] as well as results of several individual measurements by ATLAS and CMS including $W\gamma$ at $\sqrt{s}$ =7 TeV [5], [4], WW at $\sqrt{s}$ =7 and 8 TeV [27], [28], [29], and WV at $\sqrt{s}$ =7 and 8 TeV [30], [31] measurements.

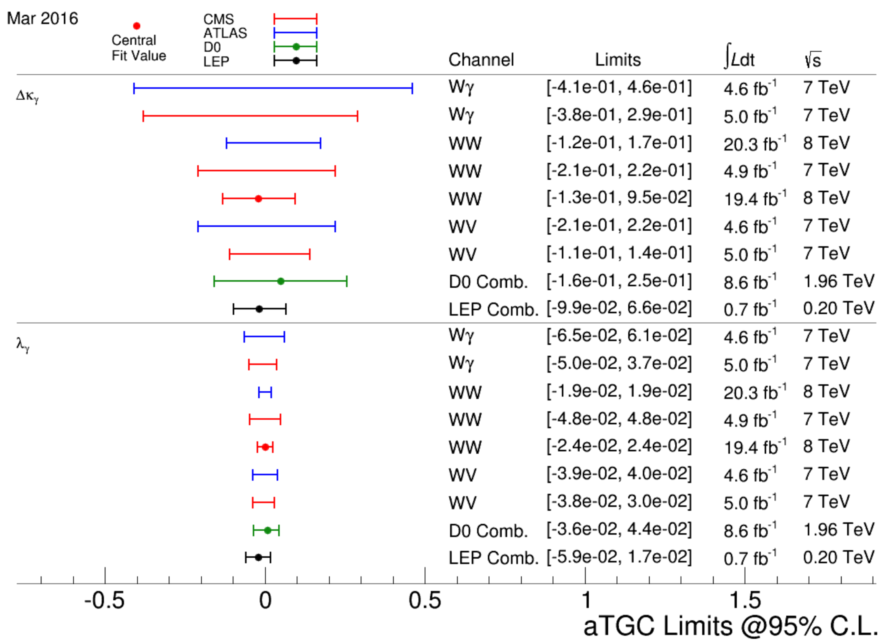

Figure 2.6: Summary of limits on the $WW\gamma$ aTGC coupling constants. Figure from [3].

The most recent measurements of $W\gamma$ production were performed by CMS [4] and ATLAS [5] collaborations with pp collisions at $\sqrt{s} = 7$ TeV collected in 2011. Both collaborations considered two channels: $W\gamma \to \mu\nu\gamma$ and $W\gamma \to e\nu\gamma$.

Diboson processes are rare in pp-collisions and analysts have to filter out events of their interest from many processes which are more likely to happen. To do that, a variety of selection criteria are applied which reject most of the background events to increase the signal fraction in the selected sample as much as possible. However, even after all possible selection criteria are applied, the majority of selected events are still background events and it is not possible to reduce the background any further without also significantly reducing signal.

The major source of such background is the fake photon background where hadronic jets are misidentified as photons. Such events originate mostly from W+jets, but Z+jets and $\bar{t}t$+jets events contribute to this source of background as well. In the electron channel there is one more significant background that is the fake photon background where an electron is misidentified as a photon. Such events are coming from Z+jets events. For the muon channels this background is small. Other sources of backgrounds for both channels include real-γ, fake lepton + real photon and fake lepton + fake photon backgrounds. The major source of real-γ background is the $Z\gamma$ process where a final state lepton and a photon mimics the $W\gamma$ final state. Fake lepton + real photon background originates from the γ+jets process where a jet is misidentified as a lepton. Fake lepton + fake photon backgrounds come from dijet and multijet events where one of the jets is misidentified as a lepton and the other one is misidentified as a photon. The probability of a jet to be misidentified as a lepton is very small, therefore fake lepton + real photon and fake lepton + fake photon backgrounds are negligible.

P_T^{γ} spectra are measured because this variable is the most sensitive to the potential aTGC. The P_T^{γ} spectra of the selected events in data superimposed with selected events in the simulation of the signal and estimated background contribution for the muon and electron channels are shown in Fig. 2.7 for CMS and in Fig. 2.8 for ATLAS measurement. Both measurements show a good agreement between data and the simulation.

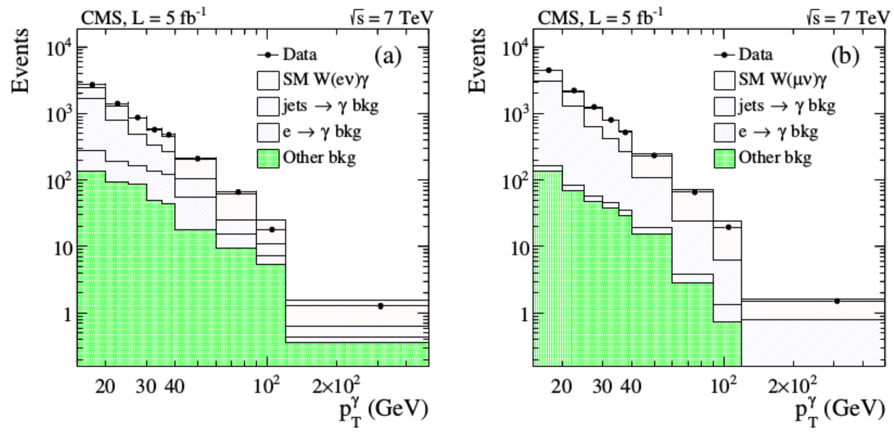

Figure 2.7: The distribution of the p_T^γ of $W\gamma$ candidates in the analysis of 7 TeV CMS data. Data vs signal simulation + background estimates. Left: $W\gamma \to e\nu\gamma$, right: $W\gamma \to \mu\nu\gamma$ [4].

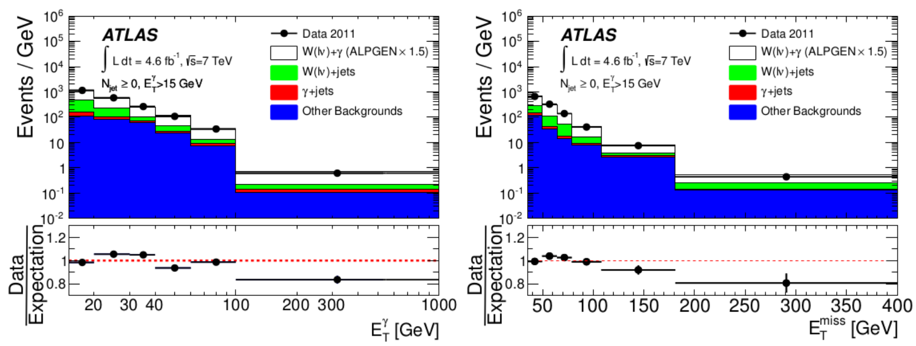

Figure 2.8: The distribution of the photon transverse momentum (left) and missing transverse momentum (right) of $W\gamma$ candidates in the analysis of 7 TeV ATLAS data. Data vs signal simulation + background estimates [5].

The phase space restrictions of $W\gamma$ measurements come from the considerations of the detector acceptance (Ch. 3.2), reducing heavily background-dominated regions and theoretical considerations such as to avoid divergence of the cross section and to reduce ISR and FSR contributions to the cross section.

CMS provides measurements of the P_T^γ spectrum, the total cross section within the phase spaces of $\Delta R > 0.7$, $P_T^\gamma > 15$ GeV, $P_T^\gamma > 60$ GeV and $P_T^\gamma > 90$ GeV.

ATLAS, in addition to the P_T^γ spectrum, total cross section and limits on aTGC constants, provides the differential cross section and cross section with different number of associated jets. The phase space restrictions for ATLAS measurement include requirements on charged lepton kinematics $P_T^l > 25$ GeV, $|\eta_l| < 2.47$, requirements on the transverse momentum of a neutrino $P_T^\nu > 35$ GeV, photon kinematics $P_T^\gamma > 15$ GeV, $|\eta^\gamma| < 2.37$, photon isolation fraction $\epsilon_h^P < 0.5$ and lepton-photon separation $\Delta R(l,\gamma) > 0.7$. For the differential cross section in number of associated jets, the requirements on jet kinematics and jet separation from leptons and photons are also applied: $E_T^{jet} > 30$ GeV, $|\eta^{jet}| < 4.4$, $\Delta R(e/\mu/\gamma, jet) > 0.3$. No evidence of new physics is observed.

The estimated cross sections with any number of associated jets for $P_T^\gamma > 15$ GeV are

$$\sigma(pp \to W\gamma \to l\nu\gamma) = 37.0 \pm 0.8 \text{ (stat.) } \pm 4.0 \text{ (syst.) } \pm 0.8 \text{ (lumi.) pb} \quad (2.34)$$

and

$$\sigma(pp \to W\gamma \to l\nu\gamma) = 2.77 \pm 0.03 \text{ (stat.) } \pm 0.33 \text{ (syst.) } \pm 0.14 \text{ (lumi.) pb} \quad (2.35)$$

for CMS and ATLAS respectively. The results differ between each other because CMS and ATLAS use different phase spaces. Results of both measurements are compared to the NLO theory predictions calculated with the MCFM [32] which is the Monte Carlo calculator designed specifically to calculate cross sections at hadron-hadron colliders at the parton level. The comparison shows an excess of the experimantal results vs the theory prediction which is 31.81 ± 1.8 pb for the phase space used by CMS and of 1.96 ± 0.17 pb for the phase space used by ATLAS. The excess can be explained by NNLO contributions which add $\sim$20% to the NLO values [23].

In addition to the cross sections, both CMS and ATLAS provide limits on aTGC coupling constants $\Delta\kappa_\gamma$ and λ_γ. To do that, samples with non-zero aTGC coupling constants are generated, run through the whole reconstruction and selection procedures, and compared to the measured results of P_T^γ spectra. The results on one-dimensional limits are quoted in Fig. 2.6 while the results on two-dimensional limits can be found in [5], [4].

In this dissertation we are measuring the total and differential $d\sigma/dP_T^\gamma$ cross section. While the aTGC limits are not derived in this dissertation, the measured differential cross section can be used to derive them. The measurement details and results are described in Chapter 5.

3 Experimental Setup

The measurement reported in this dissertation is based on data collected by the CMS detector from the LHC pp collisions in 2012 at $\sqrt{s}$ =8 TeV. The experimental setup for this measurement includes the LHC and the CMS detector that are described in Ch. 3.1 and Ch. 3.2 respectively.

3.1 Large Hadron Collider

The LHC [12, 33, 34] is the largest particle accelerator and the most ambitious particle physics research facility ever built. The LHC accelerates two particle beams up to nearly the speed of light. The beams travel in opposite directions, each in its own beam pipe, in ultrahigh vacuum. The beam is made up of protons which are grouped as bunches separated by several meters from each other. Each bunch contains approximately 10^{11} protons. The bunches of protons are accelerated by varying electromagnetic fields, focused by superconducting quadrupole magnets and steered by dipole magnets. The bunches collide at fixed collision points where particle detectors are placed. Particles are produced in the collisions and registered by the detectors to be subsequently used to accomplish physics goals of the experiments.

The LHC is located in a tunnel at a France-Switzerland border. The tunnel is located as deep as 175 meters underground, and its circumference is about 27 km.

Before entering LHC, particle beams go through several stages of acceleration, and the LHC is the final machine of the chain of the CERN's accelerator complex (Fig. 3.1). Protons are extracted from hydrogen atoms, are accelerated by Linac2 to energies of 5 MeV, and are then injected into the Proton Synchrotron Booster (PSB) where they reach energies of 1.4 GeV. After that, protons are sent to PS and then to Super PS (SPS) where they are accelerated up to 25 GeV and 450 GeV respectively. Finally, protons enter the LHC and are accelerated to reach their collision energies of several TeV per beam. Besides protons, the complex also accelerates and collides lead ions. However, in this dissertation we analyze data from pp collisions only.

Six detectors are installed at the LHC to detect products of hadron collisions and to perform the measurements of the LHC physics program. ATLAS and CMS

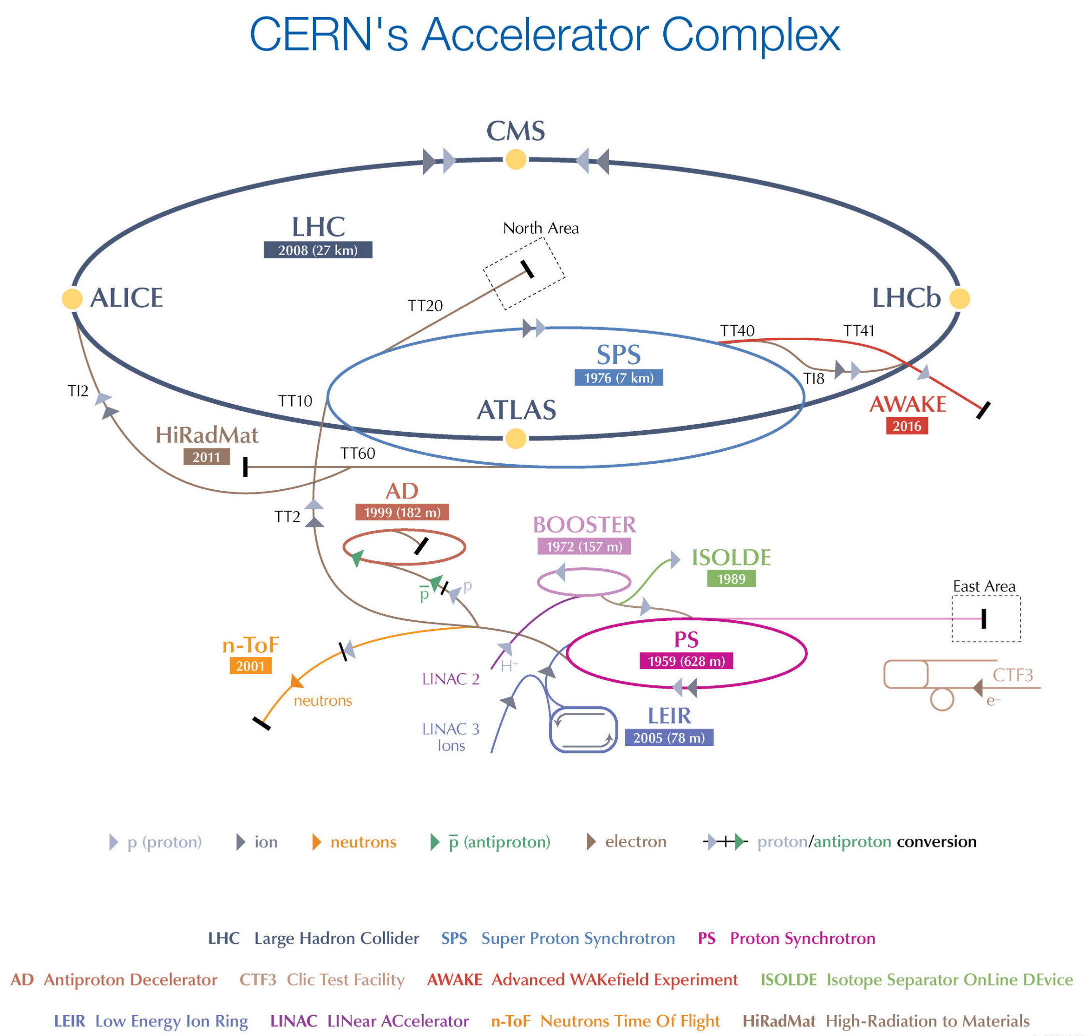

Figure 3.1: CERN's accelerator complex [6].

are general purpose detectors designed to explore a broad spectrum of particle physics questions within and beyond the SM, LHCb specializes in the physics of B mesons, ALICE is designed to detect products of heavy ion collisions, and forward detectors LHCf and TOTEM which are installed close to the ATLAS and CMS collision points respectively.

The design collision energy of the LHC is $\sqrt{s}$ =14 TeV which corresponds to 7 TeV per beam. However, several lower energy points were probed. In 2010-2011 the LHC operated at an energy of 3.5 TeV per beam which was already higher than the energy of any other collider. In 2012 the beam energy was increased up to 4 TeV. In 2013-2014 the LHC was shut down for upgrades. Collisions were restarted at 6.5 TeV in 2015 and continued at this energy in 2016. At any center of mass energy value, both LHC beams have equal energies.

All critical measurements performed at lower energies are also repeated at higher energies. For the BSM searches, the ability to probe higher energy scales increases our chances for a discovery. A SM cross section measurement needs to be done at all energies and compared to the theory since cross sections evolve with energy (Fig. 3.2). While cross sections of parton-parton collisions typically decrease with energy, pp or $\bar{p}p$ cross sections increase because as we go higher in $\sqrt{s}$, more partons in a given protons have enough energy to produce a certain type of interaction. This enables the observation of rarer processes as we increase energy.

In addition to the beam energy, there are many other collider parameters which reflect the ability of the collider to achieve stated goals. A brief summary of them is available in Tab. 3.1. One of the most critical parameters of an accelerator is the luminosity which determines how many interesting events can be produced per unit time (Ch. 2.2). The instantaneous luminosity is determined by the following expression [1]:

$$L^{inst} = f \frac{n_1 n_2}{4\pi\sigma_x\sigma_y} \tag{3.1}$$

where n_1 and n_2 are numbers of particles in colliding bunches, f is a frequency of collisions, σ_x and σ_y characterize sizes of overlapping parts of colliding beams in

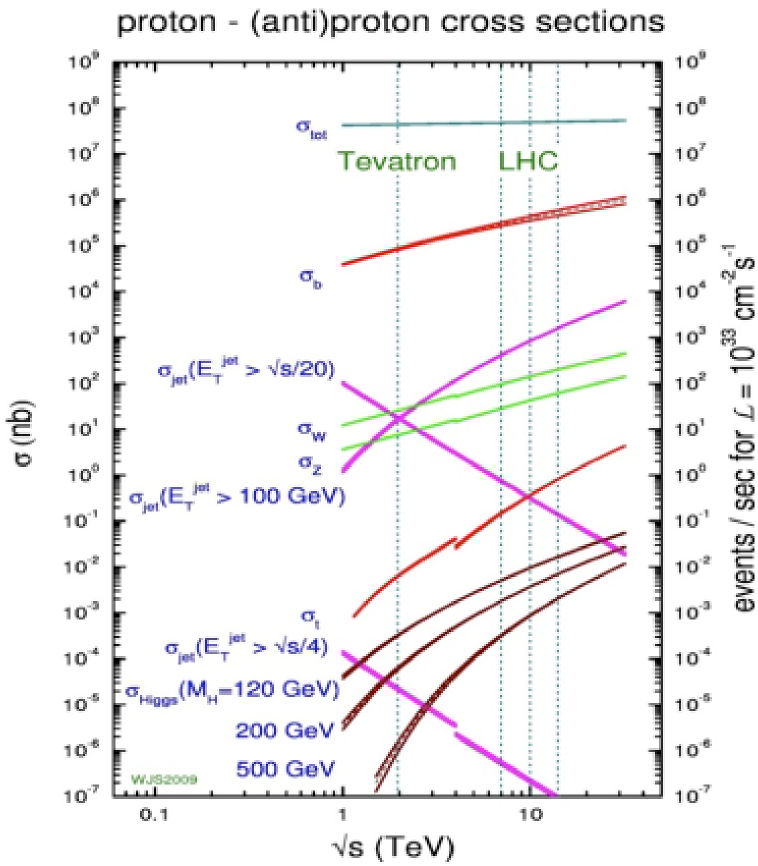

Figure 3.2: Cross sections of different processes in pp and $\bar{p}p$ collisions [7].

horizontal and vertical directions. The instantaneous luminosity multiplied by a cross section of a process gives an event rate (Eq. 2.26) of this specific process. If we know the instantaneous luminosity and the theoretically predicted cross section of the process, we can estimate how many events per unit time of this particular process will be produced by our experiment. To estimate how many events of the process will be produced during a certain time period, we have to use the integrated luminosity, which is an integral of the instantaneous luminosity over time:

$$L = \int L^{inst} dt \tag{3.2}$$

The integrated luminosity of a data sample is a measure of the size of the data sample.

The integrated luminosity of the LHC for pp collisions for different years of the operation is shown in Fig. 3.3. Run I of LHC operations covers run periods of 2010-2012. While running at the energy of $\sqrt{s} = 7$ TeV, LHC delivered L_{int} =45 pb^{-1} and L_{int} =6.1 fb^{-1} of data in 2010 and 2011 respectively. In 2012 the working energy of LHC was $\sqrt{s}$ =8 TeV, and the integrated luminosity was L_{int} =23.3 fb^{-1}. After a long shutdown, LHC was upgraded for Run II, to operate at $\sqrt{s}$ =13 TeV in 2015 and delivered L_{int} =4.2 fb^{-1} of data by the end of 2015. In 2016 LHC continued operating at $\sqrt{s}$ =13 TeV and delivered the integrated luminosity of L_{int} =41.1 fb^{-1} [35].

The measurement of this dissertation is performed at the energy of 4 TeV per beam or the center of mass energy $\sqrt{s}$ =8 TeV with 19.6 fb^{-1} of data collected in 2012. The same process was measured at $\sqrt{s}$ =7 TeV with about four times less data by both CMS and ATLAS. These measurements are discussed in greater detail in Ch. 2.5.

Table 3.1: Main parameters of LHC [12]

Circumference	27 km
Dipole operating temperature	1.9 K
Number of magnets	9593
Number of main dipoles	1232
Number of main quadrupoles	392
Number of RF cavities	8 per beam
Nominal energy, protons	7 TeV
Nominal energy, lead ions	2.76 TeV per nucleon
Peak magnetic dipole field	8.33 T
Min. distance between bunches	7 m
Design luminosity	10^{34} cm^{-2} s^{-1}
No. of bunches per proton beam	2808
No. of protons per bunch (at start)	1.1 × 1011
No. of collisions per second	600 millions

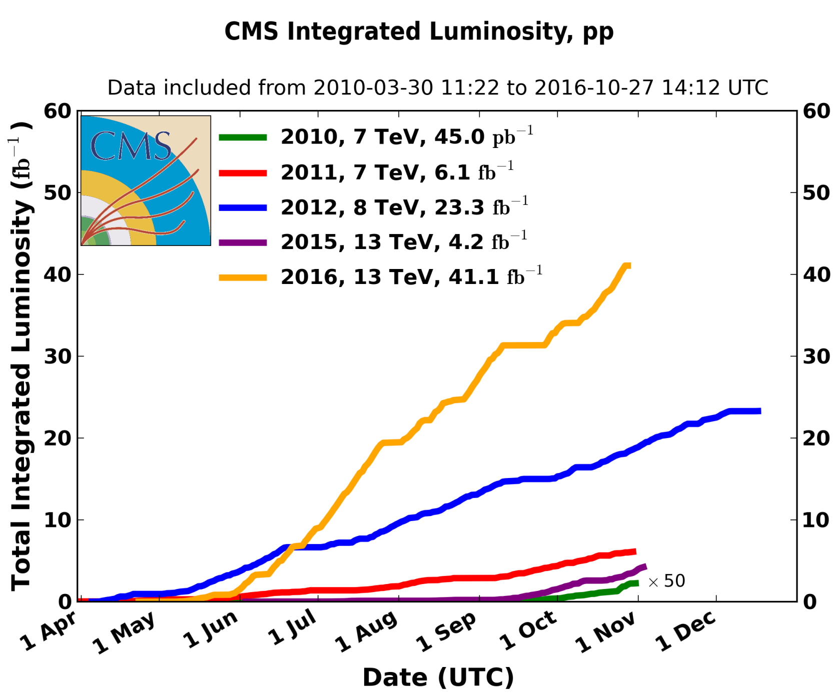

Figure 3.3: LHC integrated luminosity by year [8].

3.2 Compact Muon Solenoid

3.2.1 Introduction

CMS is a general-purpose detector designed to register particles with energies of tens and hundreds GeV that are produced in pp collisions at the LHC [36]. The CMS detector is cylindrically symmetric with the particle beam as the axis. Cartesian, cylindrical and spherical coordinates are all used to describe the CMS geometry, depending on the context. The x-axis of the CMS points towards the center of the LHC ring while the y-axis points vertically up. The orientation of the z-axis corresponds to the counterclockwise direction of the LHC beam (Fig. 3.4). Cylindrical coordinates are defined as $r = \sqrt{x^2 + y^2}$, $\phi = \arctan(y/x)$. Instead of the polar angle θ, it is more convenient to use the pseudorapidity $\eta = -\ln\tan\theta/2$. A pseudorapidity ranges from $\eta = -\infty$ to $\eta = +\infty$ with $\eta = \pm\infty$ for directions parallel to the beam axis and η =0 for a direction perpendicular to the beamline. This variable is convenient for measurements because for typical physics process in pp collisions the created particles tend to be distributed uniformly in η. Another important feature making η a convenient variable is that $\Delta\eta$ values along the beam axis are Lorentz invariants.

Certain particles produced in a collision cannot be registered by CMS due to geometrical limitations of the detector. Charged particles with very low momenta have very large track curvatures and cannot leave the beam pipe. Particles that have trajectories close to parallel to the beamline also cannot be registered by CMS. The range of geometric and kinematic parameters of a particle that allows it to be registered by the detector is called the detector acceptance. The acceptance of the CMS in η is limited and varies from $|\eta| <2.4$ to $|\eta| <5.3$ depending on a subdetector (Fig. 3.5, top).

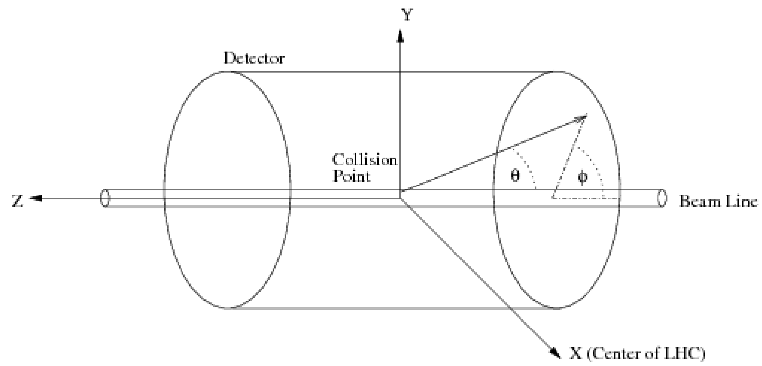

Figure 3.4: CMS coordinate system.

The detector consists, from the inner to the outer layer, of a tracking system, an electromagnetic calorimeter (ECal), a hadronic calorimeter (HCal), a magnet and a muon system. A slice of CMS in the r-ϕ plane is shown in Fig. 3.6. Most subdetectors have three geometrically distinct components: the cylindrical part at the central region (barrel) and the disk-like structures at each end (endcaps). Barrel and endcap regions vary depending on a subdetector but the barrel approximately covers $|\eta| < 1.5$, and endcap $|\eta| > 1.5$.

Most heavy particles produced in a collision decay immediately, and we detect their long-lived decay products including electrons, photons, muons, neutral or charged hadrons. Particles which can be detected by CMS are referred as "visible" particles in contrast to "invisible" particles which cannot be detected by CMS because their probabilities to interact with any part of the detector are very low. The SM example of an invisible particle is a neutrino.

We can identify the type of particle by the trace it leaves in different subdetectors. Charged particles interact with the substance of the tracking system which performs several position measurements of the particles. The sequence of these position measurements is called a track. Neutral particles do not leave any trace in the tracking system because they do not ionize atoms.

Thus, electrons and positrons leave tracks in the tracking system while photons do not. Both these types of particles induce showers in the ECal of the same shapes, and are distinguished by having or not having a spatially matching track. Hadrons normally travel through the ECal undisturbed and induce a hadronic shower in the HCal (Ch. 3.2.5). Charged and neutral hadrons are distinguished from each other by linking or not linking to the tracks, similarly to how electrons are distinguished from photons. Muons are the only particles that penetrate the ECal, the HCal and the magnet and leave tracks in the CMS muon system. Neutrinos are not directly detected by CMS.

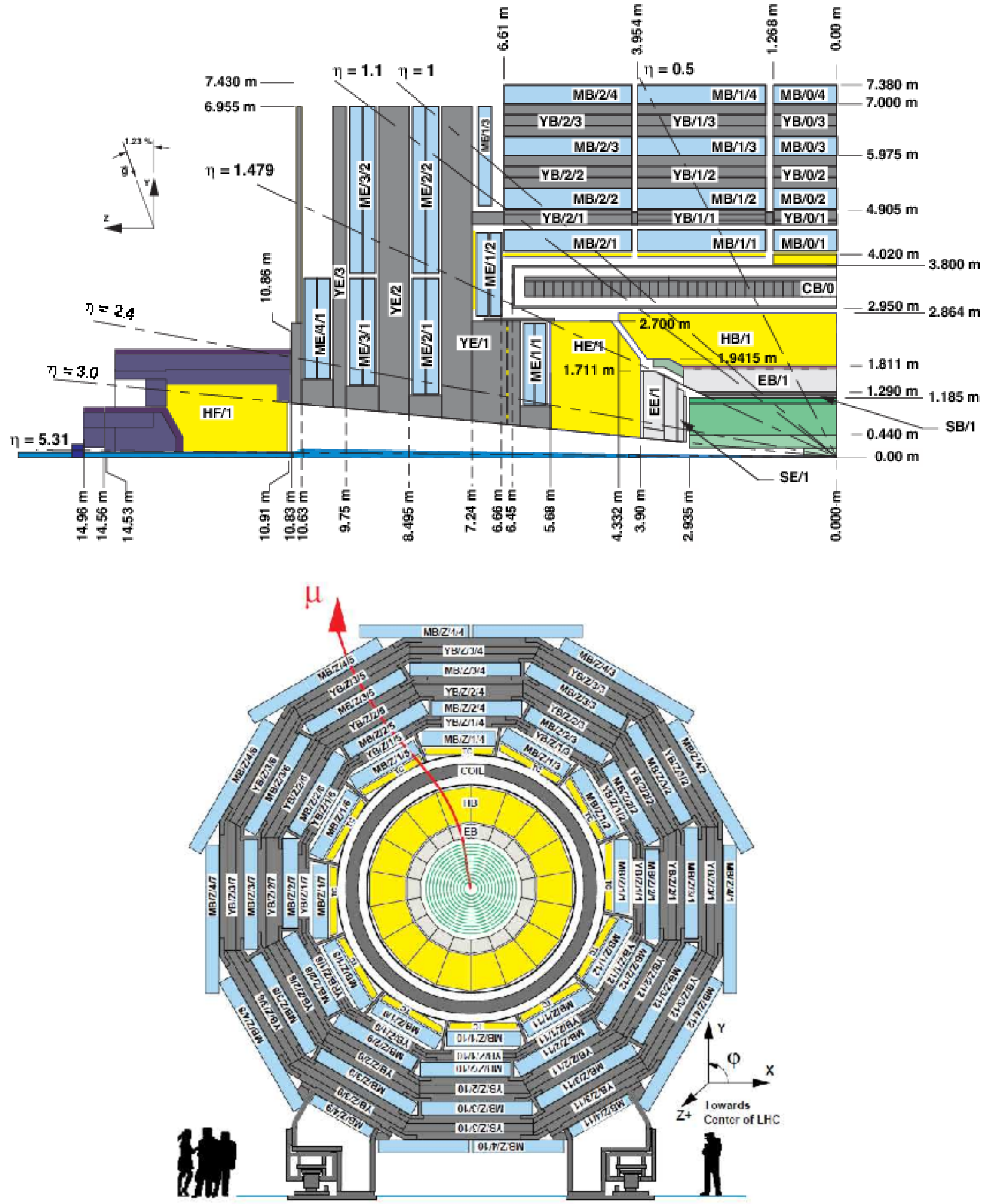

Figure 3.5: CMS detector, schematic view. Top: $r - z$ plane, bottom: $r - \phi$ plane at $z = 0$ [9]. The tracking system is shown in green, barrel and endcap parts of the electromagnetic calorimeter are shown in gray. Barrel, endcap and forward parts of the hadron calorimeter are shown in yellow. HCal is surrounded by a magnet which is shown in gray and white. Muon stations and return yokes are located outside of the magnet and are shown in blue and gray. The red line on the bottom plot is a muon trajectory demonstrating a typical muon that penetrates the whole CMS detector. People at the bottom illustrate the scale of the CMS detector.

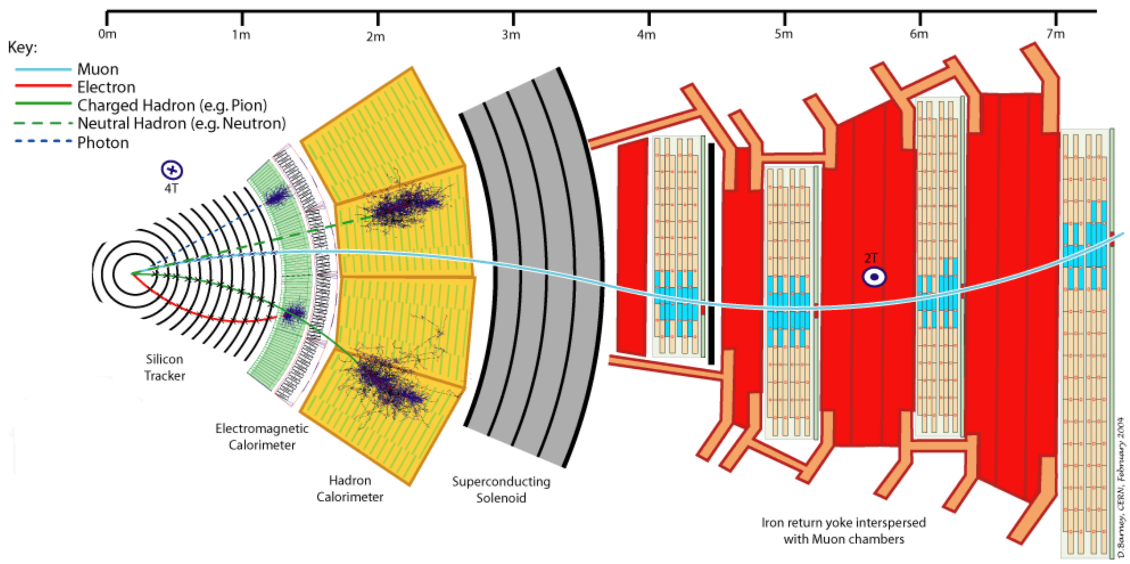

Figure 3.6: CMS detector, a schematic view of a segment in the r-ϕ plane at $z = 0$ [10]. Traces left by muons, electrons, photons, charged and neutral hadrons in different subdetectors are shown.

All subdetectors are essential for the $W\gamma$ measurement, and the remainder of this chapter describes the subdetectors in greater detail. Muons and electrons, which we have as final state particles in the $W\gamma$ measurement, are both affected by the CMS magnetic field, allowing the tracking system and the muon system to measure their trajectory parameters and momenta. ECal measures energy of electrons and photons and is also used to determine a photon's trajectory. The HCal is essential to determine the missing transverse energy which is a measure of a neutrino transverse momentum.

3.2.2 Magnet

A magnetic field in a particle detector is necessary to measure momenta of charged particles by track curvatures. The higher the momentum is, the less a particle trajectory is affected by the magnetic field. In the plane transverse to the beamline, this relation is:

$$R = \frac{P_T}{qB}, \tag{3.3}$$

where R is a radius of a projection of a charged particle's trajectory onto the transverse plane, P_T and q are the particle's transverse momentum and electric charge, and B is the magnetic field. In CMS, the tracking system measures momenta of all charged particles. Also, the muon system measures momenta of muons.

The CMS magnet is placed between the HCal and the muon system. The magnet is made of superconducting wires that are cooled to -268.5^0C by a cryogenic system based on a liquid helium flow [37]. An electric current flowing in the wires creates a uniform field of $B =$4T inside the solenoid, for the tracking system, and also provides a return magnetic field outside the solenoid, for the muon system.

3.2.3 Tracking System

The tracking system measures parameters of charged particle trajectories and their momenta, and locations of primary and secondary vertices. The tracking system is designed to disturb a particle as little as possible when it passes through to be able to accurately measure its energy deposit in the ECal or HCal or, in case of a muon, accurately reconstruct a track in the muon system. While there is a large amount of material in the tracker, the precision of the position measurements is sufficient to compensate that. CMS algorithms are capable of reconstructing a trajectory with just a few position measurements ("hits"), each as accurate as $\sim$10 μm in the transverse plane and $\sim$30 μm in the longitudinal direction [38].

Tracks that originate from proton collisions, collision tracks, start at the center and then cross the layers of the tracking system. Charged particles take helical paths in the magnetic field. Tracks are straight in the $r - z$ plane and curved by the magnetic field in the r-ϕ plane. The acceptance of the tracker system in the r-z plane is geometrically limited by the absolute value of the pseudorapidity $|\eta| \leq$2.5.

The tracking system consists of silicon pixels and silicon strips (Fig. 3.7). The pixel tracker is the closest subsystem of CMS to the collision point. Thus, it experiences the largest particle flux: at 8 cm from the collision point the flux is about 10 million/(cm^{2}s), and the pixel detector with its 65 million pixels is capable of reconstructing all these tracks. It consists of three cylindrical layers of pixel sensors in the barrel with radii of 4 cm, 7 cm and 11 cm which are referred as barrel pixel subdetectors (BPIX) and four disks in the endcap, two disks at each side, which are referred as forward pixel subdetector (FPIX). Pixel modules provide 3D position measurements as well as some of the strip modules while the other strip modules provide 2D position measurements.

The strip tracker is placed right outside the pixel tracker and occupies the detector volume up to 130 cm from the beam axis. The strip tracker consists of four parts: the tracker inner barrel (TIB), the tracker inner disks (TID), the tracker outer barrel (TOB) and the tracker endcap (TEC) as shown in Fig. 3.7.

The resolution of track parameters depends on the type of the reconstructed particle, its transverse momentum and pseudorapidity. For example, the momentum resolution of an isolated muon with P_T^{μ} =100 GeV and η^{μ} =0 is 2% and increases with $|\eta|$ as shown in [38], Fig. 14.

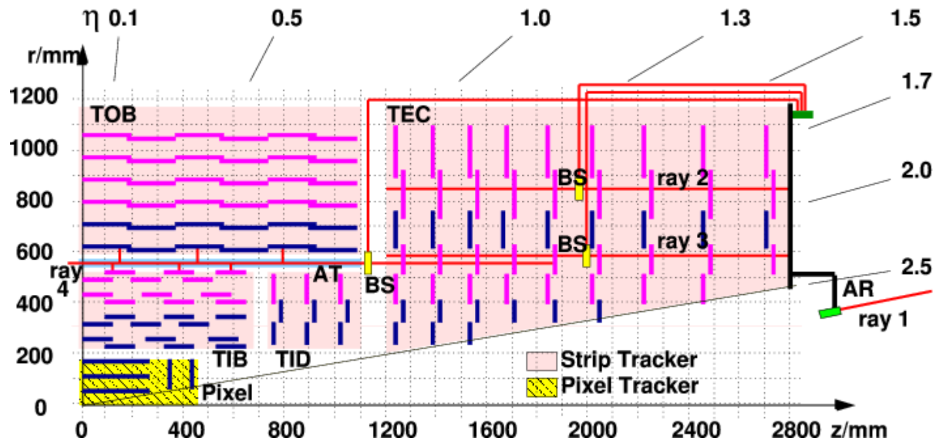

Figure 3.7: Slice of the CMS tracking system in the *r*-*z* plane [39]. Pixel modules and strip modules shown in blue provide 3D position measurements. Strip modules shown in pink provide 2D position measurements.

3.2.4 Electromagnetic Calorimeter

The ECal is placed between the tracking system and the HCal. It is made of high-density lead tungstate crystals arranged in a barrel section and two endcap sections. The crystals are scintillators. When an electron or a photon passes through the scintillators, it initiates an electromagnetic shower. A photon produces an e^+e^- pair while an electron emits a photon. These processes continue as long as photon has enough energy to produce an e^+e^- pair. With this mechanism, the whole energy of the entering particle converts to light. The scintillated light is then amplified by photomultipliers. After that, signals are digitized and taken away by fiber optic cables.

The ECal measures the energy of electrons and photons and parameters of their trajectories. In order to distinguish between electrons and photons, it is necessary to perform spatial matching to the track in the tracking system. If there is a track, then the particle is an electron (or positron), otherwise the particle is a photon.

It is important for the ECal to be able to distinguish between a single energy photons of high energy and pairs of almost collinear photons of lower energy e.g. from a π^0 decay. It is especially difficult in the endcap sections where the angle between two photon trajectories is small. It is achieved with ECal preshower detectors (PS) which are located in front of the endcaps and have ∼15 times smaller granularity. Such a small granularity is achieved by making preshower of two lead planes followed by silicon sensors. The ECal PS provide extra spatial precision.

The ECal energy resolution depends on photon or electron energy and of the ECal pseudorapidity region. The resolution is 2%-5% for electrons from $Z \to ee$, and 1%-5% for photons from $H \to \gamma\gamma$ [40].

3.2.5 Hadron Calorimeter

The HCal measures the energy of charged and neutral hadrons. It consists of the barrel, endcap and forward parts: HB, HE and HF in Fig. 3.5, top, respectively. HCal stops all hadrons passing through, thus, it extends to $|\eta| = 5.3$ for HF.

The HCal is a sampling calorimeter. It consists of alternating layers of brass absorbers and plastic scintillators. When a hadron hits an absorber, it induces a hadronic shower. Interacting strongly with the absorber's nucleons, the hadron produces secondary hadrons. When hadrons reaches the layer of the scintillator, they interact with the scintillator's nucleons, exciting the atoms. Then atoms in the scintillator release light that is collected on optic fibers and passed to the readout system. The total amount of light released in a certain region of the HCal is a measure of hadron's energy.

3.2.6 Muon System

Muons, unlike other visible particles, are not stopped by CMS calorimeters because they neither induce an electromagnetic shower in the ECal nor a hadronic shower in the HCal. The muon system, which is placed outside the magnet and which is the largest part in spatial size of the CMS detector, is designed to register muons.

There are four concentric layers of muon detectors (stations) and the iron return yoke between them. Muons induce several hits in the muon stations which are later fitted and matched to the tracking system measurements to provide the best possible resolution in the measurements of the muon's trajectory and momentum.

There are three types of muon chambers used in the CMS muon system: drift tubes (DTs), cathode strip chambers (CSCs) and resistive plate chambers (RPCs) (Fig. 3.8). Overall, there are 1400 muon chambers including 250 DTs, 540 CSCs and 610 RPCs.

The system of DTs measures positions of muons in the barrel. Each DT chamber is about 2 m by 2.5 m in size. A chamber consists of 12 layers of aluminum which are arranged in groups of four. There are up to 60 DTs in a layer. The middle group of layers measures z-coordinate and two other groups determine the perpendicular coordinate. The DT's volume is filled with a gas, and there is a wire inside. When a charged particle passes through the volume, it ionizes atoms. Released electrons drift in the electric field to the positively-charged wire. The position along the wire is registered, and the distance of the muon away from the wire is calculated providing measurements of two coordinates of the position of the muon.

CSCs are placed in the endcap regions. CSCs are arrays of anode wires crossed by copper cathode strips placed in a gas volume. When a charged particle penetrates the gas volume, it ionizes the gas. Electrons drift to the wires while ions move to the strips, and charge pulses are induced on wires as well as on strips. Strips are perpendicular to wires. Thus, we measure two coordinates for each particle.

RPCs are parallel capacitors made of high-resistivity plastic plates with a space between them filled with gas. RPCs provide quick measurements of muon momenta. A muon passing through the RPC ionizes gas atoms. Released electrons ionize more atoms inducing an avalanche in the electric field. Electrodes receive signal and pass it to external strips that provide a quick measurement of the muon's position which is subsequently transformed to the momentum measurement by the trigger's electronics.

The momentum resolution of the muon system is ∼10% for muons with P_T^{γ} =10 GeV, however, in conjunction with the tracking system it improves to ∼1%. A detailed documentation of the muon system performance is available at [41].

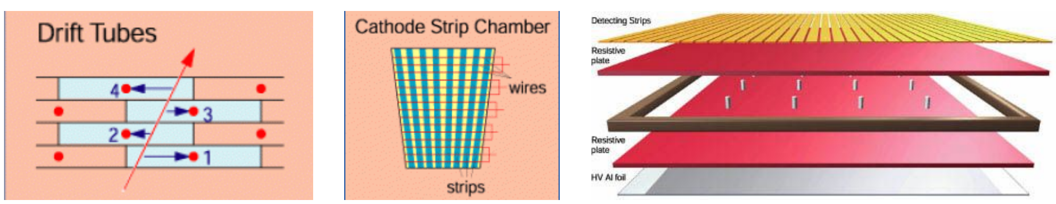

Figure 3.8: Components of the CMS muon system. Left to right: drift tubes (DTs), cathode strip chambers (CSCs), resistive plate chambers (RPCs).

3.2.7 Triggering and Data Acquisition

At peak luminosity, CMS experiences 40 million proton-proton bunch crossings per second that come in bunches separated by 25 ns. It is not technically feasible to read out all these events. Moreover, we do not need most of these events for a physics measurement because most of them have not resulted from an interesting physics process. We have resources to store about 1000 events out of 40 million, and that is why we need a trigger system that quickly decides what the best 1000 events are.

If the triggers were not strict enough, and we would select 1000 events too quickly, e.g., in 1/10 s, then we would not process the remaining 90% of events provided by LHC in a given second and we would lose 90% of potentially interesting events.

If the triggers were too strict, we would select, e.g., 100 events per second, not 1000 and lose the potential to store and process data by 90% which would significantly reduce our chances for discovery and increase statistical uncertainties for precision measurements.

Thus, the challenge of the trigger system is to select the best 1000 events per second and to do this quickly to be able to process every single event. To achieve this goal, a two-level trigger system was developed consisting of the Level 1 trigger (L1T) and the High Level Trigger (HLT) [42].

L1T is a hardware based trigger. It uses information from the ECal, HCal and muon system. L1T reduces the frequency of coming events from 40 MHz to 100 kHz. Events that did not pass the L1T are lost forever while events that pass the L1T are temporarily stored to be checked by the HLT.

HLT is a software-based trigger. It uses information from all subdetectors and runs fast reconstruction and identification algorithms to determine types of particles and their kinematics. It reduces the event rate to 1000 Hz. Events that did not pass HLT are lost forever. Events that pass HLT are arranged into appropriate datasets depending on HLT selection criteria they passed and stored for physics measurements.

There is a large variety of triggers to capture the SM and new physics processes of our interest. Typical trigger examples include at least one or two leptons or one or two jets with P_T higher than a certain threshold.

3.2.8 Particle Flow Algorithm of Event Reconstruction

A particle flow (PF) algorithm is used by CMS to identify and reconstruct stable particles [43]. It processes the information from all CMS subdetectors and identifies and reconstructs each stable particle in an event individually. The list of particles include muons, electrons, photons, and charged and neutral hadrons. Each type of particles leaves its specific trace in the CMS detector as shown in Fig. 3.6. After reconstruction of individual stable particles, jets are built, missing transverse energy E_T^{miss} is determined, and certain short-lived particles are reconstructed based on the list of individual stable particles in the event.

One particle can induce several different particle-flow elements in different subdetectors. Examples of elements include a track in the tracking or muon systems, or a calorimeter cluster. The linking algorithm checks each pairs of elements in an event and produces blocks of elements if the distance between two elements is small and, therefore, they are considered to be linked. Usually, a block has between one and three elements. Links can be connections between the tracking system and PS, ECal or HCal, between PS and ECal, between ECal and HCal, and between a tracking system and a muon system.

In each block, muons are considered first. A link between charged tracks in the tracking and muon systems produces one "particle-flow muon". The corresponding track in the tracking system is removed from the block and corresponding energy deposits are subtracted from ECal and HCal. Then electrons are reconstructed and identified using the tracking system and ECal. The corresponding tracks and ECal clusters are removed from the block. Remaining tracks and clusters are considered more carefully to identify charged hadrons, neutral hadrons, and photons.

When all particles in the event are reconstructed and identified, the algorithm determines missing transverse energy E_T^{miss} as

$$E_T^{miss} = -|\sum \mathbf{P_T}|, \tag{3.4}$$

where the summation covers all visible particles in the event. For precise measurement of E_T^{miss} it is important to capture the full energy release of all visible particles.

E_T^{miss} is used in physics measurements as a measure of P_T of neutrinos and other invisible particles in the event. Fake E_T^{miss} can originate from particles that did not fall into the detector acceptance, particles that did not reach the tracking system because their momenta was too low and, therefore, track curvature was too high, momenta mismeasurement, particle misidentification, cosmic rays particles, and machine background. Fake E_T^{miss} is a cause of background for the processes with real E_T^{miss}. For instance, in $W\gamma$ measurement we have backgrounds from Z+jets and $Z\gamma$ which do not have any real E_T^{miss}.

E_T^{miss} is corrected through the propagation of corrections applied on kinematic parameters of jets. Additionally, E_T^{miss} is corrected for the PU effect.

In the measurement of this dissertation PF muons, electrons, photons, and E_T^{miss} are used for all the major steps of the cross section measurement including event selection, background subtraction, various corrections, and determination of phase space restrictions and bin boundaries. Each step is described in greater detail in Ch. 5.

4 CMS Tracker Alignment

In the presence of a constant magnetic field, a charged particle has a helical trajectory which can be parametrized by five constants in three dimensions. While a charged particle travels through a tracking system, the tracking system detects hits. A reconstruction algorithm determines the track parameters by fitting the positions of hits assuming a helical trajectory, and also taking into account scattering. That allows the reconstruction of the full geometry of the track as well as the corresponding particle momentum, and to determine whether the particle came from the point of the pp collision or decay of a secondary particle.

High precision track reconstruction is necessary for accurate measurements of particle kinematics. Better location uncertainty leads to higher precision of the track parameters measurement. The location uncertainty depends on our knowledge of the positions and orientations in the space of the tracking system modules. For example, the hit resolution in the CMS pixel detector is $\sim$10 μm in the r-ϕ plane and $\sim$30 μm in the r-z plane [38].

When the modules of the pixel detector are mounted, their positions are known with precision of $\sim$200 μm. To take full advantage of the resolution of 10 μm, we need to know positions of modules at a better accuracy than of the single hit resolution. The procedure for the determination of the module locations and orientations is called the tracker alignment. The approach used for the tracker alignment in CMS is described in Ch. 4.1.

The procedure of tracker alignment is essential for the momentum measurement of all charged particles including electrons and muons that are the final state particles of the measurement of this dissertation as well as for the determination of the position of the primary vertex, the interaction point of a pp collision that caused a given process. The measurement of this dissertation is based on data collected in 2012, while the author of this dissertation participated in the alignment of the tracking system in 2015 (Ch. 4.2). The results of 2015 alignment are not used for the measurement of this dissertation but are used for all CMS physics measurements of 2015 data including $W\gamma$ measurement at $\sqrt{s}$ =13 TeV.

4.1 Approach

It is necessary to align a part of the tracking system whenever we suspect a physical change in a location or an orientation of this part. First of all, whenever a part of the CMS tracker is taken out and placed back, we need to realign it. Also whenever a magnet is turned on and off, different parts of the tracking system shift with respect to one another. Pixel half barrels are not screwed firmly, and are moving along each other on rails, therefore, they need to be aligned frequently.

The concept of track-based alignment can be illustrated in the example of the alignment of a toy tracker (Fig. 4.1-4.2). A charged particle crosses a toy tracker of six flat equidistant modules. Because real geometry of the tracker differs from the ideal one, hits are recorded at the places different from the design ideal places. We record and process a large number of tracks to determine positions and orientations of the modules.

The tracker alignment problem is a least squares problem. The expression to minimize is the following:

$$\chi^2(\mathbf{p},\mathbf{q}) = \sum_j^{tracks} \sum_i^{hits} \left(\frac{m_{ij} - f_{ij}(\mathbf{p},\mathbf{q_j})}{\sigma_{ij}} \right)^2 , \tag{4.1}$$

where $\mathbf{p}$ are parameters describing the tracker geometry, $\mathbf{q}_j$ are parameters of the j^{th} track, $m_{ij} - f_{ij}$ are distances between the measured hit and a position predicted by the track fit ("residuals"), σ_{ij} is the Gaussian error of the measurement.

We can align the large substructures (like pixel half barrels, pixel endcap disks and other) with respect to the global CMS coordinate system and individual modules with respect to the coordinate systems of their substructures. The parameters to align large substructures include three coordinates to determine location and

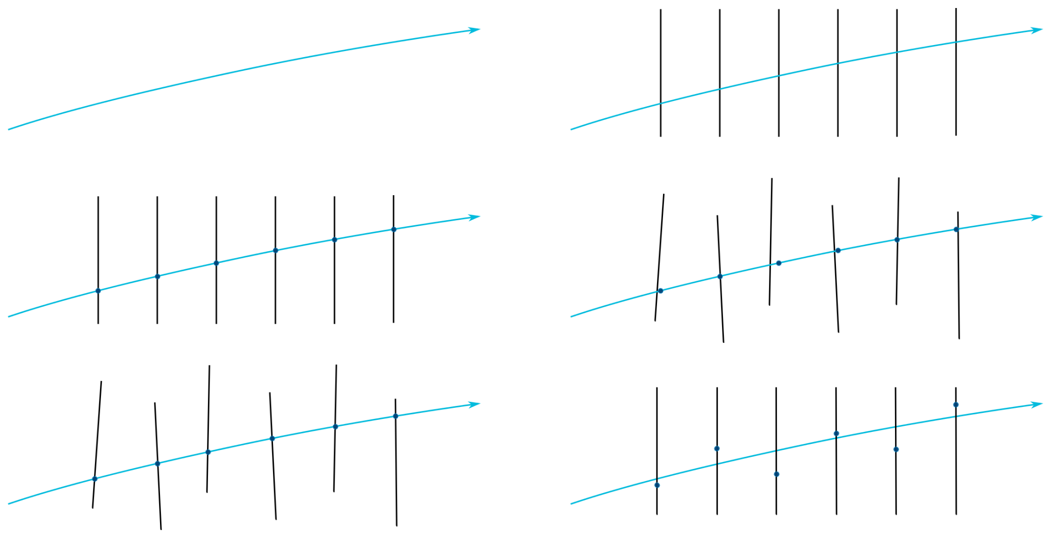

Figure 4.1: The alignment of a toy tracker, part 1. When a charged particle passes through a detector (top left), it crosses a toy tracker which consists of six flat equidistant modules (top right). If the modules were placed exactly at their design positions, we would observe the hits exactly at the points where the track crosses modules of ideal geometry (middle left). However, in reality, the positions and tilts of the modules are different from ones suggested by the ideal geometry (middle right). Hits, indeed, are recorded at the places where modules are mounted, not at the design ideal places (bottom left). If we assumed a tracker to be ideal and a track to be smooth, we would see that our hits are off-track (bottom right). Image by Frank Meier.

three angles to determine orientation of the substructure. At the module level, we align positions and rotations with respect to to the coordinate system of the substructure (Fig. 4.3). Also at the module level, we align for surface deformations which are described by three parameters per sensor.

The alignment process appears to require the inversion of giant matrices, of millions by millions of rows and columns. We have two alignment algorithms that use their ways to simplify the computation: Hits and Impact Parameter (HIP) [44] and Millepede-II [45]. HIP performs a minimization for one module at a time processing tracks that pass though this particular module. After the minimization

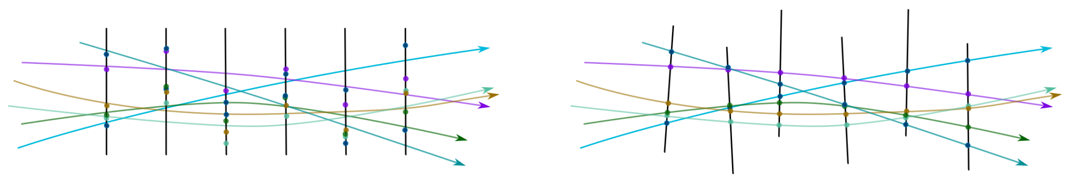

Figure 4.2: The alignment of a toy tracker, part 2. We record a large number of tracks and take into account them all to determine the alignment parameters by minimizing residuals between measured and predicted hits. Image by Frank Meier.

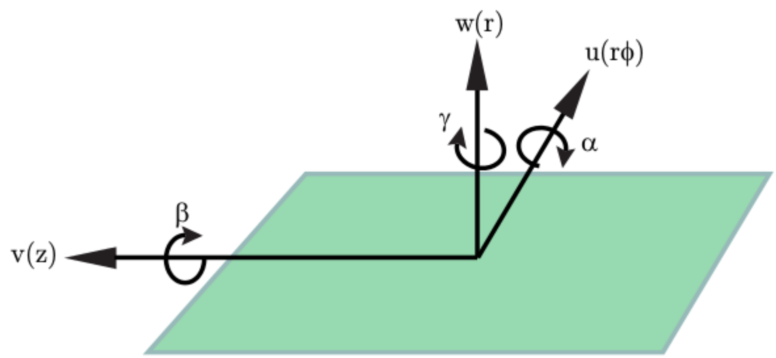

Figure 4.3: Local alignment parameters [11].

is done for all modules, HIP performs a second iteration. The iterations are stopped after module positions converge. Millepede-II performs a simultaneous fit of all alignment parameters at a time, and uses linear algebra tricks for sparse matrices to avoid dealing with most track parameters.

After the procedure of the tracking system alignment is performed, we validate the results. Chapter 4.2 discusses various tools of alignment validation using the example of the tracking system alignment based on the 2015 data.

4.2 Selected Results on Alignment of the Tracking System with 2015 Data

After the long shutdown in 2013-2014, LHC restarted collisions in 2015. Data collection periods in 2015 include the following:

- cosmic ray data with CMS magnetic field of $B =$0T (prior collisions);
- cosmic ray data at $B =$3.8T (prior to collisions);
- pp collision data at $B =$0T (interfilled with cosmic ray data);
- pp collision data at $B =$3.8T (interfilled with cosmic ray data) .

Only pp collision data at $B =$3.8T are used for physics measurements and the three other periods are preliminary. During the preliminary periods we make sure that all parts of the detector work properly and also perform the preliminary alignment of the tracking system. Collision data are interfilled with cosmic ray data when LHC does not provide any collisions. This interfill cosmic ray data are also used for the tracker alignment.

Different data collection periods correspond to different detector geometries particularly due to changes of the magnetic field. Thus, alignment constants were derived separately for each of the data collection periods using the alignment results of the previous period of data collection as a starting point.

The modules in certain parts of BPIX were repaired during the shutdown, and all pixel subdetectors were moved within the tracker. That caused one of the largest differences between Run I and Run II geometries. The first alignment of the tracker corrected for these displacements using cosmic ray data with magnetic field turned on ($B =$3.8T) and off ($B =$0T).

After the cosmic ray data collection periods, the magnetic field was turned off again due to problems with the cryogenic system, and the first collisions were detected with B =0T. This change in the magnetic field expectedly caused movements in the tracking system. The effect is the strongest in the pixel subdetectors. The alignment performed using B =0T collisions and cosmic ray data recovers the tracker performance in reconstructing kinematic parameters of charged particles. When the magnetic field was turned back on, the large substructures of BPIX and FPIX were displaced again, and, thus, the tracking system was aligned again to recover these displacements.

To validate results of tracking system alignment, the following tools are used:

- geometry comparison tool (Ch. 4.2.1);
- validation using distribution of median residuals (Ch. 4.2.2);
- cosmic track splitting validation (Ch. 4.2.3);
- primary vertex validation (Ch. 4.2.4).

The full results of the first alignment with Run II data are available in [46].

4.2.1 Geometry Comparison

The geometry comparison visualizes differences in positions of modules between two different geometries of the CMS tracking system. Figure 4.4 shows the comparison between positions of the FPIX modules between Run I and Run II geometries. Each dot in the figure corresponds to one module. Four clusters of red dots (Fig. 4.4, right) and shifted parts at ($\phi < -\pi/2$, $\phi > \pi/2$) and ($-\pi/2 < \phi < \pi/2$) (Fig. 4.4, left) represent displacements of four half-disks by 4.5 and 5.5 mm at the $-z$ side of the FPIX. At the $+z$ side of the FPIX, small relative movements of individual modules are observed only. For more intuitive visualization, a three-dimensional plot of the pixel detector is produced (Fig. 4.5).

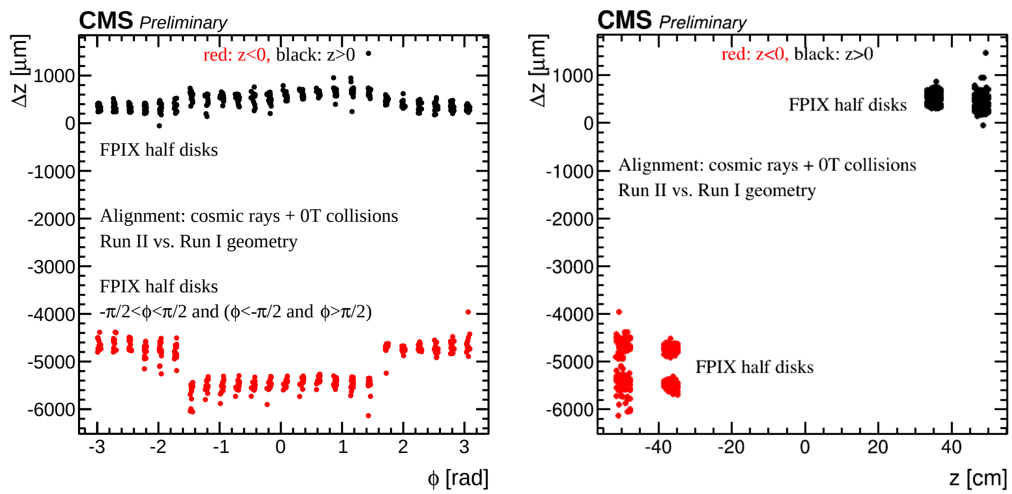

Figure 4.4: Comparison of Run II and Run I positions of the modules in the FPIX of the CMS tracking system. Positions are determined with the Millepede-II and HIP algorithms using cosmic ray data collected with the magnetic field of B =0T and B =3.8T magnetic field in the CMS solenoid. The difference Δz (Run II - Run I) is plotted as a function of z (left) and ϕ (right) in global coordinates. The plot shows the displacements of two pixel half disks by 4.5 and 5.5 mm.

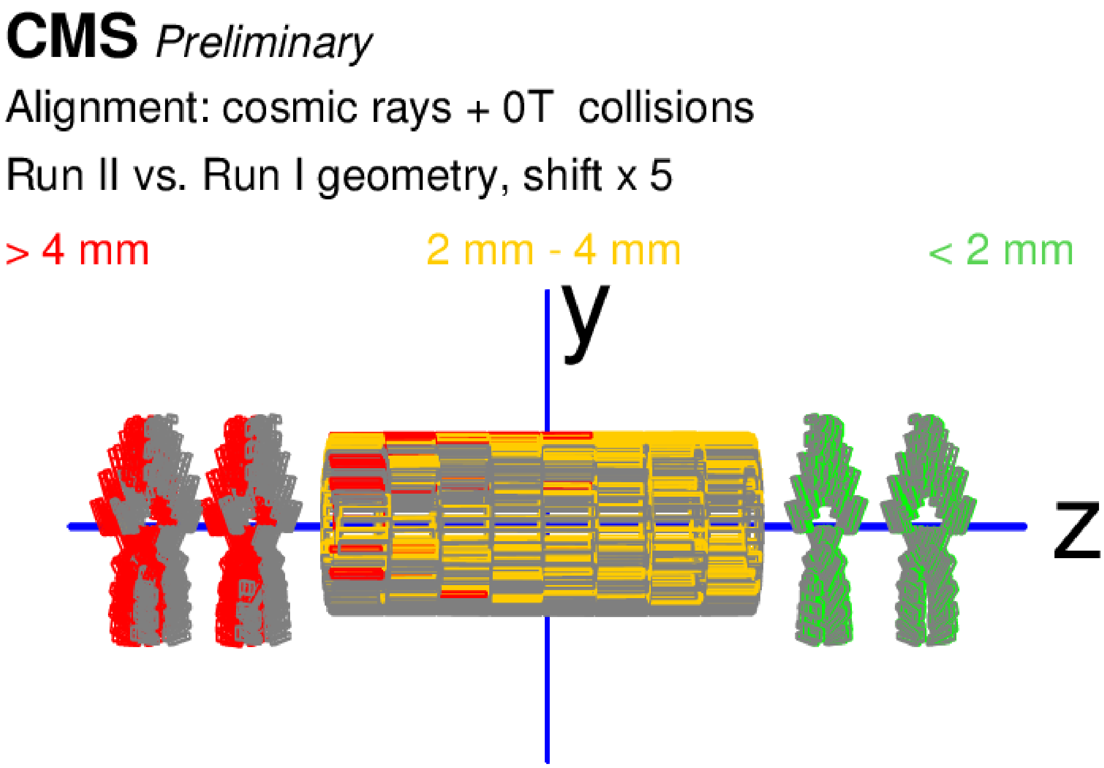

Figure 4.5: Three-dimensional geometry comparison of Run II and Run I positions in the BPIX and FPIX of the CMS tracking system. Positions are determined with the Millepede-II and HIP algorithms using cosmic ray data collected with the magnetic field of B =0T and B =3.8T magnetic field in the CMS solenoid and collision data with B =0T at $\sqrt{s}$ =13 TeV. The positions at the end of Run I are shown in gray. The module displacements between Run I and Run II are magnified by a factor of 5 for visualization purpose. The resulting positions are shown in different colors, depending on the displacement magnitude.

4.2.2 Distributions of Medians of Unbiased Track-Hit Residuals

Besides the geometry comparison, we also have the distributions of medians of unbiased track-hit residuals (DMR) validation tool. Each track from a given dataset is refitted using prepared alignment constants, and the hit for each module is predicted from all other hits of the track. After that, DMRs of all modules in a given subdetector are plotted on the same histogram. The width of the prepared DMR is a measure of the statistical precision of the derived alignment results.

The DMRs are plotted for the local x- (Fig. 4.6, left) and y-directions (Fig. 4.6, right) in the BPIX. The blue line shows the DMR for Run I while the green line shows the geometry aligned with Run II data. The RMS values show that performance of the aligned geometry is improved by a factor of 10 over the Run I geometry. Because of physical changes in the tracking system, including removing and replacing the pixel detector, replacing certain modules, and changes in the magnetic field, the Run I geometry is not expected to work well with Run II data.

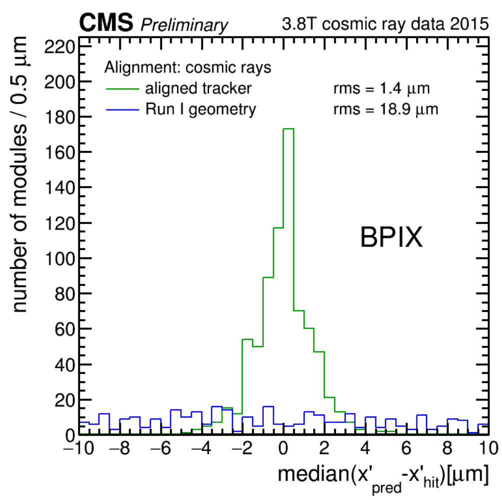

Figure 4.6: DMRs for the local x-direction (left) and for the local y-direction (right) in the BPIX of the CMS tracking system, using 2 million cosmic ray tracks collected with the magnetic field of B =3.8T. The blue line shows the Run I geometry. The green line shows the alignment produced with the Millepede-II and HIP algorithms using cosmic ray data at B =0T and B =3.8T. The aligned geometry shows reasonable performance.

4.2.3 Cosmic Track Splitting Validation

To perform the cosmic track splitting validation, cosmic tracks are split into two parts at the hit closest to the center of the detector and both parts are reconstructed separately using alignment results. After that, the distributions of the differences in track parameters are prepared. The RMS values of the distributions are measures of the precision of the alignment constants. A deviation of a central value from zero would indicate a bias. The results of this validation for 2015 alignment are shown in Fig. 4.7.

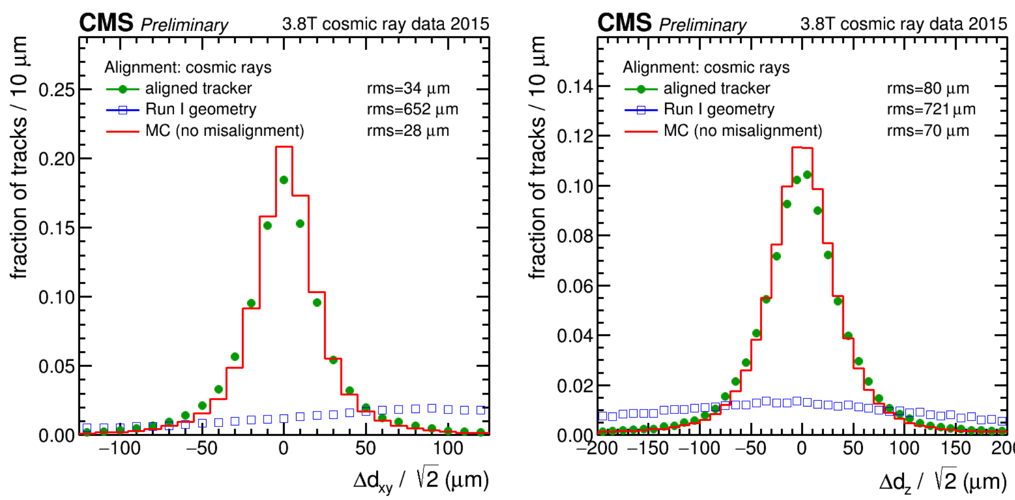

Figure 4.7: Results of the cosmic track splitting validation. The normalized differences between two parts of a cosmic track in the xy distance between the track and the origin (d_{xy}, left), and in the distance in the z direction between the track and the origin (d_z, right). Alignment is produced with the Millepede-II and HIP algorithms using cosmic ray data at the magnetic field of B =0T and B =3.8T of CMS solenoid. Geometry aligned with Run II data is shown in green, Run I geometry is shown in blue. Aligned geometry shows reasonable performance.

4.2.4 Primary Vertex Validation

The resolution of the position of the reconstructed vertex is mostly determined by the pixel subdetectors as the closest subdetectors to the interaction point which also have the best hit resolution. The primary vertex validation is based on a study the distances between tracks and the reconstructed vertex.

Figure 4.8 compares the alignment reached with cosmic rays at full magnetic field and collision data without magnetic field to the alignment reached with cosmic rays at full magnetic field without any collision data and to a detailed detector simulation with perfect alignment and calibration. The structures of the green curve indicate relative movements of the pixel half-barrels.

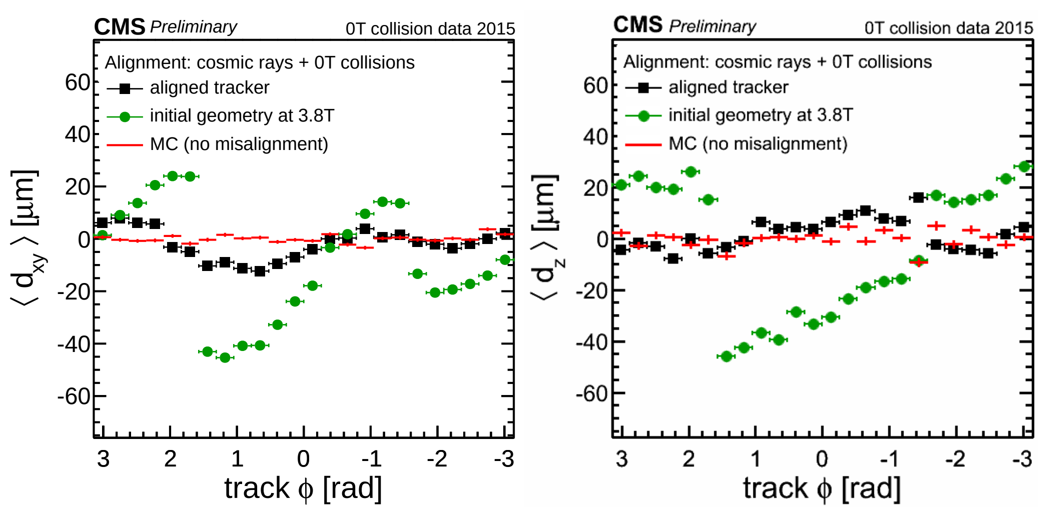

Figure 4.8: The results of the primary vertex validation. The distance of the track at its closest approach to a refit unbiased primary vertex (d_{xy}, left and d_z, right) in the transverse plane. The validation is produced with B =0T collision data. The alignment is produced with the Millepede-II and HIP algorithms using B =0T and B =3.8T cosmic ray data and B =0T collision data.

Given the complexity of the CMS detector, any single measurement based on CMS data requires an excellent understanding of the geometry and response of all systems to particles of all types. The CMS Alignment and Calibration team coordinates hundreds of CMS physicists who are working on various aspects of this. Chapter 4 of this dissertation presented one aspect of this work that concerns alignment of one system of CMS, the part in which the author of this dissertation played an important role that included running alignment and validation for various studies of the procedure performance as well as for actual alignment of the tracking system.

5 $W\gamma$ Cross Section Measurement

The goal of the work reported in this dissertation is to measure the total and differential cross section of the $W\gamma$ production in pp collisions as a function of the photon transverse momentum P_T^γ at $\sqrt{s}$ =8 TeV center-of-mass collision energy. Decay channels $W \to \mu\nu$ and $W \to e\nu$ are considered. The measurement is performed using CMS data collected in 2012.

The phase space for the cross section was chosen taking into account the limitations on the event kinematics imposed by the trigger conditions during the data collection as well as by the detector acceptance, and considering the fact that the theoretical value for the cross section diverges at P_T^γ =0 and $\Delta R(\gamma, l)$ =0. The phase space requirements on the final state photon and lepton match those of CMS $Z\gamma$ measurement at 8 TeV [47] which also had to consider all the listed factors. The full list of the phase space requirements includes:

- P_T^γ >15 GeV;
- $\Delta R(\gamma, l)$ >0.7;
- $|\eta^\gamma|$ <2.5, $|\eta^l|$ <2.5;
- P_T^l >20 GeV;
- I^γ <5 GeV, where I_γ is a sum of P_T of all particles p in the event within $\Delta R(p, \gamma)$ <0.3.

P_T^{γ} ranges (binning) for the differential cross section measurement wer chosen to match the CMS $Z\gamma$ measurement. The P_T^{γ} bin boundaries are 15-20-25-30-35-45-55-65-75-85-95-120-500 GeV.

5.1 Measurement Strategy

The process of the cross section measurement is a sequence of steps summarized in Tab. 5.1. First, we select events and obtain the number of selected events (Ch. 5.3). In Tab. 5.1 the total number of selected events is N_{sel} and numbers of selected events in P_T^{γ} bins are N_{sel}^{j}, where j is a bin number. The selected sample contains signal as well as background events. The next step is to subtract the background. This step results in background subtracted yields of signal events N_{sign} and N_{sign}^{j} (Ch. 5.4). After that, we apply an unfolding procedure that corrects for detector resolution effects in the measurement of photon transverse momentum (Ch. 5.5) and obtain yields within acceptance and selection restrictions: $N_{A\times\epsilon}^{i} = U_{ij} \cdot N_{sign}^{j}$, where U_{ij} is the unfolding operator. The detector resolution unfolding is only relevant for the measurement of the differential cross section, not the total cross section. Then corrections for kinematic and geometric acceptance and reconstruction and selection efficiency are applied (Ch. 5.6). Finally, we divide the measured number of events by integrated luminosity recorded by CMS and, in the case of the differential cross section, by the width of P_T^{γ} bins. This results in the total and differential cross section (Ch. 5.8). Each step has its systematic uncertainties associated with it, and we estimate their contributions to the final results (Ch. 5.7).

At first, we perform the measurement in a blinded way. The purpose of blinding is to avoid unintended biasing of our results in any direction. Our blinding strategy is the following:

- for p_T^{γ} <45 GeV: use 100% of data; and
- for p_T^{γ} >45 GeV: use 5% of data (every 20^{th} event).

Table 5.1: Measurement steps and algebraic representations of the steps for the differential ("$d\sigma/dP_T^\gamma$") and total ("σ") cross section measurements.

Step	$d\sigma/dP_T^\gamma$	σ
select events	N_{sel}^j	N_{sel}
subtract background	$N_{sign}^j = N_{sel}^j - N_{bkg}^j$	$N_{sign} = N_{sel} - N_{bkg}$
unfold	$N_{A\times\epsilon}^i = U_{ij} \cdot N_{sign}^j$	–
correct for the acceptance and efficiency	$N_{true}^i = \frac{N_{A\times\epsilon}^i}{(A\times\epsilon)^i}$	$N_{true} = \frac{N_{sign}}{A\times\epsilon}$
divide by luminosity and bin width	$\left(\frac{d\sigma}{dP_T^\gamma}\right)^i = \frac{N_{true}^i}{L\cdot(\Delta P_T^\gamma)^i}$	$\sigma = N_{true}/L$
estimate systematic uncertainties		

The threshold of p_T^γ =45 GeV is chosen because below that we do not expect any new physics, and the percentage of 5% is chosen because this amount of data gives us such a large statistical uncertainty so that we would not notice any new physics if it were there. After the measurement procedure is fully established, we perform the measurement using our full dataset ("unblinded" measurement). All plots in this dissertation are shown for the final, unblinded, stage of the measurement.

A brief description of the software tools used and developed for the measurement is available in App. A.

5.2 Data and Monte Carlo Samples

The data sample we use in this measurement was recorded by the CMS experiment in 2012 in LHC pp collisions at $\sqrt{s}$ =8 TeV. The integrated luminosity of the dataset is L =19.6 fb^{-1}. To select $W\gamma$ events, we use data collected by single muon and single electron triggers. The single muon trigger requires that in each event there is at least one reconstructed isolated muon with $P_T^{\mu} >$24 GeV and $|\eta| <$2.1. The isolation requirement imposes a restriction on the total energy of particles observed in a narrow cone around the muon. The single electron trigger requires at least one reconstructed electron with $P_T^{e} >$27 GeV that also passes a certain set of identification requirements, including isolation. Such trigger choice maximizes our chances to select $W\gamma$ events in pp collisions that produce mostly less interesting and much more probable events of other types, such as multijets events.

In addition to the $W\gamma$-selected data sample, we also prepare a $Z\gamma$-selected data sample which is used for the background estimation (Ch. 5.4) and cross checks (App. B). To select $Z\gamma$ events, we use double muon and double electron triggers. The double muon trigger requires a presence of at least two reconstructed muons with $P_T^{\mu} >$17 GeV and $P_T^{\mu} >$8 GeV per event. The double electron trigger requires a presence of at least two reconstructed electrons with $P_T^{e} >$17 GeV and $P_T^{e} >$8 GeV that also satisfy several quality criteria.

The simulated samples (often called "Monte Carlo" or "MC" samples) used in this measurement are produced centrally by the CMS simulation team. Information regarding MC samples used for our measurement is given in Tab. 5.2 alongside with the corresponding cross sections at 8 TeV. All cross sections are calculated with kinematic restrictions matching to the kinematic restrictions of the samples. The kinematic restrictions for different samples differ and reflect theoretical divergencies for specific processes and detector acceptance. In all cases, however, the phase space of the sample is wider than the phase space probed in this measurement.

Table 5.2: Summary of simulated samples used in the measurement.

Process	Type	σ, pb
$W\gamma \to l\nu\gamma$	signal	554
W+jets$\to$ $l\nu$+jets	background	36257
DY+jets$\to$ ll+jets	background	3504
$t\bar{t}$+jets$\to$ 1l+X	background	99
$t\bar{t}$+jets$\to$ 2l+X	background	24
$Z\gamma \to ll\gamma$	background	172

When we apply $W\gamma$ selection criteria to the data sample, selected events contain not only the events originating from the signal process but also events from other, background, processes. Tab. 5.2 contains all sources that significantly contribute to the selected sample. $W\gamma \to l\nu\gamma$ contains $W\gamma \to \mu\nu\gamma$ and $W\gamma \to e\nu\gamma$ which are our signal samples and $W\gamma \to \tau\nu\gamma$ which is a background for both channels. The other samples listed in Tab. 5.2 are background samples. They are used for the background estimation and cross checks as explained in detail in the remainder of the chapter.

All MC samples were generated with MadGraph 5 [48] interfaced with PYHTIA 6 [49]. The CTEQ6L1 PDF set was used [50]. The passage of the generated particles through the CMS detector is simulated with GEANT 4 [51].

Cross section values corresponding to all genetated samples in Tab. 5.2 are calculated by MCFM [32] or FEWZ [52] except for the $Z\gamma$ sample. The uncertainty on normalization of the $Z\gamma$ sample gives a significant contribution to the uncertainty of the measurement because $Z\gamma$ MC sample is used to estimate the most significant background (Ch. 5.4.1). MCFM provides a value of the cross section with uncertainty of 20%. To decrease the uncertainty, we use a cross section of $Z\gamma$ measured at 8 TeV by CMS [47] and recalculated for the phase space of the generated $Z\gamma$ MC sample. The recalculation procedure is described below.

The $Z\gamma$ cross section of σ =2073±95±11±53 fb has been reported in the phase space described in [47]. To determine the measured cross section σ_{ps1} in the phase space of the $Z\gamma$ MC sample, the following formula was used:

$$\sigma_{ps1} = \sigma_{ps2}^{meas.} \cdot \frac{N_{ps1}^{MC}}{N_{ps2}^{MC}}, \tag{5.1}$$

where $\sigma_{ps2}^{meas.}$ is the 8 TeV cross section measured by CMS, N_{ps1}^{MC} and N_{ps2}^{MC} are numbers of events in the full phase space of $Z\gamma$ MC samples and in the phase space corresponding to the measured cross section $\sigma_{ps2}^{meas.}$. The resulting $Z\gamma$ cross section is found to be σ_{ps1} =172 pb.

The inclusive simulated samples W+jets and DY+jets naturally contain events with the $W\gamma$ and $Z\gamma$ processes, and we explicitly exclude $W\gamma$ events from the W+jets sample and $Z\gamma$ events from the DY+jets samples. DY+jets, or DY, is a notation for the Drell Yan process, $pp \rightarrow Z/\gamma \rightarrow ll$. The requirement on the invariant mass of the final state lepton pair in the DY+jets sample is M_{ll} >50 GeV.

All MC samples are normalized to the luminosity of the dataset L_{DATA} =19.6 pb^{-1}. To perform the normalization, weights of

$$w = \frac{L_{DATA}}{L_{MC}} = \frac{L_{DATA}\sigma_{MC}}{N_{MC}} \tag{5.2}$$

are applied to each event in each MC sample, where N_{MC} is the number of events in a given MC sample, and σ_{MC} is a cross section of the process of MC sample within the phase space of the MC sample. Such weighted MC samples are used for various MC predictions mentioned in later sections and for all plots involving MC.

At the instantaneous luminosities of LHC in 2012, as a rule, multiple pp interactions occurred per bunch crossing. Multiple interactions are also simulated in the MC samples. However, MC samples are usually produced before data collection is finished, and have to be reweighted so that the distribution of the number of interactions (pileup or PU) in a simulated sample matches the data. The PU weights are assigned to each event in each MC sample to make the PU distribution in MC accurately describe PU in data.

To validate the procedure of the PU reweighting, we confirm that the agreement between data and MC in the distribution of the number of pp interaction vertices in $Z\gamma \to \mu\mu\gamma$-selected datasets is good (Fig. 5.1). We choose the $Z\gamma$ selected dataset instead of the $W\gamma$-selected dataset because the sample composition for $Z\gamma$ selection is understood better and normalizations of the MC samples that pass $Z\gamma$ selection are known better. The $Z\gamma$ selection is explained in Ch. 5.3 alongside with the $W\gamma$ selection.

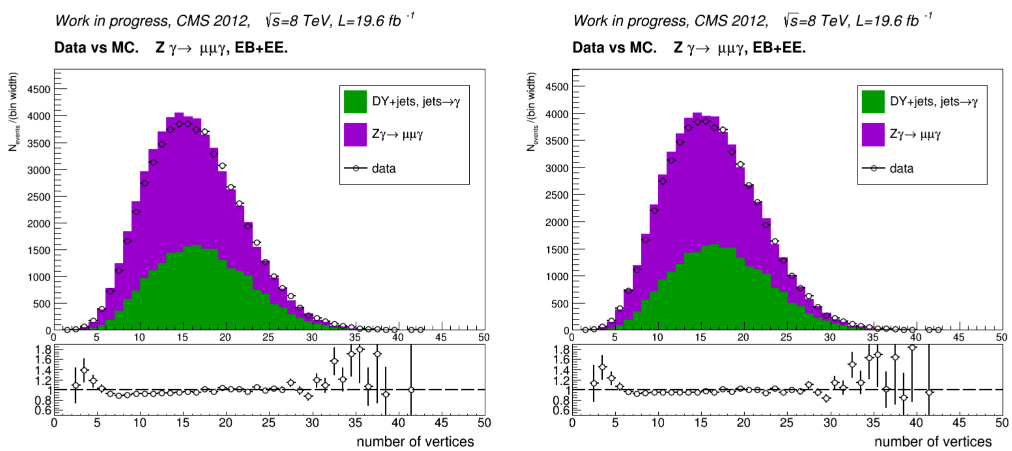

Figure 5.1: Number of pp interaction vertices of $Z\gamma$ candidates in the muon channel. Data vs MC. Left: no PU reweighting applied, right: PU reweighting applied. The ratio plot at the bottom of each panel shows data yields divided by total MC yields. EB+EE means that events with a final state photon reconstructed in the ECal barrel as well as events with a final state photon reconstructed in the ECal endcap are shown on the plots.

5.3 Event and Object Selection

5.3.1 Object Selection

Events of the $W\gamma \rightarrow l\nu\gamma$ process have a muon and a photon in the final state for the muon channel and events with an electron and a photon in the final state for the electron channel.

We apply selection requirements on transverse momenta of $P_T^{\mu} >$25 GeV on muons, $P_T^{e} >$30 GeV on electrons and $P_T^{\gamma} >$15 GeV on photons. In addition, electrons and photons must be within the barrel (EB) or the endcap (EE) sections of the ECal which corresponds to pseudorapidity ranges of $|\eta^{e,\gamma}| <$1.4442 and 1.566$<$ $|\eta^{e,\gamma}| <$2.5, respectively. The gap is determined by construction of the ECal. Muons must be within $|\eta^{\mu}| <$2.1. Selection requirements on P_T^{μ}, η^{μ}, and P_T^{e} are determined by the trigger requirements, $\eta^{e,\gamma}$ criteria are determined by the geometrical limitations of the detector acceptance, and $P_T^{\gamma} >$15 GeV is the phase space requirement.

A CMS Particle Object Group (POG) provides their recommendations for object identification (ID) criteria for any given period of data collection. To satisfy the muon ID criteria, objects, first of all, must be reconstructed as muons by the PF algorithm. Quality requirements are applied on tracks reconstructed in both the tracking system and the muon system. These two tracks must match. An isolation from the other nearby PF objects is also required. The isolation of a particle P_0 is defined as a sum of the transverse momenta of other particles P_i $\sum_i P_T^i$ within a cone $\Delta R(P_0, P_i) <$0.4.

The electron ID and photon ID criteria include requirements on the shower shape, and on ratio of energies released in ECal and HCal. The electron ID also includes requirements on the track quality. Similarly to muons, electrons and photons must be isolated from the nearby PF objects. For the photon ID, the isolation consists on three parts: charged hadron, neutral hadron, and photon isolation. To reject electrons reconstructed as photons, "conversion safe electron veto" (CSEV) is recommended as a part of any photon ID. CSEV removes a photon candidate that has an associated signal in the tracking system. While this signal is not qualified as a proper charged particle track, there is a high risk that the particle is, in fact, an electron.

In $W\gamma$ measurement, we applied object ID criteria as recommended by POG with one exception: in the electron channel, the CSEV is substituted with the "pixel seed veto" (PSV) as recommended by the CMS $W\gamma\gamma \to l\nu\gamma\gamma$ measurement team [53]. PSV rejects photons that have any track seed in the pixel detector that can match to the measured ECal supercluster. The PSV is tighter requirement than the CSEV and, therefore, is used in the electron channel only, because in the electron channel we have much larger background from electrons misidentified as photons.

Selection criteria are applied to the data sample as well as on all MC samples. When the object identification requirements are applied, the selection efficiency may differ between data and MC. The ratios between data and MC efficiencies are called the scale factors (SF). The SF for the selection criteria recommended are provided by CMS POG. For the PSV criterion in the photon selection in the electron channel, additional SF are applied as derived by the $W\gamma\gamma$ team [53]. The SF are applied as weights on each event in each MC sample at every step of the measurement where a weighted MC sample is used. All SF are listed in App. C.

5.3.2 Event Level Selection

In the final state of the $W\gamma \rightarrow l\nu\gamma$ process, there is a lepton, a photon, and a neutrino. To select events with such a signature, we require each candidate to have exactly one lepton (muon or electron) originating from the primary vertex, a photon, and significant missing transverse energy E_T^{miss}. The selection criteria for the individual electrons, muons and photons are described in Ch. 5.3.1.

The standard tool to identify a particle that decays is to reconstruct its invariant mass out of its decay products. Decay products of a W boson are a charged lepton and a neutrino. CMS does not detect neutrinos, it only measures the missing momentum in the plane, transverse to the beamline, which can be associated with a neutrino. The transverse momentum is described by two parameters: E_T^{miss} and ϕ^{miss}, an azimuthal angle of the missing transverse momentum. Because we do not have an estimate of the longitudinal component of a neutrino momentum, we cannot construct an invariant mass of a W boson. Instead, we construct its transverse mass:

$$M_T^W = \sqrt{2P_T^l E_T^{miss}(1 - \cos{(\phi^l - \phi^{miss})})}, \tag{5.3}$$

where P_T^l is a lepton transverse momentum, and ϕ^l is an azimuthal angle of the lepton momentum. To enhance a contribution from $W\gamma$ process in the sample of selected events compared to background processes without a final state neutrino, we require M_T^W >40 GeV. Value of 40 GeV was recommended by the CMS Standard Model Physics (SMP) group because the same requirement was used in $W\gamma\gamma$ measurement. The M_T^W distribution is shown in Fig. 5.2. Photons with P_T^γ <45 GeV are selected for this plot because we do not expect any new physics in this region.

After selection criteria on the physics objects as well as M_T^W are applied, a significant background from DY+jets in the electron channel remains. This background is caused by one of the electrons being misidentified as a photon. Its contribution is the most significant around the invariant mass of the electron-photon system $M_{e\gamma}$ close to the mass of the Z boson (Fig. 5.3) because the distribution of M_{ee} in the $Z \to ee$ decay is peaking at the value of the Z boson mass. To reduce this background, we reject events in the Z-mass window defined as 70 GeV$< M_{e\gamma} <$110 GeV.

To reduce backgrounds from processes with two or more leptons, such as $Z\gamma \to ll\gamma$ process, in the muon channel, we reject all events that have a second reconstructed muon candidate with $P_T^{\mu} >$10 GeV and $|\eta|^{\mu} <$2.4, and, in the electron channel, we reject events that have the second reconstructed electron candidate with $p_T^e >$10 GeV and satisfying loose ID ("Veto") criteria recommended by POG.

Finally, the separation $\Delta R = \sqrt{(\Delta\phi^2 + \Delta\eta^2)}$ between the final state lepton and photon is required to be $\Delta R(l,\gamma) >$0.7 to reduce the FSR contribution and, thus, enhance the TGC contribution. In case if there is more than one photon in the selected event, the candidate with the photon of the highest P_T^{γ} is selected.

In addition to $W\gamma$-selected datasets, we also prepare $Z\gamma$-selected datasets in the muon and electron channels which are further used for background estimation and cross checks. Selection requirements include a presence of at least two muons or electrons and at least one photon in the final state. The kinematic requirements on muons are $P_T^{\mu(1,2)} >$20 GeV, $|\eta^{\mu(1,2)}| <$2.4. The kinematic requirements on electrons are $P_T^{e(1,2)} >$20 GeV, $|\eta^{e(1,2)}|$ must be within the EB or the EE sections of the ECal. Identification requirements on the objects are the same as for the $W\gamma$ selection with the only exception: unlike $W\gamma$, in the $Z\gamma$ selection in the electron channel, photons are required to pass CSEV rather than PSV.

The invariant mass of the final state lepton pair is required to be $M_{ll} >$50 GeV, and a separation between the photon and each lepton is required to be the same as in the $W\gamma$ selection: $\Delta R >$0.7.

5.3.3 Selected Events

After the $W\gamma$ selection procedure is applied, 175889 and 85643 events survive in the muon and electron channels, respectively. These events are used for the total and differential cross section measurements with respect to P_T^γ. Distributions of P_T^γ of the selected events are shown in Fig. 5.4 and documented in Tab. 5.4-5.5. The plots and tables include information about the underflow P_T^γ bin (10-15 GeV). The measurement in this bin is used for the detector resolution unfolding (Ch. 5.5).

Selected samples are dominated by W+jets events because of jets misidentified as photons. The main mechanism of a jet to be misidentified as a photon is a $\pi^0 \rightarrow \gamma\gamma$ decay. Photon ID requirements reject most of such fragmentation photons, however, a W+jets event has much larger probability to be produced in a pp collision than a $W\gamma$ event, and, therefore, even a small fraction of fragmentation photons from W+jets events becomes a significant background to $W\gamma$.

DY+jets background in the electron channel consists of two parts: jets misidentified as photons and electron misidentified as photons. The DY+jets MC sample in the electron channel is split into two parts: jets$\rightarrow \gamma$ and $e \rightarrow \gamma$. The split is performed based on the MC truth information which is sometimes referred as "generator level" or "gen-level" information.

There are large discrepancies between data and MC predictions in all the distributions as shown in Fig. 5.2-5.4. Possible reasons for the discrepancies include but are not limited to uncerntainties in the normalizations of all MC samples involved and difficulties in modeling jet fragmentation. Therefore, the data-driven background estimates are necessary (Ch. 5.4).

MC samples in all the plots are weighted to the integrated luminosity of data. PU weights and efficiency scale factors are applied as well.

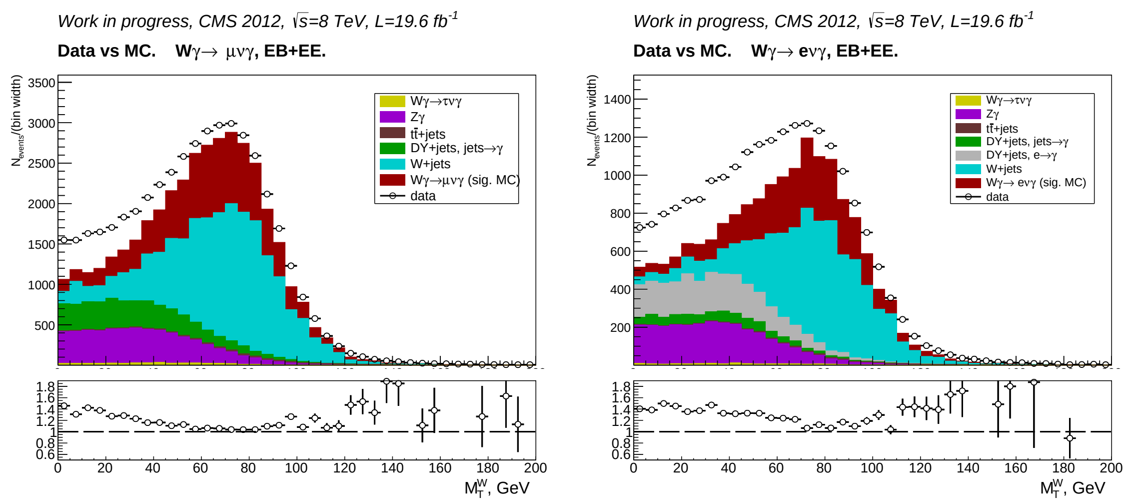

Figure 5.2: M_T^W distribution of $W\gamma$ candidates. Data vs total MC agreement in the muon channel (left) and electron channel (right) is shown. All selection criteria except M_T^W requirement are applied on all samples that are present on the plot. The P_T^γ range where we do not expect any new physics is used: 15-45 GeV. The ratio plot is data divided by the prediction from MC.

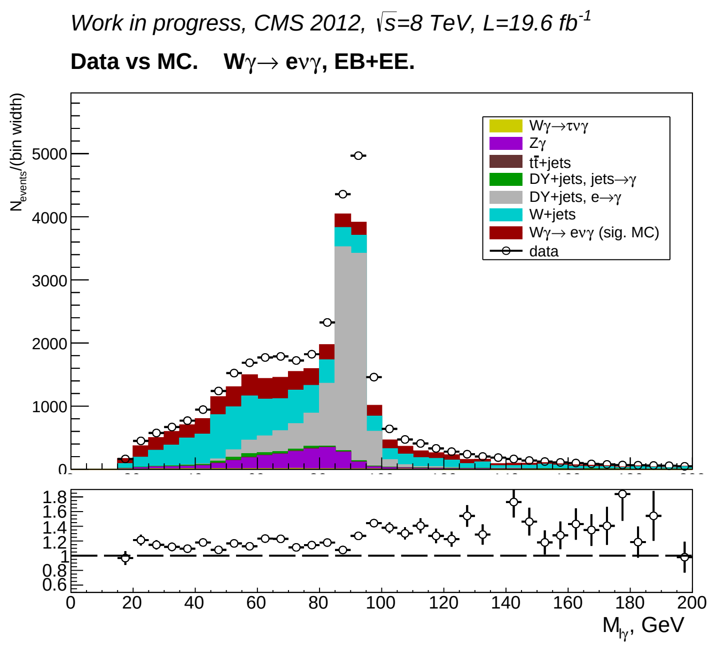

Figure 5.3: $M_{l\gamma}$ distribution of $W\gamma$ candidates in the electron channel. Data vs total MC agreement is shown. All selection criteria except Z-mass window are applied on all samples that are present on the plot. The P_T^{γ} range where we do not expect any new physics is used: 15-45 GeV. The ratio plot is data divided by total MC.

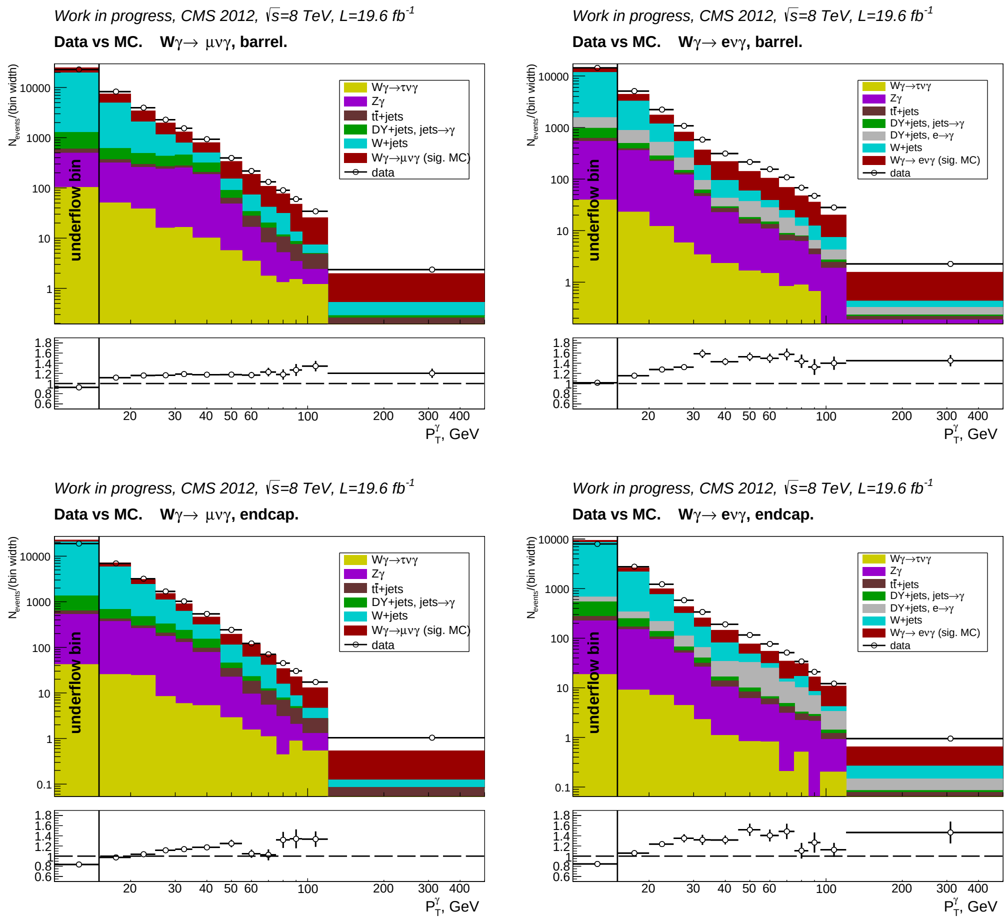

Figure 5.4: P_T^{γ} distribution of $W\gamma$ candidates in the muon (left) and electron (right) channels with photons in EB (top) and EE(bottom). Data vs total MC agreement is shown. The ratio plots are data divided by total MC.

5.4 Background Estimation and Subtraction

The selected sample contains signal events as well as events coming from various backgrounds. To compute the cross section, we need to estimate how many events in each P_T^γ bin originate from the $W\gamma$ process or, in other words, subtract the background. The main sources of backgrounds include "jets misidentified as photons (jets$\rightarrow\gamma$)" background, "electrons misidentified as photons ($e\rightarrow\gamma$)" background, and backgrounds with "real photons (real-γ)" background. Jets$\rightarrow\gamma$ and real-γ backgrounds are significant in both channels while $e\rightarrow\gamma$ background is only significant in the electron channel. The remainder of this section describes the procedure of the background estimation and provides the results of the background subtraction.

5.4.1 Background from Jets Faking Photons

The selected sample is dominated by the W+jets background which cannot be significantly reduced without reducing our signal, $W\gamma$, as well. DY+jets is another source of the jets$\rightarrow\gamma$ background, but this source is significantly suppressed by the M_W^T selection criterion in both channels and by the Z-mass window requirement in the electron channel.

The template method is used to estimate the jets$\rightarrow\gamma$ background. First of all, we choose a variable that has a significant discriminative power between the true and fake photon candidates V_{fit}. After that, we prepare real-γ (T_{true}) and fake-γ (T_{fake}) templates, binned histograms of V_{fit}, which should be accurate representations of V_{fit} distributions of real and fake photons in the $W\gamma$-selected dataset. T_{true} and T_{fake} are normalized to unit area.

The V_{fit} distribution in data is fitted by the following function:

$$F(V_{fit}) = N_{true} \cdot T_{true}(V_{fit}) + N_{fake} \cdot T_{fake}(V_{fit}), \tag{5.4}$$

where V_{fit} is a fit variable, N_{true} and N_{fake} are numbers of real and fake photons in the data sample, respectively, and $F(V_{fit})$ is a fit function. N_{true} and N_{fake} are fit parameters. We use the charged hadron isolation I^{γ}_{ch} and a variable representing ECal shower shape width, $\sigma^{\gamma}_{i\eta i\eta}$, as V_{fit}. Results of I^{γ}_{ch} fits are further propagated for the cross section calculation, and results of $\sigma^{\gamma}_{i\eta i\eta}$ fits are used for the estimation of the systematic uncertainty.

I^{γ}_{ch} is defined as

$$I^{\gamma}_{ch} = \sum_{ch} P_T, \tag{5.5}$$

where the sum runs over charged hadron candidates reconstructed by the particle flow algorithm within $\Delta R < 0.3$ from the photon.

$\sigma^{\gamma}_{i\eta i\eta}$ is defined as

$$\sigma^{\gamma}_{i\eta i\eta} = \frac{\sum (\eta_i - \eta)^2 w_i}{\sum w_i}, \tag{5.6}$$

where the sum runs over individual crystals in the 5×5 matrix around the crystal that detects the largest energy deposit, and w_i is the weight that has a logarithmic dependence on energy released by the photon.

To prepare templates, we use a $Z\gamma \to \mu\mu\gamma$-selected dataset. $Z\gamma$ is produced through two different mechanisms: FSR, when a photon is radiated from one of the final state leptons, and ISR, when a photon is radiated from the initial state quark or antiquark. The "FSR sample" is dominated by real-γ events, and we use this sample to prepare real-γ templates T_{true}. The "ISR sample" consists of true $Z\gamma$ events and events from DY+jets where reconstructed photons come from misientified jets, the main source of fake-γ candidates being the W+jets production.

The best known method in CMS for obtaining a sample with a larger fraction of photon-like jets is using a jet-enriched dataset with triggers selecting jets. However jets in such a sample are mostly gluon rather than quark or antiquark jets like our background jets. Thus, we use the ISR sample to prepare fake-γ templates T_{fake}, and subtract the non-negligible real-γ contribution using the $Z\gamma$ MC prediction. The preparation of the FSR and ISR $Z\gamma$ samples is discussed below.

The FSR $Z\gamma$ selection is very similar to nominal $Z\gamma$ selection discussed in Ch. 5.3.2 with two differences. First, the muon-photon separation requirement for the FSR selection is $\Delta R_{min}(\mu,\gamma) > 0.4$ while the nominal one is $\Delta R_{min}(\mu,\gamma) > 0.7$. The requirement for the FSR selection is looser because FSR events typically have smaller separation than ISR events and, therefore, the looser requirement on the separation increases the fraction of FSR events. Second, since for the FSR the photon is radiated off a lepton that comes mostly from the Z resonance, the three-body invariant mass should be close to the Z mass. Conversely, for ISR, it is two leptons that give us the Z resonance mass, and adding a photon radiated from a quark makes the three-body invariant mass bigger. Therefore, to supress ISR events in the $Z\gamma$-selected sample, the three-particle invariant mass required to be $M_{\gamma\mu\mu} < 101$ GeV.

The distribution of I_{ch}^{γ} of real photons does not depend on P_T^{γ} and, therefore, all events with $P_T^{\gamma} > 15$ GeV are used to prepare I_{ch}^{γ} templates for all P_T^{γ} bins. Distributions of $\sigma_{i\eta i\eta}^{\gamma}$ do depend on P_T^{γ} and, ideally, $\sigma_{i\eta i\eta}^{\gamma}$ templates should have been prepared separately for each P_T^{γ} bin. However, the production of the FSR-type $Z\gamma$ events drops quickly as a function of P_T^{γ}, therefore, the FSR sample has a small event counts in high P_T^{γ} bins. To increase the statistical power, it was decided to combine FSR events of $P_T^{\gamma} > 30$ GeV to prepare $\sigma_{i\eta i\eta}^{\gamma}$ templates for all $P_T^{\gamma} > 30$ GeV bins.

The distributions of both I_{ch}^{γ} and $\sigma_{i\eta i\eta}^{\gamma}$ depend on η^{γ}. Therefore, all templates are prepared separately for barrel and endcap photons.

To prepare fake-γ templates, we need a sample that consists of jets reconstructed and identified as photons. The $Z\gamma \to \mu\mu\gamma$-selected dataset consists of $Z\gamma$ and DY+jets events, where jets from the DY+jets are reconstructed and identified as photons, similar to the $W\gamma$-selected sample containing events with jets faking photons from W+jets, DY+jets and $t\bar{t}$+jets event types. To increase the fraction of jets, on top of the nominal $Z\gamma$ selection conditions described in Ch. 5.3.2, we apply ISR requirements. The ISR requirements include the lepton-photon separation $\Delta R_{min}(\mu, \gamma) > 1.0$, and the invariant mass of the three final state particles $M_{ll\gamma} > 101$ GeV.

FSR and ISR selections are illustrated in App. D. Distributions of $M_{ll\gamma}$ and M_{ll} for nominally selected $Z\gamma$ dataset are shown in Fig. D.1. Distributions of $\Delta R(l, \gamma)$ for ISR and FSR $Z\gamma$ events are shown in Fig. D.2. Distributions of P_T^{γ} for ISR and FSR $Z\gamma$ events are shown in Fig. D.3.

Fits are performed in the extended binned maximum likelihood way separately in each P_T^{γ} bin, separately for candidates with the photon in EB and EE. Plots of the template fits are available in App. E. The fits result in the yields of the candidates with true and fake photons (N_{true} and N_{fake} from Eq. 5.4) as well as the errors on the yields.

N_{true} is the number of real-γ events in $W\gamma$ dataset after all selection criteria applied except the selection condition on V_{fit} which is either I_{ch}^{γ} or $\sigma_{i\eta i\eta}^{\gamma}$. However, our goal is to extract number of real-γ events in $W\gamma$ dataset after all selection criteria applied including the selection condition on V_{fit}. N_{true} obtained from the fit is corrected by the efficiency of the selection condition on V_{fit}. The efficiency is estimated using the $Z\gamma$-selected FSR sample as

$$\epsilon_{Vfit} = \frac{N_{passed\_Vfit\_condition}}{N_{no\_Vfit\_condition}}, \tag{5.7}$$

where $N_{passed\_Vfit\_condition}$ is a number of events in a specific P_T^γ range is the FSR sample which pass all $Z\gamma$ FSR selection criteria including the selection condition on V_{fit}, and $N_{no\_Vfit\_condition}$ is a number of events in a specific P_T^γ range in the FSR sample which pass all $Z\gamma$ FSR selection criteria except the selection condition on V_{fit}.

5.4.2 Background from Electrons Faking Photons in the Electron Channel

For the electron channel, DY+jets is the main source of the $e \to \gamma$ background. Such misidentification happens when an electron from DY is detected in the calorimeter, but the tracking system fails to find the electron, and therefore the calorimeter response is considered to be due to a photon. The Z-mass window requirement of ($M_{e\gamma} < 70$ GeV or $M_{e\gamma} > 110$ GeV) significantly suppresses this background, however, the remaining contribution is non-negligible.

The contribution of the $e \to \gamma$ background is estimated separately for each P_T^γ bin and separately for candidates with photons in EB and EE by scaling the number of the nominally selected events in DY+jets MC sample $N^{e\to\gamma}_{MC-nom}$ to the ratio of numbers of events in the $e \to \gamma$-enriched data ($N^{e\to\gamma}_{data-Zpeak}$) and DY+jets MC ($N^{e\to\gamma}_{MC-Zpeak}$) samples under the Z-peak:

$$N^{e\to\gamma}_{data-nom} = N^{e\to\gamma}_{MC-nom} \cdot \frac{N^{e\to\gamma}_{data-Zpeak}}{N^{e\to\gamma}_{MC-Zpeak}}. \tag{5.8}$$

MC samples are normalized to data luminosity.

To estimate $N^{e\to\gamma}_{data-Zpeak}$, $e \to \gamma$-enriched data and DY+jets MC samples are prepared by applying all $W\gamma$ selection requirements except the Z-mass window requirement. After that, numbers of events in DY+jets MC samples $N^{e\to\gamma}_{MC-Zpeak}$ and $N^{e\to\gamma}_{MC-nom}$ are found by counting. The number $N^{e\to\gamma}_{data-Zpeak}$ is extracted from fitting the $M_{e\gamma}$ distribution in the Z-peak region.

The fits are performed in an extended unbinned maximum likelihood way, separately in each P_T^γ bin in fine η^γ binning. We use fine η^γ binning because the probability of an electron track to be reconstructed and, therefore, the amount of the $e \to \gamma$ background, depends strongly on η. The η^γ binning for different P_T^γ ranges is described in Tab. 5.3. The fit outputs in fine η^γ bins are summed up to form EB and EE yields.

Because of the very small fraction of $e \to \gamma$ events in the underflow bin (10-15 GeV), fits in this bin do not converge properly. The MC prediction from the nominally selected DY+jets sample is used as a background estimate for this bin.

Table 5.3: Fine η^γ binning for fits for $e \to \gamma$ background estimation.

P_T^γ ranges, GeV	η^γ binning in barrel	η^γ binning in endcap
15-20-25-30-35-45-55-65	0.00-0.10-0.50-1.00-1.44	1.56-2.10-2.20-2.40-2.50
65-75-85-95	0.00-0.50-1.44	1.56-2.20-2.50
95-120-500	0.00-1.44	1.56-2.50
10-15 (underflow)	no fits; MC prediction used	

The $M_{e\gamma}$ distribution has two distinct types of events. The first is the events from DY+jets$\to$ ee+jets with one of the electrons misidentified as a photon. The distribution of $M_{e\gamma}$ of these events has a Z peak and a non-resonant component rising to low masses. The second type of events are all the other sources ($W\gamma$,

W+jets, etc.) that do not have a Z peak. The fit function is:

$$F_{fit}^{e\to\gamma}(M_{e\gamma}) = N_{e\to\gamma} \cdot P_{e\to\gamma}(M_{e\gamma}) + N_{other} \cdot P_{other}(M_{e\gamma}), \tag{5.9}$$

where $N_{e\to\gamma}$ and N_{other} are the numbers of $e \to \gamma$ events and events from other sources, respectively, and $P_{e\to\gamma}$ and P_{other} are $M_{e\gamma}$ distribution functions of these two types of events.

The $P_{e\to\gamma}$ is the template-based function $RooNDKeysPdf$ [54] convolved with the Gaussian

$$P_{e\to\gamma} = RooNDKeysPdf * Gaussian. \tag{5.10}$$

$RooNDKeysPdf$ is a function of the RooFit package that creates a continuous probability distribution function out of a binned template. The templates are prepared from $e \to \gamma$-enriched DY+jets MC sample, separately for each P_T^{γ} and η^{γ} range. The convolution with the Gaussian is necessary because the template shapes are extracted from MC, and the energy scale and resolution in MC slightly differ from those in data. The parameters of the Gaussian distribution correct for these differences.

The P_{other} is $RooCMSShape$ [55] which is a product of an exponential decay and a step function. $RooCMSShape$ is described by four parameters, and they all are used as fit parameters in $F_{fit}^{e\to\gamma}$.

Overall, $F_{fit}^{e\to\gamma}$ has eight fit parameters. This includes two parameters of the Gaussian distribution, four parameters of $RooCMSShape$, $N_{e\to\gamma}$ and N_{other}.

The fit plots, as well as the explanation of parameters on the plots, are provided in App. F and the tables with the parameter values determined from the fits in different P_T^{γ} ranges are provided in App. G.

5.4.3 Other Backgrounds

In addition to the backgrounds discussed before, there is also the non-negligible real-γ background. The main sources of this background are $Z\gamma \rightarrow ll\gamma$ and $W\gamma \rightarrow \tau\nu\gamma$ processes. Their contributions are estimated based on MC predictions.

Other background sources include $e \rightarrow \gamma$ background in the muon channel, jets→lepton, and jets→lepton+jets→ γ. MC studies shows these backgrounds to be negligible.

5.4.4 P_T^γ Spectra before and after the Background Subtraction

The results of the background estimation and subtraction procedure are summarized in Fig. 5.5-5.6 and in Tab. 5.4-5.5. The top and middle plots in Fig. 5.5-5.6 show the P_T^γ spectrum in data superimposed with the signal MC and background estimates that includes jets→ γ and real-γ backgrounds in both channels and $e \rightarrow \gamma$ background in the electron channel. The bottom plots show data yields after full background subtraction superimposed with signal MC. Left and right plots correspond to fit results produced with I_{ch}^γ and $\sigma_{i\eta i\eta}^\gamma$ templates, respectively.

The results produced with two methods of jets→ γ background estimation differ significantly, and both show significant disagreement with the MC prediction. From the MC side, the $W\gamma$ and W+jets MC samples are produced and normalized to NLO cross section. Those samples have NLO kinematics that affects the shape of the spectrum. For backgrounds, the systematic errors are not included. The conclusions regarding the agreement between the $W\gamma$ extracted P_T^γ spectrum should wait until the later sections when all effects are taken into account, and systematic uncertainties are computed.

The possible causes of the disagreement related to jets→ γ background estimation are considered in greater detail. The causes include possible differences between real-γ/fake-γ templates and the corresponding components in the fitted dataset. The differences may arise from the differences in shapes of $I_{ch}^{\gamma}/\sigma_{i\eta i\eta}^{\gamma}$ distributions between $W\gamma/W$+jets and $Z\gamma$/DY+jets events, from the incorrect normalization of the $Z\gamma$ MC sample that is used to prepare fake-γ templates, and from the effect of P_T^{γ} dependence of the template shapes for merged P_T^{γ} bins. Another possible cause of the disagreement related to the jets$\rightarrow \gamma$ background estimation is a bias of the fit machinery associated with the likelihood estimators. For better understanding the sources of disagreements related to jets$\rightarrow \gamma$ background estimation, we perform two MC closure checks and a $Z\gamma$ check where some of the effects listed above are not present by construction (Ch. 5.4.5).

The effects related to $e \rightarrow \gamma$ and real-γ background estimation are smaller. They are discussed in Ch. 5.7.

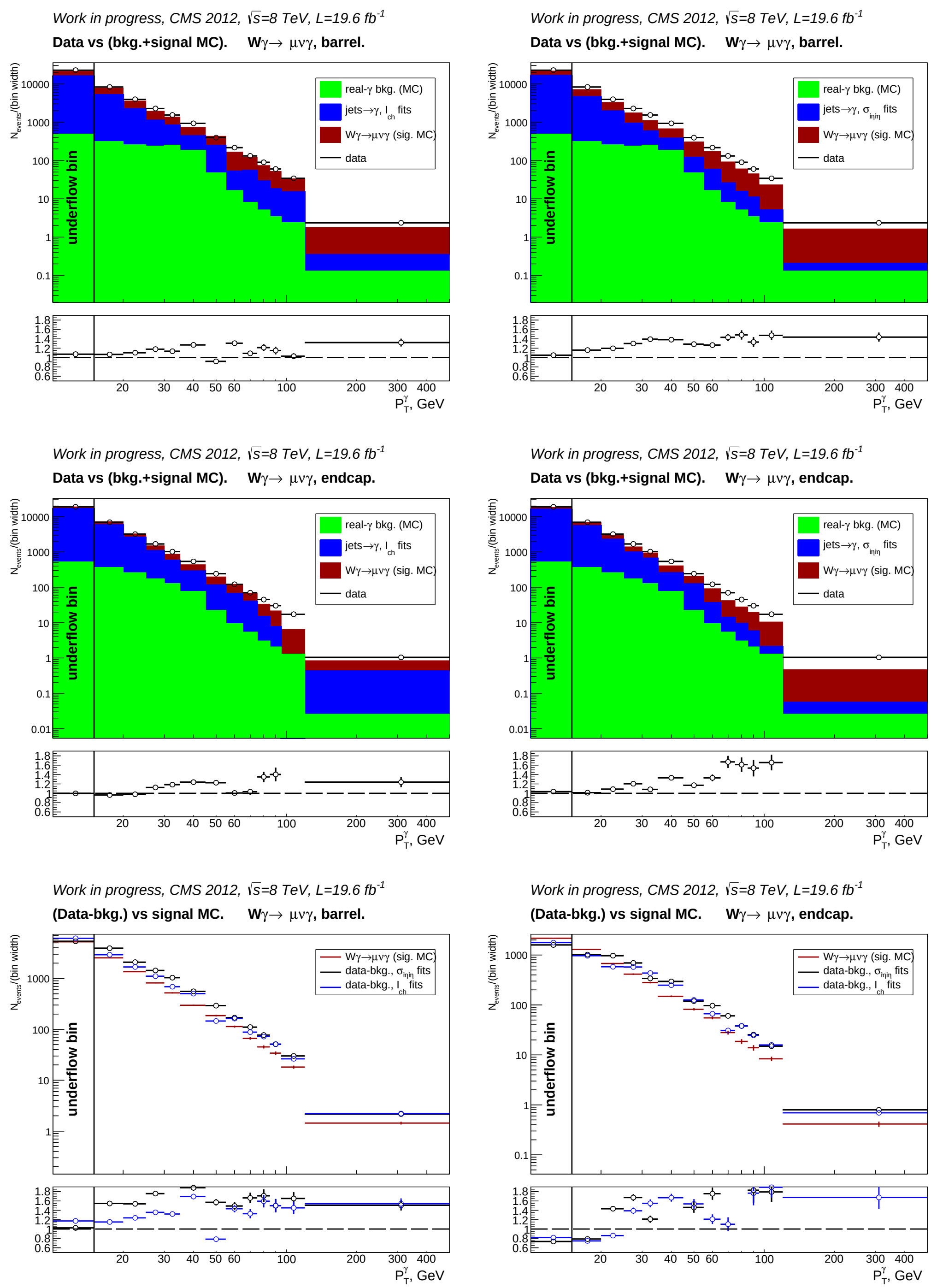

Figure 5.5: P_T^{γ} spectrum of the $W\gamma \rightarrow \mu\nu\gamma$ candidates. I_{ch} vs $\sigma_{i\eta i\eta}$ fit results in the muon channel are compared. Top and middle: data vs fake-γ background derived from the template method + real-γ background predicted by dedicated MC samples + signal MC, with I_{ch} (left) and $\sigma_{i\eta i\eta}$ (right) used as fit variables in EB (top) and EE (middle). Bottom: data yields after full background subtraction vs signal MC in EB (left) and EE (right).

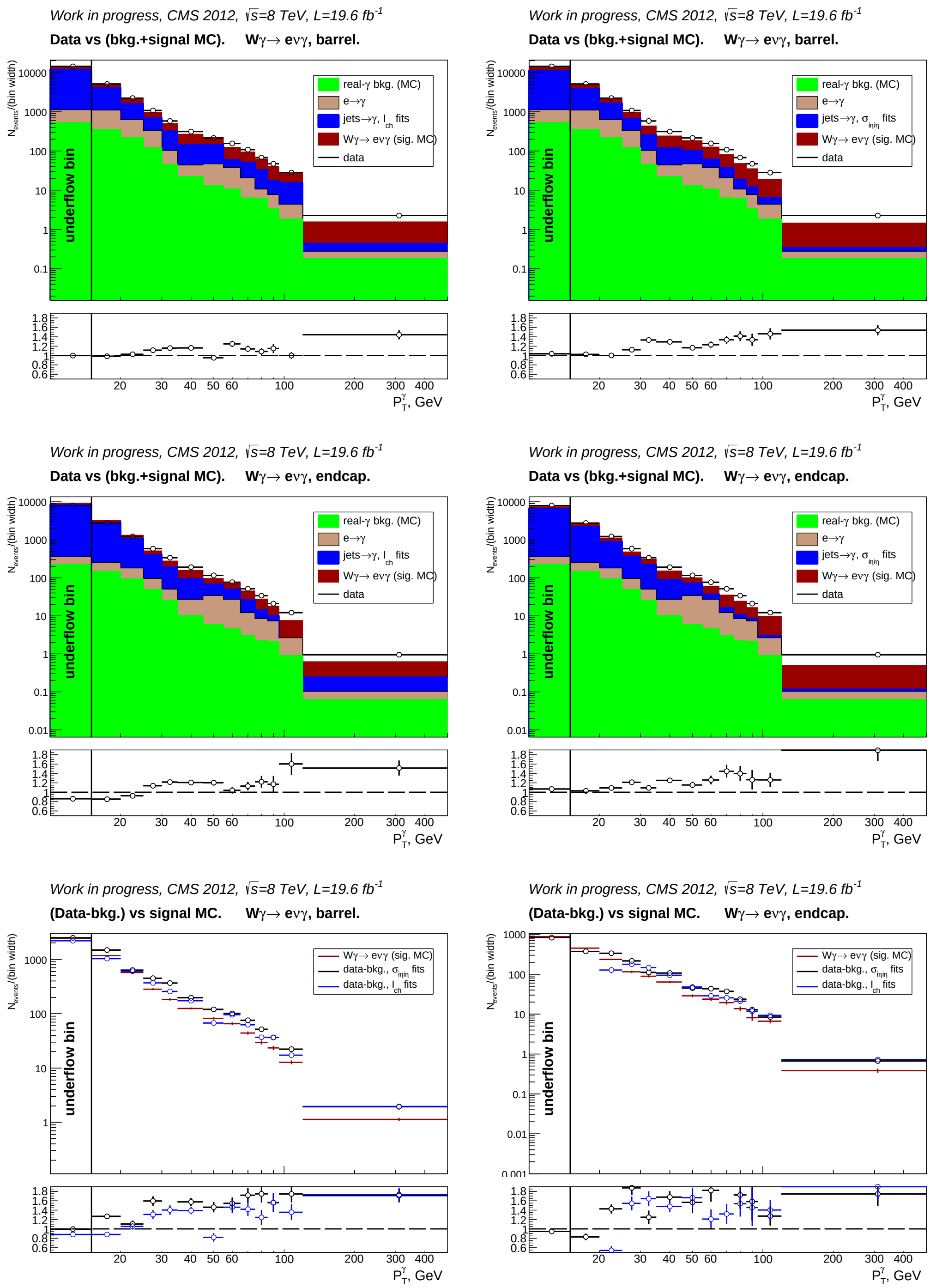

Figure 5.6: P_T^γ spectrum of the $W\gamma \to e\nu\gamma$ candidates. I_{ch} vs $\sigma_{i\eta i\eta}$ fit results in the electron channel are compared. Top and middle: data vs fake-γ background derived from the template method + real-γ background predicted by dedicated MC samples + signal MC, with I_{ch} (left) and $\sigma_{i\eta i\eta}$ (right) used as fit variables in EB (top) and EE (middle). Bottom: data yields after full background subtraction vs signal MC in EB (left) and EE (right).

Table 5.4: The $W\gamma$ yields in the muon channel, including selected data yields, jets→ γ and real-γ background estimates, yieds after the background subtraction ("data-bkg"), and signal $W\gamma$ yields predicted by MC ("signal MC").

P_T^γ, GeV	data yields	background estimates jets→ γ I_{ch}^γ	$\sigma_{i\eta i\eta}^\gamma$	MC real-γ	data-bkg	signal MC
barrel photons						
10-15	114047±338	79833±251	77612±322	2453±46	26867±385	26251±240
15-20	41411±203	21434±150	24543±143	1566±34	19642±245	12707±164
20-25	19801±141	8466±101	9878±78	1283±31	10446±168	6793±120
25-30	11409±107	3509±68	4402±46	1180±27	7180±123	4087±93
30-35	7717±88	1687±49	2944±40	1253±27	5181±99	2604±75
35-45	9339±97	1947±56	2540±33	1840±33	5587±114	2971±80
45-55	3950±63	731±40	1964±40	477±18	2923±75	1861±63
55-65	2172±47	415±25	363±11	164±12	1694±50	1135±50
65-75	1320±36	177±17	466±19	81±8	1106±39	664±38
75-85	899±30	103±13	238±16	51±7	773±32	452±31
85-95	600±24	76±11	146±11	34±6	510±26	341±27
95-120	856±29	67±11	319±25	60±9	750±31	454±31
120-500	897±30	28±7	83±7	50±8	825±31	547±34
endcap photons						
10-15	94370±307	77649±215	81161±426	2632±41	7937±306	10823±154
15-20	34643±186	25902±142	27661±184	1835±34	5089±213	6474±120
20-25	15988±126	10018±93	11659±102	1294±29	4842±138	3377±86
25-30	8429±92	4061±58	4558±51	871±23	3460±98	2068±67
30-35	5110±71	2669±54	2268±32	641±19	1700±81	1404±56
35-45	5414±74	1807±44	2113±29	771±22	2957±83	1489±57
45-55	2422±49	1025±50	936±19	222±13	1196±68	819±43
55-65	1217±35	270±19	564±16	94±9	966±36	551±35
65-75	703±27	87±11	346±13	54±7	604±28	280±25
75-85	451±21	63±9	117±6	30±5	379±22	186±20
85-95	303±17	37±7	56±4	21±5	255±18	139±18
95-120	433±21	20±5	-81±5	32±6	374±21	209±22
120-500	396±20	11±4	153±12	10±2	302±18	157±19

Table 5.5: The $W\gamma$ yields in the electron channel, including selected data yields, jets$\rightarrow\gamma$, $e\rightarrow\gamma$ and real-γ background estimates, yieds after the background subtraction ("data-bkg"), and signal $W\gamma$ yields predicted by MC ("signal MC").

P_T^γ, GeV	data yields	background estimates				data-bkg	signal MC
		jets$\rightarrow\gamma$		$e\rightarrow\gamma$	MC real-γ		
		I_{ch}^γ	$\sigma_{i\eta i\eta}^\gamma$				
barrel photons							
10-15	71649±268	51004±200	53577±266	2923±80	2688±41	12425±316	12480±164
15-20	25455±160	13487±118	14474±110	3715±178	1779±32	7422±262	5858±110
20-25	11130±105	5112±78	4846±55	2023±137	1101±25	3168±186	2869±77
25-30	5388±73	1748±47	1790±29	1031±72	603±18	2251±111	1412±54
30-35	2907±54	752±32	1079±24	286±33	229±12	1831±68	916±44
35-45	3128±56	735±34	1003±21	215±27	223±12	1965±70	1248±51
45-55	2147±46	551±31	964±28	335±37	134±10	1200±65	821±42
55-65	1556±39	228±19	211±8	272±39	108±9	1011±57	654±37
65-75	1083±33	163±16	300±15	143±27	64±7	757±44	441±31
75-85	680±26	79±11	224±15	45±13	62±7	516±31	295±26
85-95	473±22	43±9	99±9	43±17	34±5	366±29	234±23
95-120	703±27	53±9	274±24	63±19	47±5	555±34	318±27
120-500	859±29	23±6	61±6	34±12	71±8	735±33	430±31
endcap photons							
10-15	39746±199	31043±138	40022±13	666±38	1120±27	4130±204	4368±97
15-20	13818±118	9920±88	12692±124	509±56	744±21	1870±145	2253±68
20-25	6133±78	3538±56	4558±63	433±36	473±17	1680±92	1177±49
25-30	2924±54	1358±34	1516±29	229±24	250±12	1079±62	575±34
30-35	1690±41	850±31	694±18	120±16	130±9	555±49	445±31
35-45	1905±44	613±26	670±16	167±19	103±8	1071±51	638±37
45-55	1162±34	377±30	337±11	281±28	61±6	450±53	287±24
55-65	767±28	98±12	228±11	227±28	46±6	433±40	238±22
65-75	513±23	40±8	139±9	90±18	31±4	372±29	194±21
75-85	340±18	22±6	57±5	62±15	22±5	236±24	137±18
85-95	210±14	11±4	25±3	52±19	21±3	129±24	81±14
95-120	304±17	8±3	-43±4	43±13	23±5	212±22	166±20
120-500	360±19	5±3	53±7	15±7	24±4	254±18	146±19

5.4.5 Cross Checks for the Jets$\rightarrow\gamma$ Background Estimation

For the first MC closure check, we prepare the pseudodata sample by mixing simulated W+jets and $W\gamma$ together to mimic real data. Events in both samples are weighted to the same luminosity L =19.6 fb^{-1}. Real-γ templates are prepared from the $W\gamma$ subsample of the mixture while the fake-γ templates are prepared from the W+jets subsample. Then fits on this sample of pseudodata are performed and the number of real-γ and fake-γ events determined from fit are compared to the known numbers of simulated events that went into preparing the mixture. The outcome of this cross check cannot be affected by the effects of possible wrong normalizations of MC samples and the difference between real-γ and fake-γ I^{γ}_{ch} and $\sigma^{\gamma}_{i\eta i\eta}$ distributions in $W\gamma/W$+jets and $Z\gamma$/DY+jets samples, and therefore gives us a cleaner test of a bias of the fitting machinery and effect of merging events in several P^{γ}_{T} bins when preparing $\sigma^{\gamma}_{i\eta i\eta}$ templates. The real-γ yields extracted from fits and the $W\gamma$ MC prediction are in agreement within 20%, however, the fake-γ yields extracted from fits have larger discrepancies with W+jets MC predictions in certain high P^{γ}_{T} bins where real-γ fraction is higher, and a small discrepancy in real-γ yields leads to large discrepancies in fake-γ yields (App. H, Fig. H.1-H.2). The discrepancies indicate a presence of a bias in fitting machinery which is taken care of by the estimation of the systematic uncertainties as described in Ch. 5.7.1.

The second check is more realistic: the $W\gamma$ selection requirements are applied on MC samples $W\gamma$, W+jets, $Z\gamma$, Z+jets, and $t\bar{t}$+jets, and afterwards these samples and mixed together into the pseudodata sample I. To prepare templates, $Z\gamma$ and DY+jets MC samples are mixed together to constitute a $Z\gamma$-selected pseudodata sample II which is used the same way as $Z\gamma$-selected dataset is used to prepare templates for the background estimation in the data analysis. Then the pseudodata I histograms are fitted and the fit results are superimposed with MC predictions same as it is done for the real data. The outcome of this closure check is not affected by the effects of possible wrong normalizations of MC samples but is affected by the effect of the possible difference between real-γ and fake-γ I^{γ}_{ch} and $\sigma^{\gamma}_{i\eta i\eta}$ distributions in $W\gamma/W$+jets and $Z\gamma$/DY+jets samples. The results of this closure check show better agreement of pseudodata I vs estimated background + signal MC than we observe in data, however the disagreement in certain P^{γ}_{T} bins remains significant (App. H, Fig. H.3-H.6).

In addition to the checks described above, we also perform a $Z\gamma$ check on data and MC mixture. The $Z\gamma$ check tests the effects of possibly incorrect $Z\gamma$ normalization, effects of merging several P_T^{γ} bins, and bias in the fit machinery, while is not affected by possible differences in I_{ch}^{γ} and $\sigma_{i\eta i\eta}^{\gamma}$ distirbutions between $W\gamma/W$+jets and $Z\gamma/$DY+jets events. Both the $Z\gamma$ data analysis and the $Z\gamma$ MC closure check show very good agreement between data and background estimates + signal MC as well as between the two methods of the background estimation. The detailed description of the $Z\gamma$ check is available at App. B.

The results of the cross checks show that our main sources of disagreements in Fig. 5.5-5.6 related to jets$\rightarrow\gamma$ background estimation are differences in I_{ch}^{γ} and $\sigma_{i\eta i\eta}^{\gamma}$ distirbutions between $W\gamma/W$+jets and $Z\gamma/$DY+jets events, and sometimes there is also an impact from bias in the fitting machinery. Related systematic uncertainties are discussed in Ch. 5.7.

5.5 Detector Resolution Unfolding

Finite detector resolution in measuring the energy of a photon causes bin-to-bin migration in the P_T^{γ} spectrum. The reconstructed $P_T^{\gamma(reco)}$ may not coincide with the true $P_T^{\gamma(true)}$, and, therefore, the event reconstructed in a P_T^{γ} bin j may, in fact, belong to the bin $i \neq j$. To recover the true P_T^{γ} spectrum, we apply a procedure of the detector resolution unfolding.

The reconstructed P_T^{γ} spectrum is related to the true P_T^{γ} spectrum as:

$$N_j^{reco} = R_{ji} N_i^{A\times\epsilon}, \tag{5.11}$$

where N_j^{reco} and $N_i^{A\times\epsilon}$ are numbers of events in a given $P_T^{\gamma(reco)}$ and $P_T^{\gamma(true)}$ bins, respectively, R_{ji} is the "response matrix" where each element is the probability of an event with true P_T^{γ} in the bin "i" to be reconstructed with P_T^{γ} in the bin "j". The notation $N_i^{A\times\epsilon}$ is used because this yield is further corrected for the acceptance and efficiency (Ch. 5.6) and is consistent with the definition given in Tab. 5.1.

The simplest method to recover the true spectrum is to solve the system of linear equations Eq. 5.11 if the R_{ji} is known. However, this method often encounters numerical difficulties due to possible matrix singularity, large statistical fluctuations and the effect of oscillations of the unfolded spectrum. To avoid these difficulties, we use the D'Agostini method [56] as recommended by the CMS SMP group. The D'Agostini method is based on the Bayes theorem and unfolds the reconstructed spectrum iteratively.

The migration matrix M_{ji} is prepared using the signal MC sample ($W\gamma \rightarrow \mu\nu_{\mu}\gamma / W\gamma \rightarrow e\nu_e\gamma$) where both true (gen-level) and reconstructed P_T^{γ} spectra are known. The M_{ji} contains the number of selected signal events in each [j,i] bin.

After that, we pass the migration matrix M_{ji}, generated and reconstructed yields from signal MC N_i^{gen-MC} and $N_j^{reco-MC}$ and reconstructed yields from data to the RooUnfold class [57] which performs unfolding using D'Agostini method with five iterations. Yields before and after detector resolution unfolding are compared in Tab. 5.6 for the muon channel and in Tab. 5.7 for the electron channel.

Table 5.6: P_T^γ yields of $W\gamma$ before and after unfolding in the muon channel. Diagonal elements of the error matrix are shown as uncertainties for the unfolded yields.

P_T^γ, GeV	yields	
	pre-unfolded	unfolded
10 - 15	39621 ± 678	38843 ± 718
15 - 20	19449 ± 361	19662 ± 438
20 - 25	11315 ± 230	11443 ± 275
25 - 30	8417 ± 160	8714 ± 196
30 - 35	5613 ± 128	5529 ± 155
35 - 45	7518 ± 133	7895 ± 149
45 - 55	2716 ± 95	2605 ± 108
55 - 65	2293 ± 62	2307 ± 70
65 - 75	1191 ± 53	1198 ± 62
75 - 85	1101 ± 41	1165 ± 48
85 - 95	757 ± 33	776 ± 41
95 - 120	1054 ± 44	1064 ± 50
120 - 500	1107 ± 39	1141 ± 40

Table 5.7: P_T^γ yields of $W\gamma$ before and after unfolding in the electron channel. Diagonal elements of the error matrix are shown as uncertainties for the unfolded yields.

P_T^γ, GeV	yields	
	pre-unfolded	unfolded
10 - 15	9209 ± 378	9192 ± 413
15 - 20	4920 ± 319	4850 ± 380
20 - 25	3660 ± 212	3698 ± 249
25 - 30	2734 ± 127	2948 ± 159
30 - 35	2015 ± 84	2075 ± 102
35 - 45	2677 ± 83	2770 ± 91
45 - 55	1152 ± 81	1116 ± 93
55 - 65	1244 ± 70	1214 ± 80
65 - 75	881 ± 56	911 ± 63
75 - 85	579 ± 42	590 ± 48
85 - 95	483 ± 38	490 ± 45
95 - 120	664 ± 46	692 ± 50
120 - 500	1020 ± 40	1052 ± 40

After P_T^γ spectrum is unfolded, measurements in different P_T^γ bins become correlated. Correlation matrices are shown in Fig. 5.7.

For illustration purposes, in addition to the migration matrix we also prepare the response matrix R_{ji} (Fig. 5.8) by normalizing the migration matrix in each j bin to all events reconstructed in this bin. The response matrix is shown in Fig. 5.8.

To validate this procedure of detector resolution unfolding, we perform MC closure checks. Gen-level and reconstructed yields are prepared using the signal MC. Then reconstructed yields are smeared by a Gaussian distribution according to the statistical uncertainties on the yields. The smeared yields are unfolded and compared to the gen-level yields. In addition to the D'Agostini method, we check the performance of the matrix inversion method for the unfolding which recovers the true yields as $N_i^{A\times\epsilon} = (R_{ji})^{-1} N_j^{reco}$.

The results of the MC closure checks are summarized in Tab. 5.8-5.9 for the muon and electron channels respectively. The unfolded yields show reasonable agreement to the gen-level yields except for the underflow bin ($10-15$ GeV). The disagreement in the underflow bin may be caused by migration between P_T^γ <10 GeV and 10< P_T^γ <15 GeV ranges because events with P_T^γ <10 GeV are not present in the signal MC samples.

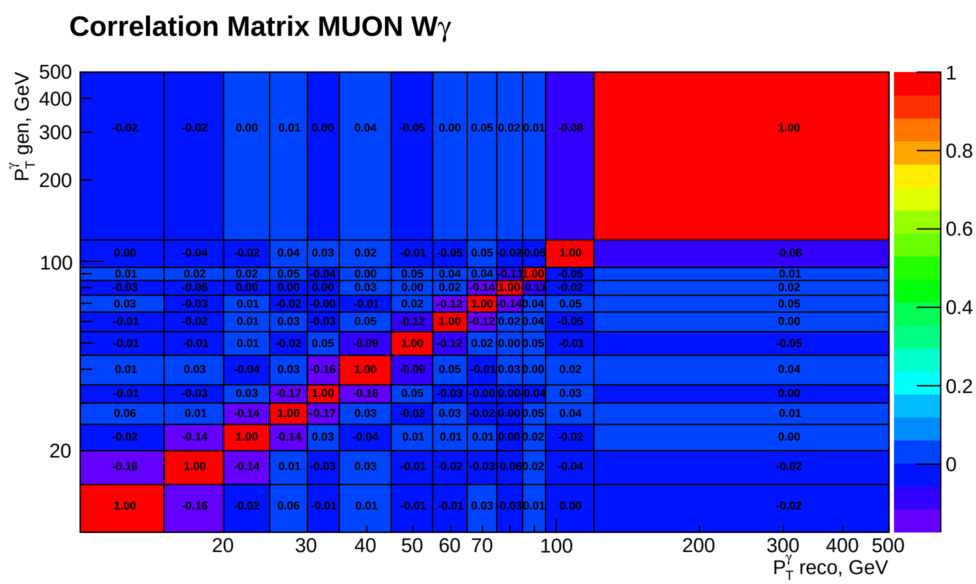

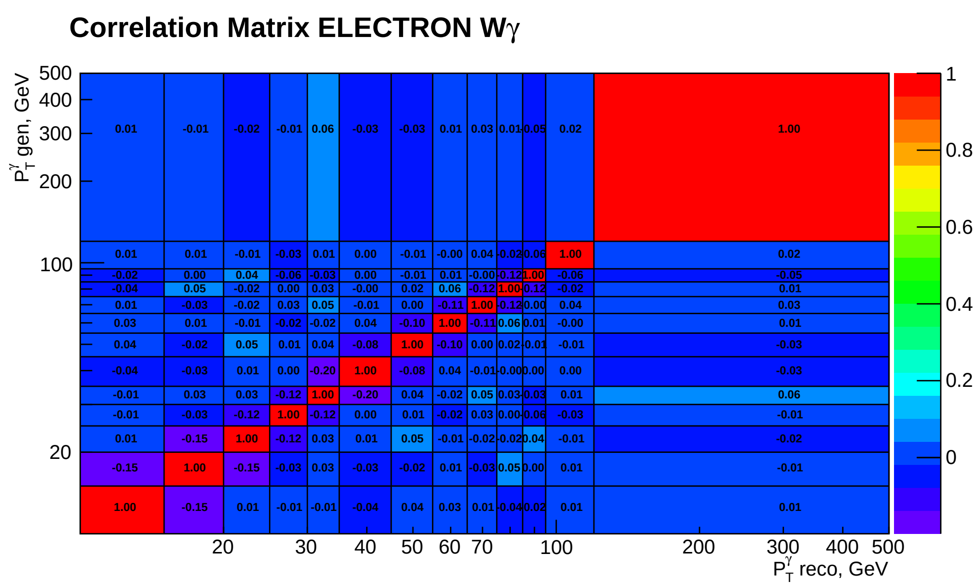

Figure 5.7: Correlation matrices of statistical uncertainties on unfolded $W\gamma$ yields in the muon (top) and electron (bottom) channels.

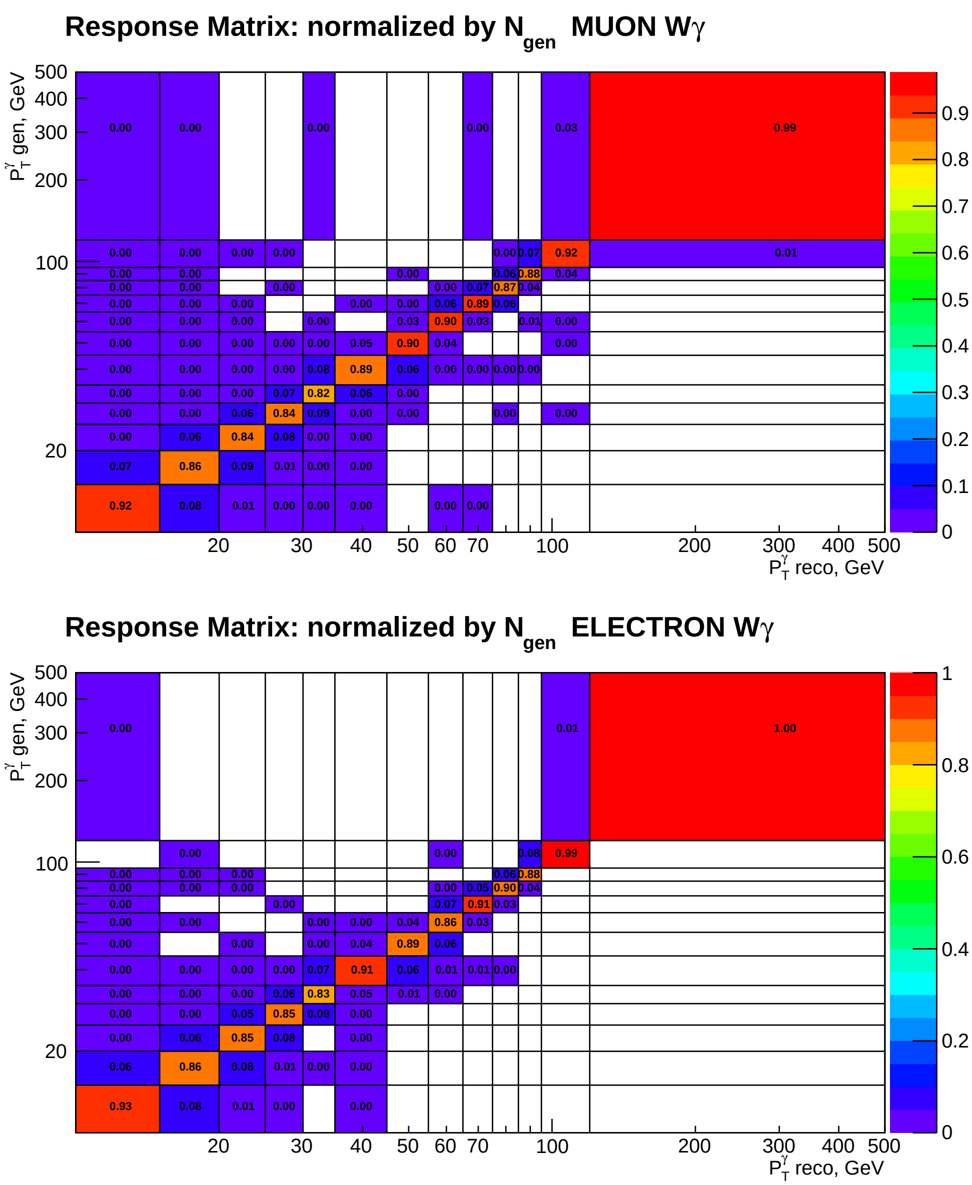

Figure 5.8: Response matrix derived from the signal MC in the muon (top) and electron (bottom) channels.

Table 5.8: Results of the MC closure test of the detector resolution unfolding of P_T^γ yields of $W\gamma$ in the muon channel. The unfolding procedure is applied on the "MC truth yields", and the results of the matrix inversion ("inversion") and D'Agostini ("D'Agostini") unfolding methods are compared to "reconstructed yields" and to each other.

P_T^γ, GeV	MC truth yields	reconstructed yields	unfolded yields inversion	unfolded yields D'Agostini
10 - 15	33888 ± 273	37074 ± 286	36226 ± 206	36222 ± 204
15 - 20	19736 ± 207	19181 ± 203	19612 ± 171	19619 ± 169
20 - 25	10364 ± 149	10171 ± 148	10358 ± 122	10354 ± 119
25 - 30	6254 ± 116	6156 ± 115	6233 ± 96	6234 ± 96
30 - 35	4026 ± 93	4007 ± 93	4010 ± 81	4010 ± 78
35 - 45	4516 ± 99	4461 ± 98	4502 ± 79	4502 ± 79
45 - 55	2731 ± 77	2680 ± 76	2724 ± 57	2724 ± 60
55 - 65	1662 ± 60	1686 ± 61	1655 ± 45	1655 ± 46
65 - 75	987 ± 46	945 ± 45	979 ± 38	979 ± 35
75 - 85	659 ± 38	638 ± 37	654 ± 30	653 ± 30
85 - 95	495 ± 33	480 ± 32	489 ± 27	489 ± 25
95 - 120	664 ± 38	663 ± 38	661 ± 28	661 ± 28
120 - 500	726 ± 40	704 ± 39	720 ± 26	720 ± 27
500 - 2000	2 ± 2	2 ± 2	2 ± 1	2 ± 1

Table 5.9: Results of the MC closure test of the detector resolution unfolding of P_T^γ yields of $W\gamma$ in the electron channel. The unfolding procedure is applied on the "MC truth yields", and the results of the matrix inversion ("inversion") and D'Agostini ("D'Agostini") unfolding methods are compared to "reconstructed yields" and to each other.

P_T^γ, GeV	MC truth yields	reconstructed yields	unfolded yields inversion	unfolded yields D'Agostini
10 - 15	16025 ± 185	16849 ± 190	17117 ± 143	17116 ± 141
15 - 20	8246 ± 131	8111 ± 130	8194 ± 109	8196 ± 108
20 - 25	4093 ± 92	4046 ± 92	4083 ± 75	4082 ± 74
25 - 30	2080 ± 66	1987 ± 64	2072 ± 55	2072 ± 55
30 - 35	1387 ± 54	1361 ± 54	1378 ± 47	1378 ± 46
35 - 45	1925 ± 64	1886 ± 63	1915 ± 51	1915 ± 50
45 - 55	1124 ± 49	1108 ± 48	1116 ± 37	1116 ± 38
55 - 65	855 ± 42	892 ± 43	848 ± 33	848 ± 34
65 - 75	655 ± 38	635 ± 37	649 ± 30	649 ± 28
75 - 85	447 ± 32	433 ± 32	442 ± 24	442 ± 24
85 - 95	316 ± 27	316 ± 27	311 ± 21	311 ± 20
95 - 120	507 ± 34	484 ± 33	501 ± 23	501 ± 23
120 - 500	593 ± 37	575 ± 36	587 ± 23	587 ± 24
500 - 2000	4 ± 3	4 ± 3	4 ± 2	4 ± 2

5.6 Acceptance and Efficiency Correction

The unfolded P_T^γ spectrum needs to undergo several corrections in order to obtain the true P_T^γ spectrum in the chosen phase space: the selection efficiency, the reconstruction efficiency, and the acceptance corrections. The total background-subtracted yield needs to undergo these corrections as well. The nature of these corrections and the methods of their application are explained below.

The selection requirements in the $W\gamma$ measurement are stricter than the phase space requirements for the cross section measurement (Ch. 5), thus, during the selection procedure, we discard a large number of signal events that are within the phase space. The ratio between the number of selected signal events and the number of signal events reconstructed within the phase space is called a "selection efficiency."

In addition to the event loss due to the selection requirements, a certain number of events are truly within our phase space but are reconstructed outside of the phase space or are not reconstructed at all and vice versa. The ratio between the number of signal events that are reconstructed within our phase space and the number of events that truly appear within our phase space is called a "reconstruction efficiency". The procedure of detector resolution unfolding (Ch. 5.5) takes care of this effect for the P_T^γ phase space requirement in the P_T^γ yields, however effects of other phase space requirements for both P_T^γ and total yields and the P_T^γ requirement for the total yield still need to be taken into account.

Finally, certain events that are truly within the phase space may not be caught by the detector due to the detector acceptance restrictions. Examples of such events include events with final state photons or electrons that go into the gap between the EB and EE, with corresponding $1.44 < |\eta^{\gamma,e}| < 1.56$. The ratio between the number of events truly reconstructed within the phase space and the number of events that are also registered by the detector is called the "acceptance."

To correct our selected, background-subtracted, unfolded yields from Tab. 5.6-5.7 for these effects, we introduce a correction $A \times \epsilon$ that accumulates all three effects described above. The correction is estimated using the signal MC sample, separately for the total yield and P_T^γ yields.

The numerator $N^{A\epsilon}$ for the correction of the total yield is defined as the number of selected events in the signal MC with the PU weight applied. The numerator $N_i^{A\epsilon}$ for the correction of the P_T^γ yields is determined as selected signal MC yields with the PU weight applied in $P_T^{\gamma(gen)}$ bins at the gen-level. Index i stands for P_T^γ bins.

The denominator $D^{A\epsilon}$ of the $A \times \epsilon$ correction is determined as the number of events that are within the phase space based on their kinematic parameters. For the correction $(A \times \epsilon)_i$ of the P_T^γ yields, the numbers $D_i^{A\epsilon}$ are determined separately for each P_T^γ bin.

The $A \times \epsilon$ correction is determined then as $A \times \epsilon = N^{A\epsilon}/D^{A\epsilon}$ for the total yield and as $(A \times \epsilon)_i = N_i^{A\epsilon}/D_i^{A\epsilon}$ for the P_T^γ yields where index i stands for a P_T^γ bin. The $A \times \epsilon$ for the total yield are 0.2891±0.0006 for the muon channel and 0.1229±0.0004 for the electron channel. The uncertainties are determined by the statistical power of the $W\gamma$ MC sample. The values of the $(A \times \epsilon)_i$ correction for the P_T^γ yields are plotted in Fig. 5.9.

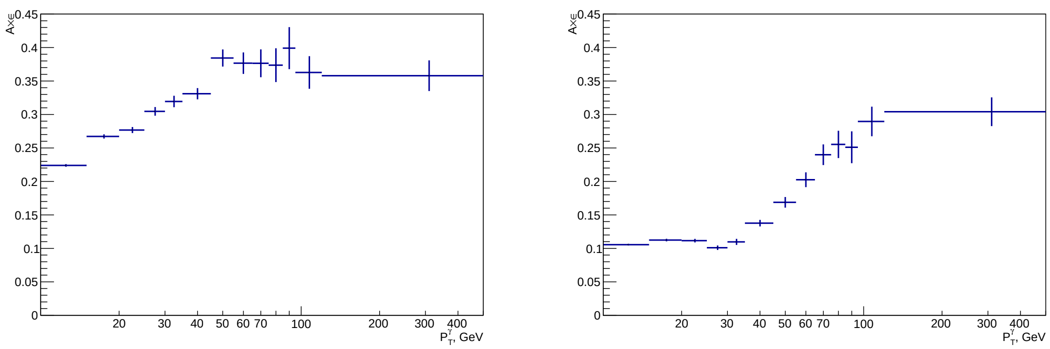

Figure 5.9: $A \times \epsilon$ corrections in the muon (left) and electron (right) channels. Plots are produced with $W\gamma$ MC sample at $\sqrt{s}$ =8 TeV.

5.7 Systematic Uncertainties

Each step of the measurement has uncertainties associated with the step. Each uncertainty is estimated as an uncertainty on yields, and is propagated through the further measurement steps to be converted into the uncertainty on the cross section.

Uncertainties related to the subtraction of various backgrounds lead to uncertainties on the extracted signal yields ("data-bkg. yields"). The uncertainties on the differential cross section are estimated from the uncertainties on signal yields by propagating through the unfolding and the $A \times \epsilon$ correction, then dividing by the luminosity and the P_T^{γ} bin width. For the total cross section, the uncertainties on "data-bkg." yields are divided by the $A \times \epsilon$ correction and luminosity.

When an uncertainty is propagated through the unfolding, the yields in the different P_T^{γ} bins become correlated. The correlation matrices on the unfolded yields corresponding to each uncertainty related to the background subtraction are provided in App. I, as well as the correlation matrix related to the unfolding procedure itself. Uncertainties related to post-unfolding steps of the $W\gamma$ measurement do not have to be propagated through unfolding and, thus, do not have corresponding correlation matrices.

Uncertainties related to jets$\rightarrow\ \gamma$ background estimation are described in Ch. 5.7.1 while uncertainties related to the other measurement steps are described in Ch. 5.7.2. Ch. 5.7.3 summarizes relative systematic uncertainties originating from different sources.

5.7.1 Uncertainties Related to Jets$\rightarrow\gamma$ Background Estimation

The selected data samples in both muon and electron channels are composed mostly of jets$\rightarrow\gamma$ events. Because there are more background than signal events in our selected sample in the low P_T^γ region, any uncertainty on the background yields translates to larger relative uncertainty of the signal yields in this region. The uncertainties related to jets$\rightarrow\gamma$ background estimation are dominant sources of uncertainties in all P_T^γ bins in the muon channels and in bins with P_T^γ <55 GeV in the electron channel.

The following sources contribute to the uncertainty of the jets$\rightarrow\gamma$ background estimation:

- biases in the template shapes and the fit procedure;
- uncertainty on the normalizations of $Z\gamma$ and DY+jets MC samples when the real-γ (fake-γ) portions are subtracted from the ISR (FSR) templates; and
- limited statistical power of the fake-γ and real-γ templates.

The systematic uncertainty on "data-bkg." yields due to the bias in the template shapes and the fit procedure is computed as the difference between fit results of I_{ch}^γ and $\sigma_{i\eta i\eta}^\gamma$ distributions

$$\Delta N_{Ich\_vs\_\sigma i\eta i\eta} = |N_{Ich} - N_{\sigma i\eta i\eta}|, \tag{5.12}$$

where N_{Ich} and $N_{\sigma i\eta i\eta}$ are signal yields obtained with fits of I_{ch}^γ and $\sigma_{i\eta i\eta}$, respectively. These two variables are chosen because they are fairly independent: I_{ch}^γ indicates charged particle activity around the photon, while $\sigma_{i\eta i\eta}^\gamma$ describes the shape of the shower induced by this photon in the ECal. If the template shapes were correct representations of the real-γ and fake-γ I_{ch}^{γ} and $\sigma_{i\eta i\eta}$ distributions in data, and fits always resulted in a correct numbers of real-γ and fake-γ events, then the results of fits of these two variables would be consistent. However, the two sets of fit results are found to dramatically disagree. The difference between the results $|N_{Ich} - N_{\sigma i\eta i\eta}|$ is assigned as a measure of the systematic uncertainty on "data-bkg." yields.

The uncertainty related to the limited statistical power of the data which are used to prepare templates is computed by separately randomizing the real-γ and the fake-γ templates. We prepare 20 real-γ and 100 fake-γ templates by randomizing our nominal templates with the Gaussian distribution. Then we perform fits with new templates and take the standard deviation of the fit results as an uncertainty. The uncertainties are computed separately for the real-γ and the fake-γ templates. The statistical uncertainty of the fake-γ template is larger.

The results of the systematic uncertainty of $|N_{Ich} - N_{\sigma i\eta i\eta}|$ and the template statistical uncertainty are summarized in the Tab. 5.10-5.11. The column "yield data-bkg." is the background subtracted yield which is used for the cross section measurement. The central values of these yields are taken from the "data I_{ch}^{γ}" column. The uncertainties in column "sig. MC ($W\gamma \to [\mu/e]\nu\gamma$)" are statistical uncertainties of the signal MC samples. The uncertainties in columns "data I_{ch}^{γ}", "data $\sigma_{i\eta i\eta}^{\gamma}$", "MC closure I_{ch}^{γ}", "MC closure $\sigma_{i\eta i\eta}^{\gamma}$" include statistical uncertainties and systematic uncertainties originated from the limited statistical power of (pseudo)data used to prepare templates for jets$\to$ γ background estimation. Two uncertainties in the column "yield data-bkg." are uncertainties estimated as $|N_{Ich} - N_{\sigma i\eta i\eta}|$ and uncertainties originated from the limited statistical power of data used to prepare real-γ and fake-γ templates. The values are shown in a format

$N \pm \Delta N(I_{ch}$ vs $\sigma_{i\eta i\eta}$ templ.$) \pm \Delta N($templ. stat.$)$

to compare these two uncertainties side-by-side.

Table 5.10: The P_T^γ yields of $W\gamma \to \mu\nu\gamma$ data and pseudodata after the full background subtraction with jets$\to \gamma$ background subtracted based on fits of I_{ch}^γ and $\sigma_{i\eta i\eta}^\gamma$ distributions. The "yields data-bkg." are the background subtracted yields that are passed to the further measurement steps. The central values for these yields coincide with "data I_{ch}^γ", the first uncertainties are estimated as $|N_{Ich} - N_{\sigma i\eta i\eta}|$, and the second uncertainties are uncertaintries related to the limits of the statistical power of data samples used to prepare I_{ch}^γ templates. The signal MC yields "sig. MC ($W\gamma \to \mu\nu\gamma$)" are provided for the comparison purpose.

P_T^γ, GeV	sig. MC ($W\gamma \to \mu\nu\gamma$)	data		pseudodata		yields data-bkg.
		I_{ch}^γ	$\sigma_{i\eta i\eta}^\gamma$	I_{ch}^γ	$\sigma_{i\eta i\eta}^\gamma$	
barrel photons						
10-15	26250±240	30779±1919	26866±3134	29753±2476	35169±3726	30779±3913±1865
15-20	12706±164	14620±1070	19641±1771	10809±1079	14990±2123	14620±5021±1041
20-25	6793±120	8412±711	10446±4313	7746±626	9447±1741	8412±2033±693
25-30	4087±93	5543±685	7179±3437	4459±532	5061±2094	5543±1636±675
30-35	2603±74	3438±500	5181±2581	3451±197	3296±1156	3438±1742±490
35-45	2971±80	5033±466	5587±3366	4515±308	4394±1632	5033±554±454
45-55	1861±63	1458±410	2923±593	1828±277	2493±146	1458±1464±402
55-65	1135±49	1626±207	1693±501	1165±214	1497±311	1626±67±201
65-75	664±37	881±43	1105±271	787±193	694±162	881±223±7
75-85	451±31	720±34	772±88	631±106	711±143	720±52±0
85-95	340±27	511±139	510±175	464±62	451±98	511±0±136
95-120	453±31	658±105	749±31	730±113	593±83	658±91±98
120-500	546±34	842±214	824±63	809±105	710±191	842±18±211
endcap photons						
10-15	10823±154	8840±2242	7936±2947	16556±2900	-2631±1967	8840±903±2184
15-20	6474±119	4829±1132	5089±1518	6490±1142	2686±2124	4829±260±1101
20-25	3377±86	2902±729	4842±1329	5418±578	4483±1291	2902±1939±710
25-30	2068±67	2873±408	3460±1514	3154±356	3920±975	2873±586±394
30-35	1403±55	2174±306	1699±693	1821±401	1495±545	2174±474±295
35-45	1489±57	2485±339	2956±1009	2405±279	2204±935	2485±471±329
45-55	818±42	1257±243	1196±595	905±176	1150±226	1257±61±237
55-65	550±34	666±208	966±375	581±219	329±260	666±299±204
65-75	280±24	308±169	604±206	476±80	457±141	308±295±166
75-85	186±20	380±162	378±91	249±69	200±66	380±1±161
85-95	139±17	245±60	254±28	322±19	203±30	245±8±57
95-120	208±21	395±55	374±195	353±41	173±54	395±21±51
120-500	157±18	263±88	302±17	265±53	189±30	263±38±85

Another source of the systematic uncertainty related to the jets$\to \gamma$ background estimation ΔN_{Norm} originates from the uncertainty on the $Z\gamma$ MC normalization. The $Z\gamma$ MC sample is used to prepare fake-γ template, and the normalization of this sample significantly affects the template shape. In fact, uncertainty on DY+jets

Table 5.11: The P_T^γ yields of $W\gamma \to e\nu\gamma$ data and pseudodata after the full background subtraction with jets$\to \gamma$ background subtracted based on fits of I_{ch}^γ and $\sigma_{i\eta i\eta}^\gamma$ distributions. The "yields data-bkg." are the background subtracted yields that are passed to the further measurement steps. The central values for these yields coincide with "data I_{ch}^γ", the first uncertainties are estimated as $|N_{Ich} - N_{\sigma i\eta i\eta}|$, and the second uncertainties are uncertaintries related to the limits of the statistical power of data samples used to prepare I_{ch}^γ templates. The signal MC yields "sig. MC ($W\gamma \to e\nu\gamma$)" are provided for the comparison purpose.

P_T^γ, GeV	sig. MC ($W\gamma \to e\nu\gamma$)	data		MC closure		yield data-bkg.
		I_{ch}^γ	$\sigma_{i\eta i\eta}^\gamma$	I_{ch}^γ	$\sigma_{i\eta i\eta}^\gamma$	
barrel photons						
10-15	12480±163	10994±1331	12425±2000	10640±1500	14995±2225	10994±1430±1277
15-20	5857±110	5160±668	7421±1173	4124±602	5721±1927	5160±2261±613
20-25	2868±77	3022±384	3168±2937	3390±258	3699±1261	3022±145±338
25-30	1411±54	1846±293	2250±1984	1365±152	1339±1167	1846±404±273
30-35	915±43	1283±193	1831±971	877±111	891±278	1283±547±180
35-45	1247±51	1732±190	1965±882	1359±111	1330±277	1732±232±178
45-55	820±41	673±207	1199±485	698±118	933±65	673±526±196
55-65	654±37	956±302	1010±157	566±95	666±152	956±53±296
65-75	440±30	625±252	756±47	357±99	458±123	625±131±248
75-85	295±25	367±137	516±134	339±45	285±84	367±148±132
85-95	234±22	364±29	366±33	315±63	283±83	364±1±2
95-120	318±26	430±88	555±66	397±77	400±135	430±124±78
120-500	429±30	743±234	734±40	568±54	537±236	743±9±231
endcap photons						
10-15	4368±96	-1785±122	4129±1180	2286±1356	-1502±1196	-1785±5915±108
15-20	2253±68	-241±537	1869±762	1541±483	352±759	-241±2110±506
20-25	1177±49	637±298	1679±534	1308±192	1414±481	637±1042±277
25-30	574±34	887±147	1078±646	674±117	1125±370	887±190±131
30-35	445±31	731±107	555±249	451±119	355±155	731±176±96
35-45	638±37	943±116	1071±326	773±76	789±189	943±127±104
45-55	287±24	478±106	449±449	307±67	347±78	478±28±95
55-65	237±22	287±155	433±44	225±51	220±114	287±145±150
65-75	194±21	255±73	372±38	154±45	37±87	255±116±67
75-85	137±18	210±47	236±28	201±59	155±73	210±25±40
85-95	81±14	118±47	128±30	146±39	44±40	118±10±40
95-120	166±20	233±51	211±21	224±21	192±49	233±21±46
120-500	145±18	276±21	254±24	227±31	194±46	276±22±3

MC sample normalization also contributes to the uncertainty of the cross section because the DY+jets MC sample is used to subtract fake-γ contribution from FSR-selected $Z\gamma \to \mu\mu\gamma$ sample. Both of these contributions are accumulated in $\Delta\sigma^{Norm}$, however, the contribution from the uncertainty on the DY+jets MC sample normalization is very small compared to the contribution from the uncertainty on the $Z\gamma$ MC sample normalization.

The uncertainty on the $Z\gamma$ normalization is set to be 4.6% as reported by CMS $Z\gamma$ measurement at $\sqrt{s}$=8 TeV [47]. To estimate ΔN_{Norm}, we prepare templates with $Z\gamma$ normalizations deviated by $\pm$4.6% from the nominal value. After that, we perform fits with such deviated templates, and compare results among the fits with templates of nominal normalization and with two deviated ones. The spread among three results is a systematic uncertainty on the "data-bkg." yields.

Systematic uncertainties related to the jets$\rightarrow\gamma$ background estimation are propagated through unfolding and other measurement steps. The resulting uncertainties in the cross section are listed among the major uncertainties in Tab. 5.12-5.13 in columns "syst $|N_{Ich} - N_{\sigma i\eta i\eta}|$", "$Z\gamma$ MC norm", and "temp stat".

5.7.2 Other Sources of the Systematic Uncertainties

Another significant uncertainty only appears in the electron channel; it is the uncertainty related to $e\rightarrow\gamma$ background estimation. This uncertainty has components related to the fit bias and to the limited statistical power of MC samples involved in this background estimation.

To estimate the uncertainty due to fit bias, we perform fits of Z-peak on two data samples. One of them is prepared by applying all the $W\gamma$ selection criteria except the Z-mass window requirement, and the other one is prepared by applying all the $W\gamma$ selection criteria except Z-mass window and M_T^{γ} requirements. For the second case, we apply the efficiency of M_T^W selection requirement to the fit result. Whether the M_T^W selection requirement is applied or not, the data sample can be described by the same function, which must result in the amount of $e\rightarrow\gamma$ events in the nominally selected sample. The difference in the number of $e\rightarrow\gamma$ background events indicates a fit bias. The plots with the fit results of the datasets before and after M_W^T requirement applied are shown in App. J and F respectively.

Another source of uncertainty originates from the limited statistical power of all MC samples involved in the $e \to \gamma$ background estimation. This uncertainty is taken care of by RooFit [54] which provides us with uncertainties on the $N_{e\to\gamma}$ determined by fit (Eq. 5.9) and by ROOT [58] which treats properly the uncertainties on weighted $M_{e\gamma}$ histograms involved in the algebraic expression 5.8. Values of $e \to \gamma$ uncertainties from both sources are propagated through unfolding and other measurement steps and summarized in Tab. 5.14.

For the real-γ background subtraction, the statistical uncertainties of $Z\gamma$ and $W\gamma \to \tau\nu\gamma$ MC samples and their normalization uncertainties are taken into account. The normalization uncertainty applied for the $Z\gamma$ sample is 4.6% as reported by CMS 8 TeV $Z\gamma$ measurement and for $W\gamma \to \tau\nu\gamma$ is 20% because we use the NLO value, and the NNLO contribution is estimated to have an order of 20%. These uncertainties are minor. They are propagated through unfolding and other measurement steps, and are listed in Tab. 5.15-5.16 in "real-γ bkg" columns.

The migration matrix for the unfolding and $A \times \epsilon$ correction constants are derived from the signal MC sample. The limited statistical power of the signal MC sample contributes to the systematic uncertainty of the differential cross section through the unfolding procedure and to both the differential and total cross section through the $A \times \epsilon$ correction.

To evaluate the uncertainty related to the limited signal MC statistical power for the migration matrix, first, we randomize the migration matrix 100 times by a Gaussian distribution as $M_{ji} \to Gaus(M_{ji}, \sigma_{ji})$ where σ_{ji} is the signal MC statistical uncertainties in particular $[j, i]$ bin. After that, the procedure of unfolding is repeated for each migration matrix. The standard deviation out of all unfolding outputs is taken as an uncertainty on unfolded yields in each P_T^γ bin, and, finally, the uncertainty is propagated through the $A \times \epsilon$ correction and is divided by the luminosity and the bin width to estimate the uncertainty on the cross section.

To evaluate the uncertainty related to the limited signal MC statistical power for the $A \times \epsilon$ correction constants, we use the expression

$$\Delta N^i_{true} = N^i_{A\times\epsilon} \cdot \frac{\Delta(A\times\epsilon)^i}{((A\times\epsilon)^{i2})}, \tag{5.13}$$

where $N^i_{A\times\epsilon}$ are unfolded yields, before the $A \times \epsilon$ correction as defined in Tab. 5.1. To estimate the uncertainty on the cross section, ΔN^i_{true} is divided by the luminosity and by the bin width. These uncertainties are minor, and are listed in Tab. 5.15-5.16 in "unf. MC stat" and "$A \times \epsilon$ MC stat" columns.

Another source of the systematic uncertainty originates from biases in E_T^{miss} modeling in the MC. These biases affect the procedures of detector resolution unfolding and $A \times \epsilon$ correction. To estimate this uncertainty, we prepare two additional signal MC samples with $M_T^W \to M_T^W \pm \sigma^{\pm}_{MTW}$. To determine $\sigma^{\pm}_{MTW}$, we change values of P_T of the photons, electrons (for the electron channel) and jets in the event by their uncertainties as prescribed by CMS EGamma and JetMET POG as $P_T^{\gamma} \to P_T^{\gamma} \pm \Delta P_T^{\gamma}$, $P_T^{e} \to P_T^{e} \pm \Delta P_T^{e}$, $P_T^{jets} \to P_T^{jets} \pm \Delta P_T^{jets}$. Then sum up all the listed contributions as the Lorentz vectors, and recalculate values of E_T^{miss} and, therefore, of M_T^W. In these new MC samples we apply selection requirements on these alternative M_T^W values, and, therefore, obtain new selected signal MC samples. Using these new samples, we compute $A \times \epsilon$ and prepare migration matrices. After that, we compute two additional cross section values based on new $A \times \epsilon$ values and migration matrices. The spread in the cross section among the three results, including the nominal one, is the systematic uncertainty. This uncertainty is minor, and the values are provided in Tab. 5.15-5.16 in "M_T^W req."

column.

The contribution from the uncertainties of the efficiency SFs is also estimated. The SFs are varied by $\pm 1\sigma$, then the new $A \times \epsilon$ values and migration matrices are obtained, and new values of the cross section are found. The spread in the cross section among the three results, with $+1\sigma$, -1σ and the nominal scale factor values, is the systematic uncertainty. The contribution of the SF systematic uncertainty in the muon channel is minor, however, in the electron channel it is significant and in certain P_T^{γ} bins is even dominant (Tab. 5.12-5.13). The SF uncertainty in the electron channel is so large because we required PSV instead of CSEV to select $W\gamma \to e\nu\gamma$ events, therefore, we could not use SFs provided by EGamma POG but had to use the SFs provided by $W\gamma\gamma$ measurement team instead. Those SFs were prepared using a very small data sample resulting in large uncertainties of SFs which convert into large uncertainties of the $W\gamma \to e\nu\gamma$ cross section.

The systematic uncertainty related to PU reweighting is estimated by varying the PU cross section by $\pm 5\%$. Similarly to the uncertainties related to E_T^{miss} and SFs, we prepare two additional signal MC samples with alternative values of PU weight, prepare new $A \times \epsilon$ constants and migration matrices, and compute new cross section values. The spread in the cross section among the three results corresponding to the nominal PU cross section and those changed by $\pm 5\%$ is the systematic uncertainty. This uncertainty is minor, and the values are provided in Tab. 5.15-5.16 in the "PU weight" column.

The luminosity uncertainty is 2.6% which converts to 2.6% uncertainty on the cross section in all P_T^{γ} bins. This systematic uncertainty is listed among the major uncertainties in Tab. 5.12-5.13 in the "syst lumi" column.

5.7.3 Summary of the Systematic Uncertainties

The relative systematic uncertainties are summarized in Tab. 5.12 and Tab. 5.13 for the muon and electron channels respectively. The systematic uncertainties related to pre-unfolding measurement steps have to be propagated through unfolding. For each of such uncertainties, a correlation matrix appears. All these correlation matrices are plotted in App. I.

Table 5.12: Relative uncertainties (%) on the $W\gamma$ differential cross section in the muon channel. The details of the "other" column are provided in Tab. 5.15. The "total" is the total relative systematic uncertainty on $d\sigma/dP_T^\gamma$.

P_T^γ, GeV	stat err	systematic errors: related to jets→ γ: $\lvert N_{Ich} - N_{\sigma i\eta i\eta}\rvert$	$Z\gamma$ MC norm	templ. stat	SFs	lumi	other	total
total	1	10	24	4	2	3	4	27
15-20	2	31	12	10	3	3	6	35
20-25	2	29	13	11	1	3	6	34
25-30	2	24	13	11	1	3	5	30
30-35	3	40	15	13	2	3	7	45
35-45	2	11	12	8	2	3	6	19
45-55	4	62	19	20	2	3	8	68
55-65	3	15	12	14	1	3	7	24
65-75	6	36	19	17	1	3	10	44
75-85	4	6	11	16	1	3	10	21
85-95	5	2	9	23	1	3	13	25
95-120	5	10	8	12	1	3	9	18
120-500	3	4	11	21	2	3	9	24

Table 5.13: Relative uncertainties (%) on the $W\gamma$ differential cross section in the electron channel. The details of the "other" column are provided in Tab. 5.15. The details of the "syst other" and "$e \to \gamma$" columns are provided in Tab. 5.16 and 5.14 respectively. The "total" is the total relative systematic uncertainty on $d\sigma/dP_T^\gamma$.

P_T^γ, GeV	stat err	systematic errors							
		related to jets$\to \gamma$							
		$\|N_{Ich} - N_{\sigma i\eta i\eta}\|$	$Z\gamma$ MC norm	templ. stat	SFs	lumi	$e \to \gamma$	other	total
total	2	15	35	5	19	3	4	5	44
15-20	8	80	27	19	17	3	18	11	90
20-25	7	38	20	14	12	3	11	10	48
25-30	5	25	16	12	14	3	8	8	36
30-35	5	35	14	12	14	3	3	8	42
35-45	3	14	13	8	18	3	2	7	28
45-55	8	53	20	22	36	3	7	11	71
55-65	7	17	12	30	44	3	5	10	58
65-75	7	23	15	32	44	3	4	11	61
75-85	8	32	17	27	44	3	6	13	64
85-95	9	9	7	9	40	3	8	14	44
95-120	7	19	9	14	44	3	5	11	51
120-500	4	12	6	24	39	3	1	9	48

Table 5.14: Relative systematic uncertainties (%) on the $W\gamma$ differential cross section in the electron channel related to $e \to \gamma$ background estimation. The "fit bias" is the systematic uncertainty evaluated as the difference between results when fits are performed before and after M_T^W selection requirement, the "samp. stat" is the systematic uncertainty related to limited statistical power of all MC samples involved into the background estimation, and "total syst." is a quadrature sum of them.

P_T^γ, GeV	total syst.	fit bias	samples stat
total	4	4	1
15-20	18	17	4
20-25	11	10	4
25-30	8	7	3
30-35	3	1	2
35-45	2	1	1
45-55	7	4	5
55-65	5	3	4
65-75	4	1	4
75-85	6	4	4
85-95	8	5	6
95-120	5	3	4
120-500	1	0	1

Table 5.15: Relative systematic uncertainties (%) of smaller contributions on the $W\gamma$ differential cross section in the muon channel (details of the column "syst other" from Tab. 5.12). The "syst other" is a quadrature sum of all contributions listed in the table.

P_T^{γ}, GeV	syst other	real-γ bkg	$A \times \epsilon$ MC stat	M_T^W req.	PU weight	unf MC stat
total	4	1	0	1	4	1
15-20	6	2	1	1	4	2
20-25	6	3	2	2	4	3
25-30	5	3	2	2	2	2
30-35	7	4	3	1	4	3
35-45	6	3	3	2	3	2
45-55	8	3	3	1	4	5
55-65	7	2	4	2	4	3
65-75	10	2	6	3	5	6
75-85	10	1	7	3	3	5
85-95	13	2	8	4	6	7
95-120	9	2	7	2	2	6
120-500	9	1	6	1	4	4

Table 5.16: Relative systematic uncertainties (%) of smaller contributions on the $W\gamma$ differential cross section in the electron channel (details of the column "syst other" from Tab. 5.13). The "syst other" is a quadrature sum of all contributions listed in the table

P_T^{γ}, GeV	syst other	real-γ bkg	$A \times \epsilon$ MC stat	M_T^W req.	PU weight	unf MC stat
total	5	2	0	1	4	2
15-20	11	6	2	1	4	8
20-25	10	5	2	1	4	7
25-30	8	3	3	1	3	6
30-35	8	2	4	1	3	6
35-45	7	1	4	1	4	4
45-55	11	2	5	3	4	9
55-65	10	2	5	3	5	7
65-75	11	1	6	1	4	8
75-85	13	2	8	2	3	9
85-95	14	2	9	2	2	9
95-120	11	1	8	1	4	7
120-500	9	1	7	2	3	4

5.8 Cross Section

The cross section of $pp \to W\gamma \to l\nu\gamma$, where $l = \mu, e$, is measured following the procedure described in Ch. 5.1 based on CMS data at $\sqrt{s}$ =8 TeV in the phase space defined in the beginning Ch. 5.

The total measured cross section in the muon and electron channel is

$$\sigma(W\gamma \to \mu\nu\gamma) = 11040 \pm 91(\text{stat.}) \pm 2954(\text{syst.}) \text{ fb}$$
$$\sigma(W\gamma \to e\nu\gamma) = 9146 \pm 185(\text{stat.}) \pm 3981(\text{syst.}) \text{ fb}$$

Table 5.17 and Fig. 5.10 summarize the results of the differential cross section. Because we applied the detector resolution unfolding procedure, the measurements in different P_T^γ bins are correlated. Correlation matrices are provided in Ch. 5.5 and App. I. The uncertainties provided in the Tab. 5.17 and Fig. 5.10 are square roots of diagonal elements of covariance matrices.

The measured cross section is compared to the phase-space-corrected MCFM calculation at NLO which is referred to as "NLO theory". The NLO cross section of the $W\gamma$ production was computed with MCFM with the phase space constraints at which the simulated $W\gamma$ sample was produced. The NLO cross section equals to σ_1 =554 pb. NNLO and higher order corrections are expected to have an effect of $\sim$20%.

The cross section in our selected phase space was computed as

$$\sigma_2 = \sigma_1 \cdot \tfrac{N_2}{N_1},$$

where N_2 and N_1 are the total MC sample event count and event count in the phase space of this measurement, respectively. The resulting cross section σ_2 is referred as "NLO theory".

For the differential cross section, N_2 is number of events falling into specific P_T^{γ} bin, and to compute $\frac{d\sigma_2}{dP_T^{\gamma}}$, we divide the cross section by the bin width.

The total NLO theory cross section is

$$\sigma_2(W\gamma \rightarrow l\nu\gamma) = 9101 \text{ fb},$$

and the values of the differential cross section are available in Table 5.17 and Fig. 5.10, alongside with the measured results.

The measured cross sections in different channels agree with each other as well as with the NLO theory cross section provided the uncertainties of the measured cross section. The systematic uncertainties on the measured cross section are dominant over the statistical uncertainties. In the muon channel and in P_T^{γ} <55 GeV bins of the electron channel, the most significant sources of the systematic uncertainty are sources associated with the jets$\rightarrow \gamma$ background estimation. In high P_T^{γ} bins of the electron channel, uncertainties on photon efficiency scale factors become more significant.

For validation of the measurement procedure, we measure the cross section of $Z\gamma$ and compare the result with the published CMS result for $Z\gamma$ at 8 TeV. We measure the cross section in the muon and electron channels in the same phase space as the published CMS measurement [47].

$Z\gamma \rightarrow \mu\mu\gamma$ FSR and ISR datasets which are used to prepare real-γ and fake-γ templates for jets$\rightarrow \gamma$ background estimation largely overlap with nominally selected $Z\gamma$ dataset. Therefore, the measurement of the $Z\gamma$ cross section in the muon channel is a closure check while the measurement of the $Z\gamma$ cross section in the electron channel is a fully valid physics measurement. The results of our $Z\gamma$ measurement agree well with the published results as well as with the theory predictions, and the systematic uncertainties on our $Z\gamma$ measured cross section are much smaller than on our $W\gamma$ measured cross section. The details of the $Z\gamma$ check are available in App. B.

The ongoing $W\gamma$ measurement based on 2015 and 2016 datasets has higher chances to discover a potential new physics because of higher energy of $\sqrt{s}$ =13 TeV and higher statistical power of over 30 fb^{-1}. Although the largest uncertainties of the 8 TeV measurement are systematic uncertainties, many of them depend on the amount of data in control samples. Thus, the increased size of the data sample will help to reduce those uncertainties. Higher collision energy allows us to observe more signal events in high P_T^γ ranges where the effect of potential aTGC is the largest.

Table 5.17: Cross section and uncertainties. The first uncertainty is statistical and the second one is systematic.

P_T^γ, GeV	$d\sigma/dP_T^\gamma$, fb/GeV NLO theory $W\gamma \to l\nu\gamma$	measured $W\gamma \to \mu\nu\gamma$	measured $W\gamma \to e\nu\gamma$
15-20	751	751 ± 17 ± 257	440 ± 35 ± 396
20-25	378	422 ± 10 ± 145	338 ± 23 ± 163
25-30	210	292 ± 7 ± 86	298 ± 16 ± 107
30-35	129	177 ± 5 ± 80	193 ± 9 ± 82
35-45	70	122 ± 2 ± 23	103 ± 3 ± 29
45-55	35	35 ± 1 ± 23	34 ± 3 ± 24
55-65	22	31 ± 1 ± 8	31 ± 2 ± 18
65-75	14	16 ± 1 ± 7	19 ± 1 ± 12
75-85	9	16 ± 1 ± 3	12 ± 1 ± 8
85-95	6.4	9.9 ± 0.5 ± 2.4	10.0 ± 0.9 ± 4.3
95-120	3.7	6.0 ± 0.3 ± 1.0	4.9 ± 0.4 ± 2.5
120-500	0.27	0.43 ± 0.01 ± 0.10	0.46 ± 0.02 ± 0.22

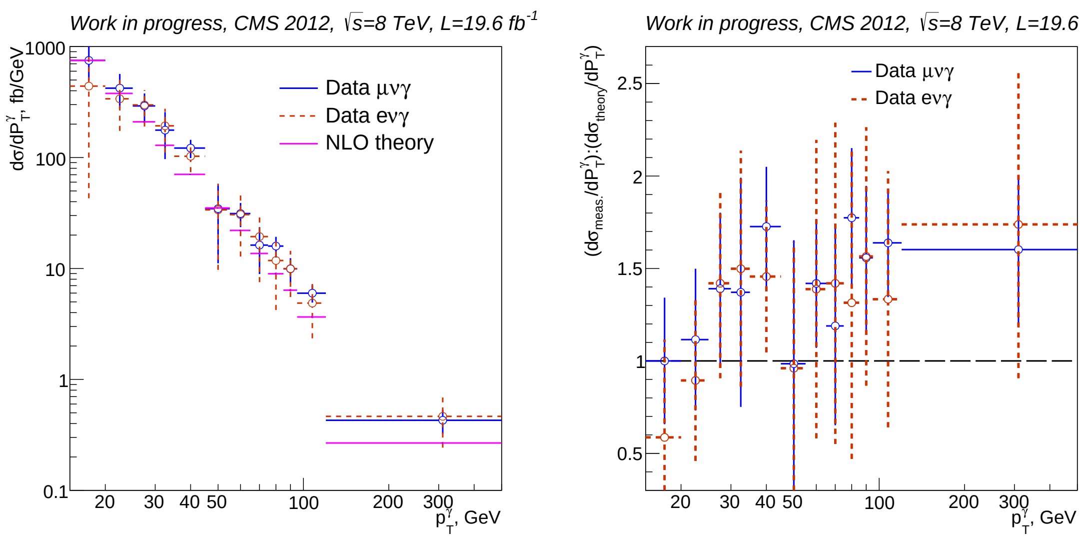

Figure 5.10: Left: the differential cross section of the $W\gamma$ production $d\sigma/dP_T^\gamma$; right: the ratio between the measured and the NLO theory differential cross section of the $W\gamma$ production.

6 Summary and Conclusions

This dissertation reports a measurement of the total and differential cross sections, σ and $\frac{d\sigma}{dP_T^{\gamma}}$, for $W\gamma$ production in the muon and the electron channels using full 2012 dataset of L =19.6 fb^{-1} collected by CMS at $\sqrt{s}$ =8 TeV. This is the first measurement of the differential cross section of the $W\gamma$ production at the CMS experiment. The results are in agreement between two channels and also agree with the predictions computed at NLO using the MCFM program and the Madgraph 5 Monte Carlo generator. The agreement with theory means agreement with the MC predictions with no clear indication of new physics.

The differential cross section measurement has the special significance because new physics would be difficult to detect in the total production cross section, however an accurate measurement of the differential cross section with respect to an observable kinematic variable of the final state particles, and especially with respect to the P_T^{γ}, is a sensitive probe to BSM models. The results of the differential spectrum measurement could be used to set limits on aTGC parameters.

In addition to $W\gamma$ cross section, we also measure $Z\gamma$ cross section and compare the results with the published $Z\gamma$ CMS measurement at $\sqrt{s}$ =8 TeV. The good agreement between our and published results on $Z\gamma$ cross section validates parts of our $W\gamma$ measurement that are the same between $Z\gamma$ and $W\gamma$ measurements including lepton and photon selection, jets$\rightarrow \gamma$ background estimation, detector resolution unfolding, acceptance and efficiency corrections.

Measurements of $W\gamma$ and the other diboson and triboson productions at higher energies and luminosities will provide more opportunities to discover new physics if it is present. That is one of the reasons why these measurements remain a significant part of CMS physics program for studies at $\sqrt{s}$ =13 TeV.

A Code and Software

The CMS software (CMSSW) [59] is the tool developed to process responses from all CMS detector elements, reconstruct particles and prepare data for physics measurements. CMSSW is mostly written in C++ and Python programming languages. It has hundreds of contributors that use GITHUB [60] to share their work. All CMS physics measurements use CMSSW.

The procedure of the tracker alignment and validation described in Ch. 4 is also a part of the CMSSW although the Millepede-II algorithm itself is implemented in an external software tool.

The samples for the physics measurements are stored in a format of ROOT trees. The ROOT tree contains multiple parameters for each entry and allows easy access to all parameters. These properties make it convenient to use ROOT trees for particle physics measurements where, usually, one entry corresponds to one event or one candidate. The ROOT trees provided by reconstruction algorithms of CMSSW are referred as “tuples”. Tuples are further processed by different large physics subgroups that prepare “ntuples”. Ntuples store only information that is necessary for a specific class of measurements and arrange it in a more convenient way for this specific class of measurements.

The author of this dissertation used “ntuples” prepared by Central Taiwan University and Kansas State University groups mostly for various diboson and triboson measurements. The code of the program that prepares the “ntuples” is available in [61].

The code for the CMS $W\gamma$ measurement at $\sqrt{s} = 8$ TeV was written by the author of this dissertation using the C++ language, ROOT and RooFit [54] packages, the *RooUnfold* [57] class for the detector resolution unfolding, and *RooCMSShape* [55] for $e \rightarrow \gamma$ background estimation. Auxiliary shell scripts are used to run the chain of C++ programs corresponding to separate physics measurement steps. The code is available in [60].

Several cross checks were performed with other collaborators to make sure the code is free of major errors. The event selection and background estimation for the electron channel is implemented completely independently by both Kansas State University group and the author of this dissertation in separate frameworks. These procedures are carefully cross checked between two developers.

B $Z\gamma$ Check

The poor agreement in all distributions of $W\gamma$ candidates in Ch. 5.4.4 brought up the necessity of cross checks that would help to identify the sources of the disagreements. One of such cross check is the $Z\gamma$ check which is the $Z\gamma$ cross section measurement performed following the same strategy as used for the $W\gamma$ cross section measurement (Ch. 5.1). In addition to the comparison of results of jets$\rightarrow \gamma$ background estimation provided by two different methods, the measured $Z\gamma$ cross section is compared to the CMS published $Z\gamma$ cross section at 8 TeV [47]. The comparison of the cross section to the independently obtained result provides the check for all $W\gamma$ measurement steps except those that are not relevant for the $Z\gamma$ measurement like $e \rightarrow \gamma$ and real-γ background estimation, selection requirements on M_T^W and $M_{e\gamma}$, and corrections for "PixelSeedVeto" SF.

The $Z\gamma$ event selection is described in Ch. 5.3.2, and the P_T^γ distribution of $Z\gamma$ candidates in data and MC is shown in Fig. B.1. The selected sample mostly consists of $Z\gamma$ signal and DY+jets background events. DY+jets background is a source of jets$\rightarrow \gamma$ background and is estimated the same way as it is done for our nominal $W\gamma$ measurement.

The templates are derived from $Z\gamma \rightarrow \mu\mu\gamma$ sample. Therefore, the $Z\gamma$ check in the muon channel is not a valid physics measurement but a closure check because the templates for the jets$\rightarrow \gamma$ background estimation procedure largely overlap with the fitted data. At the same time, the $Z\gamma$ check in the electron channel is a valid physics measurement. Fit results on data and pseudodata (MC mixtures) show good agreement for both channels (Fig. B.2-B.5).

Major systematic uncertainties are estimated the same way as it is done for $W\gamma$ measurement and are listed in Tab. B.1-B.2. Measured cross section values compared to the MC-based cross section are listed in the Tab. B.3. Figure B.6 shows an agreement between muon and electron channels, agreement with the MC-based cross section and with the published CMS $Z\gamma$ measurement at $\sqrt{s}$ =8 TeV [47].

The good agreement between the $Z\gamma$ cross section of our measurement and the published one validates steps of the $W\gamma$ measurement that are the same between $Z\gamma$ and $W\gamma$ measurements. The list of these steps includes muon, electron, and photon selection, jets$\rightarrow \gamma$ background estimation, detector resolution unfolding, acceptance, efficiency, and SF corrections, PU reweighting.

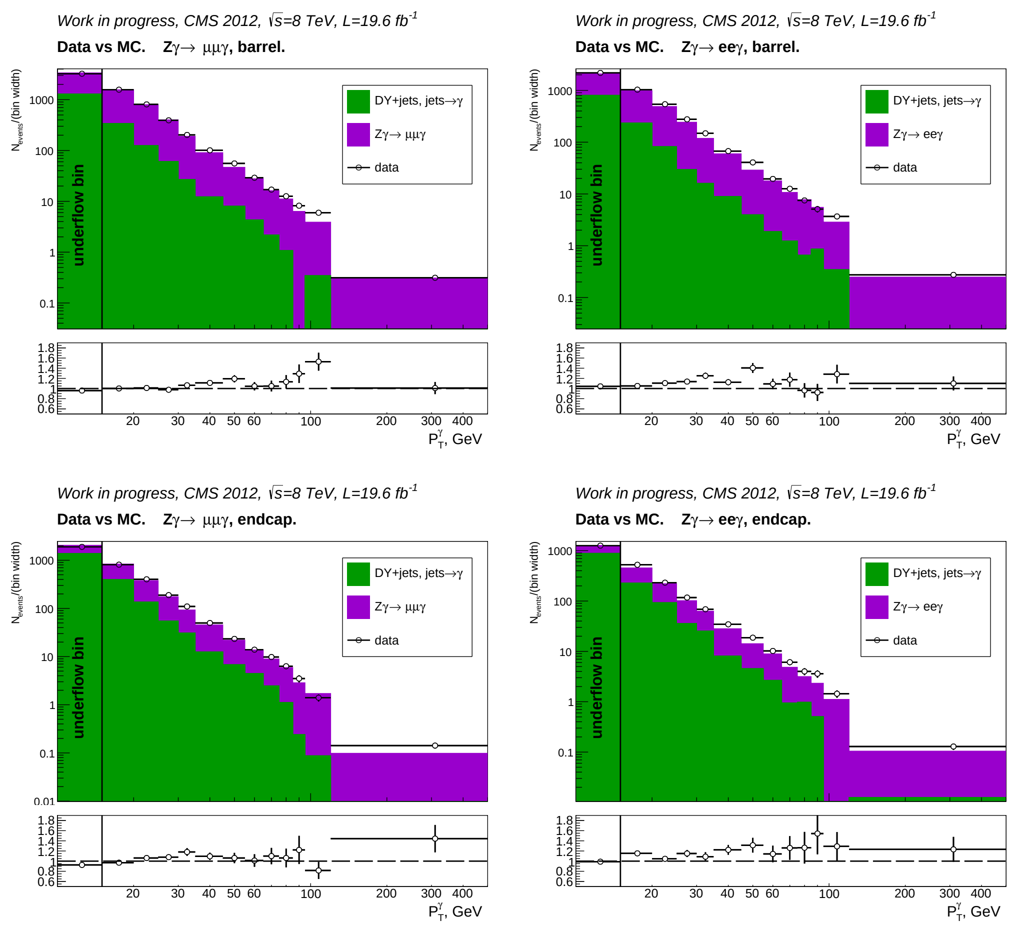

Figure B.1: P_T^{γ} distribution of $Z\gamma$ candidates in the muon (left) and electron (right) channels with photons in EB (top) and EE(bottom). Data vs total MC agreement is shown. The ratio plots are data divided by total MC.

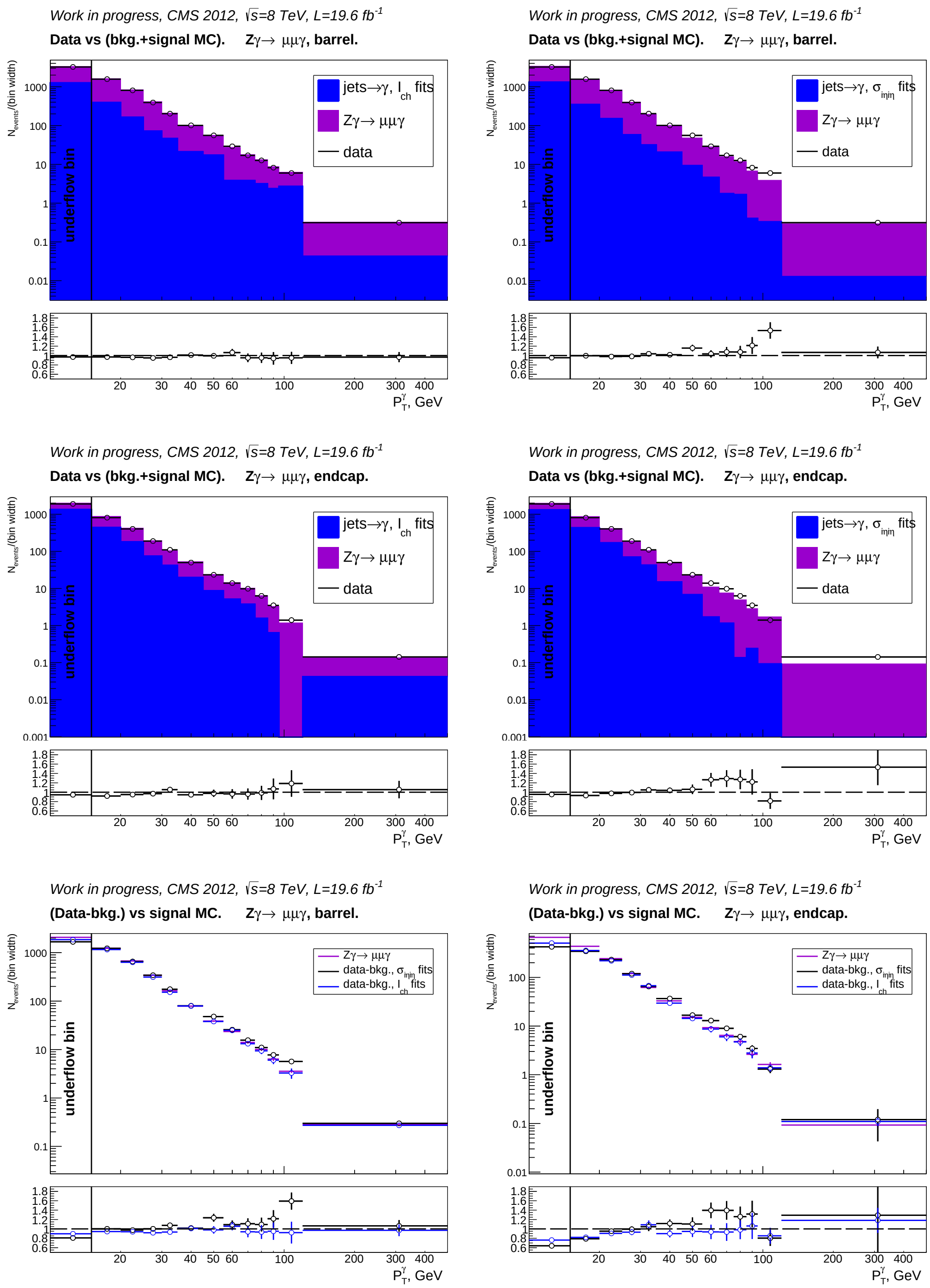

Figure B.2: P_T^{γ} distribution of $Z\gamma$ candidates in the muon channel. Top and middle: data vs fake-γ background derived from the template method + real-γ background predicted by dedicated MC samples + signal MC, with I_{ch} (left) and $\sigma_{i\eta i\eta}$ (right) used as fit variables for candidates with photons in EB (top) and EE (middle). Bottom: data yields after full background subtraction vs signal MC for candidates with photons in in EB (left) and EE (right).

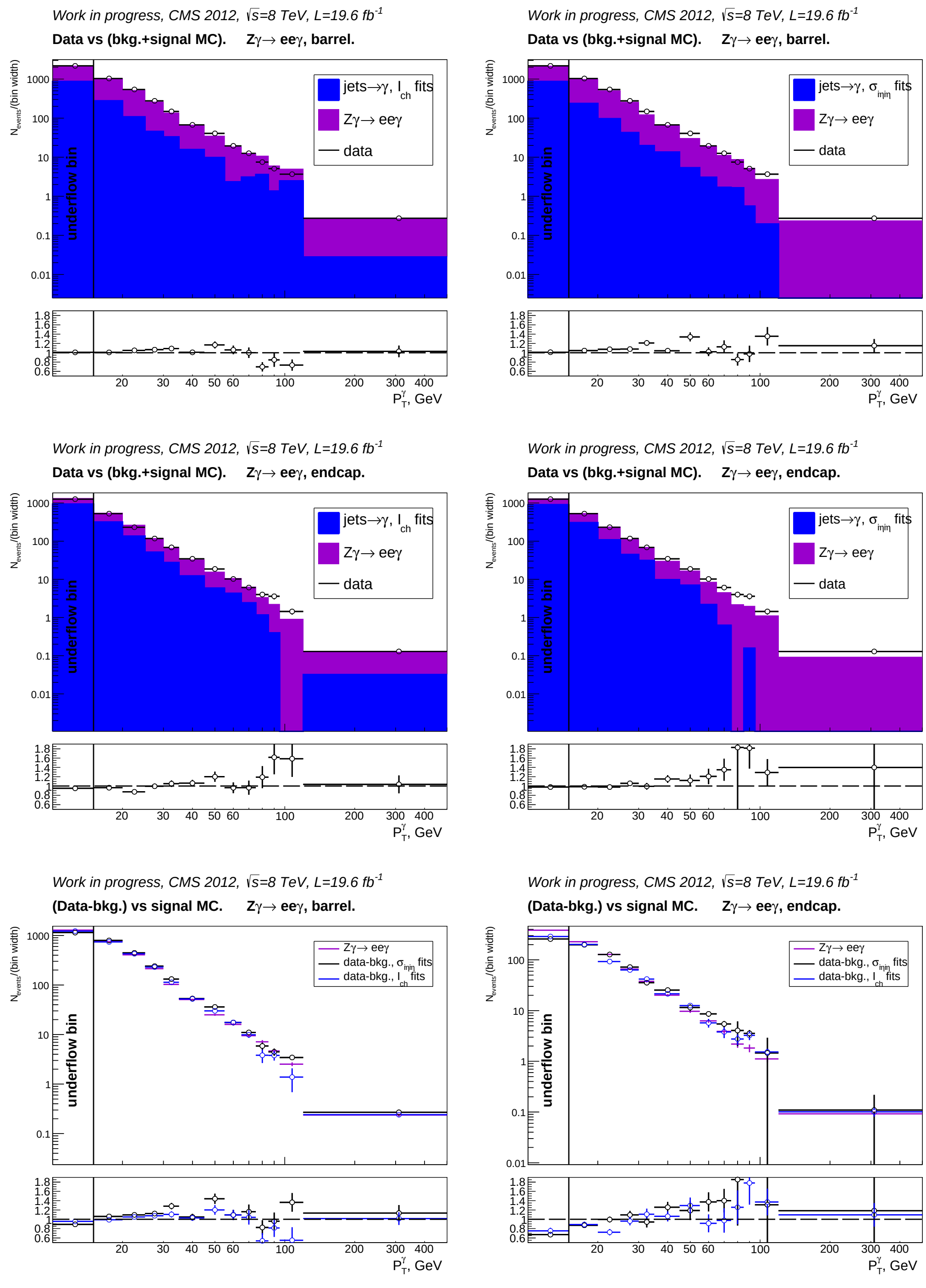

Figure B.3: P_T^{γ} distribution of $Z\gamma$ candidates in the electron channel. Top and middle: data vs fake-γ background derived from the template method + real-γ background predicted by dedicated MC samples + signal MC, with I_{ch} (left) and $\sigma_{i\eta i\eta}$ (right) used as fit variables in EB (top) and EE (middle). Bottom: data yields after full background subtraction vs signal MC in EB (left) and EE (right).

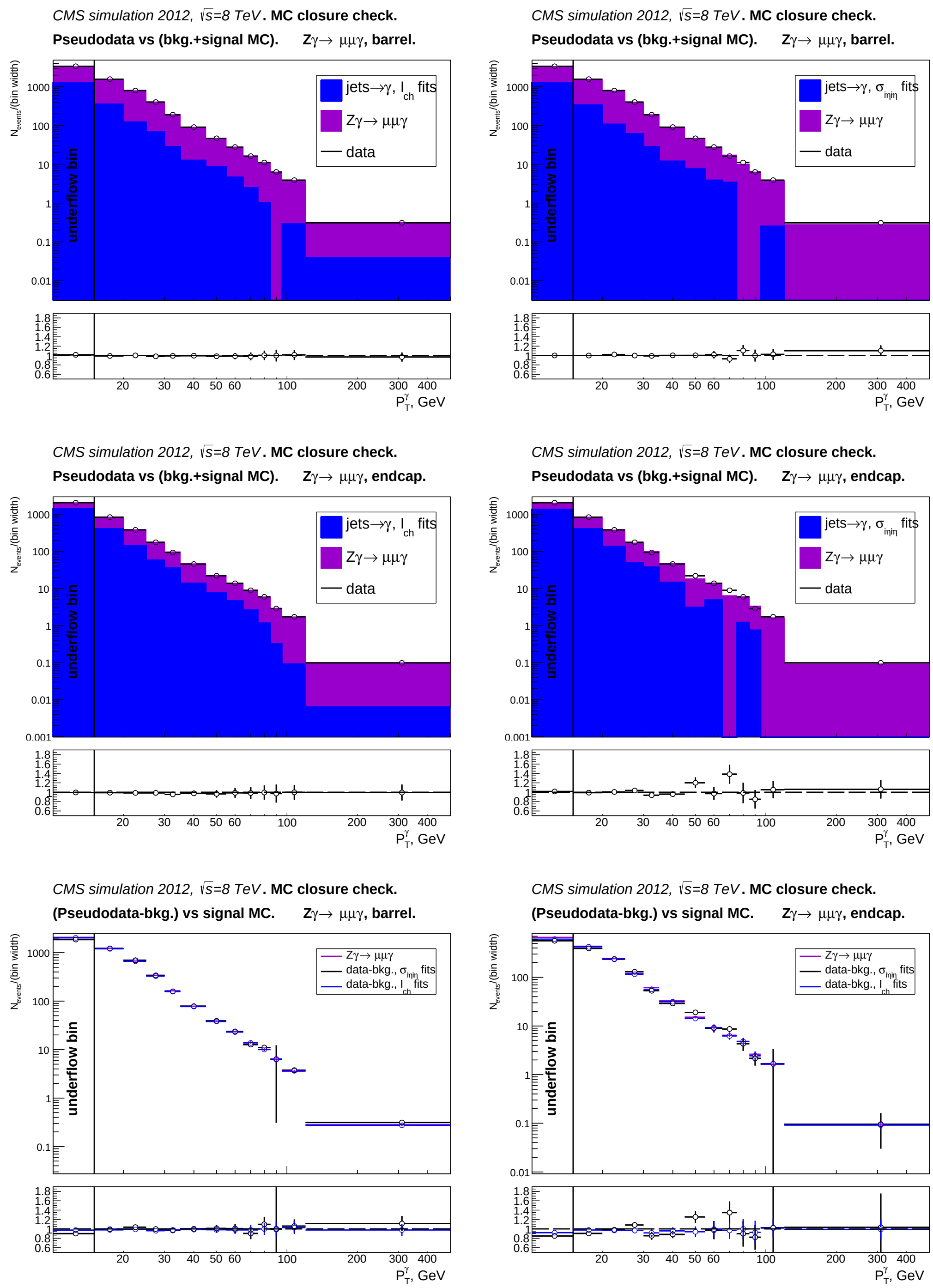

Figure B.4: P_T^{γ} distribution of $Z\gamma$ candidates in the muon channel prepared with pseudodata. Top and middle: pseudodata vs fake-γ background derived from the template method + real-γ background predicted by dedicated MC samples + signal MC, with I_{ch} (left) and $\sigma_{i\eta i\eta}$ (right) used as fit variables for candidates with photons in EB (top) and EE (middle). Bottom: data yields after full background subtraction vs signal MC for candidates with photons in in EB (left) and EE (right).

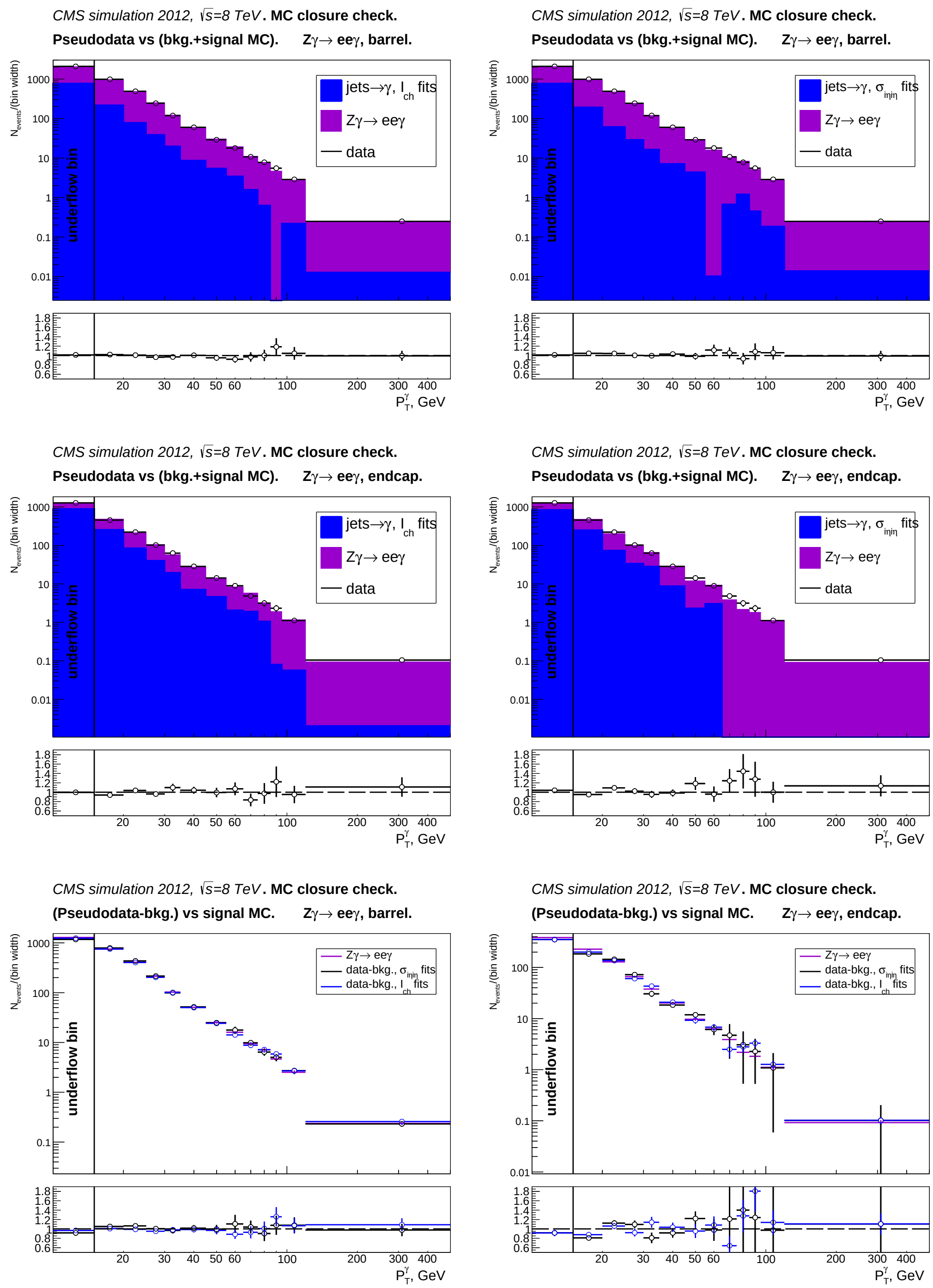

Figure B.5: P_T^{γ} distribution of $Z\gamma$ candidates in the electron channel prepared with pseudodata. Top and middle: pseudodata vs fake-γ background derived from the template method + real-γ background predicted by dedicated MC samples + signal MC, with I_{ch} (left) and $\sigma_{i\eta i\eta}$ (right) used as fit variables for candidates with photons in EB (top) and EE (middle). Bottom: data yields after full background subtraction vs signal MC for candidates with photons in in EB (left) and EE (right).

Table B.1: Relative uncertainties [%] on the $Z\gamma$ differential and total (row "total") cross section in the muon channel.

P_T^γ, GeV	err stat	syst $\lvert N_{Ich} - N_{\sigma i\eta i\eta}\rvert$	$Z\gamma$ MC norm	$A \times \epsilon$ MC stat	syst lumi	unf MC stat	syst total	syst + stat total
total	1	1	1	0	3	1	3	3
15-20	2	2	2	1	3	2	4	5
20-25	2	2	3	1	3	2	5	5
25-30	3	3	4	2	3	3	7	8
30-35	4	6	5	3	3	5	10	10
35-45	4	3	6	3	3	4	9	9
45-55	6	8	8	4	3	6	14	15
55-65	7	5	7	5	3	7	13	14
65-75	9	7	8	6	3	9	16	18
75-85	10	8	6	7	3	10	16	19
85-95	12	8	8	9	3	12	19	23
95-120	11	10	6	8	3	11	18	21
120-500	8	5	9	7	3	9	16	18

Table B.2: Relative uncertainties [%] on the $Z\gamma$ differential and total (row "total") cross section in the electron channel.

P_T^γ, GeV	err stat	syst $\lvert N_{Ich} - N_{\sigma i\eta i\eta}\rvert$	$Z\gamma$ MC norm	$A \times \epsilon$ MC stat	syst lumi	unf MC stat	syst total	syst + stat total
total	1	1	1	0	3	1	3	4
15-20	2	3	3	1	3	2	5	6
20-25	3	2	3	1	3	3	5	6
25-30	4	3	4	2	3	4	7	8
30-35	5	4	5	3	3	6	10	11
35-45	5	4	6	3	3	5	10	11
45-55	6	6	6	4	3	7	11	13
55-65	9	7	8	5	3	9	15	17
65-75	10	8	8	7	3	11	18	20
75-85	14	11	12	9	3	16	25	28
85-95	15	9	6	10	3	17	23	28
95-120	10	5	6	9	3	11	16	19
120-500	9	3	7	8	3	10	15	17

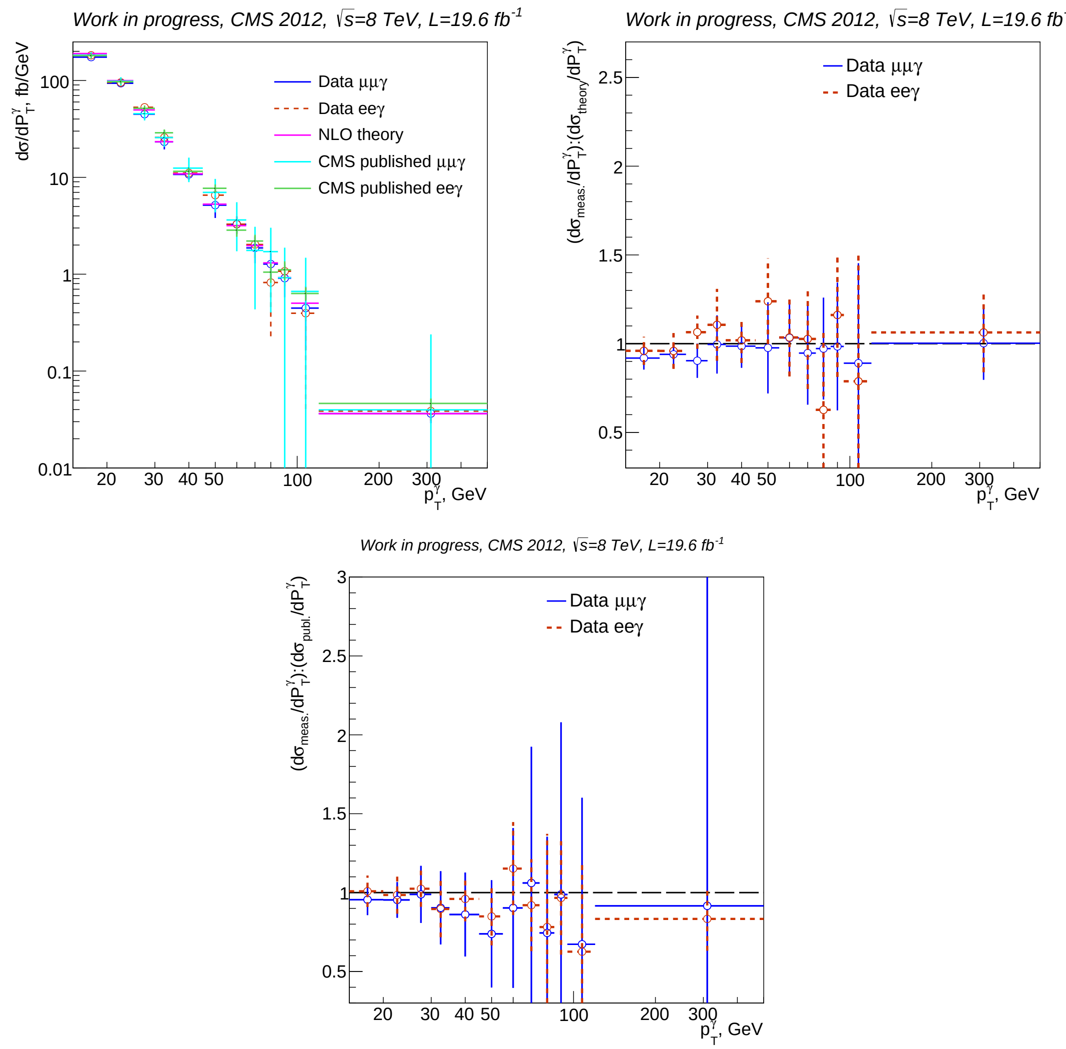

Figure B.6: Top left: the $Z\gamma$ differential cross section; top right: the ratio of measured over the NLO theory $Z\gamma$ differntial cross section; bottom: the ratio of the measured over the CMS published $Z\gamma$ differential cross section.

Table B.3: Cross section and errors

P_T^γ, GeV	$d\sigma/dP_T^\gamma$, fb/GeV		
	NLO theory	measured	
	$Z\gamma \to ll\gamma$	$Z\gamma \to \mu\mu\gamma$	$Z\gamma \to ee\gamma$
total	2073	$1938 \pm 20 \pm 78$	$2058 \pm 27 \pm 93$
15-20	190	$174 \pm 3 \pm 12$	$182 \pm 5 \pm 14$
20-25	100	$94 \pm 2 \pm 5$	$96 \pm 3 \pm 10$
25-30	50	$45 \pm 1 \pm 5$	$53 \pm 2 \pm 4$
30-35	23	$23 \pm 1 \pm 4$	$26 \pm 1 \pm 5$
35-45	11	$11 \pm 0 \pm 1$	$11 \pm 1 \pm 1$
45-55	5.3	$5.2 \pm 0.4 \pm 1.3$	$6.5 \pm 0.5 \pm 1.2$
55-65	3.2	$3.3 \pm 0.2 \pm 0.6$	$3.3 \pm 0.3 \pm 0.6$
65-75	2.0	$1.9 \pm 0.2 \pm 0.5$	$2.0 \pm 0.3 \pm 0.5$
75-85	1.3	$1.3 \pm 0.2 \pm 0.3$	$0.82 \pm 0.21 \pm 0.55$
85-95	0.92	$0.91 \pm 0.15 \pm 0.30$	$1.1 \pm 0.2 \pm 0.3$
95-120	0.50	$0.45 \pm 0.09 \pm 0.27$	$0.40 \pm 0.11 \pm 0.34$
120-500	0.036	$0.036 \pm 0.003 \pm 0.007$	$0.039 \pm 0.004 \pm 0.007$

C Efficiency Scale Factors

This appendix summarizes efficiency SF that are applied to MC events to make selection efficiency in MC match the selection efficiency in data. Tables C.1-C.2 contain the SF for the muon ID (ρ^{μ}_{ID}) and the muon isolation (ρ^{μ}_{iso}) requirements. A full SF on a muon object is a product of ID and isolation SF. Electron ID SF are listed in Tab. C.3 (ρ^{e}_{ID}). Photon ID (ρ^{γ}_{ID}) and PSV (ρ^{γ}_{PSV}) SF are summarized in Tab. C.4 and Tab. C.5.

For each $W\gamma$ candidate in any MC sample we apply a lepton and a photon SF. PSV SF is used in the electron channel only. For each $Z\gamma$ candidate in any MC sample we apply two lepton and one photon SF. For instance, in the $Z\gamma$ MC sample selected in the $W\gamma$ selection conditions for the purpose of the real-γ background subtraction, we apply SF as for $W\gamma$ candidates, while in the $Z\gamma$ MC sample selected in the $Z\gamma$ selection conditions for the purposes of the $Z\gamma$ check or template construction, we apply SF as for $Z\gamma$ candidates.

A full event SF is a multiplication of individual object SF. Full SF for each type of candidate are summarized in Tab. C.6.

Table C.1: Muon ID SF as recommended by POG depending on P_T^{μ} and $|\eta^{\mu}|$.

P_T^{μ}	$\|\eta^{\mu}\| < 0.9$	$0.9 < \|\eta^{\mu}\| < 1.2$	$1.2 < \|\eta^{\mu}\| < 2.1$
25-30	0.992±0.001	0.995±0.001	0.998±0.001
30-35	0.993±0.001	0.993±0.001	0.997±0.001
35-40	0.994±0.000	0.992±0.001	0.997±0.001
40-50	0.992±0.000	0.992±0.000	0.997±0.000
50-60	0.992±0.001	0.995±0.001	0.995±0.001
60-90	0.989±0.001	0.990±0.002	0.992±0.002
90-140	1.004±0.003	1.009±0.006	1.023±0.005
>140	1.004±0.017	1.009±0.035	1.023±0.030

Table C.2: Muon isolation SF as recommended by POG depending on P_T^{μ} and $|\eta^{\mu}|$.

P_T^{μ}	$\|\eta\| < 0.9$	$0.9 < \|\eta\| < 1.2$	$1.2 < \|\eta\| < 2.1$
25-30	0.999±0.001	1.002±0.001	1.002±0.001
30-35	0.999±0.000	1.002±0.001	1.003±0.000
35-40	0.999±0.000	1.001±0.001	1.002±0.000
40-45	0.998±0.000	1.000±0.000	1.000±0.000
45-50	1.000±0.000	1.000±0.000	1.000±0.000
50-60	0.999±0.000	1.000±0.000	1.000±0.000
60-90	1.000±0.000	1.001±0.001	1.000±0.000
90-140	1.001±0.001	1.001±0.001	1.000±0.001
>140	1.001±0.002	1.004±0.005	0.997±0.002

Table C.3: Electron ID SF as recommended by POG depending on P_T^{e} and $|\eta^{e}|$.

P_T^{e}	$\|\eta^{e}\| \leq 0.80$	$0.80 < \|\eta^{e}\| \leq 1.44$	$1.57 < \|\eta^{e}\| \leq 2.00$	$\|\eta^{e}\| > 2.00$
≤40	0.978±0.001	0.958±0.002	0.909±0.003	0.987±0.004
40-50	0.981±0.001	0.969±0.001	0.942±0.002	0.991±0.003
>50	0.982±0.002	0.969±0.002	0.957±0.004	0.999±0.005

Table C.4: Photon ID SF as recommended by POG depending on P_T^{γ} and $|\eta^{\gamma}|$.

P_T^{γ}	$\|\eta^{\gamma}\| \leq 0.80$	$0.80 < \|\eta^{\gamma}\| \leq 1.44$	$1.57 < \|\eta^{\gamma}\| \leq 2.00$	$\|\eta^{\gamma}\| > 2.00$
15-20	0.95±0.02	0.99±0.02	1.00±0.02	1.02±0.02
20-30	0.96±0.01	0.97±0.01	0.98±0.01	1.00±0.01
30-40	0.98±0.01	0.98±0.01	0.99±0.01	1.00±0.01
40-50	0.98±0.01	0.98±0.01	1.00±0.01	1.01±0.01
>50	0.98±0.01	0.98±0.01	1.00±0.01	1.01±0.01

Table C.5: Additional photon SF for "PixelSeedVeto" as reported in $W\gamma\gamma$ measurement depending on P_T^{γ} and $|\eta^{\gamma}|$.

P_T^{γ}	barrel	endcap
15-20	0.996±0.020	0.960±0.041
20-25	0.994±0.024	0.977±0.051
25-30	0.996±0.030	0.951±0.062
30-40	0.999±0.033	1.029±0.081
40-50	1.009±0.073	0.971±0.150
50-70	0.993±0.128	0.965±0.294
>70	1.047±0.111	1.145±0.371

Table C.6: Full event SF for each type of candidate.

type of candidate	full SF
$W\gamma \rightarrow \mu\nu\gamma$	$\rho_{ID}^{\mu} \times \rho_{iso}^{\mu} \times \rho_{ID}^{\gamma}$
$W\gamma \rightarrow e\nu\gamma$	$\rho_{ID} \times \rho_{ID}^{\gamma} \times \rho_{PSV}^{\gamma}$
$Z\gamma \rightarrow \mu\mu\gamma$	$\rho_{ID}^{\mu 1} \times \rho_{iso}^{\mu 1} \times \rho_{ID}^{\mu 2} \times \rho_{iso}^{\mu 2} \times \rho_{ID}^{\gamma}$
$Z\gamma \rightarrow ee\gamma$	$\rho_{ID}^{1} \times \rho_{ID}^{2} \times \rho_{ID}^{\gamma}$

D $Z\gamma$ FSR and ISR Plots

The$Z\gamma \to \mu\mu\gamma$-selected data sample where photon selection is the same as for $W\gamma$ selection is used to prepare real-γ and fake-γ templates for the jets$\to \gamma$ background estimation. The nominal $Z\gamma$ events selection is described in Ch. 5.3.2, and we considered four variables to introduce changes to the nominal selection to increase either real-γ or fake-γ fractions: the three-particle invariant mass $M_{\mu\mu\gamma}$, the invariant mass of the dimuon system $M_{\mu\mu}$ (Fig. D.1), and the separations between muons and the photon $\Delta R(\mu_1, \gamma)$, $\Delta R(\mu_2, \gamma)$ (Fig. D.2), where μ_1 is the muon with the smaller separation from the photon out of two muons in the given candidate.

The two peaks in the $M_{\mu\mu\gamma}$ and $M_{\mu\mu}$ distributions correspond to FSR and ISR mechanisms of the $Z\gamma$ production, where FSR peak is highly dominated by real-γ events, and ISR peak contains a significant number of both $Z\gamma$ and DY+jets events. It is also seen in Fig. D.2 that events with smaller separation $\Delta R(\mu_1, \gamma)$ have a larger fraction of $Z\gamma$ than events with the larger separation. The selection chosen to prepare real-γ templates can be referred as FSR selection, while the selection chosen to prepare fake-γ templates can be referred as ISR selection. The differences for the FSR and ISR selection from the nominal one are:

- FSR: $M_{\mu\mu\gamma}$ <101 GeV, $\Delta R(\mu_{1,2}, \gamma)$ >0.4;
- ISR: $M_{\mu\mu\gamma}$ >101 GeV, $\Delta R(\mu_{1,2}, \gamma)$ >1.0.

The fake-γ contribution into the FSR region is subtracted based on DY+jets MC predictions while the real-γ contribution into the ISR region is subtracted based on $Z\gamma$ MC predictions. The number of real-γ and fake-γ events in different P_T^γ bins is shown in Fig. D.3. The I_{ch}^γ and $\sigma_{i\eta i\eta}^\gamma$ distributions are shown in Fig. D.4-D.9.

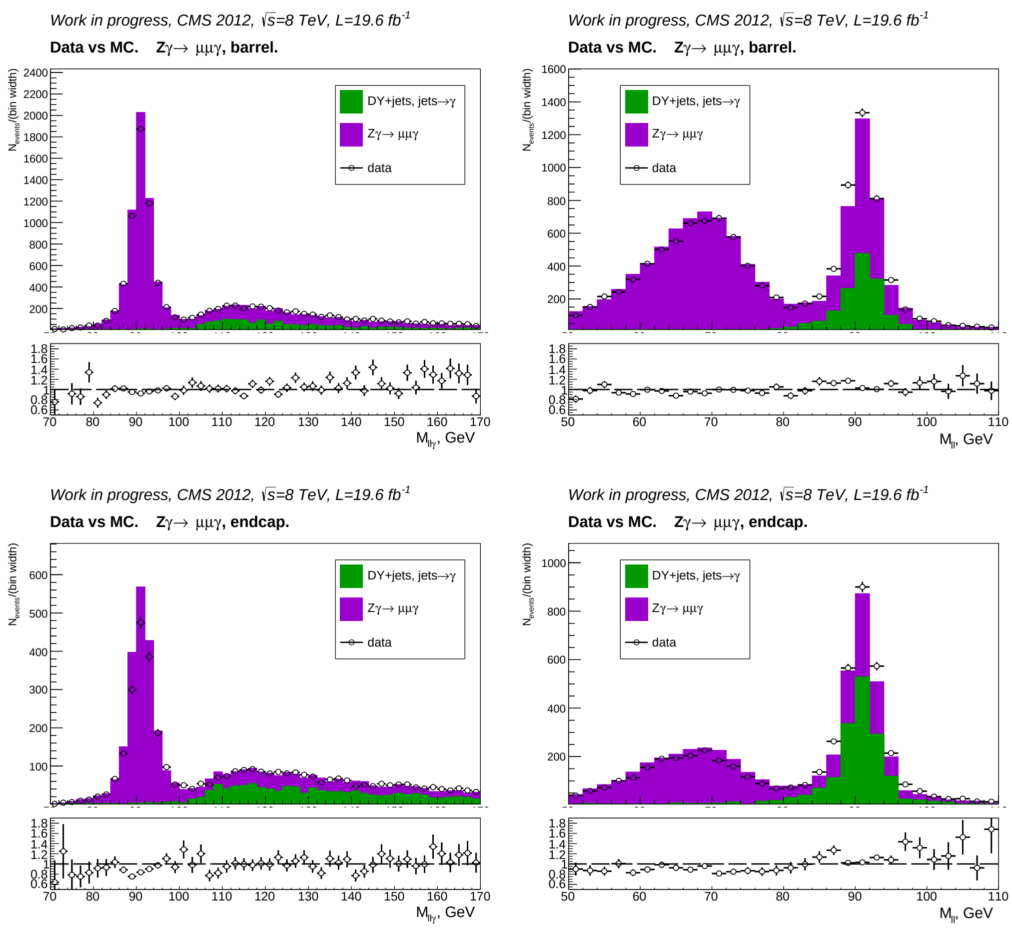

Figure D.1: Distributions of $M_{\mu\mu\gamma}$ (left) and $M_{\mu\mu}$ (right) in $Z\gamma \to \mu\mu\gamma$-selected events, data vs MC. P_T^γ :15-500 GeV. Left: $M_{\mu\mu\gamma}$, right: $M_{\mu\mu}$. Top: barrel photons, bottom: endcap photons. Peak highly dominated by $Z\gamma$ events corresponds to FSR.

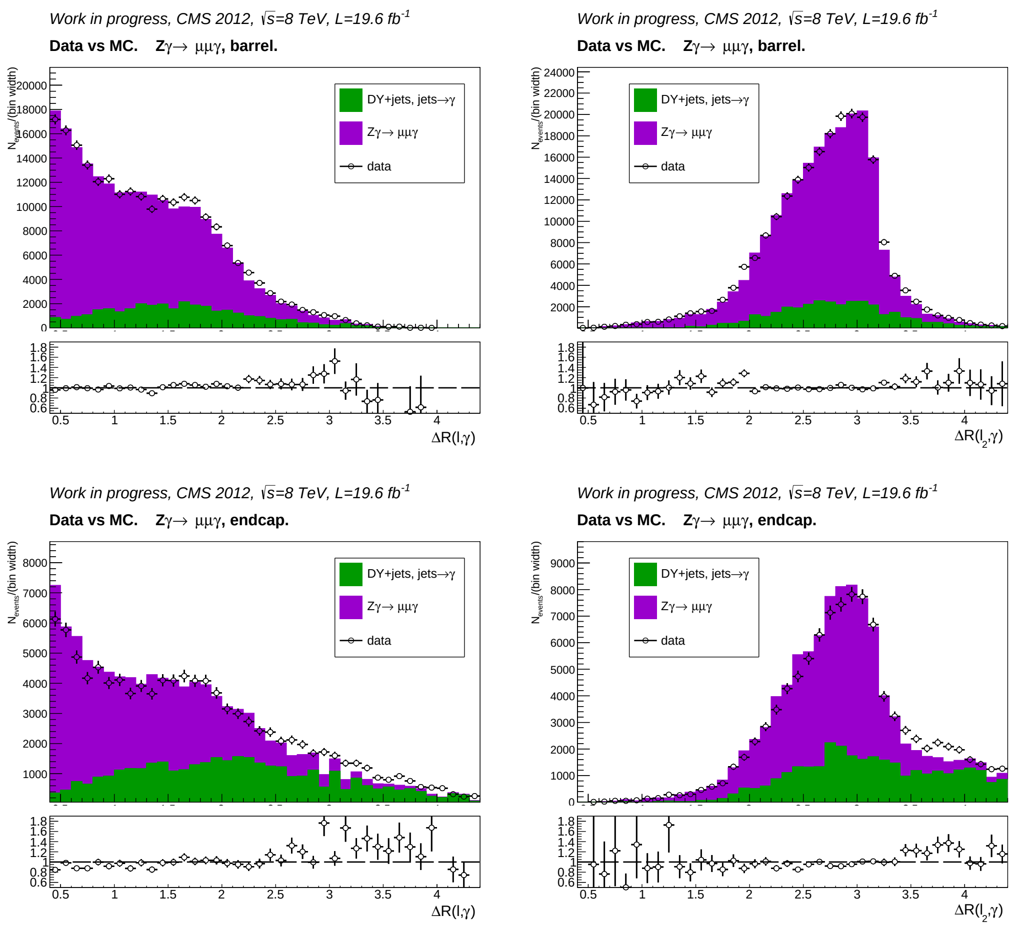

Figure D.2: Distributions of $\Delta R(\mu_1, \gamma)$ (left) and $\Delta R(\mu_2, \gamma)$ (right) in $Z\gamma \to \mu\mu\gamma$-selected events, data vs MC. P_T^γ :15-500 GeV. Left: $M_{\mu\mu\gamma}$, right: $M_{\mu\mu}$. Top: barrel photons, bottom: endcap. Peak highly dominated by $Z\gamma$ events corresponds to FSR.

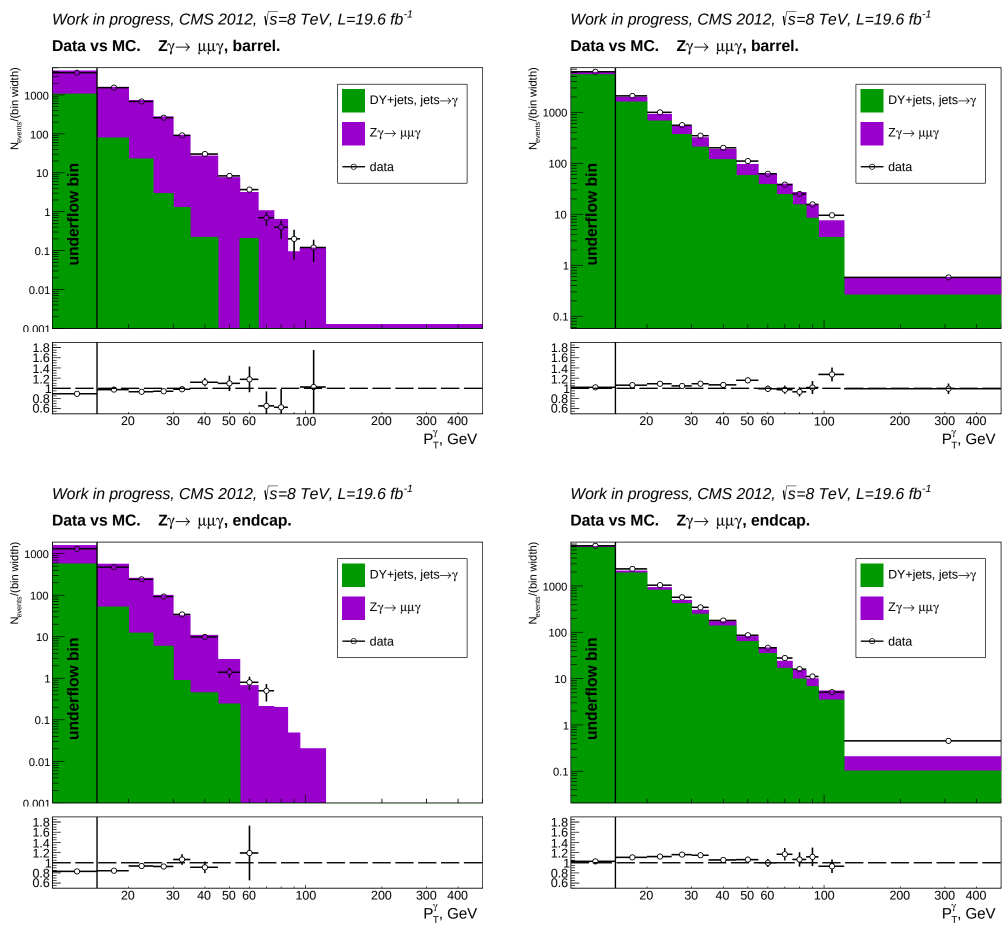

Figure D.3: $Z\gamma$-selected FSR (left) and ISR (right) events, data vs MC.

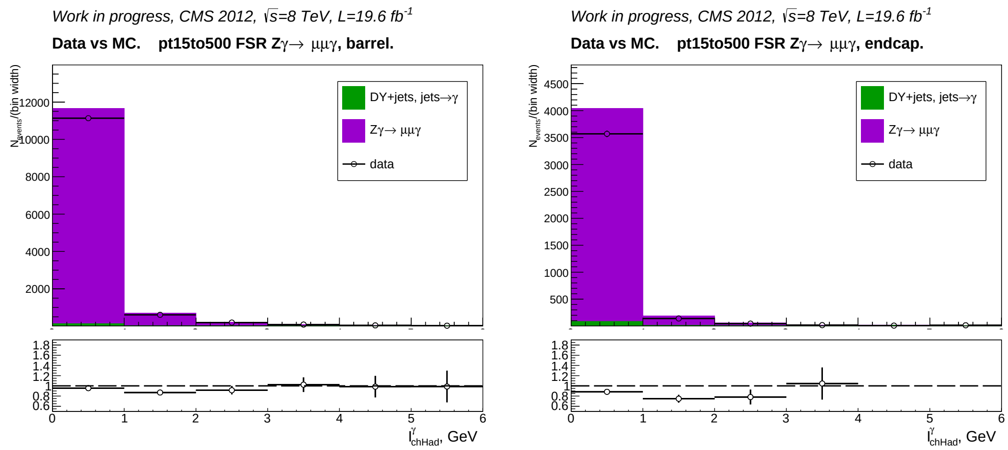

Figure D.4: $Z\gamma$-selected FSR events, data vs MC. P_T^{γ} >15 GeV. Distributions of I_{chHad}^{γ} used for preparing real-γ templates. Fake-γ contribution to FSR region is subtracted based on DY+jets MC prediction to prepare real-γ templates.

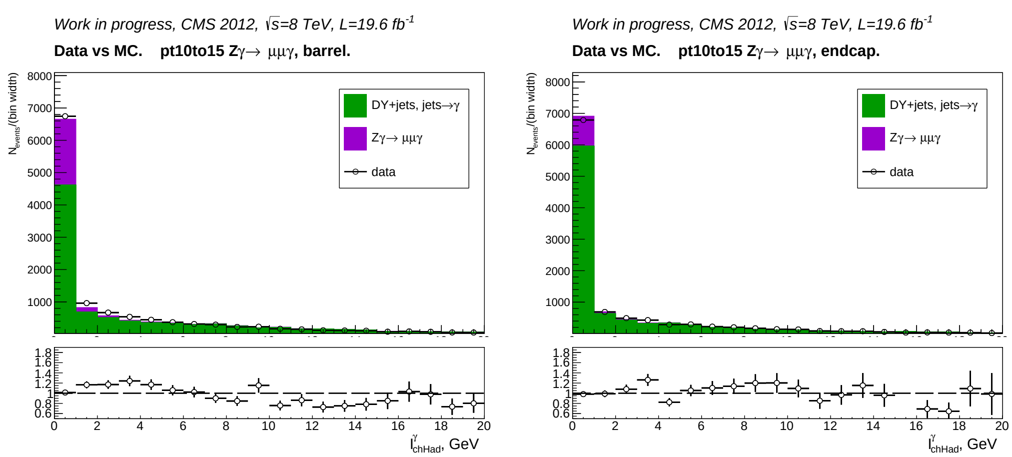

Figure D.5: $Z\gamma$-selected ISR events, data vs MC. 10 GeV< P_T^{γ} <15 GeV. Distributions of I_{chHad}^{γ} used for preparing fake-γ templates. Real-γ contribution to ISR region is subtracted based on $Z\gamma$ signal MC prediction to prepare fake-γ templates.

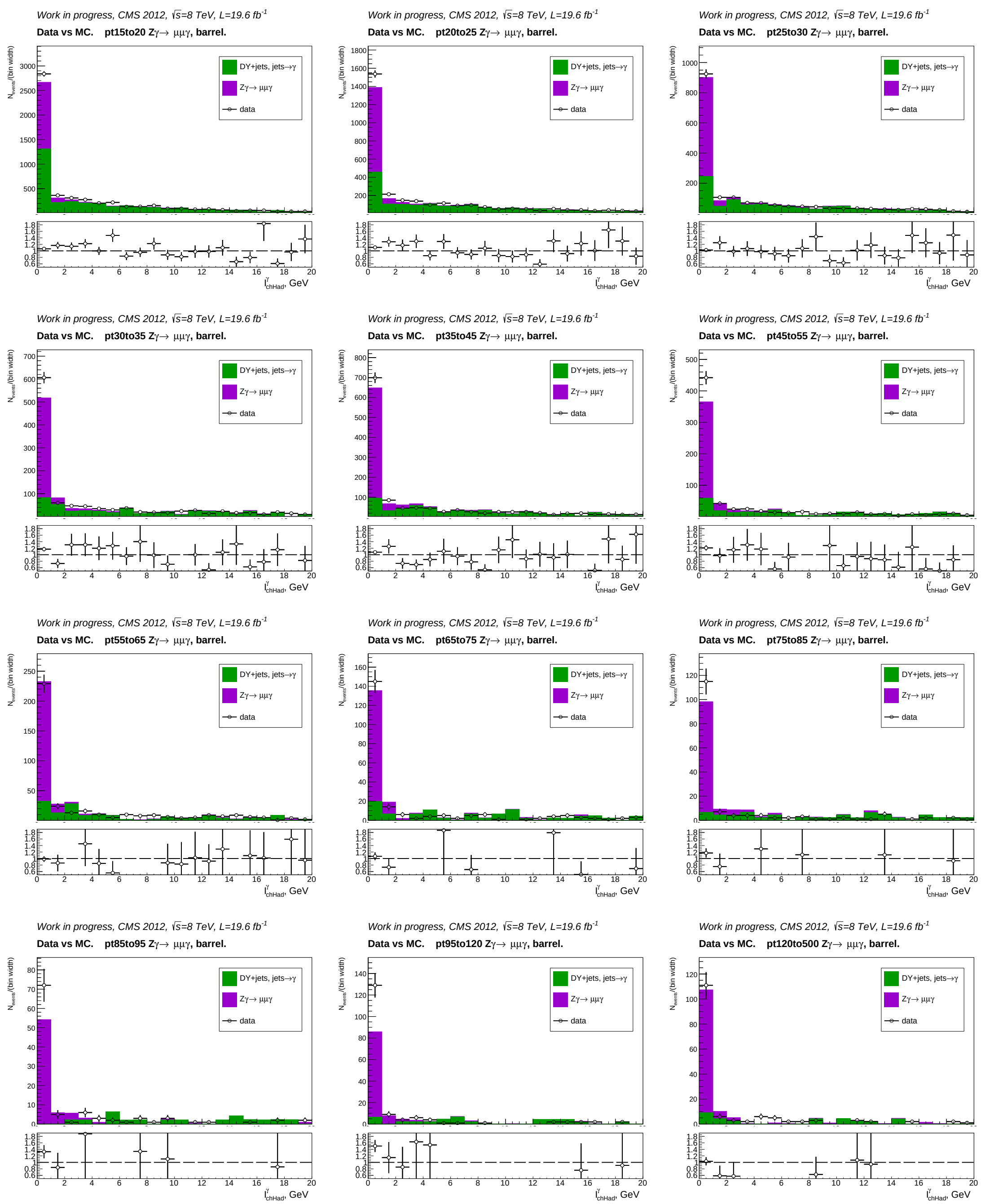

Figure D.6: $Z\gamma$-selected ISR events, data vs MC. Distributions of I^{γ}_{chHad} used for preparing fake-γ templates. Real-γ contribution to ISR region is subtracted based on $Z\gamma$ signal MC prediction to prepare fake-γ templates. Ranges of $< P_T^{\gamma}$ are shown in the plot titles and cover the total range of 15 GeV$< P_T^{\gamma} <$500 GeV. EB photons.

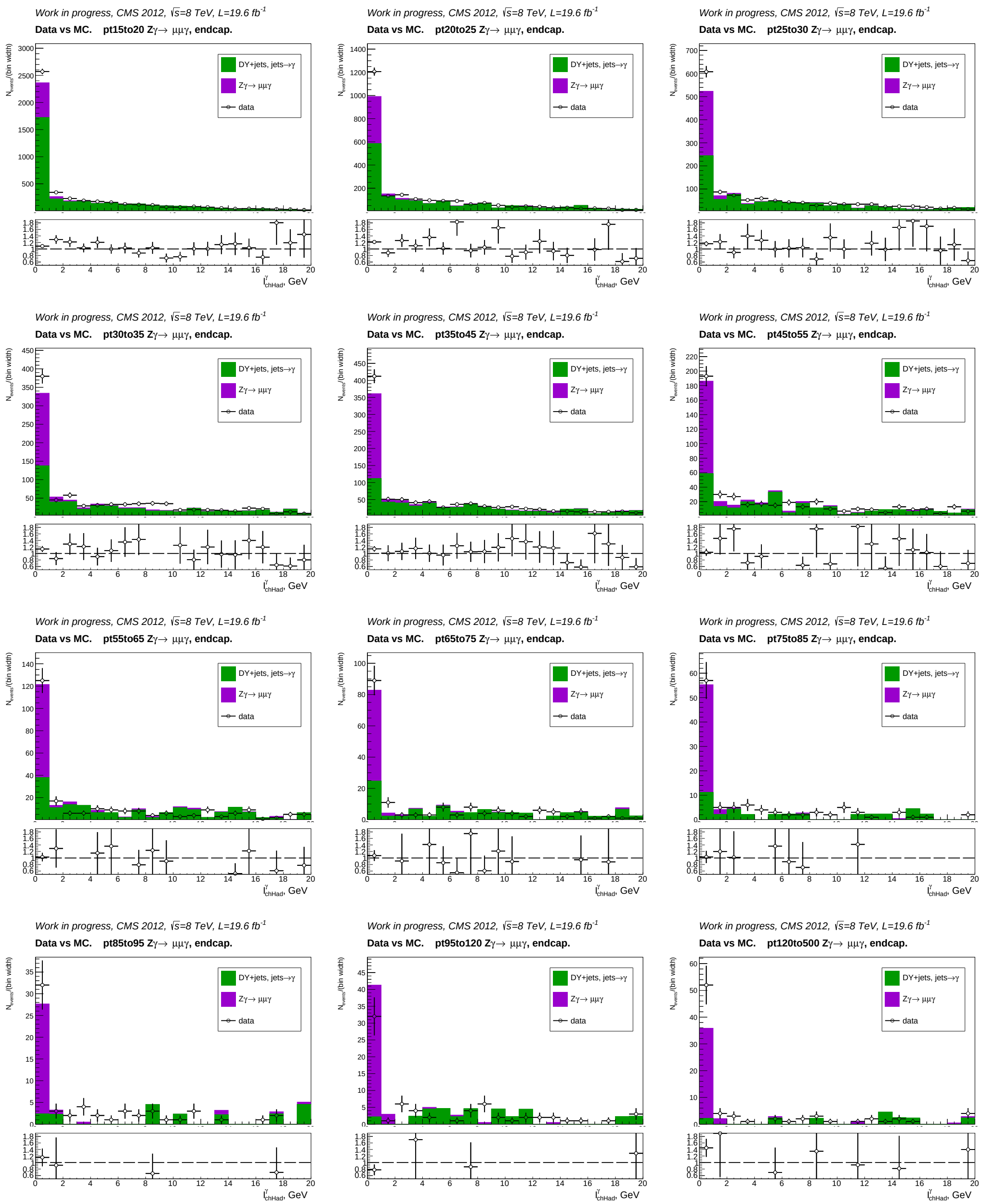

Figure D.7: $Z\gamma$-selected ISR events, data vs MC. Distributions of I^{γ}_{chHad} used for preparing fake-γ templates. Real-γ contribution to ISR region is subtracted based on $Z\gamma$ signal MC prediction to prepare fake-γ templates. Ranges of P^{γ}_{T} are shown in the plot titles and cover the total range of 15 GeV< P^{γ}_{T} <500 GeV. EE photons.

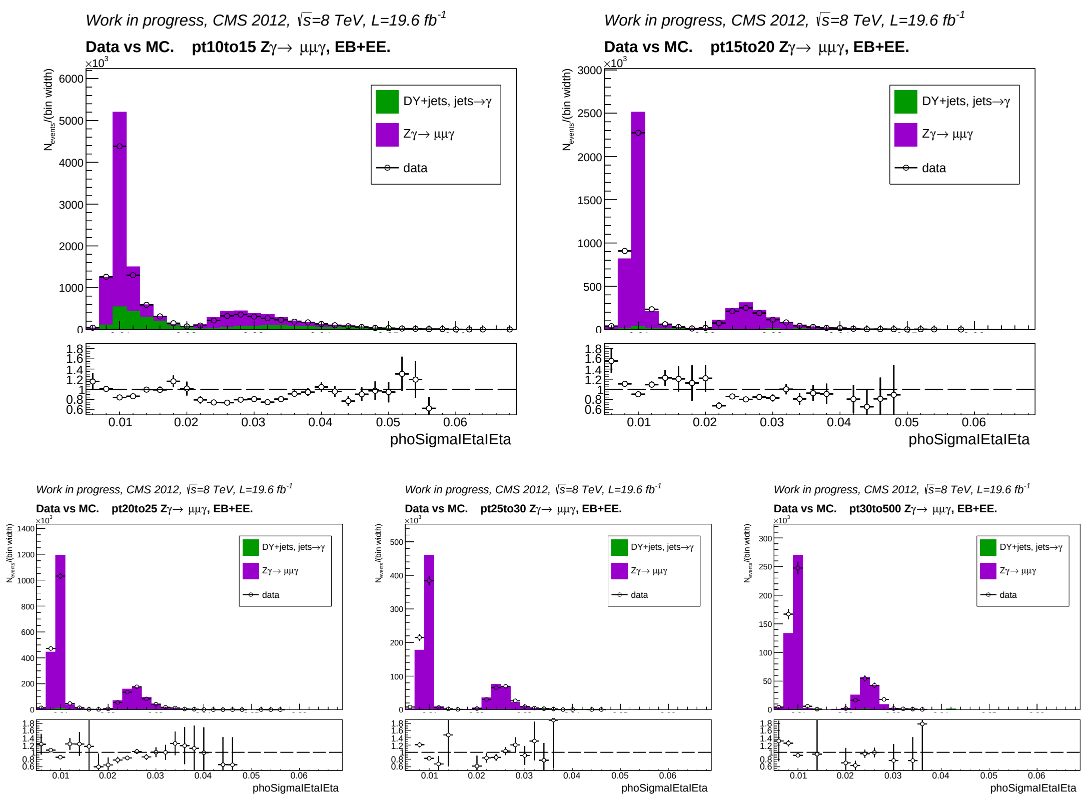

Figure D.8: $Z\gamma$-selected FSR events, data vs MC. Distributions of $\sigma_{i\eta i\eta}$ are used for preparing real-γ templates. Fake-γ contribution to FSR region is subtracted based on DY+jets MC prediction to prepare real-γ templates. The templates are prepared separately for barrel and endcap photons.

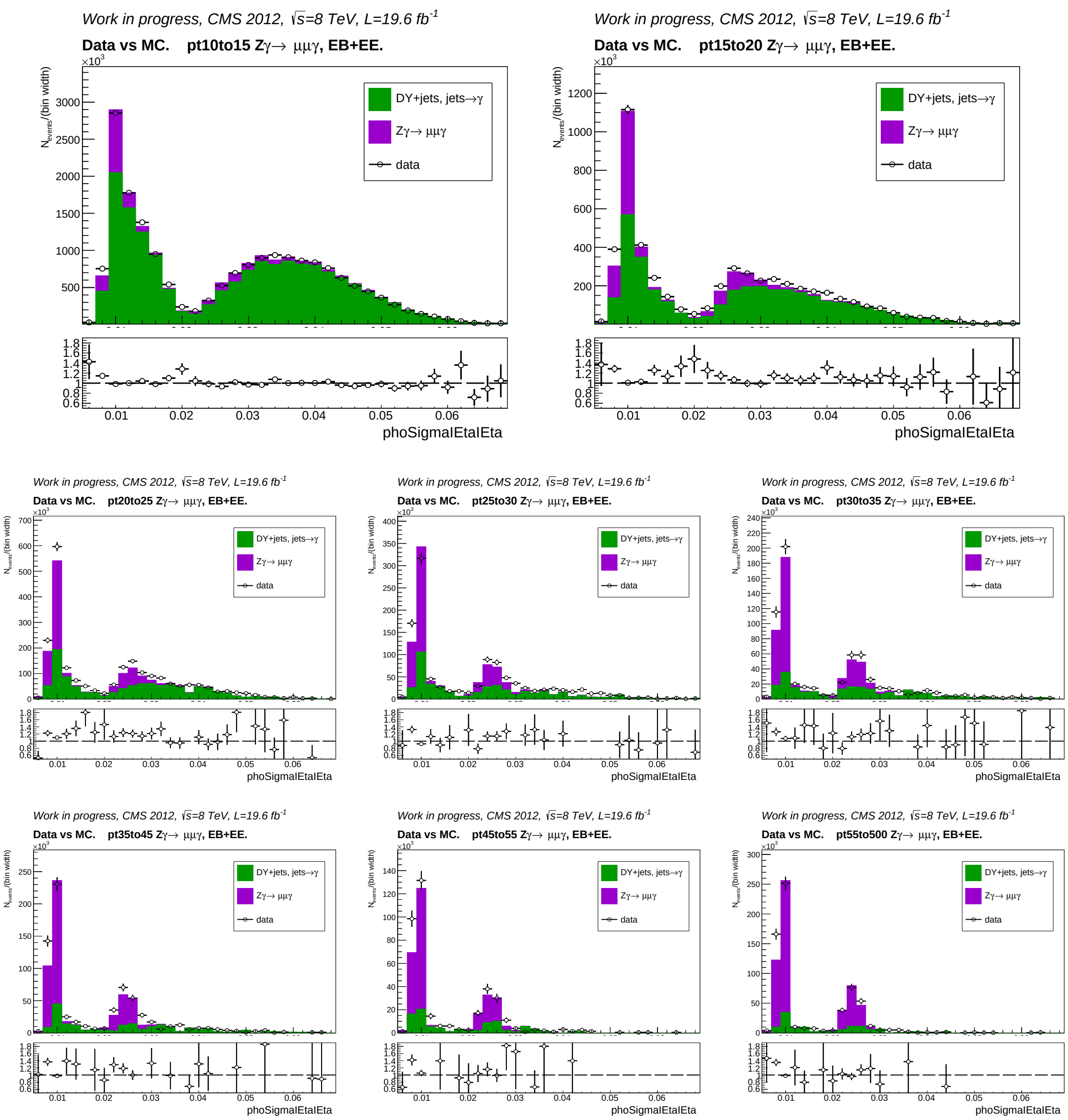

Figure D.9: $Z\gamma$-selected ISR events, data vs MC. Distributions of $\sigma_{i\eta i\eta}$ are used for preparing real-γ templates. Fake-γ contribution to ISR region is subtracted based on DY+jets MC prediction to prepare real-γ templates. The templates are prepared separately for barrel and endcap photons.

E Template Fit Plots, $W\gamma$, Data

This appendix contains fit results for jets$\rightarrow\gamma$ background estimation in the $W\gamma$-selected data sample. On any plot, the black histogram is data, the green is a real-γ template, the blue is a fake-γ template, and the red is the fit function. These fits are part of the procedure of jets$\rightarrow\gamma$ background estimation which is described in Ch. 5.4.1.

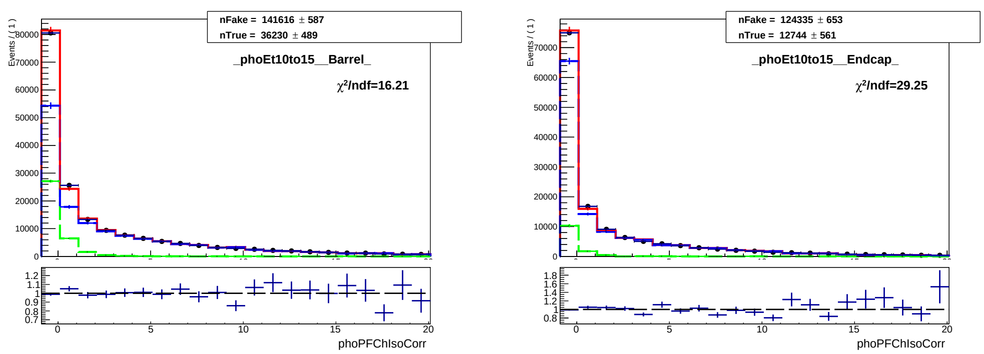

Figure E.1: Fits of I^{γ}_{ch} templates, $W\gamma$, muon channel, underflow bin $(10-15$ GeV$)$.

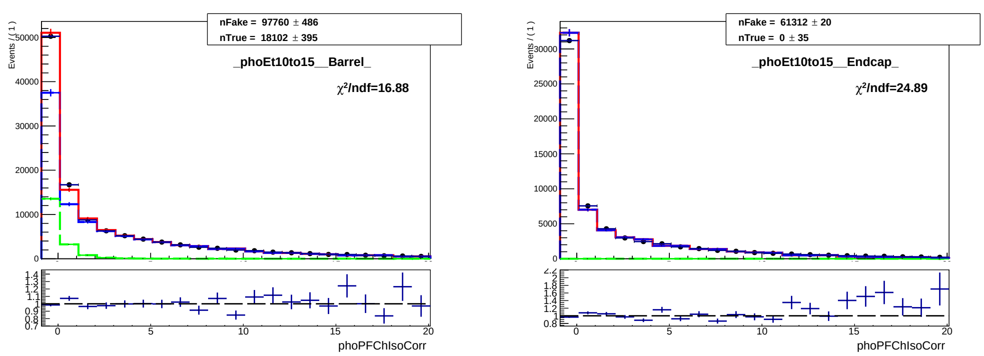

Figure E.2: Fits of I_{ch}^{γ} templates, $W\gamma$, electron channel, underflow bin $(10 - 15$ GeV).

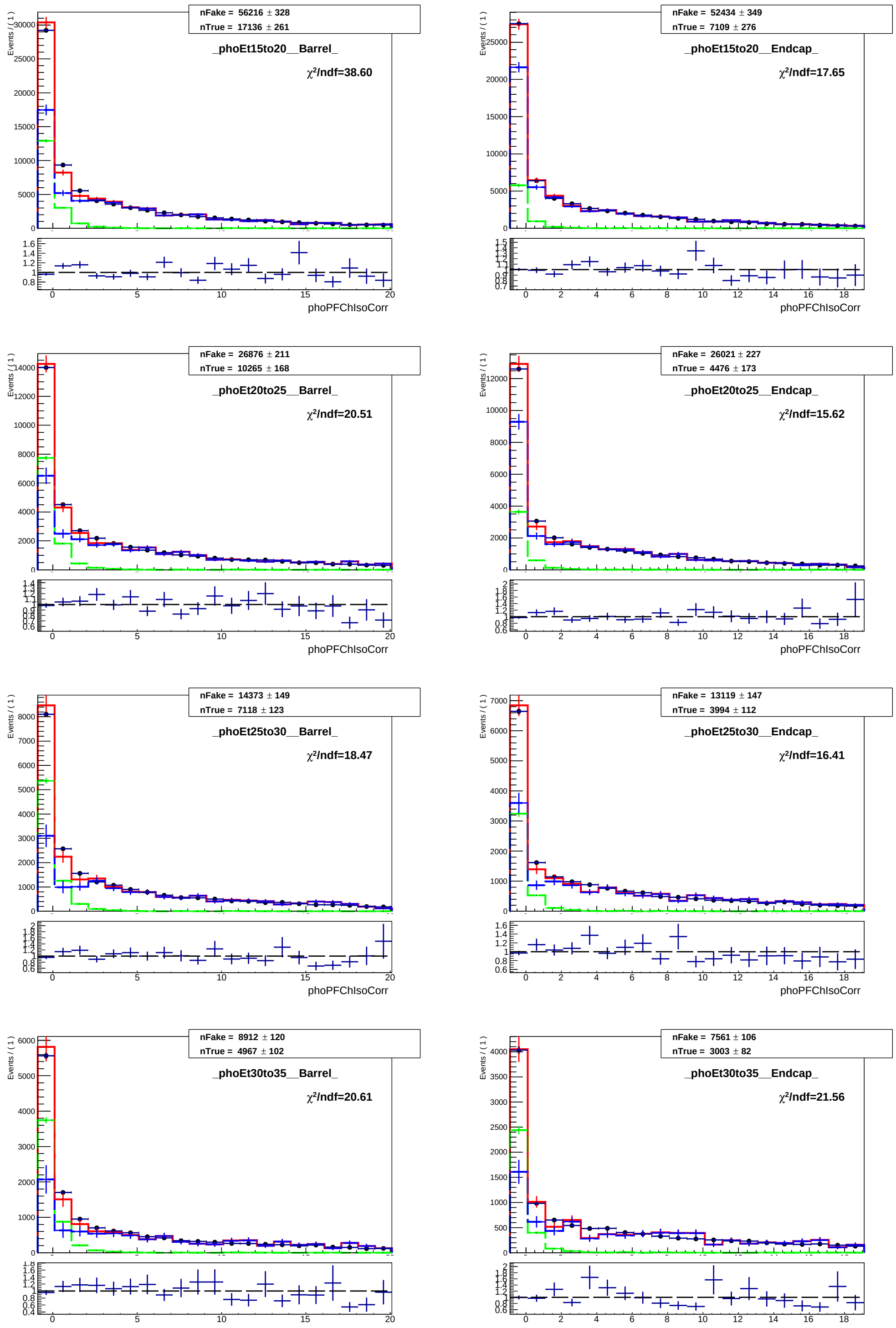

Figure E.3: Fits of I_{ch}^{γ} templates, $W\gamma$, muon channel.

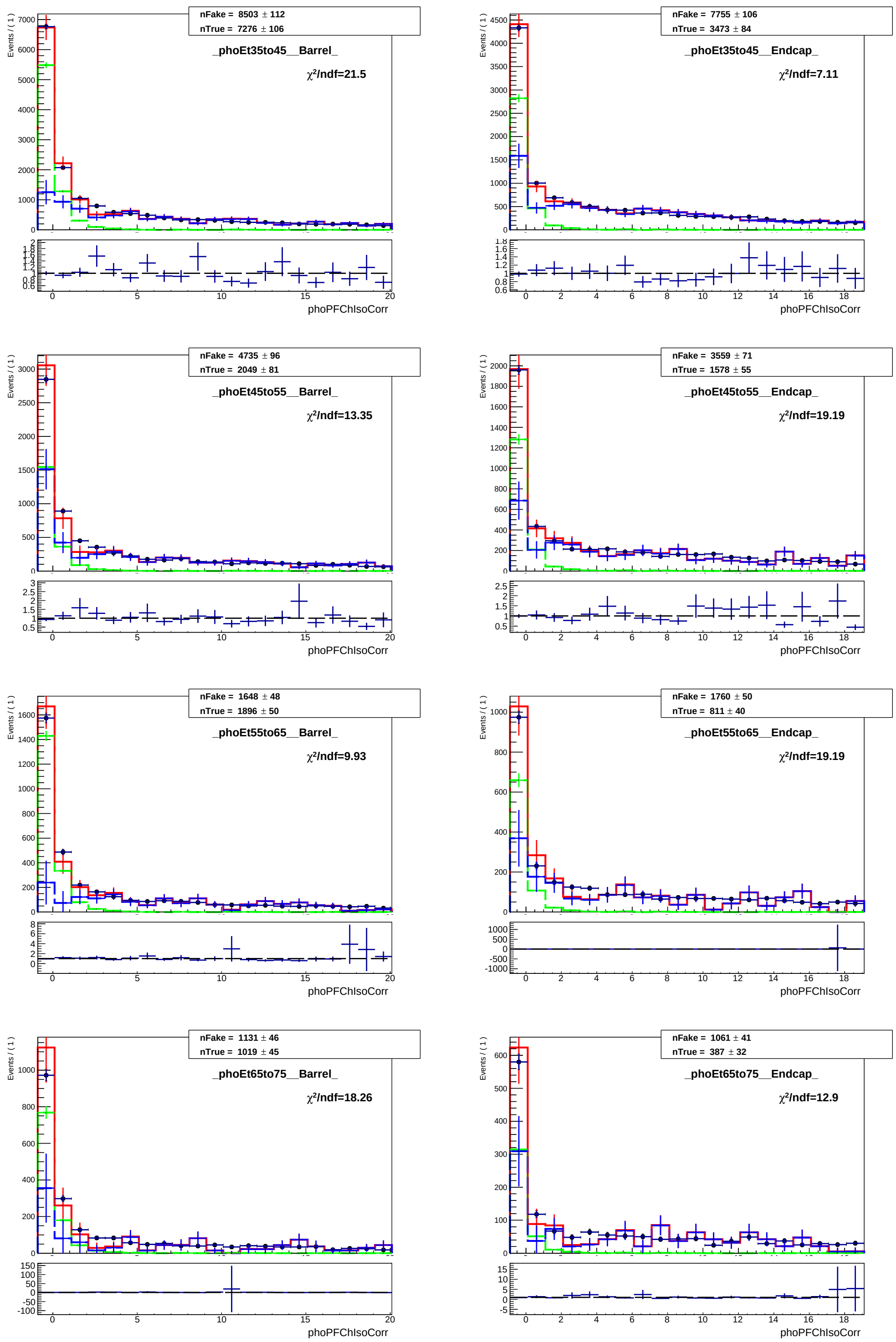

Figure E.4: Fits of I_{ch}^{γ} templates, $W\gamma$, muon channel.

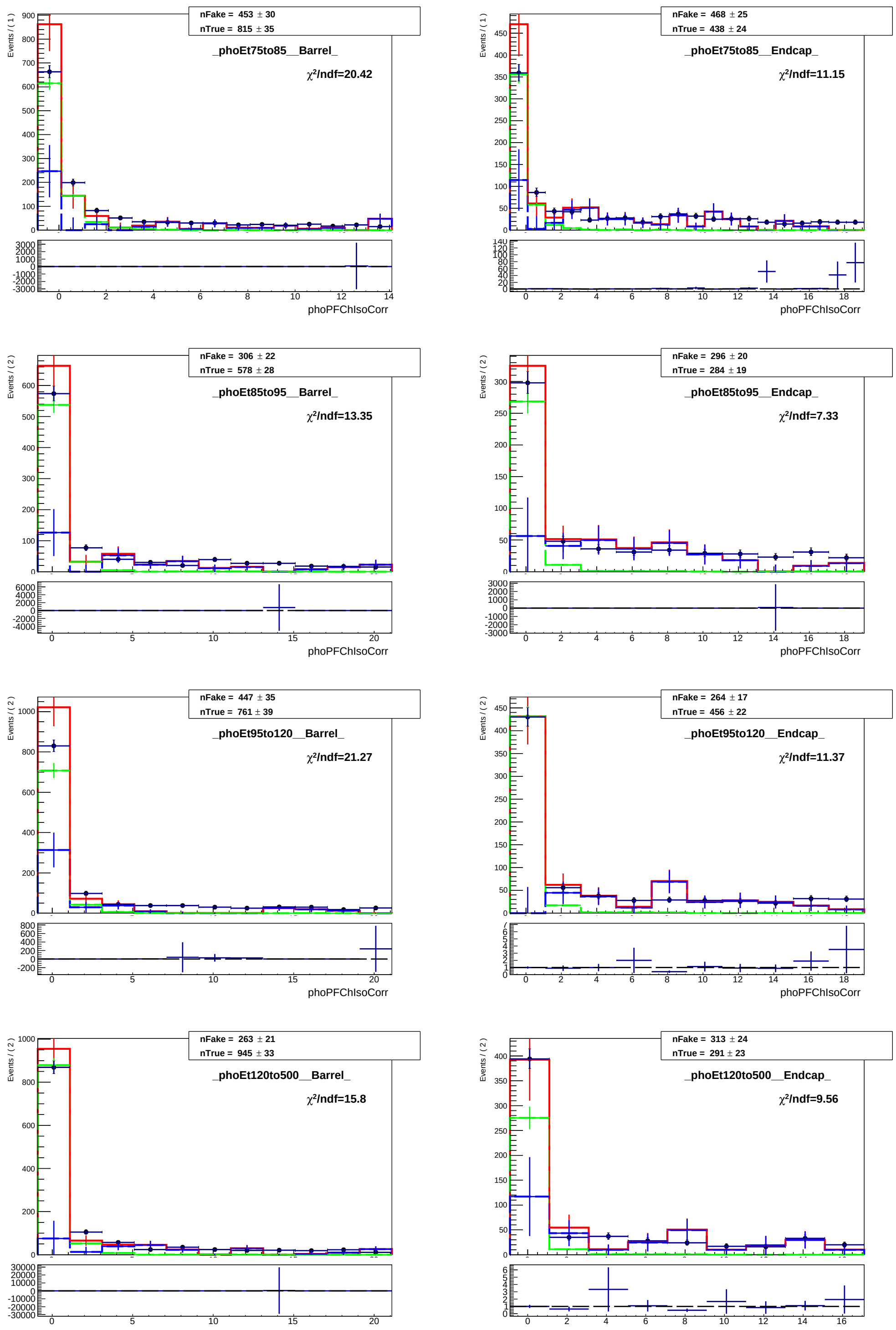

Figure E.5: Fits of I_{ch}^{γ} templates, $W\gamma$, muon channel.

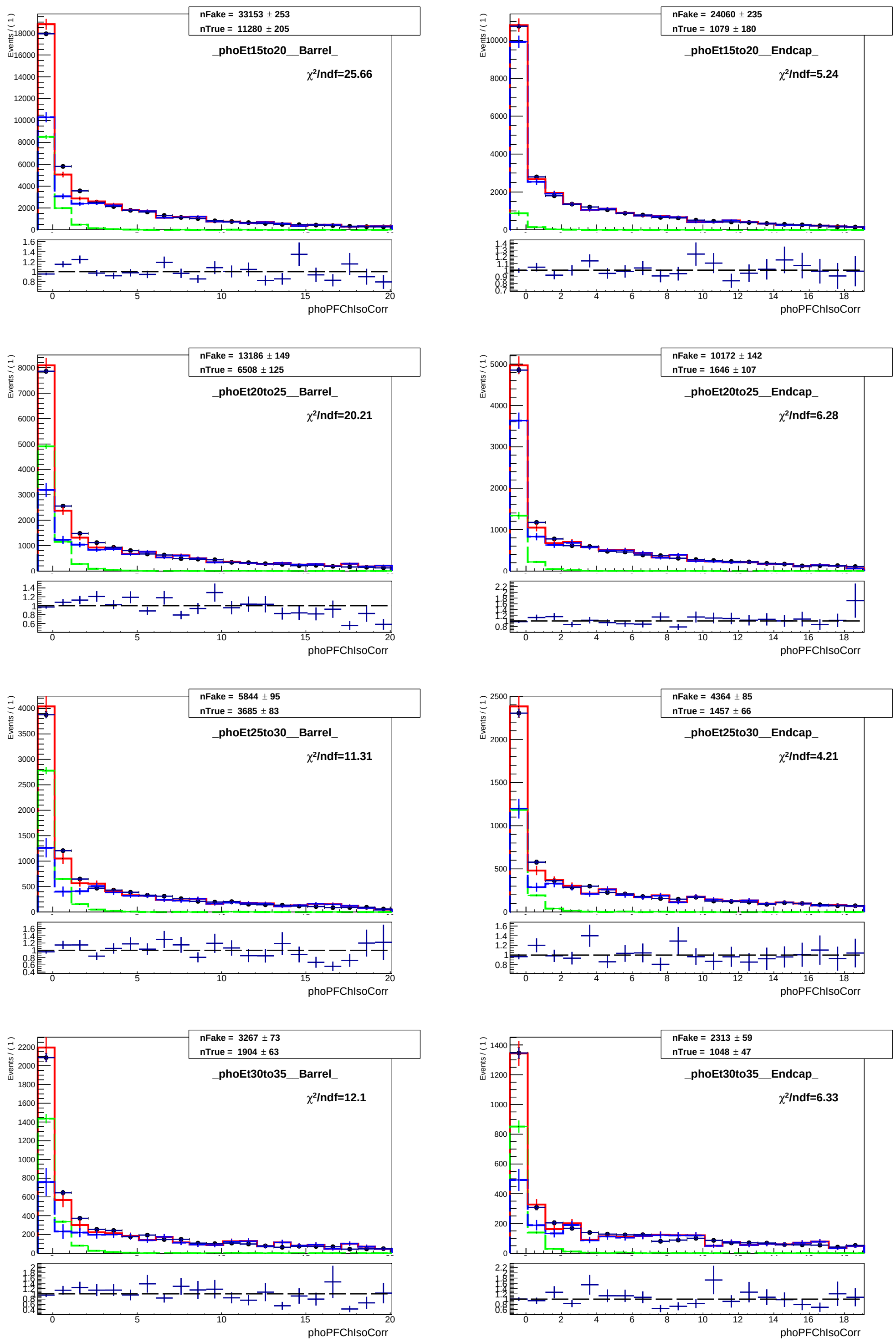

Figure E.6: Fits of I_{ch}^{γ} templates, $W\gamma$, electron channel.

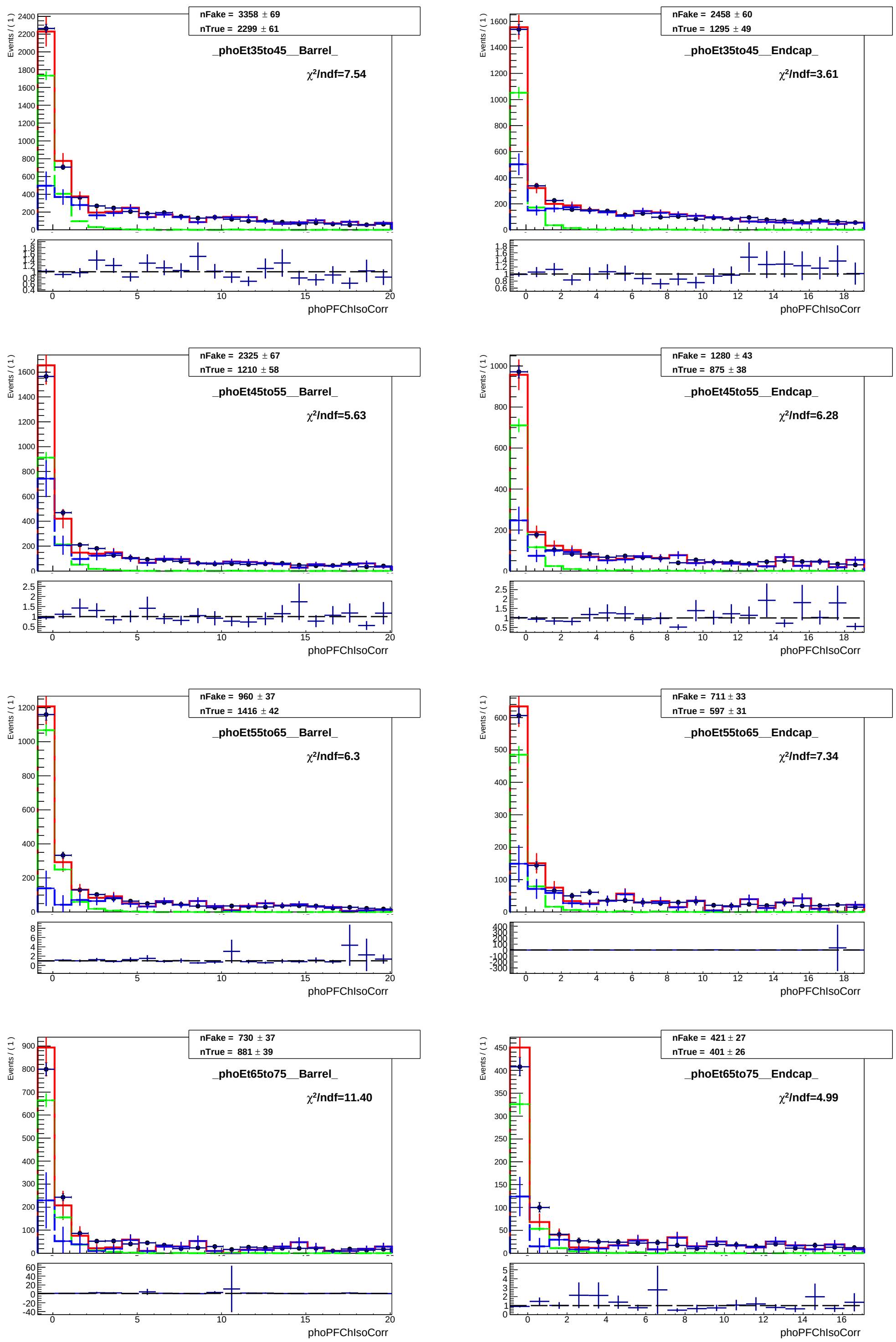

Figure E.7: Fits of I_{ch}^{γ} templates, $W\gamma$, electron channel.

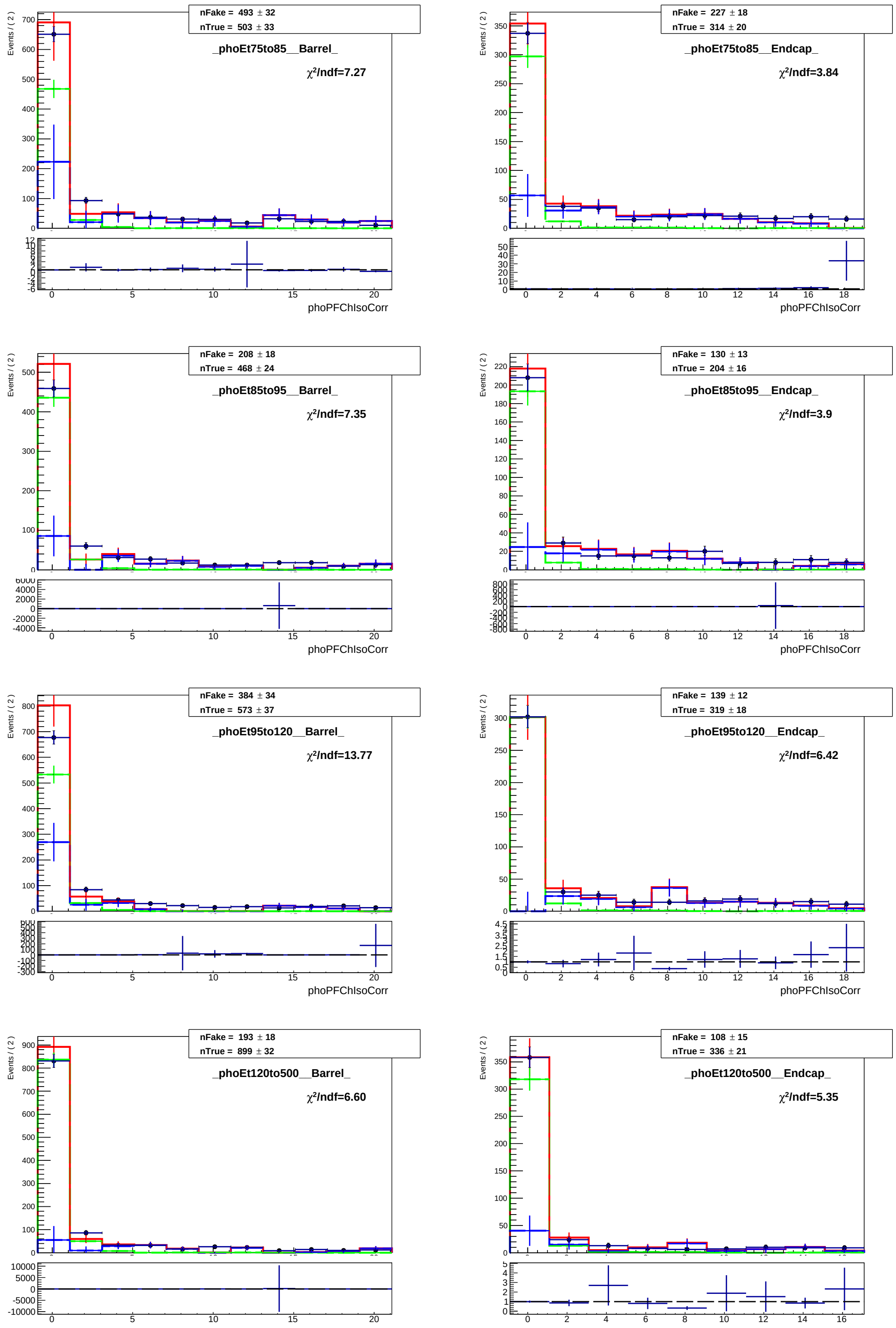

Figure E.8: Fits of I_{ch}^{γ} templates, $W\gamma$, electron channel.

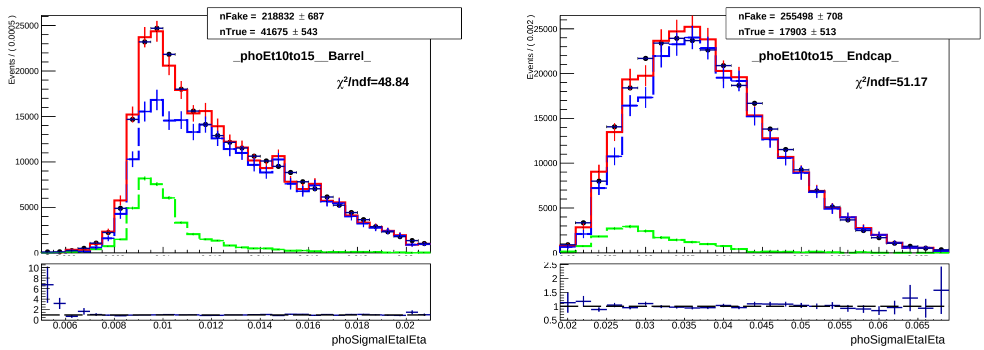

Figure E.9: Fits of $\sigma_{i\eta i\eta}$ templates, $W\gamma$, muon channel, underflow bin ($10-15$ GeV).

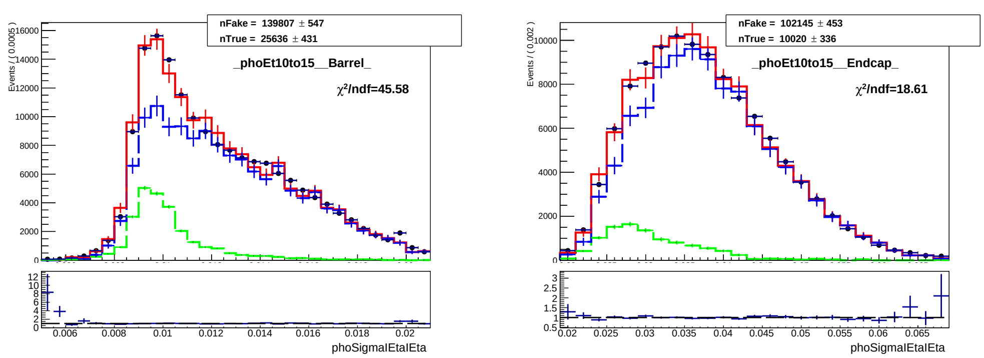

Figure E.10: Fits of $\sigma_{i\eta i\eta}$ templates, $W\gamma$, electron channel, underflow bin ($10-15$ GeV).

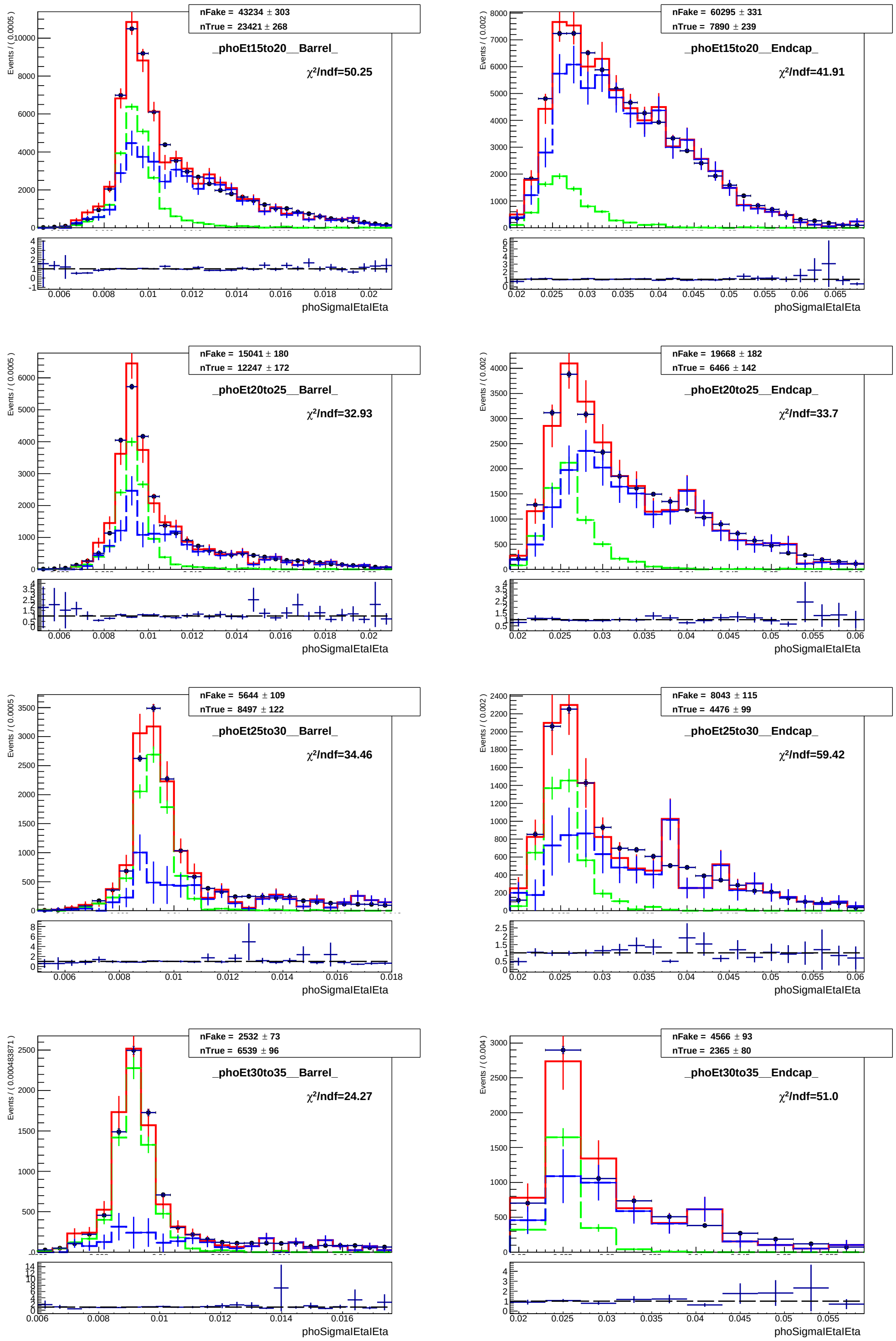

Figure E.11: Fits of $\sigma_{i\eta i\eta}$ templates, $W\gamma$, muon channel.

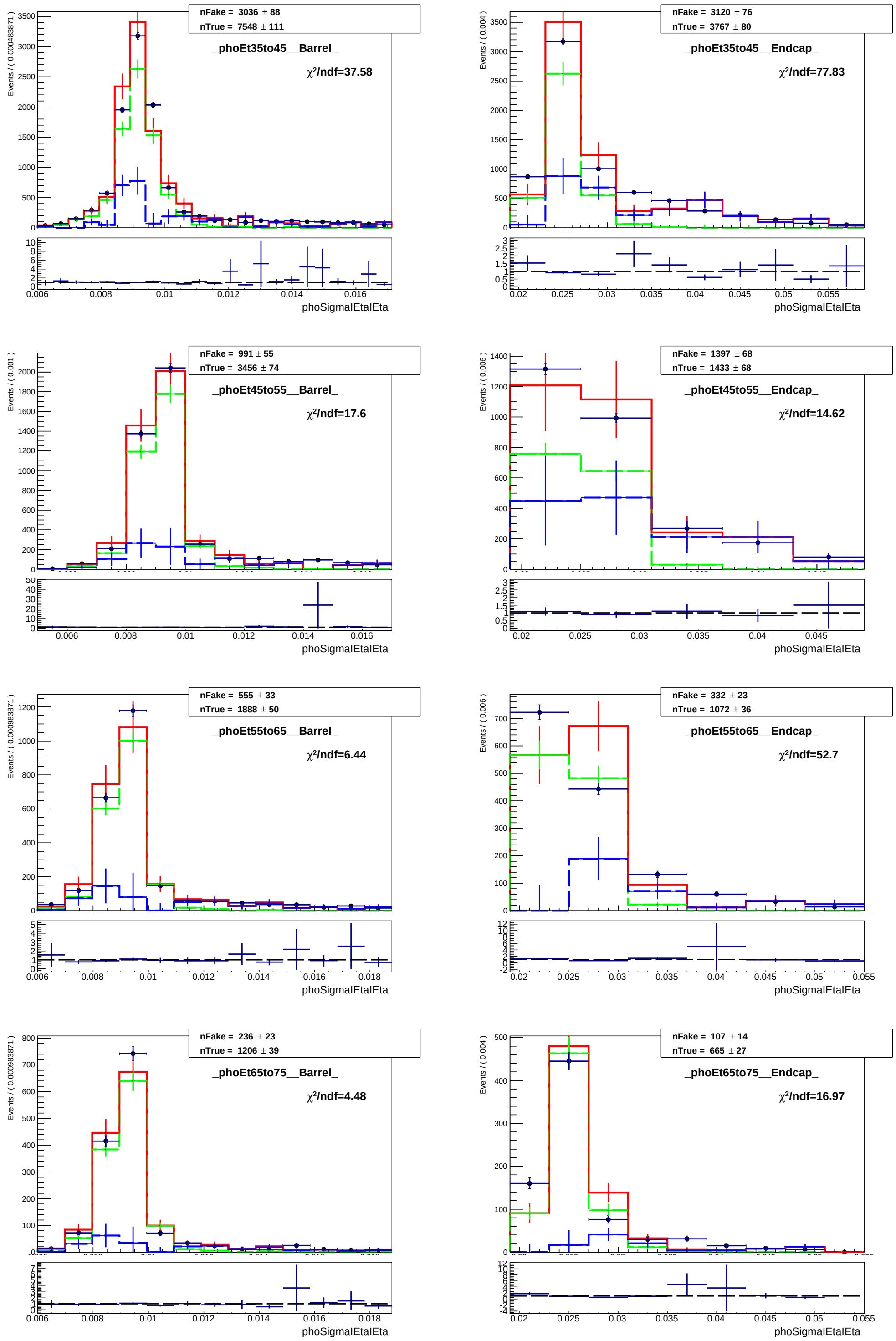

Figure E.12: Fits of $\sigma_{i\eta i\eta}$ templates, $W\gamma$, muon channel.

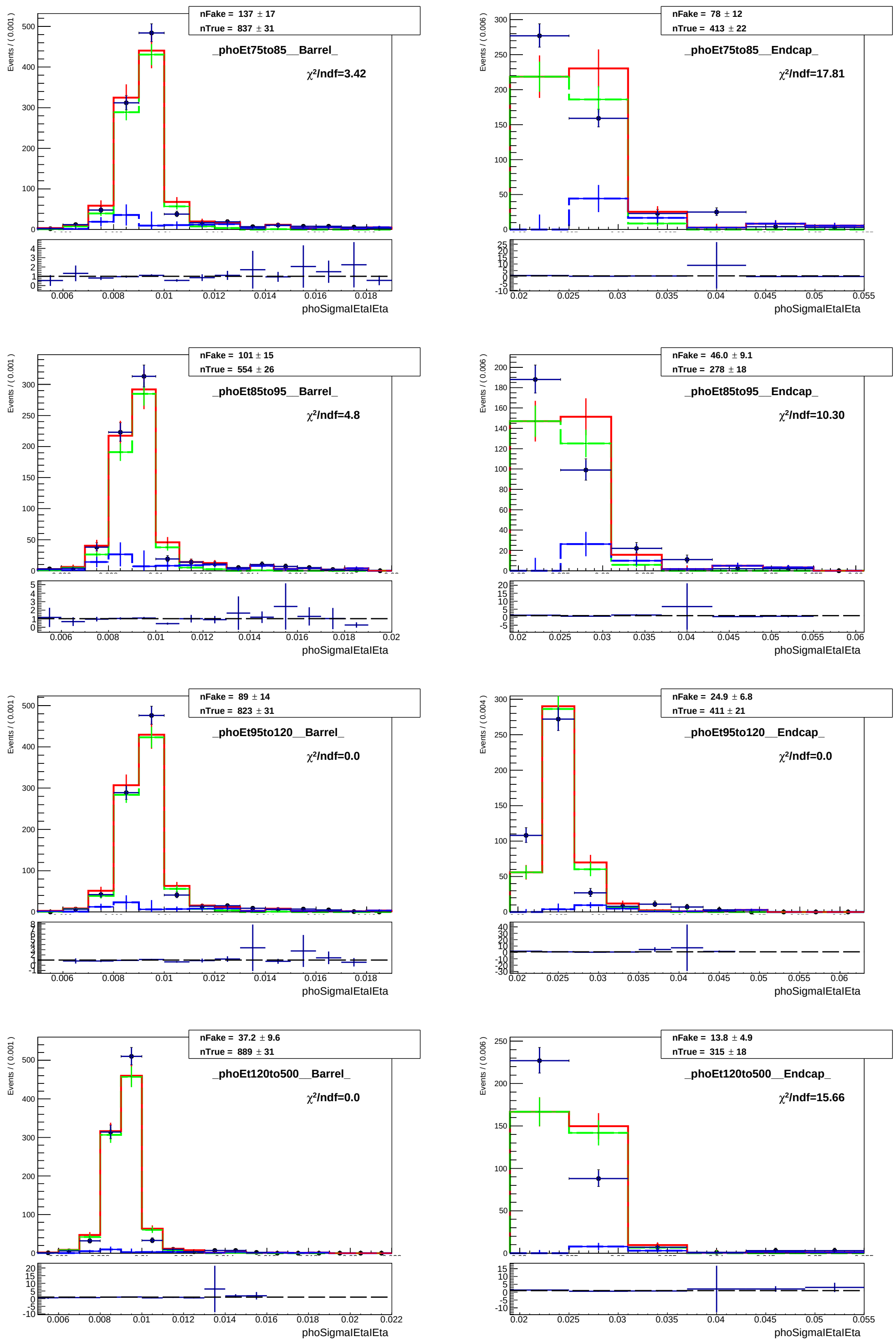

Figure E.13: Fits of $\sigma_{i\eta i\eta}$ templates, $W\gamma$, muon channel.

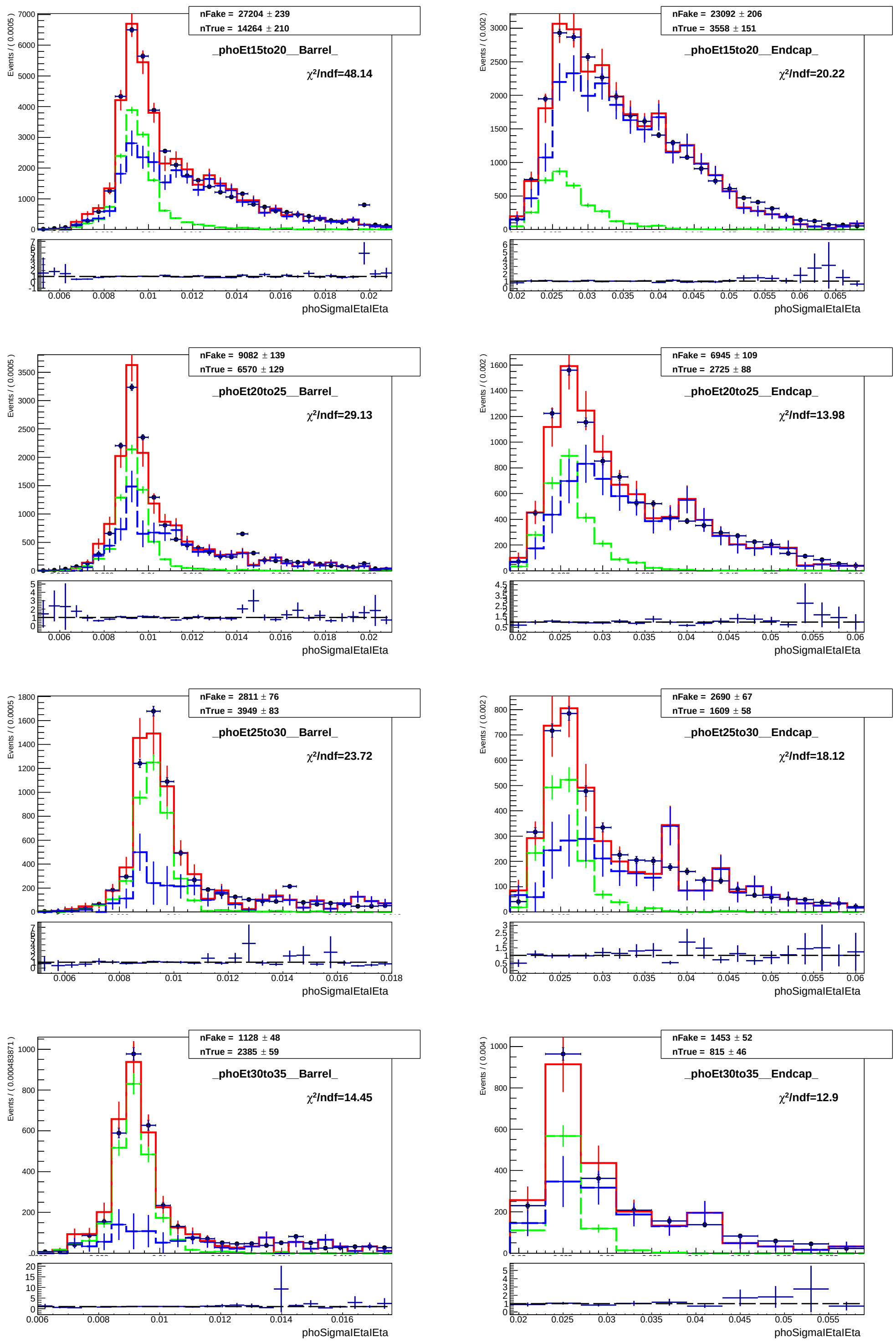

Figure E.14: Fits of $\sigma_{i\eta i\eta}$ templates, $W\gamma$, electron channel.

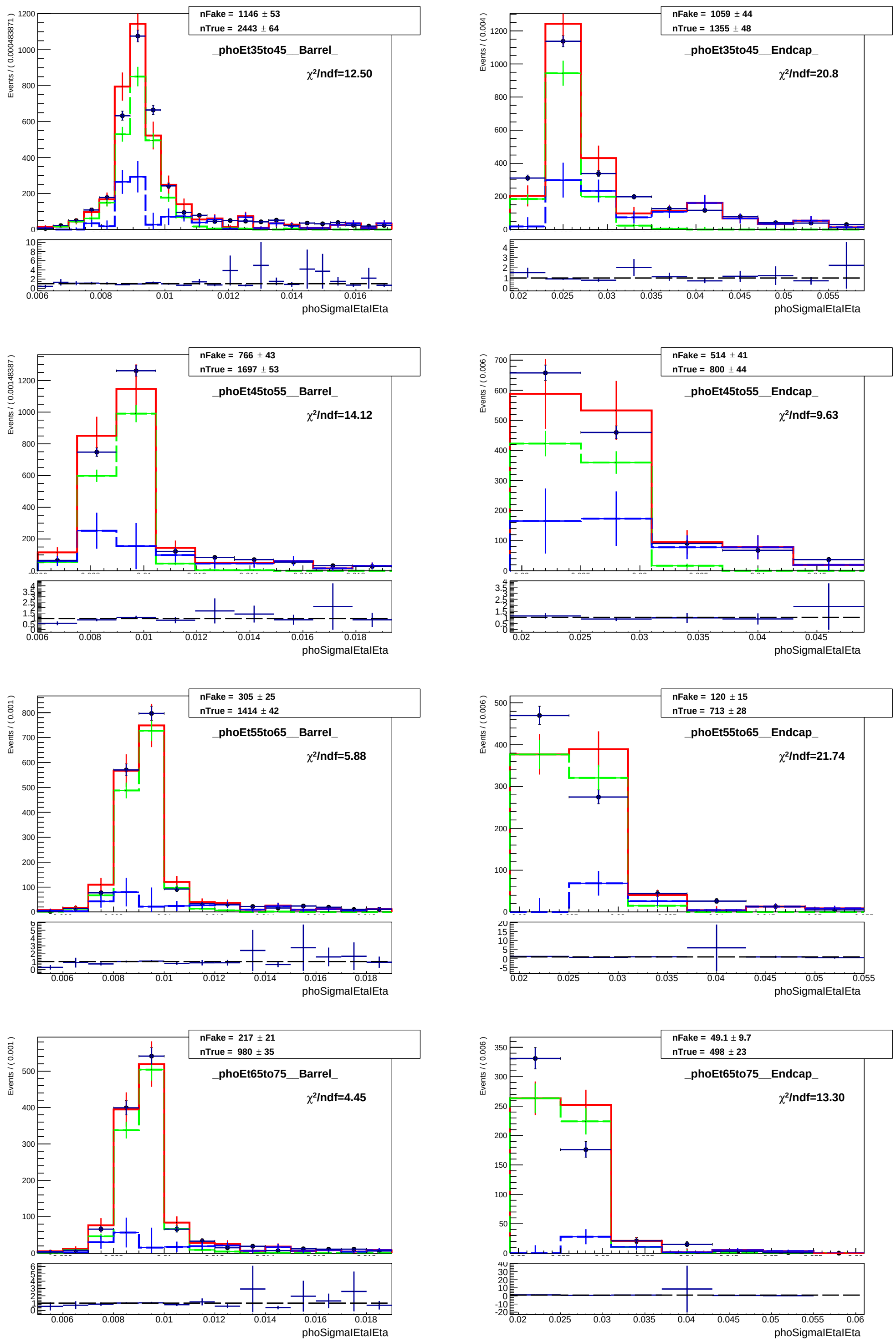

Figure E.15: Fits of $\sigma_{i\eta i\eta}$ templates, $W\gamma$, electron channel.

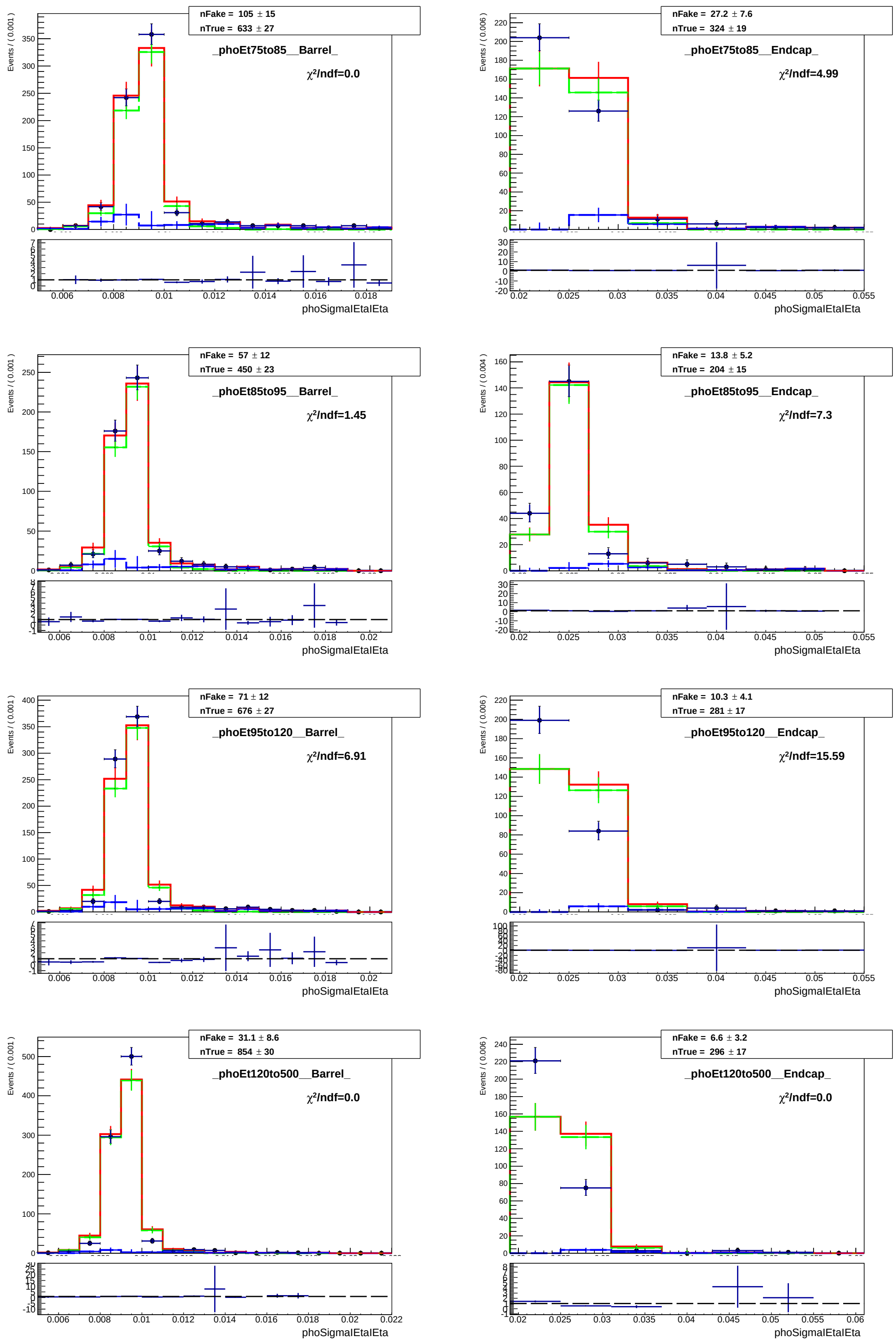

Figure E.16: Fits of $\sigma_{i\eta i\eta}$ templates, $W\gamma$, electron channel.

F Fit Plots of $M_{e\gamma}$

This appendix contains fit plots of electron-photon invariant mass $M_{e\gamma}$ distributions for the $e \rightarrow \gamma$ data-driven estimation in the electron channel. The procedure of the background estimation is described in Ch. 5.4.2.

The number of $e\gamma$ events in data under the Z-peak $N^{e\rightarrow\gamma}_{MC-Zpeak}$ is extracted from the fit of the model:

$$F^{e\rightarrow\gamma}_{fit} = N_{e\rightarrow\gamma} \cdot (RooNDKeysPdf * Gaussian) + N_{other} \cdot (RooCMSShape). \quad \text{(F.1)}$$

The function $RooNDKeysPdf$ is part of the RooFit package [54] and the $RooCMSShape$ was developed specifically for CMS [55].

The $F^{e\rightarrow\gamma}_{fit}$ has eight fit parameters. The parameters "Nsig" and "Nbkg" is the plots are $N_{e\rightarrow\gamma}$ and N_{other}, respectively, "mean_gau" and "sigma_gau" are parameters of the Gaussian distribution, "CMS_alpha" and "CMS_beta" are parameters of the exponential component of the $RooCMSShape$, and "CMS_gamma" and "CMS_peak" are parameters of the turn over component of the $RooCMSShape$.

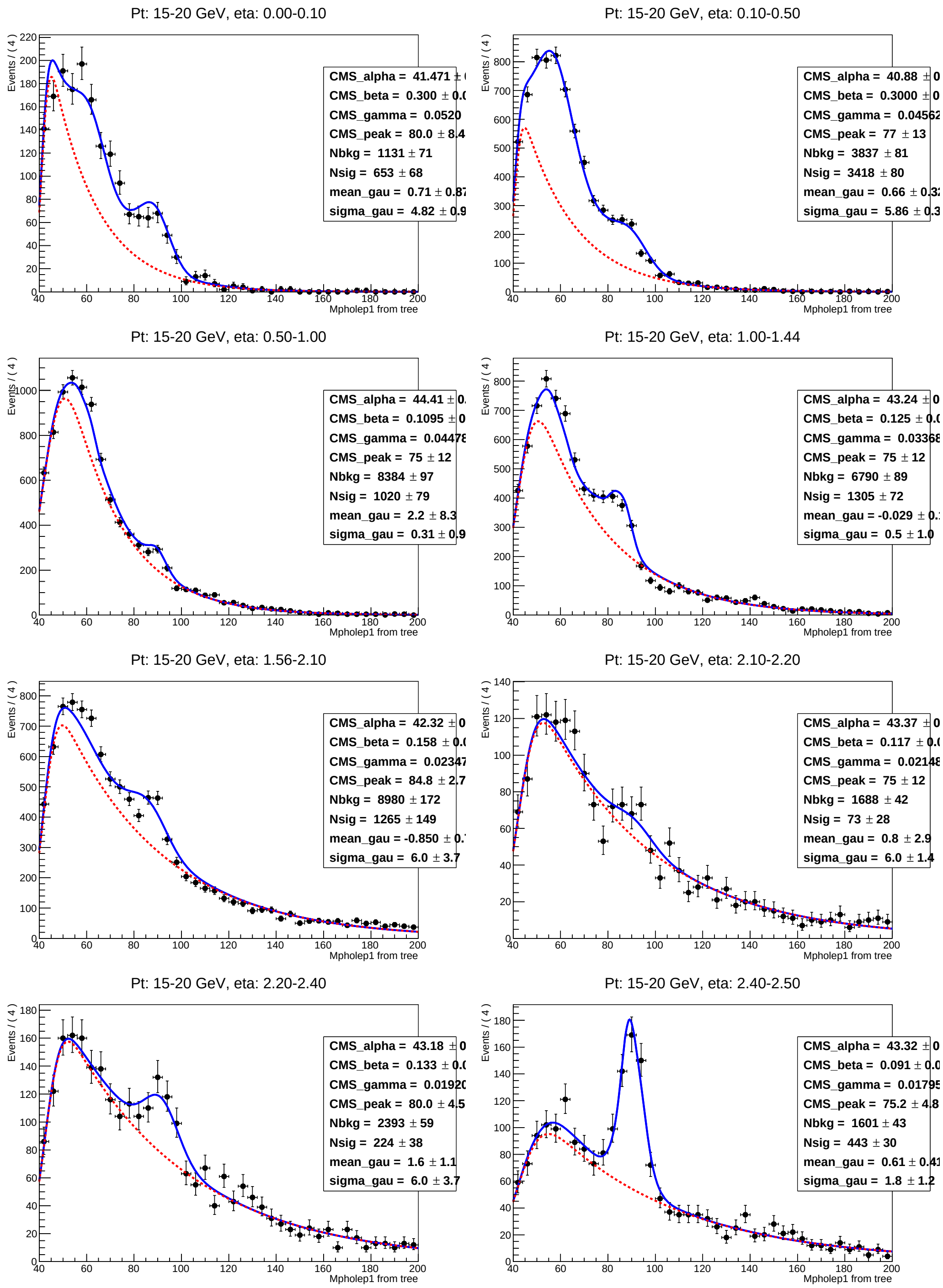

Figure F.1: $M_{e\gamma}$ fits, $W\gamma$, electron channel, 15-20 GeV, 8 η^{γ} bins.

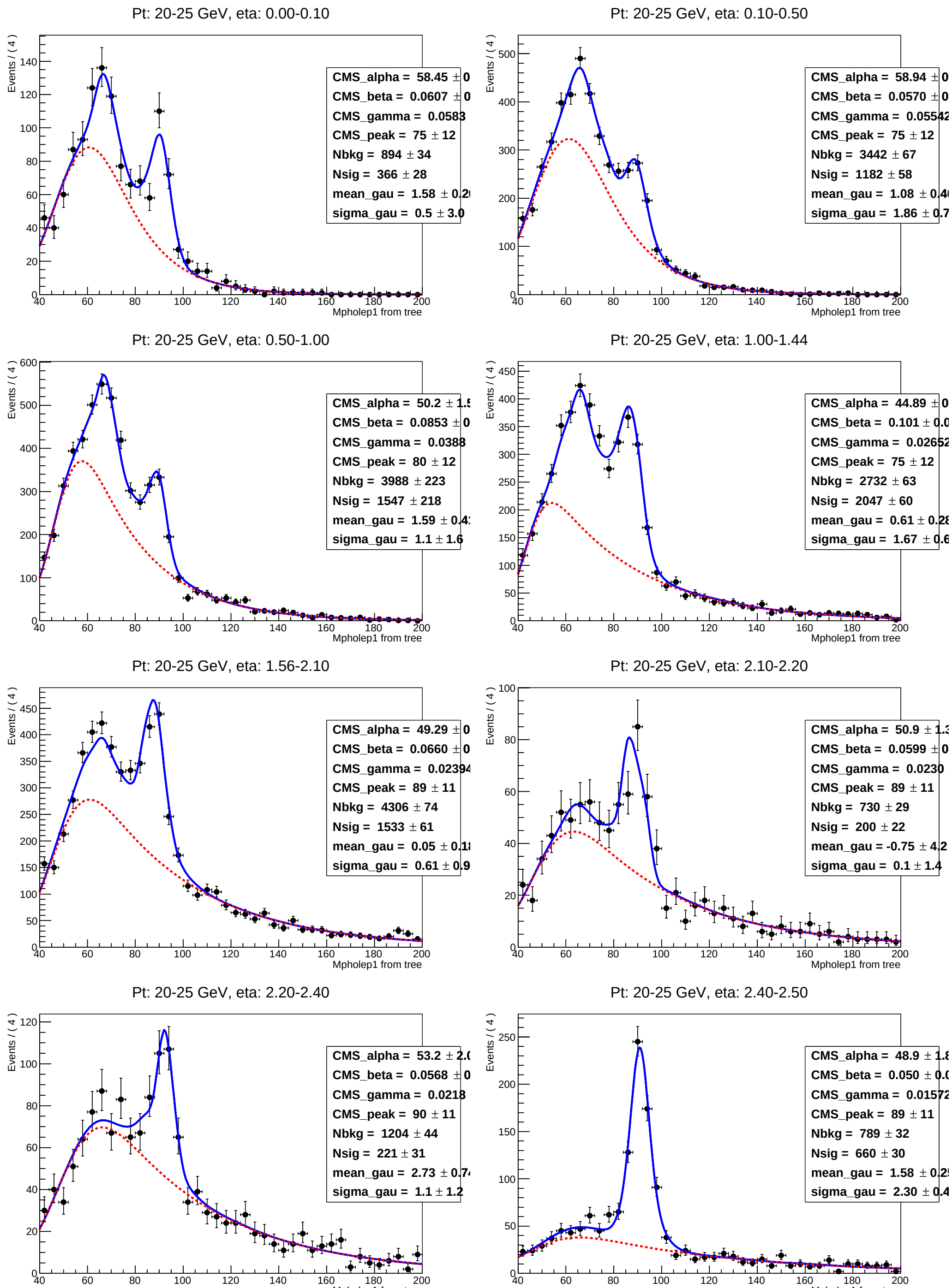

Figure F.2: $M_{e\gamma}$ fits, $W\gamma$, electron channel, 20-25 GeV, 8 η^{γ} bins.

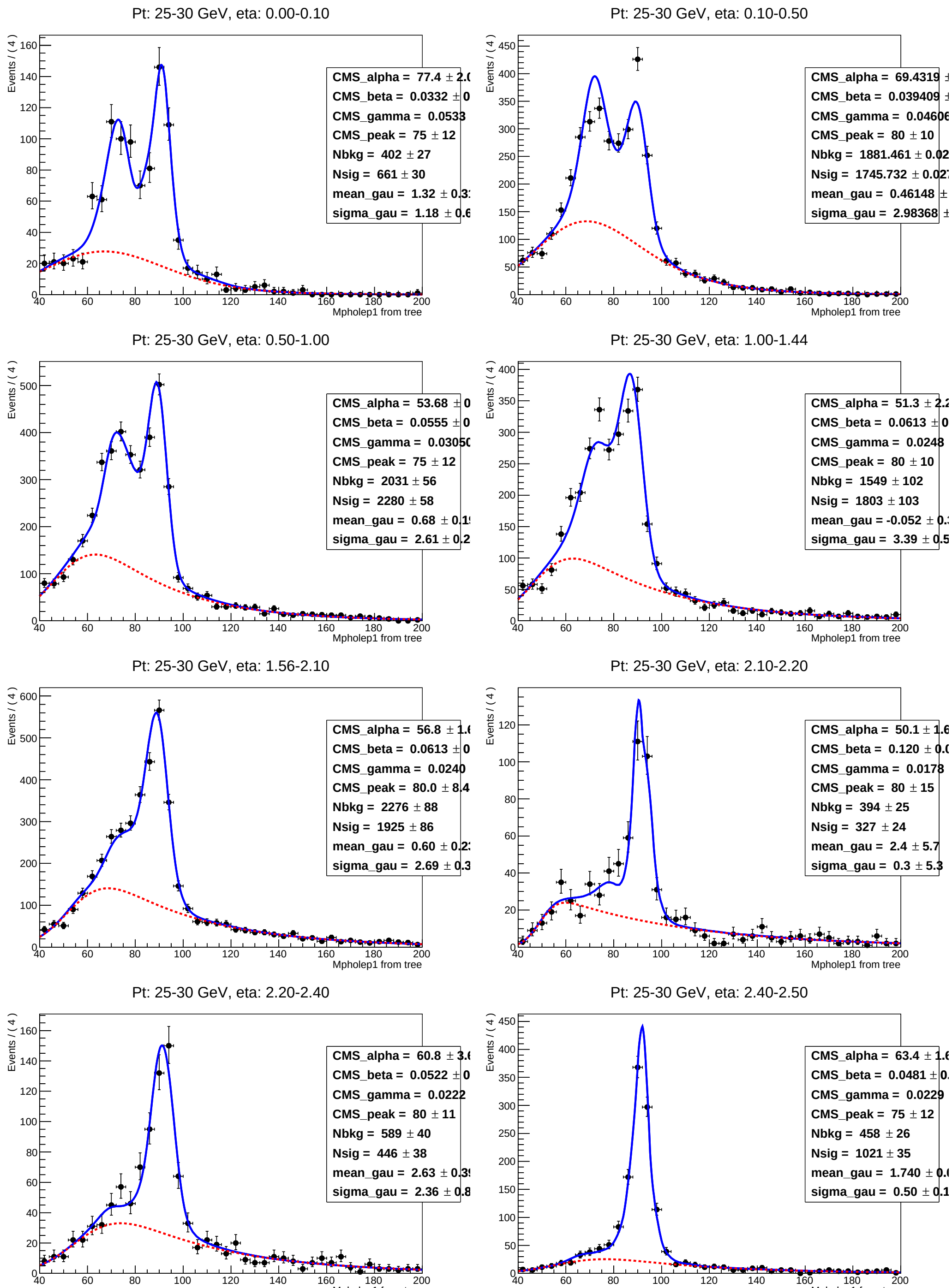

Figure F.3: $M_{e\gamma}$ fits, $W\gamma$, electron channel, 25-30 GeV, 8 η^{γ} bins.

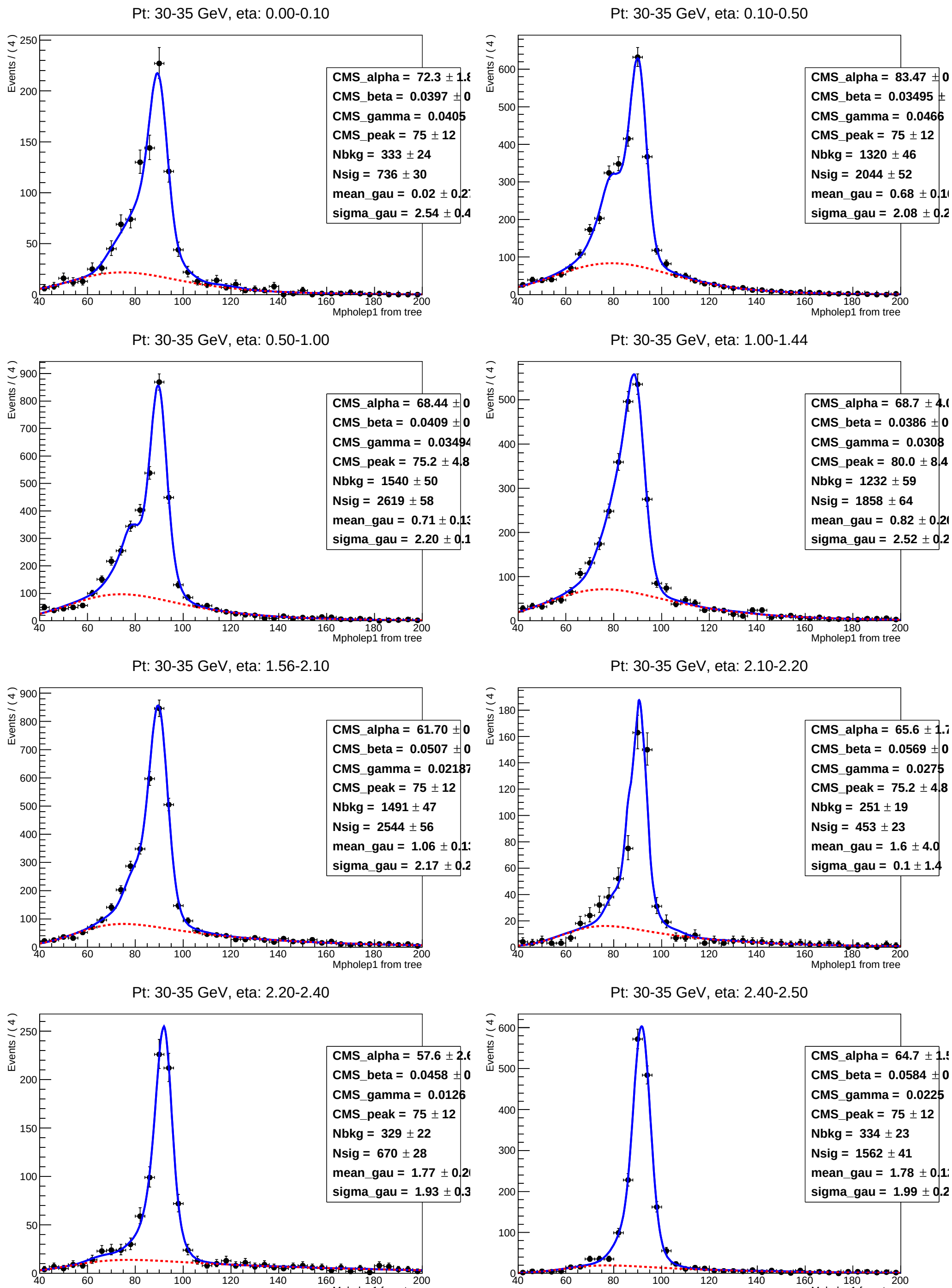

Figure F.4: $M_{e\gamma}$ fits, $W\gamma$, electron channel, 30-35 GeV, 8 η^{γ} bins.

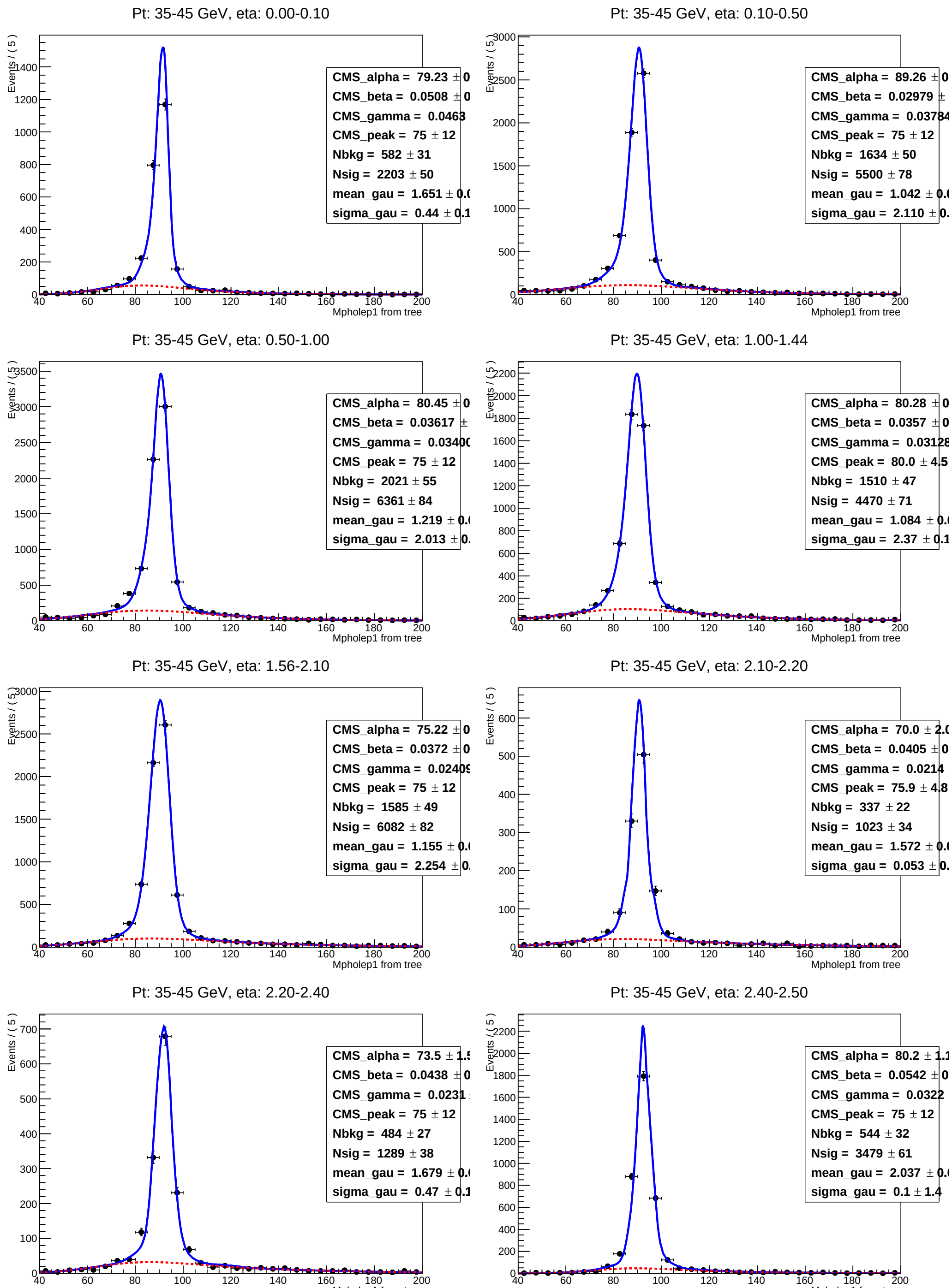

Figure F.5: $M_{e\gamma}$ fits, $W\gamma$, electron channel, 35-45 GeV, 8 η^{γ} bins.

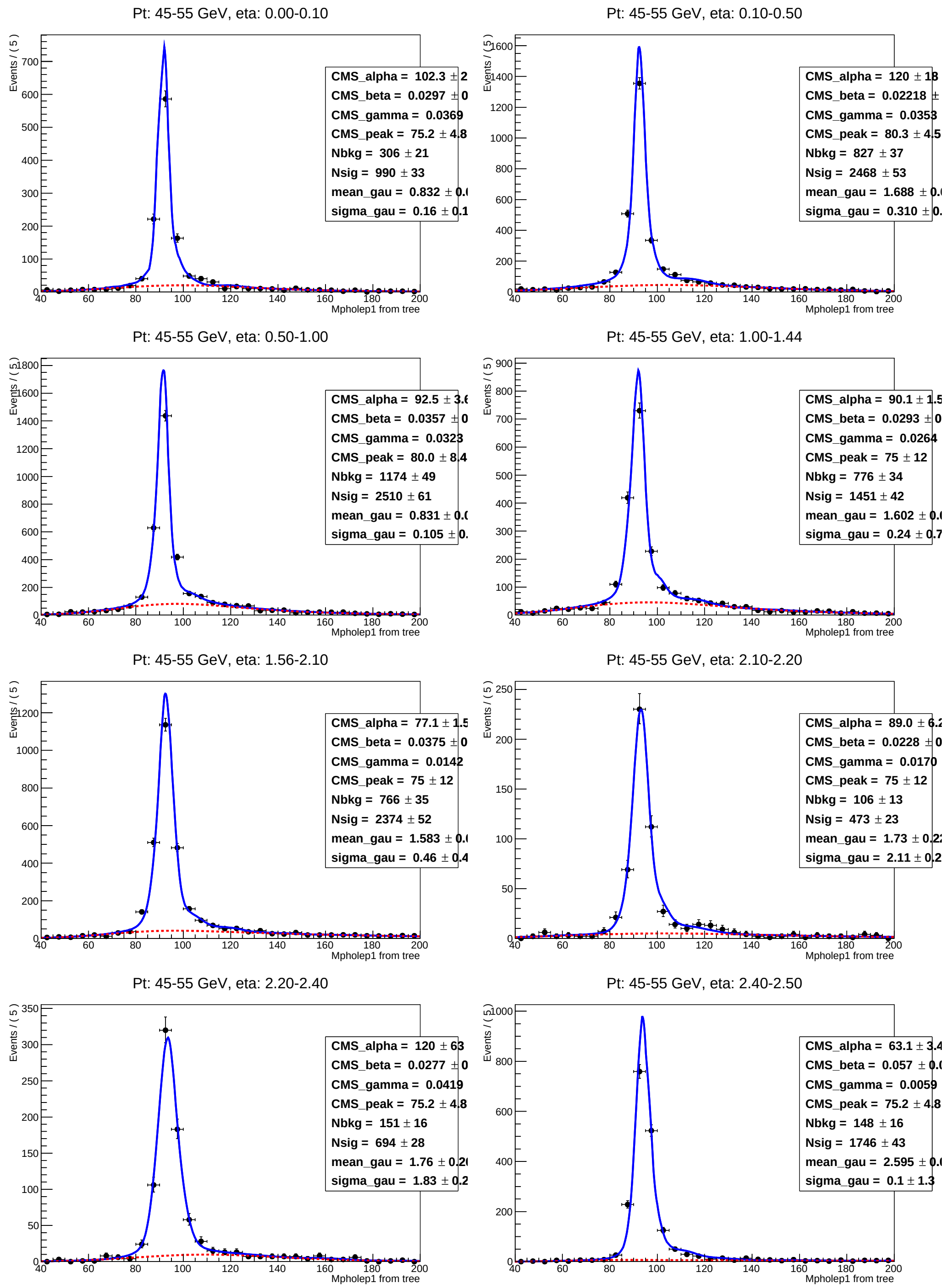

Figure F.6: $M_{e\gamma}$ fits, $W\gamma$, electron channel, 45-55 GeV, 8 η^{γ} bins.

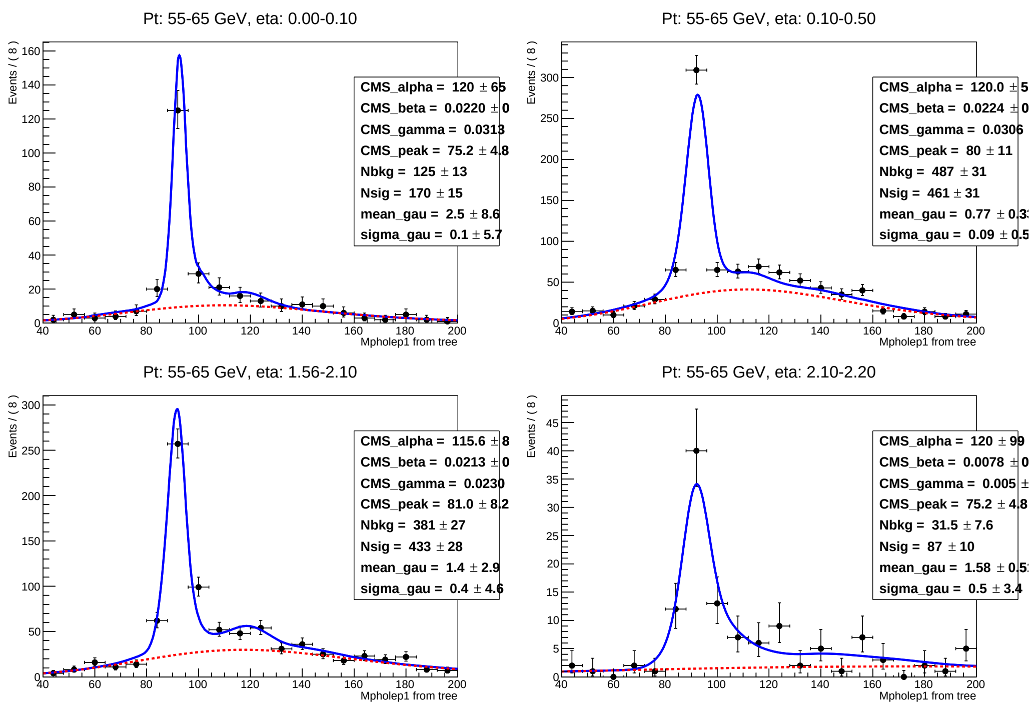

Figure F.7: $M_{e\gamma}$ fits, $W\gamma$, electron channel, 55-65 GeV, 4 η^{γ} bins.

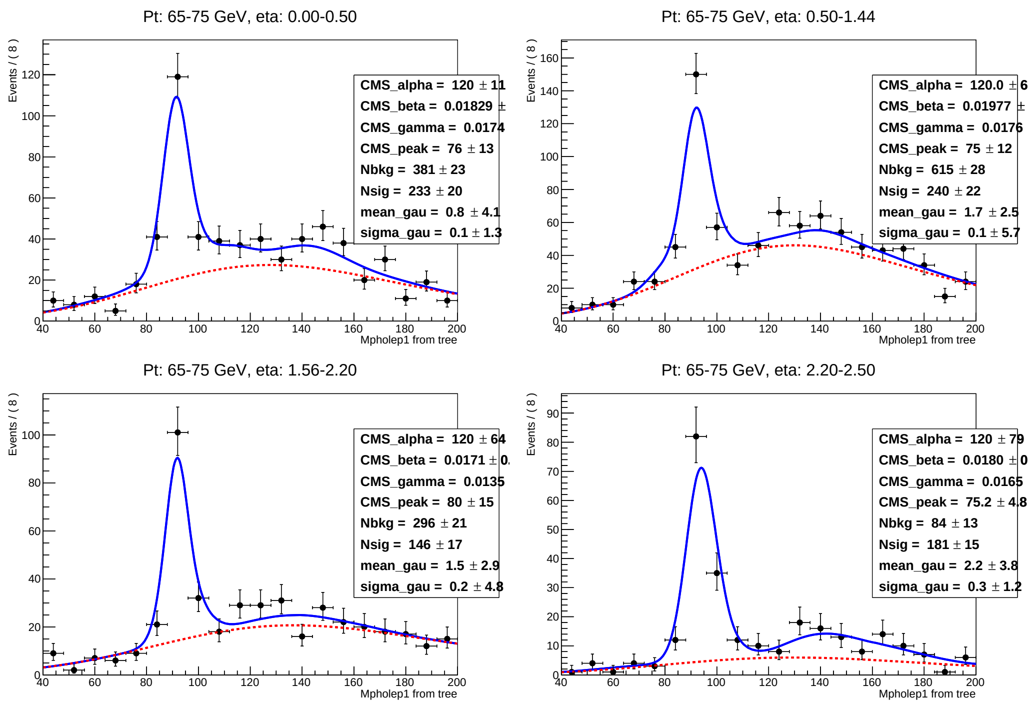

Figure F.8: $M_{e\gamma}$ fits, $W\gamma$, electron channel, 65-75 GeV, 4 η^{γ} bins.

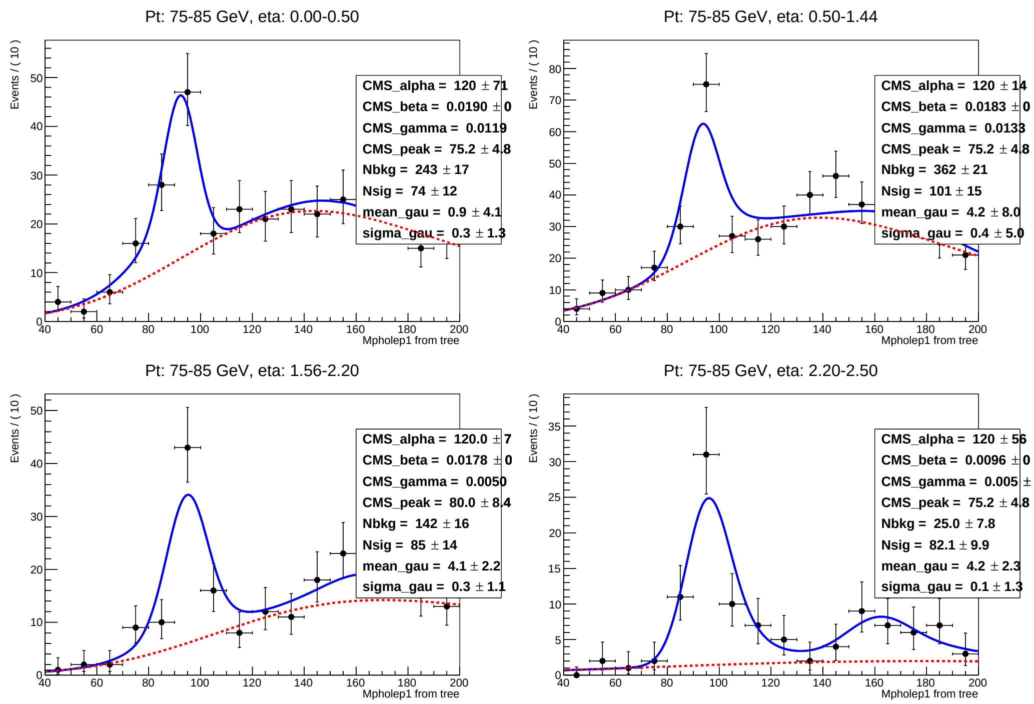

Figure F.9: $M_{e\gamma}$ fits, $W\gamma$, electron channel, 75-85 GeV, 4 η^{γ} bins.

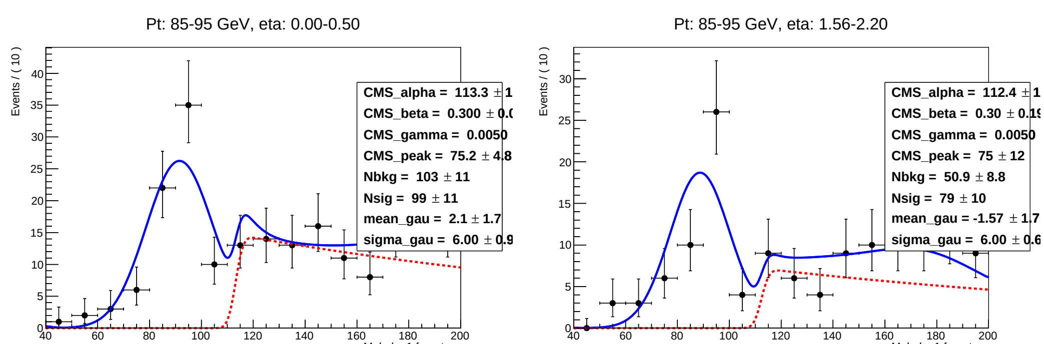

Figure F.10: $M_{e\gamma}$ fits, $W\gamma$, electron channel, 85-95 GeV, 2 η^{γ} bins.

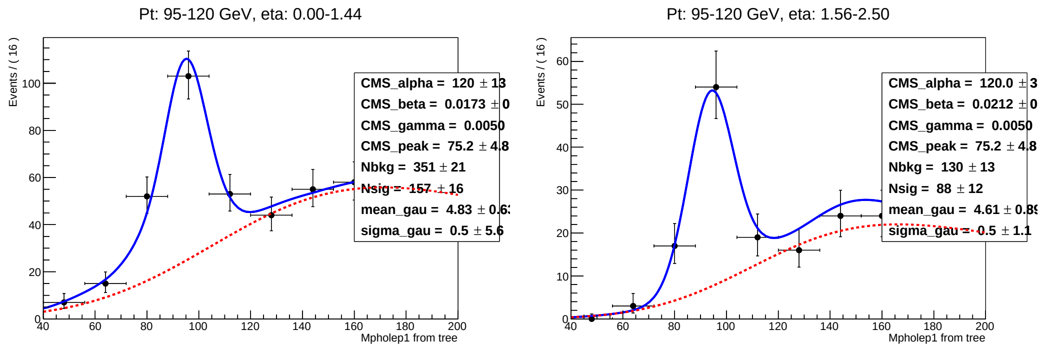

Figure F.11: $M_{e\gamma}$ fits, $W\gamma$, electron channel, 95-120 GeV, 2 η^{γ} bins.

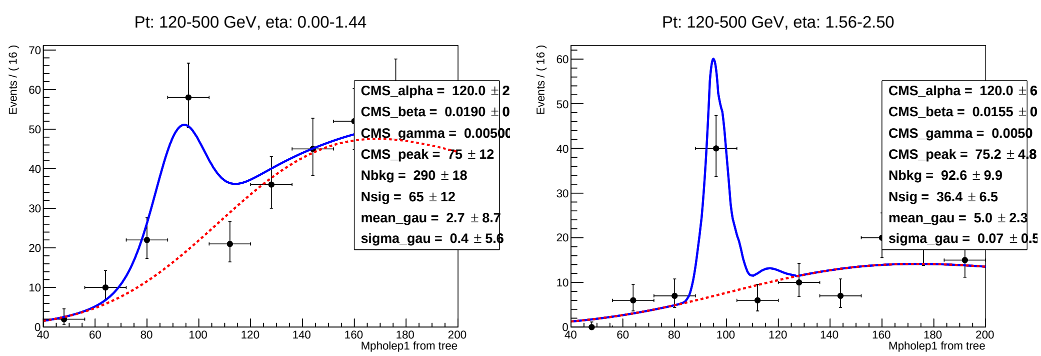

Figure F.12: $M_{e\gamma}$ fits, $W\gamma$, electron channel, 120-500 GeV, 2 η^{γ} bins.

G Tables for $e \to \gamma$ Background Estimation

This appendix presents results of $e \to \gamma$ background estimation. Tab. G.1 show results of $e \to \gamma$ background estimation when fits are performed on data with all selection criteria applied except Z-mass window requirement. These results are used for background subtraction. Table G.2 show results of $e \to \gamma$ background estimation when fits are performed on data without an M_T^W requirement. These results are used for the estimation of the systematic uncertainties.

In each table, the first column is a P_T^γ bin, the second column is yields of weighted DY+jets MC in conditions of full nominal selection, the third column is yields of $e \to \gamma$-enriched dataset with or without M_T^W requirement. These yields are extracted from a fit. The fourth column is yields of weighted DY+jets MC is conditions of $e \to \gamma$-enriched selection with or without M_T^W requirement, consistently with the dataset. The fifth column is the scale which is computed as the yield in the third column divided over the yield in the fourth column. The sixth column is the estimated $e \to \gamma$ background in the nominally selected dataset. The value is computed as the yield in the second column multiplied by the scale. The values in the sixth column as used for the background subtraction (Tab. G.1) or estimation fo the systematic uncertainty (Tab. G.2). The seventh column is yields of the weighted signal MC ($W\gamma \to e\nu\gamma$) in the nominally selected conditions, it is quoted for comparison purposes, to estimate how significant is $e \to \gamma$ background compared to the signal.

Table G.1: Results of the $e \to \gamma$ background estimation with fits performed after the M_T^W requirement was applied.

P_T^γ, GeV	DY+jets nom. sel.	Data $e \to \gamma$ enr.	DY+jets $e \to \gamma$ enr.	scale	$e \to \gamma$ yield	SigMC ($W\gamma \to e\nu\gamma$)
candidates with photons in EB						
15-20	1917±63	6395±149	3300±83	1.94±0.0667	3715±177	5857±110
20-25	1175±49	5141±235	2987±79	1.72±0.091	2023±137	2868±77
25-30	543±33	6489±122	3418±84	1.9±0.0591	1030±71	1411±54
30-35	166±18	7257±105	4215±94	1.72±0.0461	286±33	915±43
35-45	134±16	18534±144	11597±158	1.6±0.0251	215±27	1247±51
45-55	186±20	7417±97	4134±94	1.79±0.0473	335±37	820±41
55-65	130±16	1426±48	685±38	2.08±0.136	272±39	654±37
65-75	86±13	473±29	286±24	1.65±0.177	143±27	440±30
75-85	42±9	174±19	165±19	1.05±0.168	45±12	295±25
85-95	20±6	140±14	66±12	2.1±0.445	42±16	234±22
95-120	38±9	156±16	94±14	1.65±0.307	63±19	318±26
120-500	36±9	64±11	67±12	0.957±0.246	34±12	429±30
candidates with photons in EE						
15-20	458±31	2004±159	1805±61	1.11±0.096	508±55	2253±68
20-25	402±29	2613±77	2432±72	1.07±0.0451	432±36	1177±49
25-30	216±21	3719±102	3527±85	1.05±0.0388	228±23	574±34
30-35	123±16	5228±78	5374±109	0.973±0.0247	120±16	445±31
35-45	173±19	11873±114	12355±164	0.961±0.0158	166±18	638±37
45-55	223±21	5286±75	4212±94	1.25±0.0334	280±28	287±24
55-65	182±19	1010±38	813±41	1.24±0.0787	226±28	237±22
65-75	82±13	327±22	299±25	1.09±0.121	89±17	194±21
75-85	68±13	167±17	184±21	0.907±0.141	61±15	137±18
85-95	40±10	107±22	82±14	1.29±0.35	52±19	81±14
95-120	48±11	88±11	97±15	0.901±0.188	43±13	166±20
120-500	22±7	36±6	54±11	0.662±0.184	15±6	145±18

Table G.2: Results of the $e \to \gamma$ background estimation with fits performed before the M_T^W requirement was applied.

P_T^γ, GeV	DY+jets nom. sel.	Data $e \to \gamma$ enr.	DY+jets $e \to \gamma$ enr.	scale	$e \to \gamma$ yield	SigMC ($W\gamma \to e\nu\gamma$)
candidates with photons in EB						
15-20	1917±63	11771±321	7491±125	1.57±0.0503	3012±138	5857±110
20-25	1175±49	10162±201	6933±120	1.47±0.0387	1722±85	2868±77
25-30	543±33	12055±173	7526±125	1.6±0.0353	869±57	1411±54
30-35	166±18	15580±138	9753±144	1.6±0.0275	265±30	915±43
35-45	134±16	39220±218	27310±242	1.44±0.015	193±24	1247±51
45-55	186±20	16343±135	10411±149	1.57±0.0261	293±31	820±41
55-65	130±16	3256±65	1722±60	1.89±0.0765	247±33	654±37
65-75	86±13	938±39	600±36	1.56±0.115	135±23	440±30
75-85	42±9	405±24	274±24	1.48±0.162	63±16	295±25
85-95	20±6	156±19	125±16	1.25±0.226	25±9	234±22
95-120	38±9	189±18	155±18	1.22±0.188	46±13	318±26
120-500	36±9	96±13	89±14	1.08±0.226	38±12	429±30
candidates with photons in EE						
15-20	458±31	3798±158	4004±92	0.948±0.0452	434±35	2253±68
20-25	402±29	5631±103	5586±109	1.01±0.027	405±31	1177±49
25-30	216±21	8755±138	8528±132	1.03±0.0228	222±22	574±34
30-35	123±16	12865±120	13762±175	0.935±0.0148	115±15	445±31
35-45	173±19	29009±176	29847±254	0.972±0.0102	168±19	638±37
45-55	223±21	12339±114	10099±145	1.22±0.021	273±27	287±24
55-65	182±19	2012±50	1700±59	1.18±0.0511	215±25	237±22
65-75	82±13	646±32	606±36	1.07±0.0842	87±16	194±21
75-85	68±13	260±19	316±28	0.823±0.0957	56±12	137±18
85-95	40±10	139±15	148±19	0.944±0.16	38±11	81±14
95-120	48±11	115±13	185±21	0.626±0.104	30±8	166±20
120-500	22±7	54±8	85±14	0.632±0.149	14±5	145±18

H MC Closure Check

This Appendix contains the results of the two MC-based closure cross checks discussed in Ch. 5.4.5. The results of the MC closure check with the pseudodata prepared by mixing $W\gamma$ and W+jets samples are shown in Fig. H.1-H.2. The results of the MC realistic check with the pseudodata prepared by mixing several MC samples, are shown in Fig. H.3-H.6.

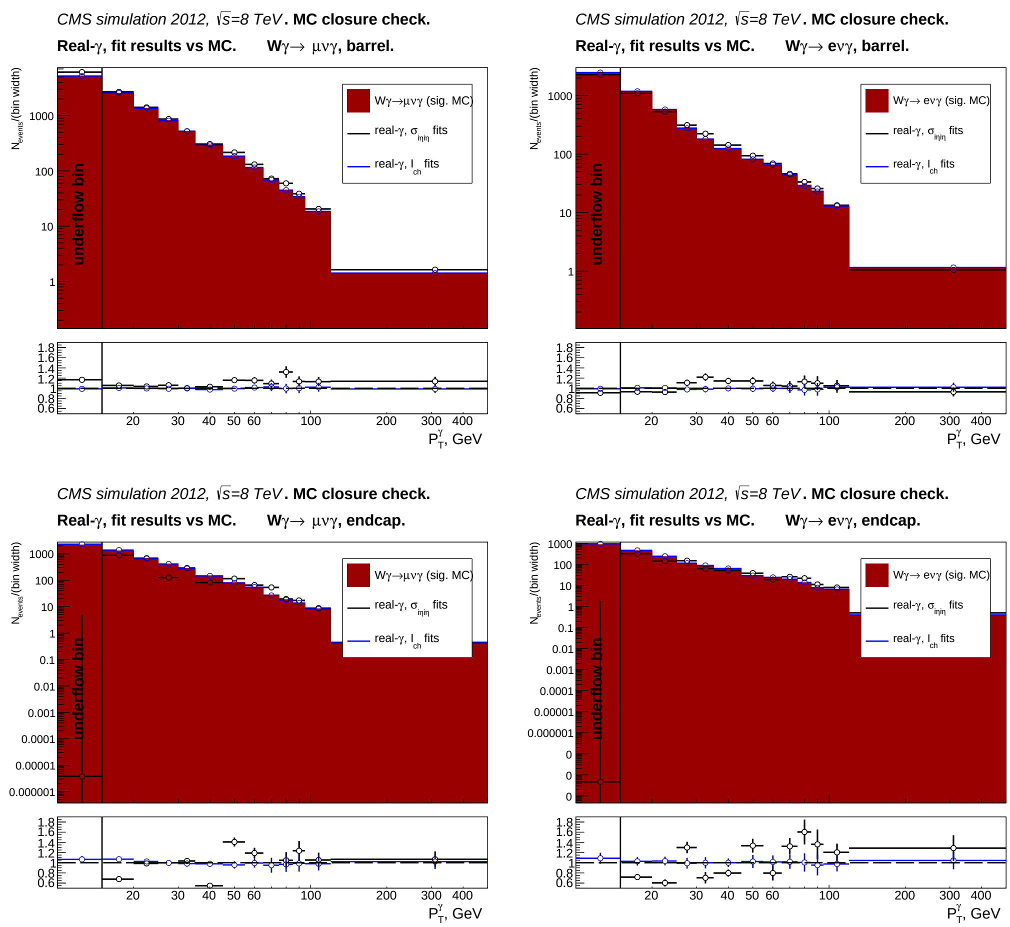

Figure H.1: Real-γ yields derived from fits of pseudodata superimposed with $W\gamma$ MC in the muon (left) and electron (right) channels. Top to bottom: barrel and endcap photons.

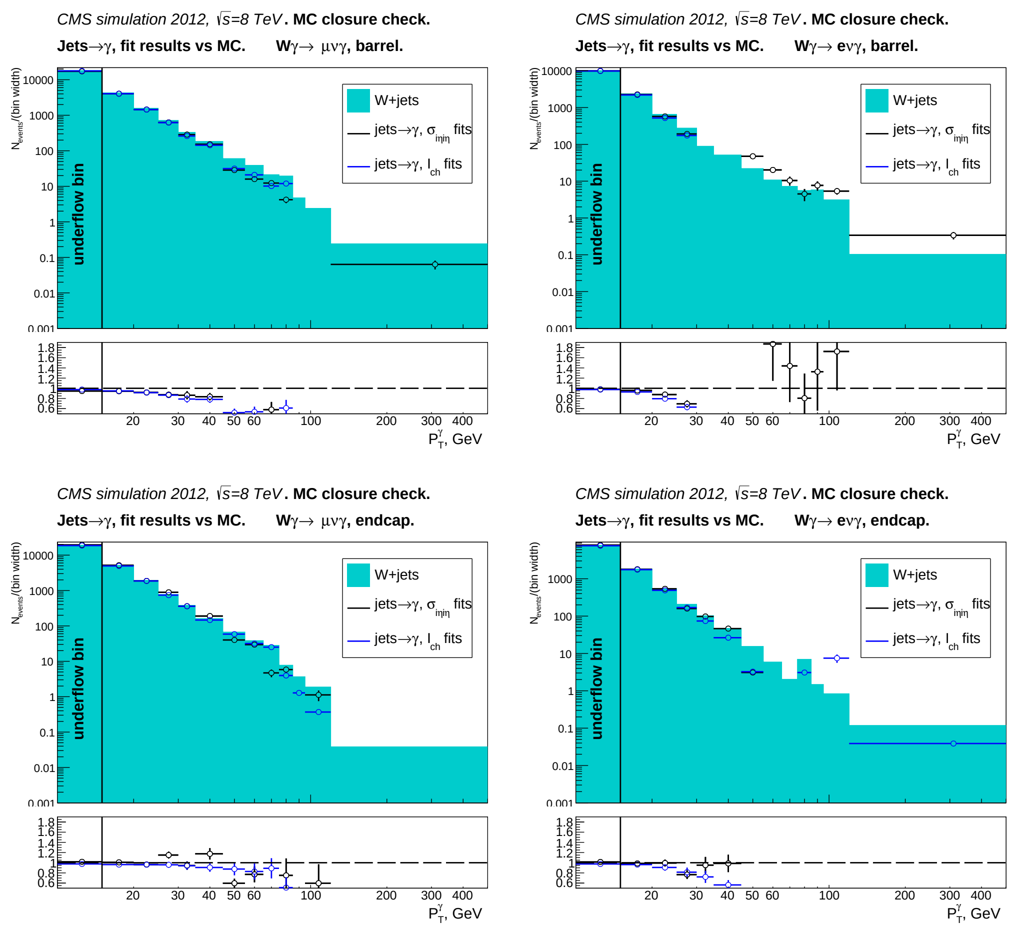

Figure H.2: *W*+jets yields derived from fits of pseudodata superimposed with *W*+jets MC in the muon (left) and electron (right) channels. Top to bottom: barrel and endcap photons.

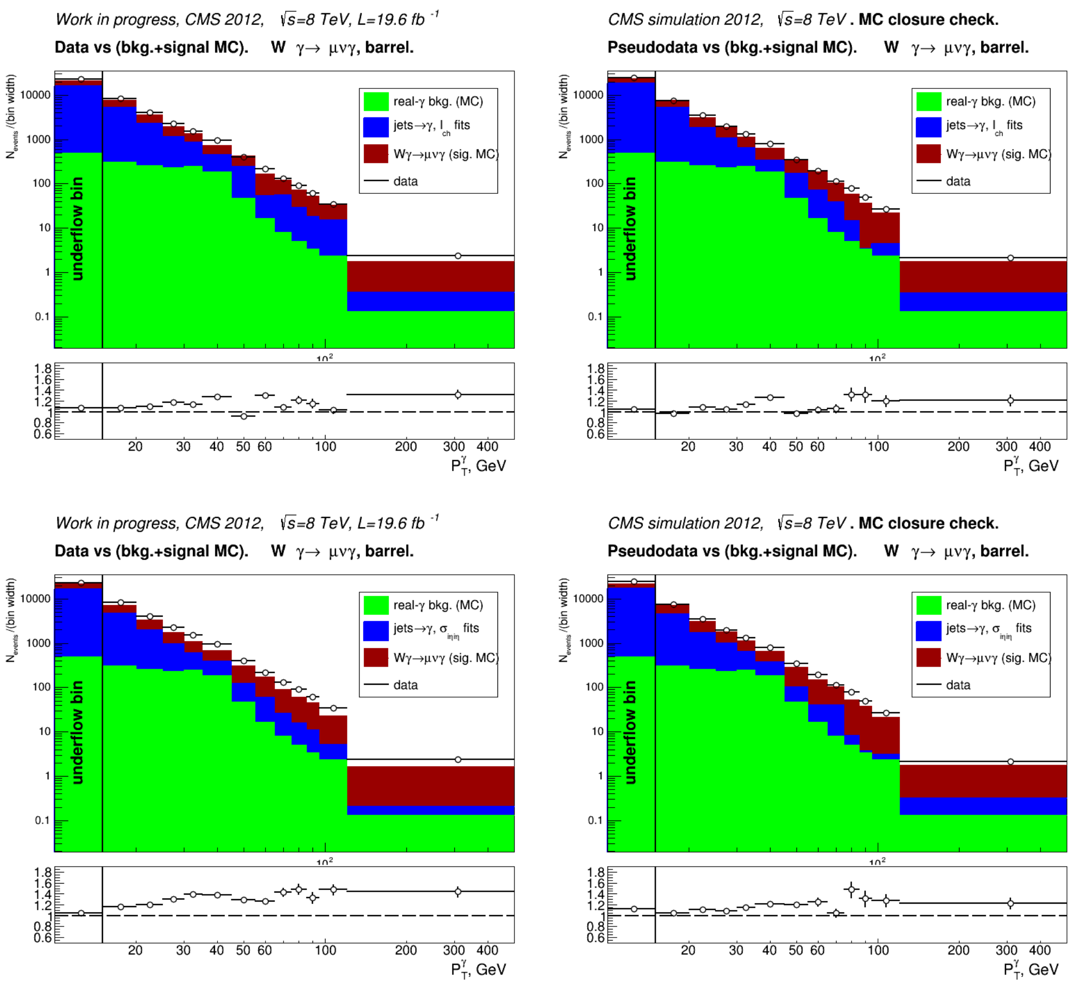

Figure H.3: Data (left) and pseudodata (right) vs background estimates and signal MC in bins of P_T^{γ} in the muon channel. Jets→ γ background estimated from fits of I_{ch}^{γ} (top) and $\sigma_{i\eta i\eta}^{\gamma}$ (bottom). Barrel photons.

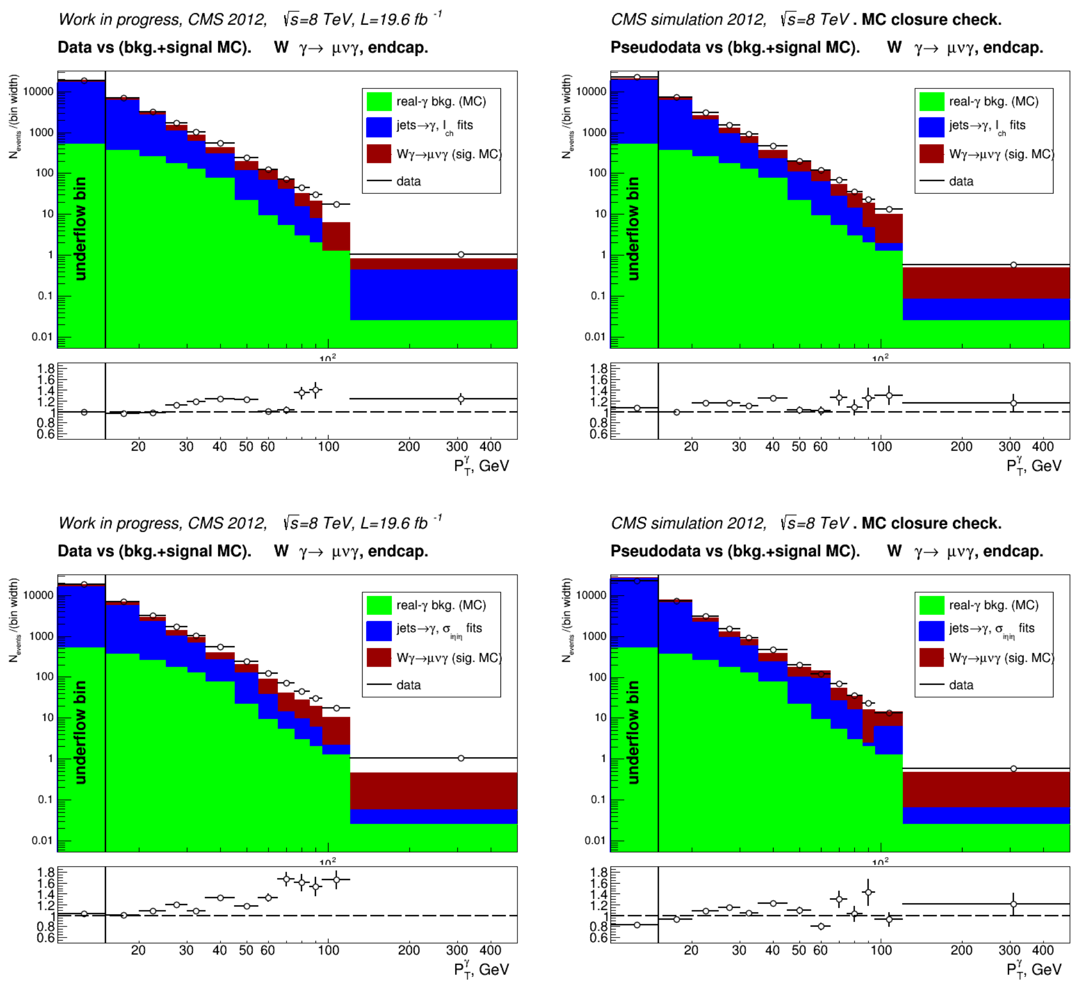

Figure H.4: Data (left) and pseudodata (right) vs background estimates and signal MC in bins of P_T^γ in the muon channel. Jets→ γ background estimated from fits of I_{ch}^γ (middle) and $\sigma_{i\eta i\eta}^\gamma$ (bottom). Endcap photons.

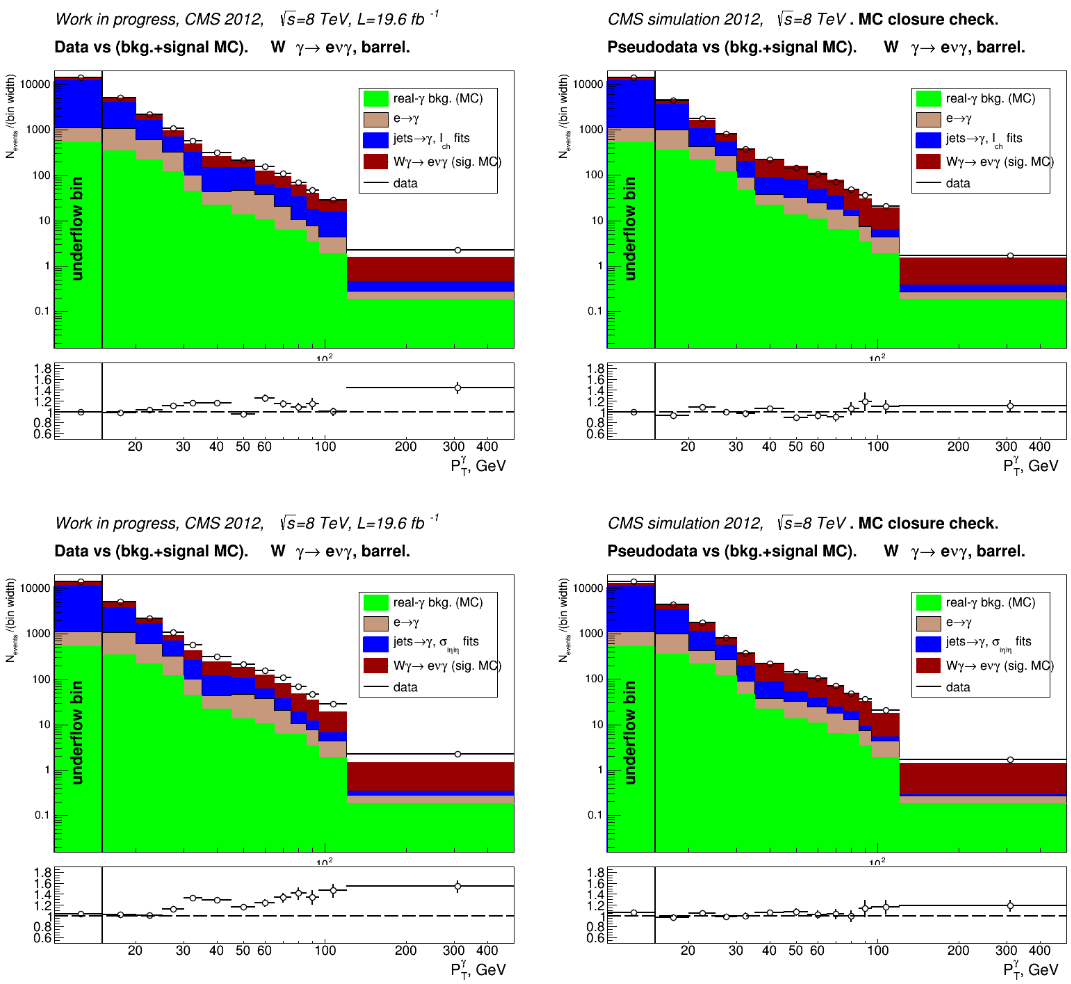

Figure H.5: Data (left) and pseudodata (right) vs background estimates and signal MC in bins of P_T^{γ} in the electron channel. Jets$\rightarrow \gamma$ background estimated from fits of I_{ch}^{γ} (middle) and $\sigma_{i\eta i\eta}^{\gamma}$ (bottom). Barrel photons.

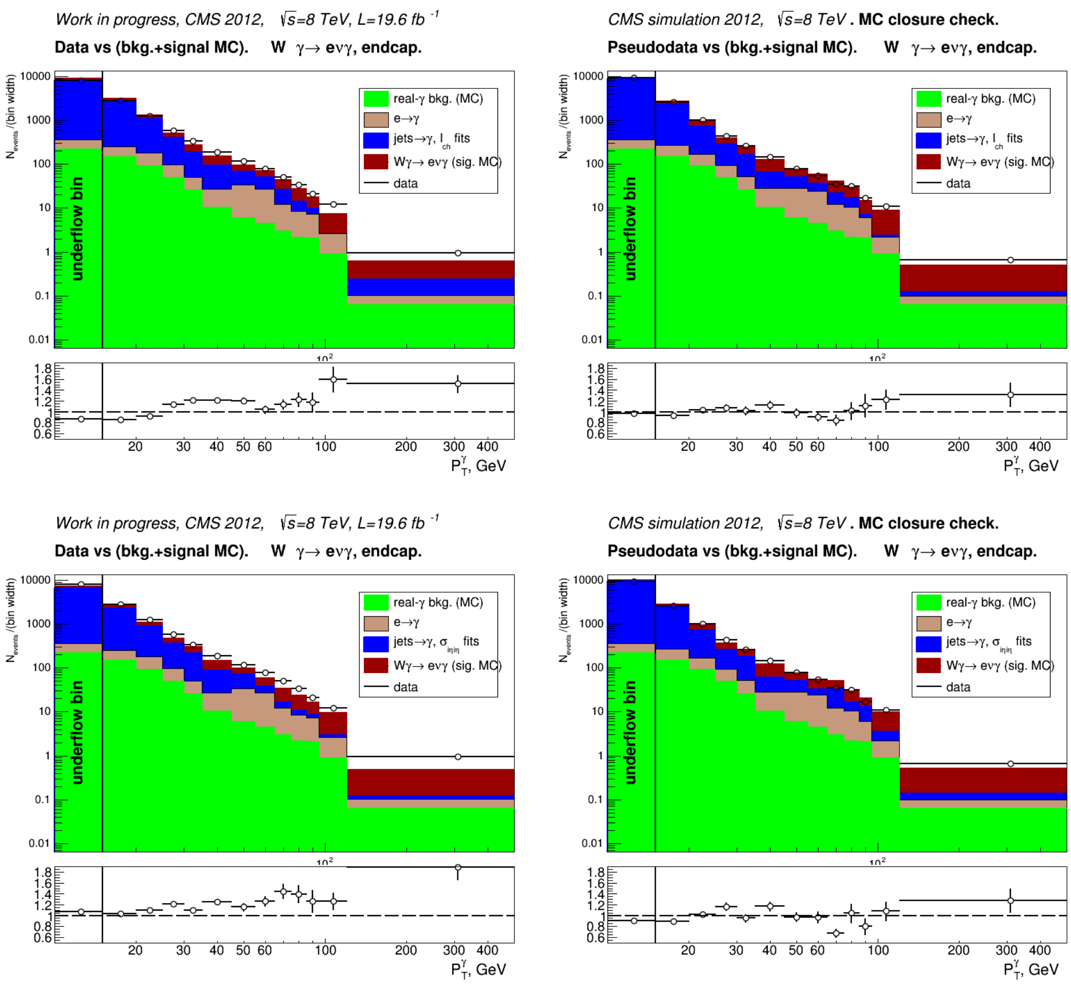

Figure H.6: Data (left) and pseudodata (right) vs background estimates and signal MC in bins of P_T^{γ} in the electron channel. Jets$\rightarrow \gamma$ background estimated from fits of I_{ch}^{γ} (middle) and $\sigma_{i\eta i\eta}^{\gamma}$ (bottom). Endcap photons.

I Correlation Matrices for Different Sources of the Systematic Uncertainties

When an uncertainty is propagated through unfolding, the uncertainties on the unfolded yields become correlated. This appendix contain correlation matrices for all sources of the systematic uncertainties that were, at first, estimated on pre-unfolded yields, and then propagated through unfolding. Plot captions explain the uncertainty sources.

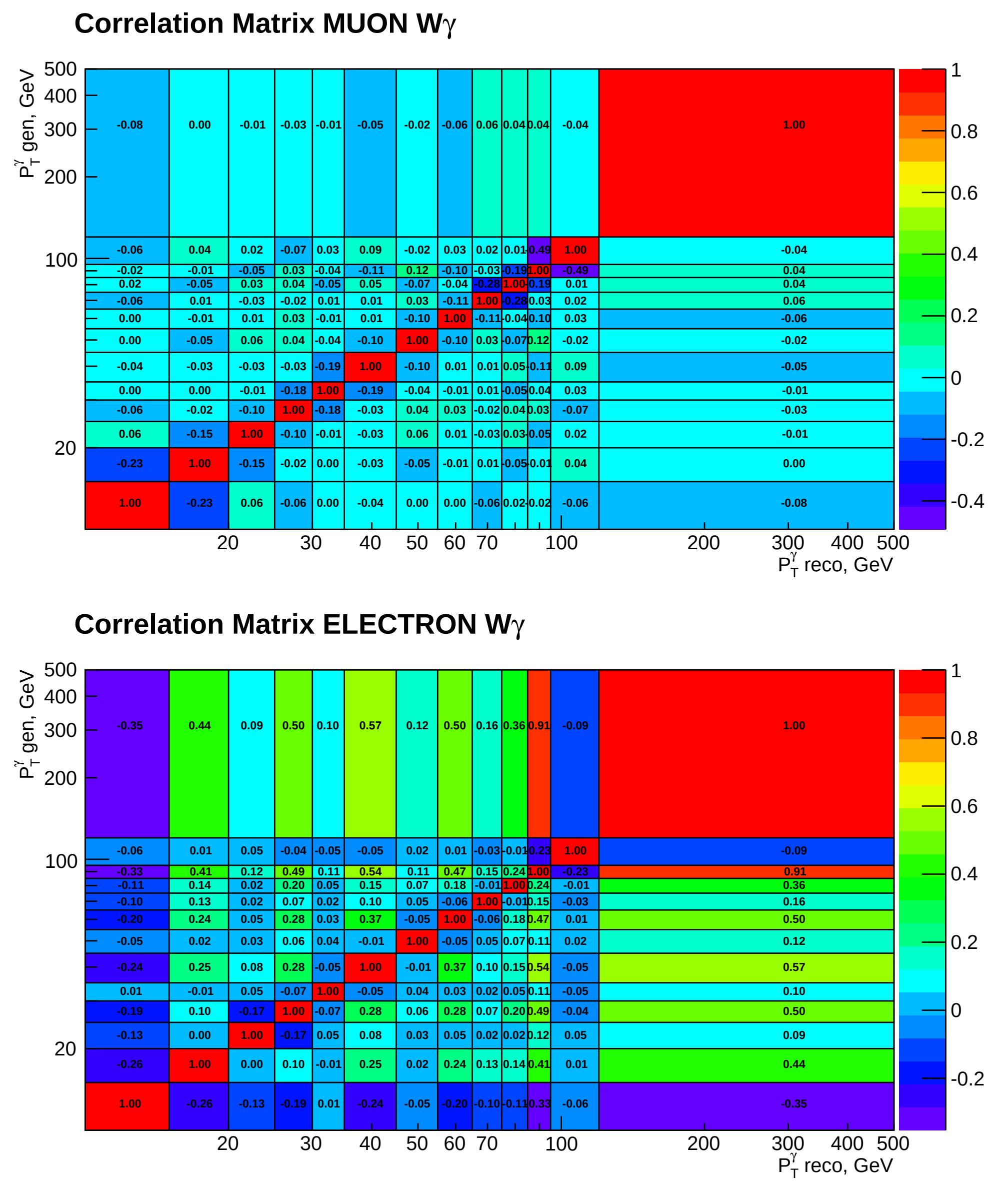

Figure I.1: Correlation Matrices for systematic error due to the difference between I_{ch}^{γ} and $\sigma_{i\eta i\eta}^{\gamma}$ fit results.

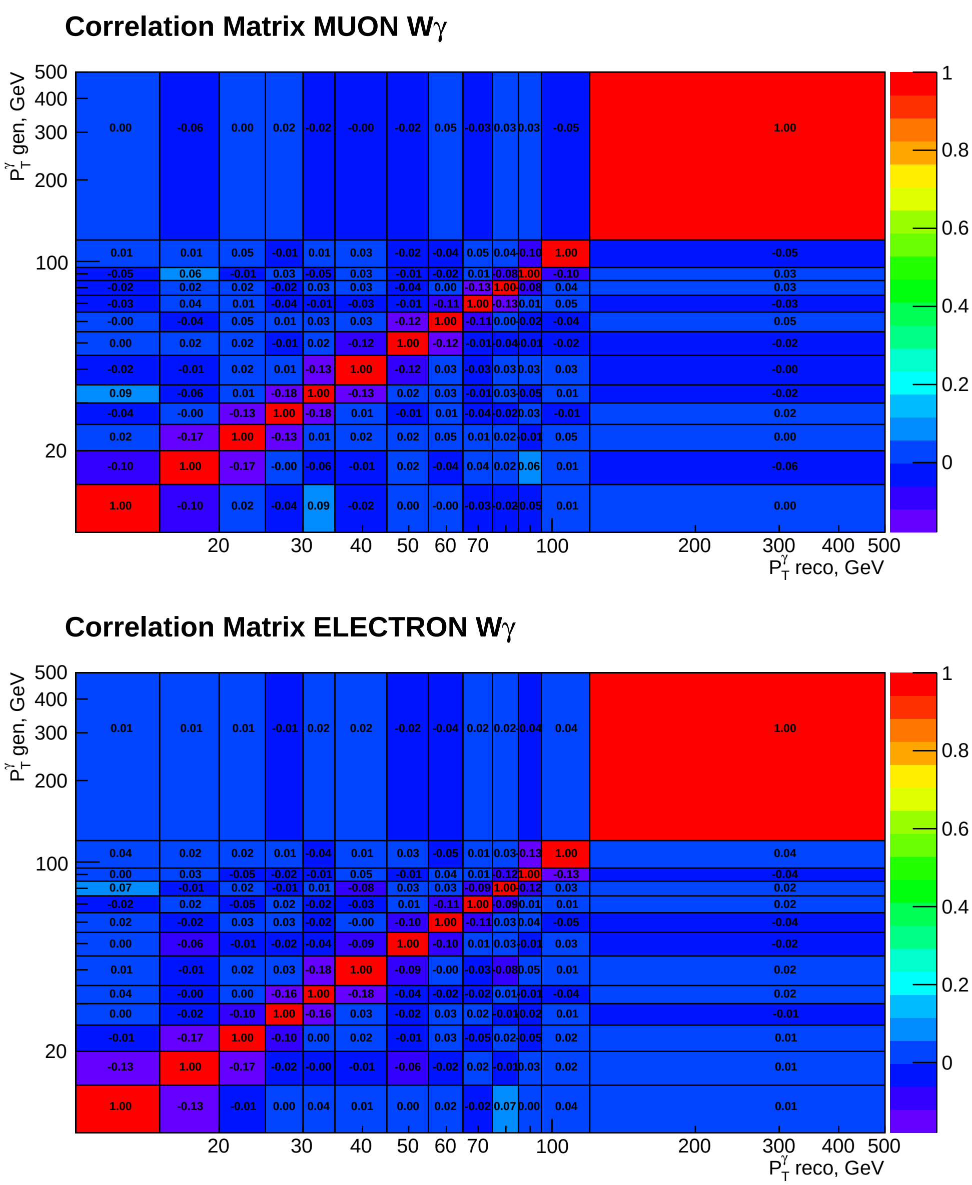

Figure I.2: Correlation Matrices for systematic error due to uncertainty on the $Z\gamma$ MC sample normalization.

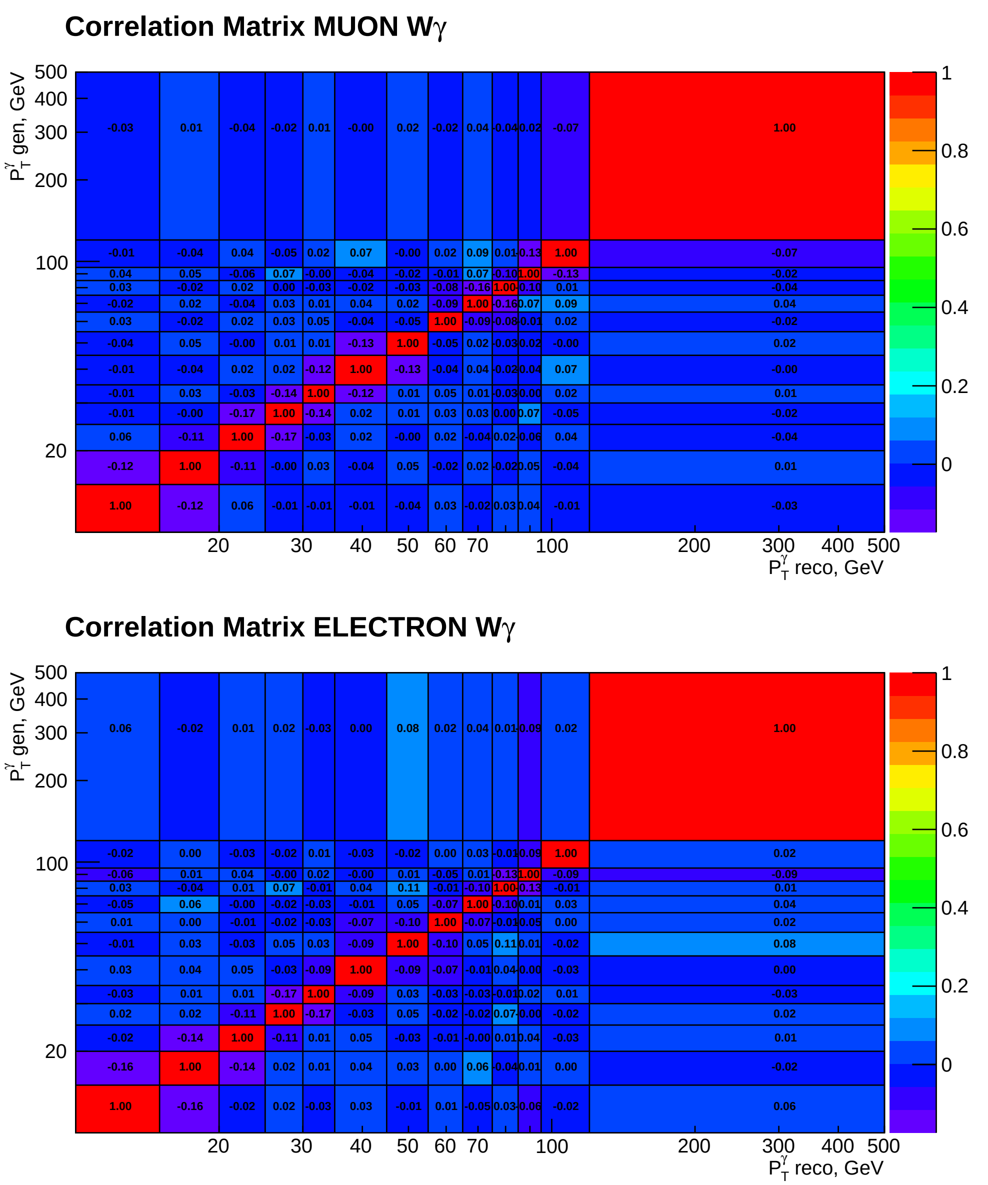

Figure I.3: Correlation Matrices for systematic error due to the template statistical power.

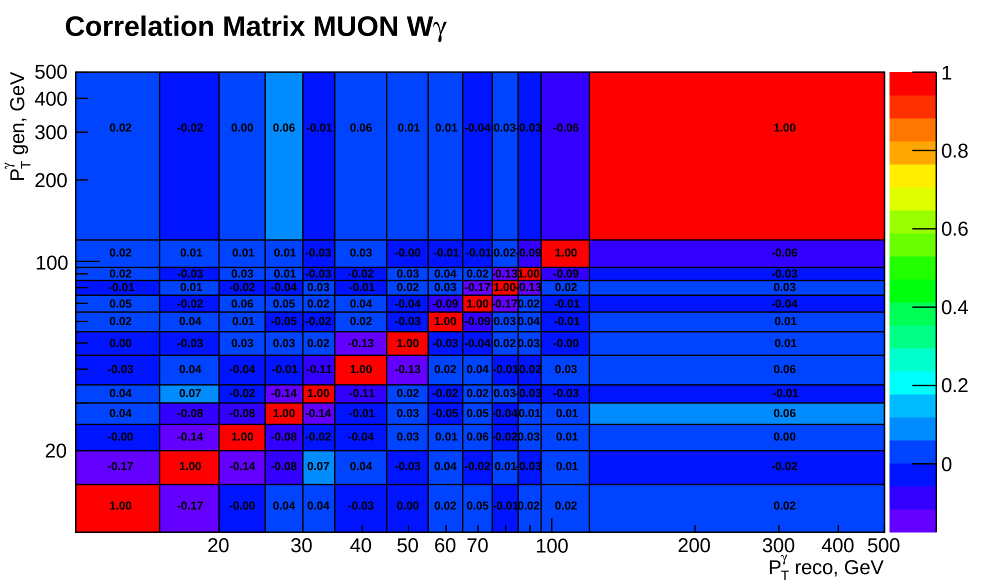

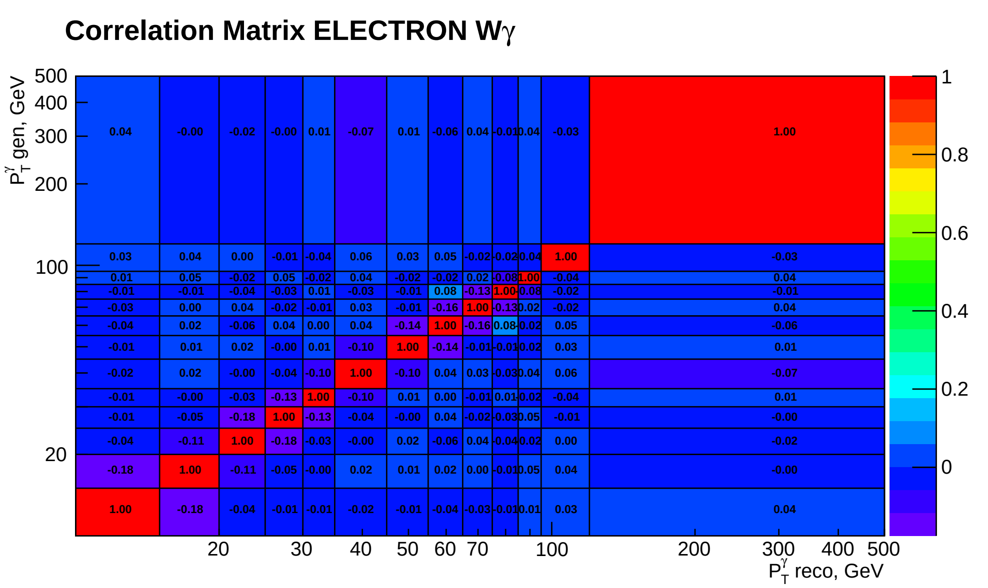

Figure I.4: Correlation Matrices for systematic error due to real-γ background subtraction.

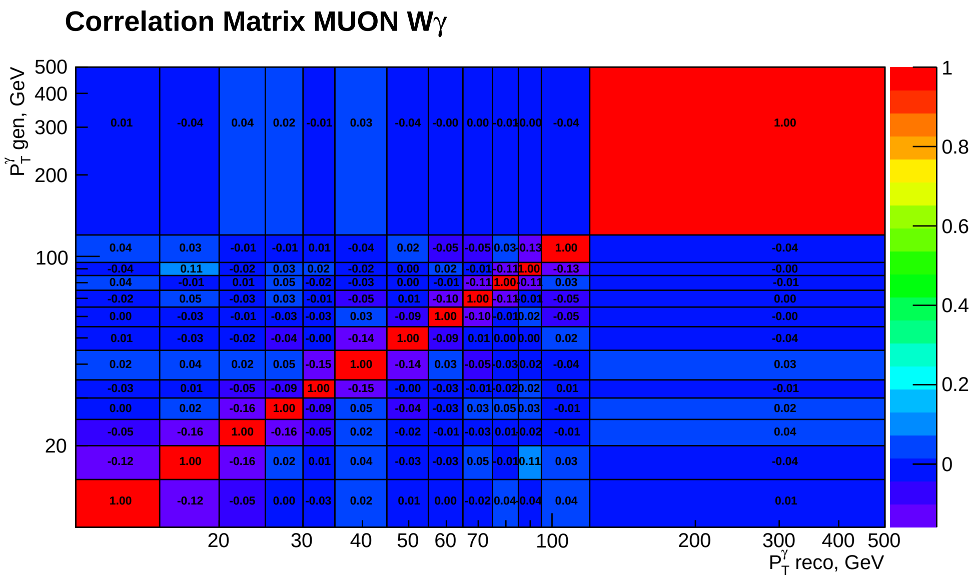

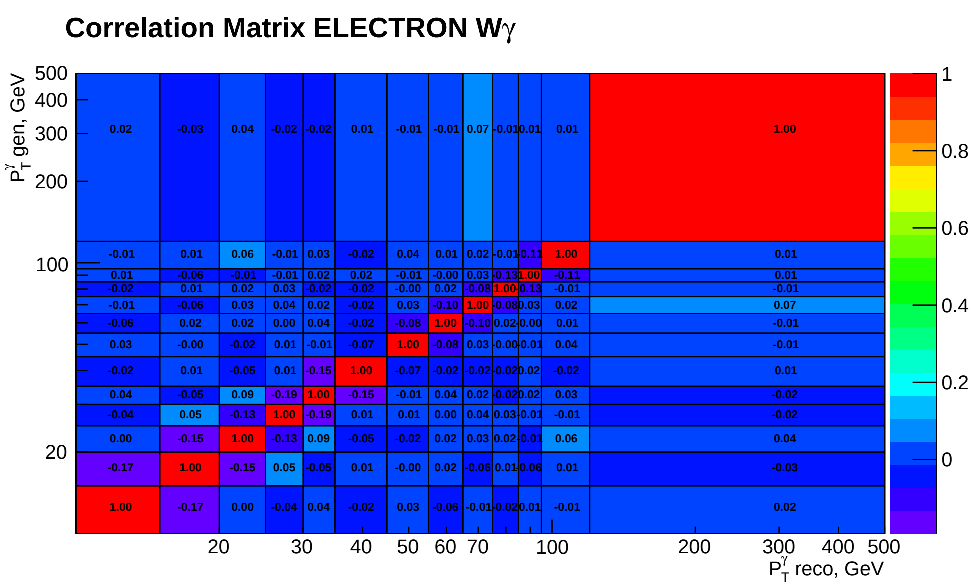

Figure I.5: Correlation Matrices for systematic error due to signal MC statistics for unfolding.

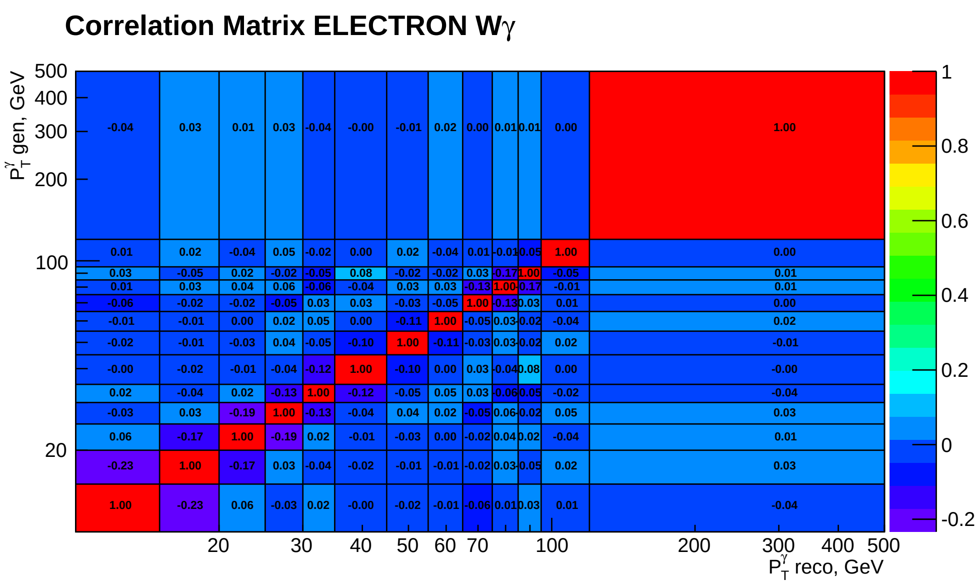

Figure I.6: Correlation Matrix for systematic error due to statistics of different samples for $e \to \gamma$ background estimation.

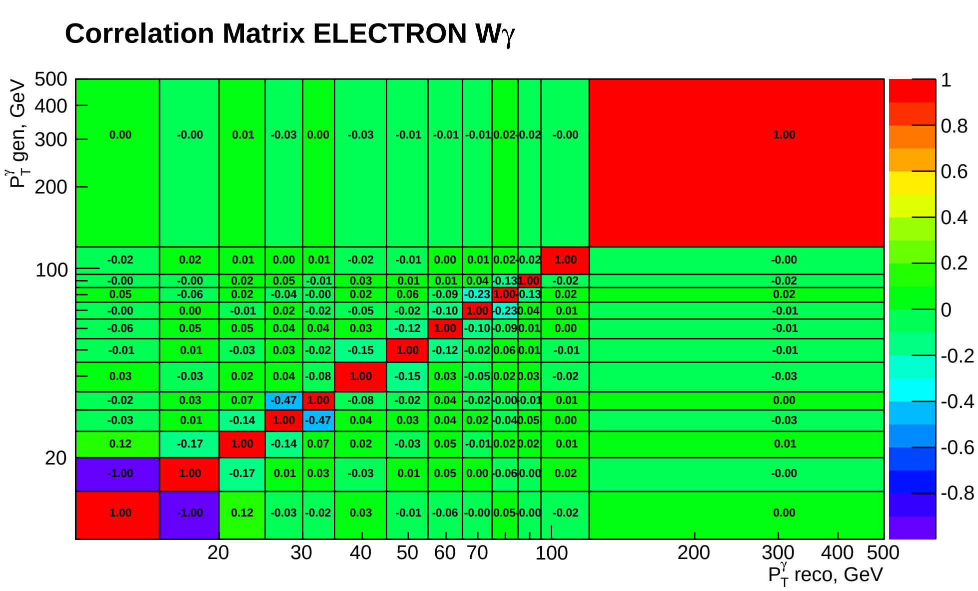

Figure I.7: Correlation Matrix for systematic error due to fit bias for $e \to \gamma$ background estimation.

J Fit Plots of $M_{e\gamma}$ without Requirement on M_T^W

This appendix provides fit plots of the electron-photon invariant mass $M_{e\gamma}$ of $W\gamma \rightarrow ee\gamma$-selected data prior to M_T^W and $M_{e\gamma}$ requirements being applied. These fit results are used for the estimation of the systematic uncertainty related to possible bias in fit machinery and template shapes in the procedure of the $e \rightarrow \gamma$ background estimation in the electron channel. The procedure of the background estimation is described in Ch. 5.4.2, the procedure of the estimation of the systematic uncertainty is described in Ch. 5.7.2.

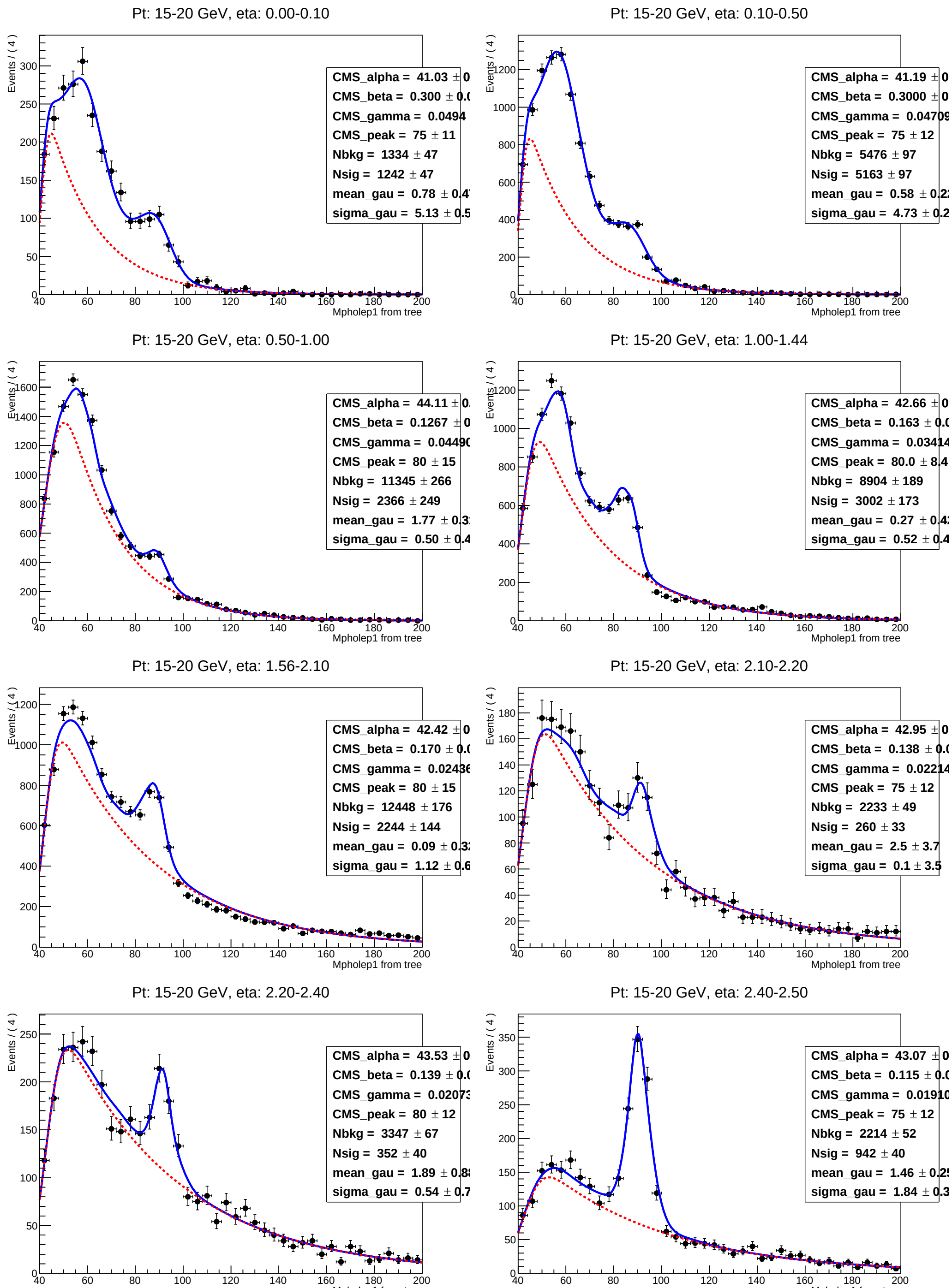

Figure J.1: $M_{e\gamma}$ fits, $W\gamma$, electron channel, underflow bin (15-20 GeV), 8 η^{γ} bins.

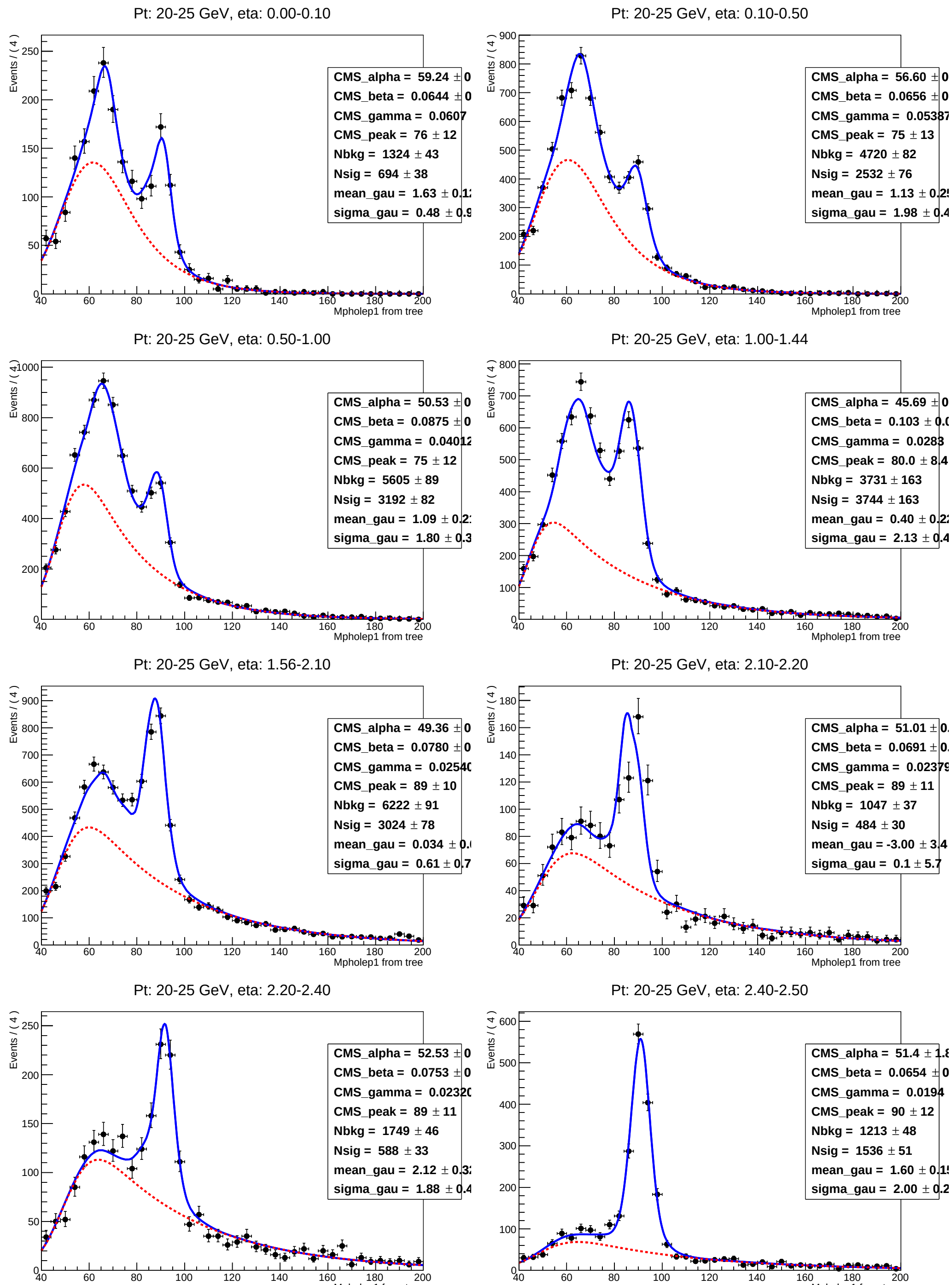

Figure J.2: $M_{e\gamma}$ fits, $W\gamma$, electron channel, underflow bin (20-25 GeV), 8 η^{γ} bins.

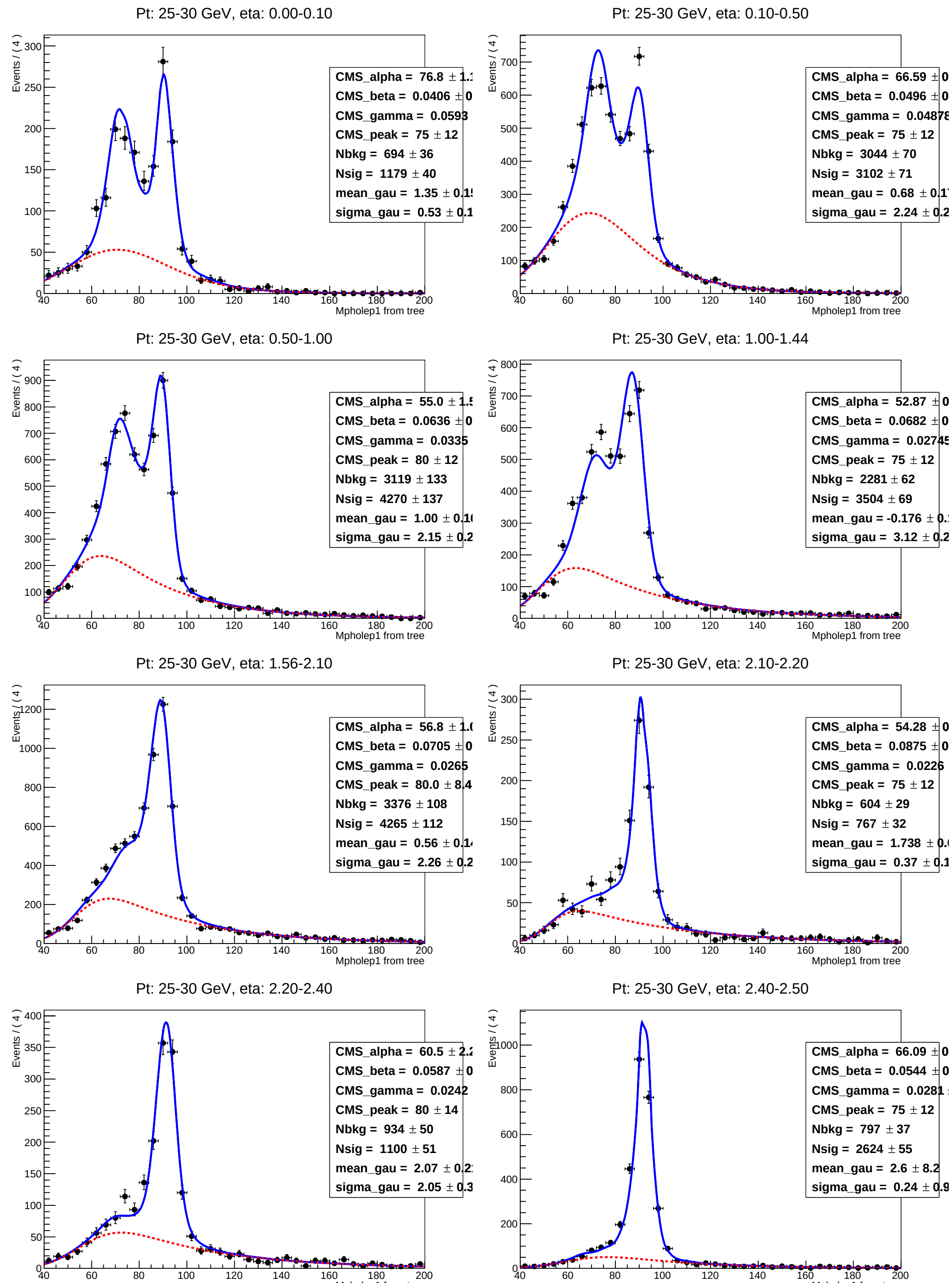

Figure J.3: $M_{e\gamma}$ fits, $W\gamma$, electron channel, underflow bin (25-30 GeV), 8 η^{γ} bins.

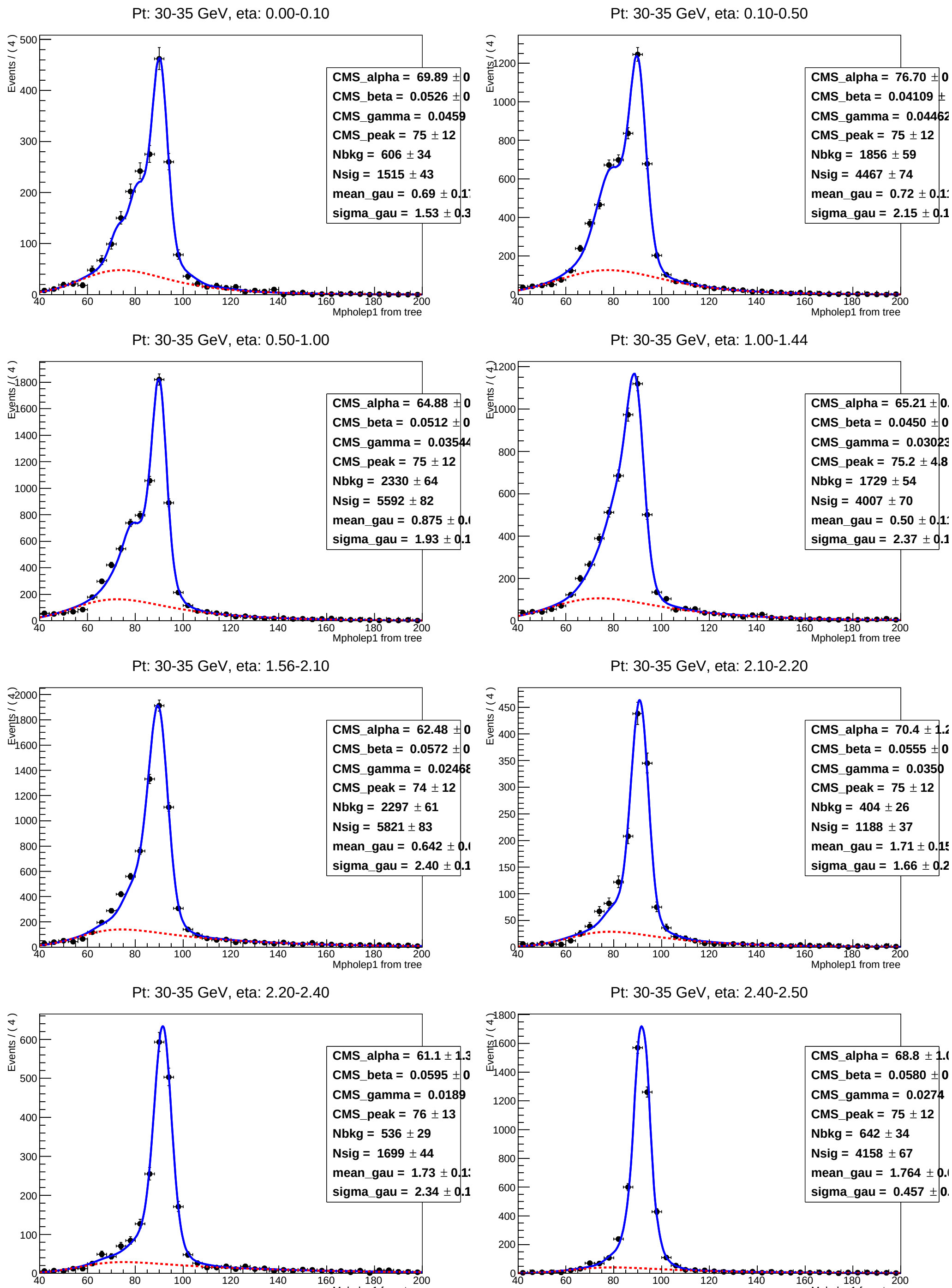

Figure J.4: $M_{e\gamma}$ fits, $W\gamma$, electron channel, underflow bin (30-35 GeV), 8 η^{γ} bins.

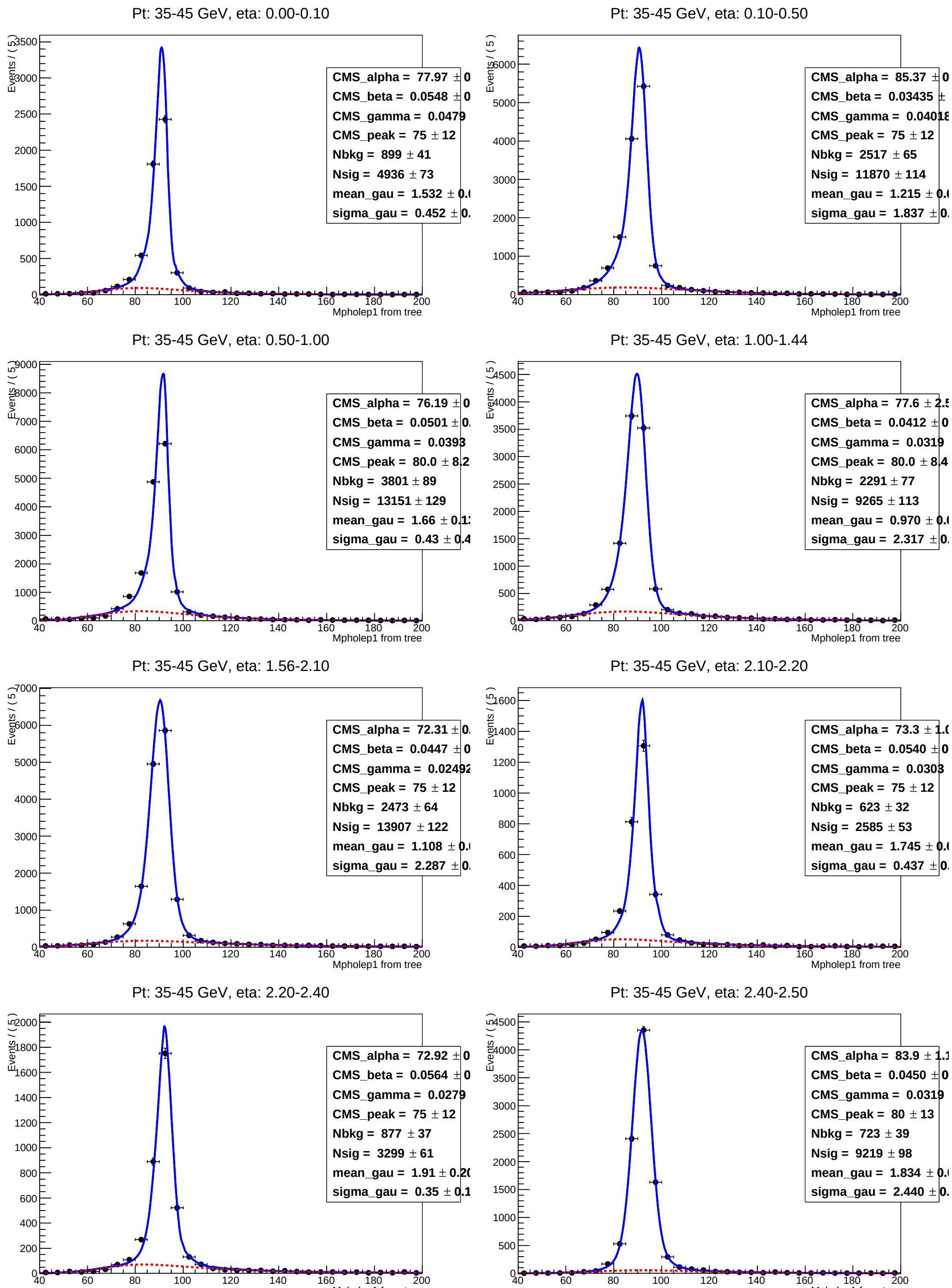

Figure J.5: $M_{e\gamma}$ fits, $W\gamma$, electron channel, underflow bin (35-45 GeV), 8 η^{γ} bins.

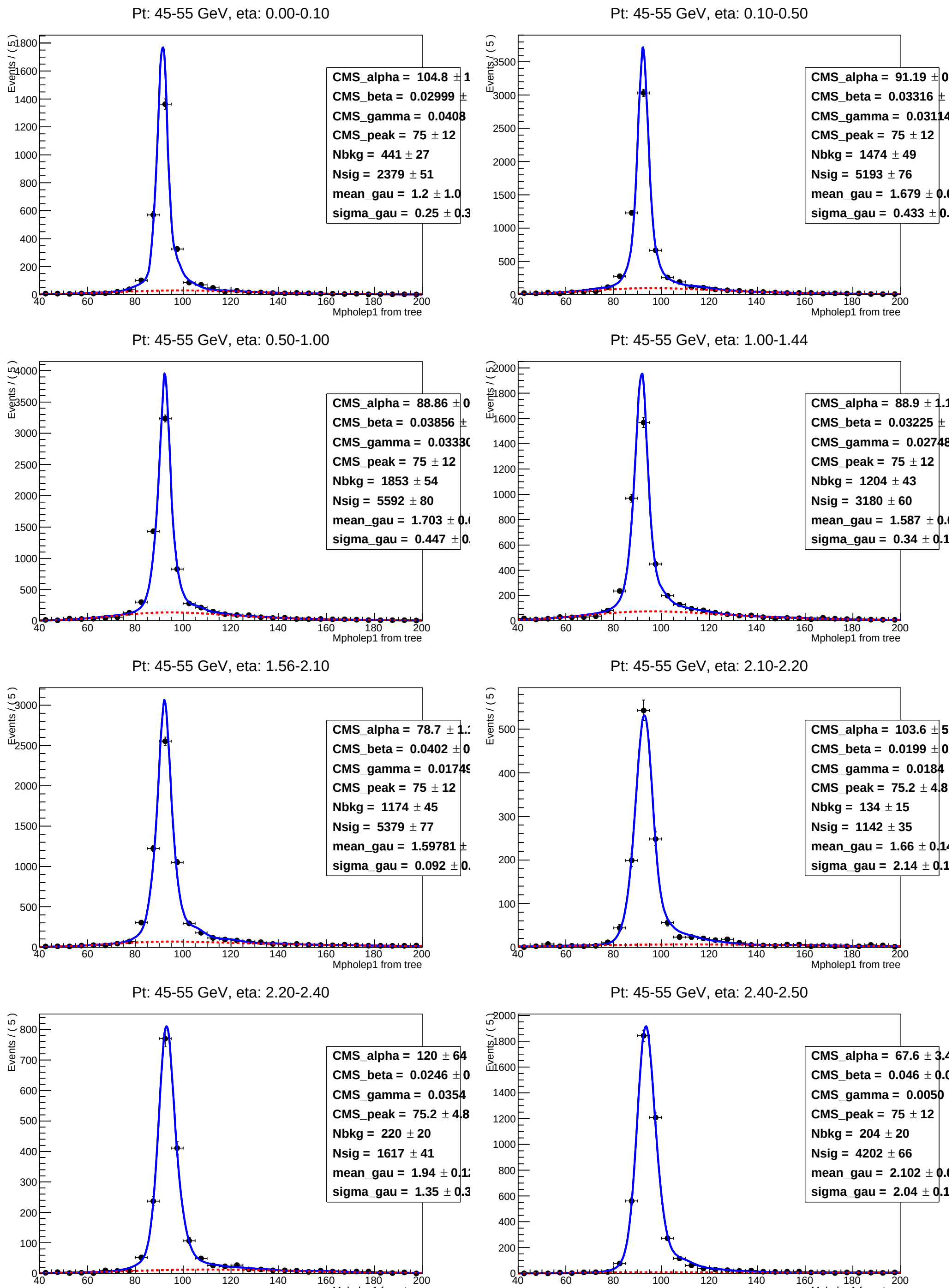

Figure J.6: $M_{e\gamma}$ fits, $W\gamma$, electron channel, underflow bin (45-55 GeV), 8 η^{γ} bins.

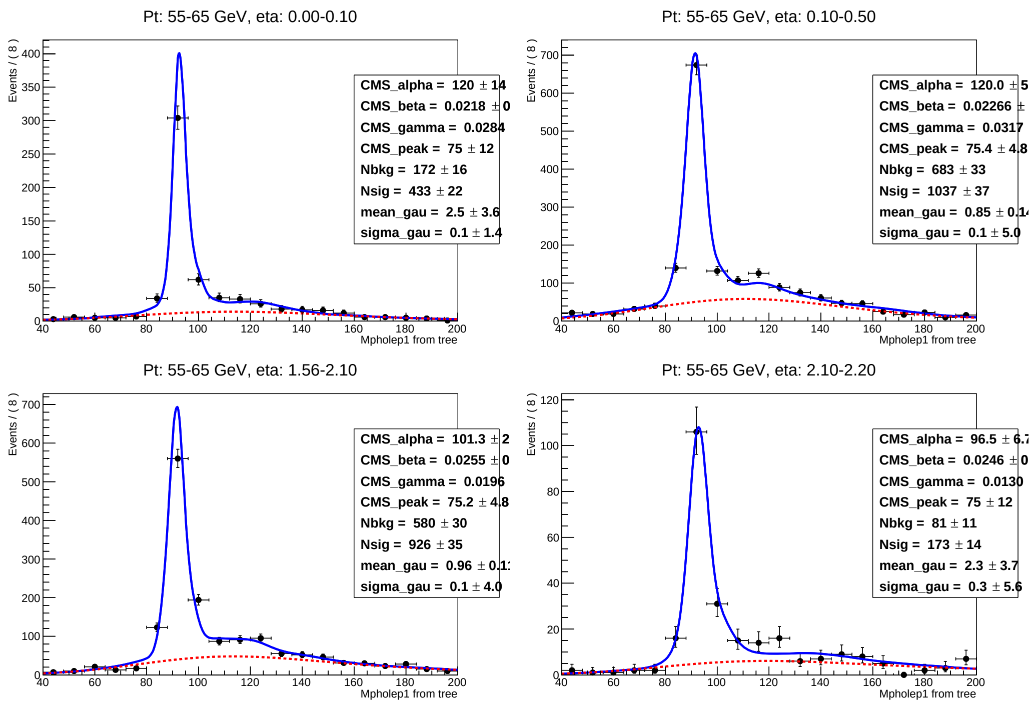

Figure J.7: $M_{e\gamma}$ fits, $W\gamma$, electron channel, underflow bin (55-65 GeV), 4 η^{γ} bins.

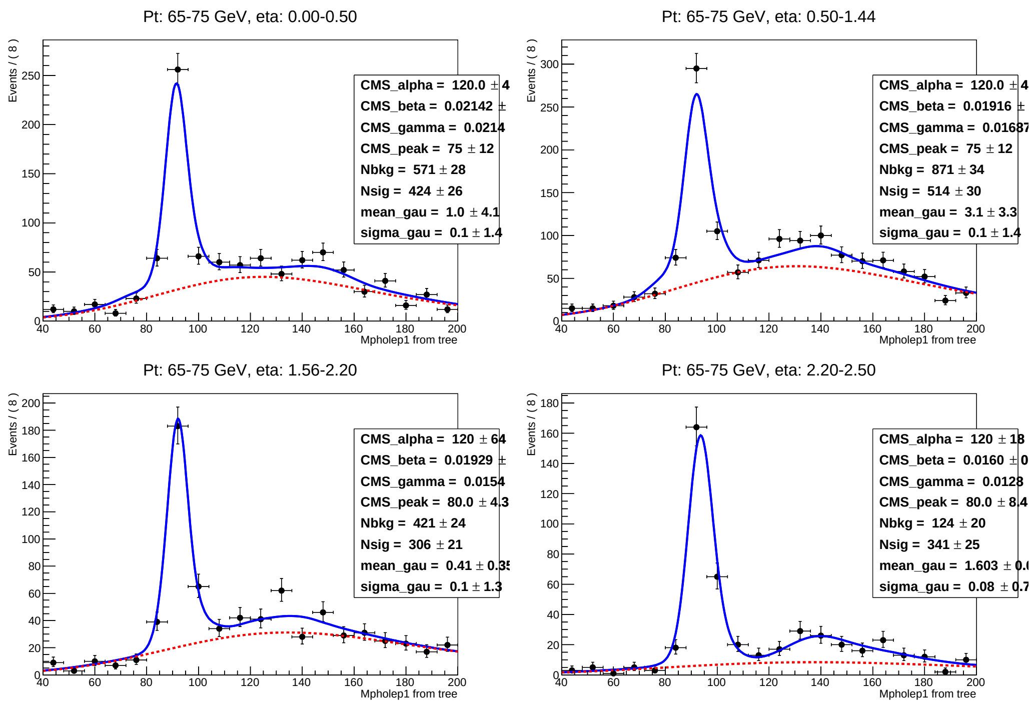

Figure J.8: $M_{e\gamma}$ fits, $W\gamma$, electron channel, underflow bin (65-75 GeV), 4 η^{γ} bins.

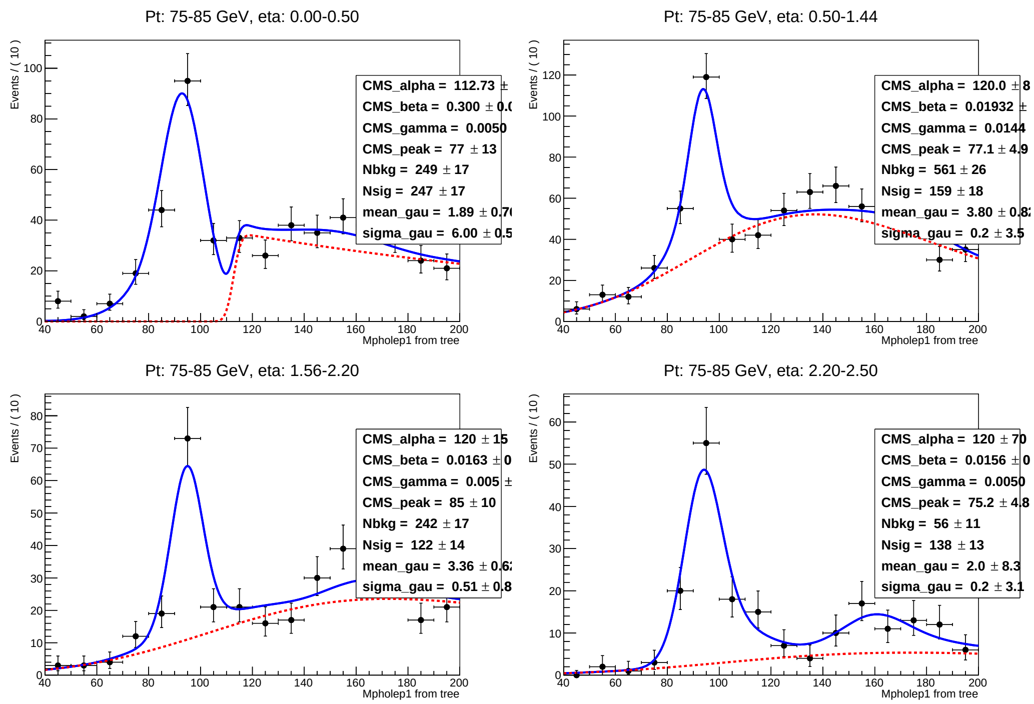

Figure J.9: $M_{e\gamma}$ fits, $W\gamma$, electron channel, underflow bin (75-85 GeV), 4 η^{γ} bins.

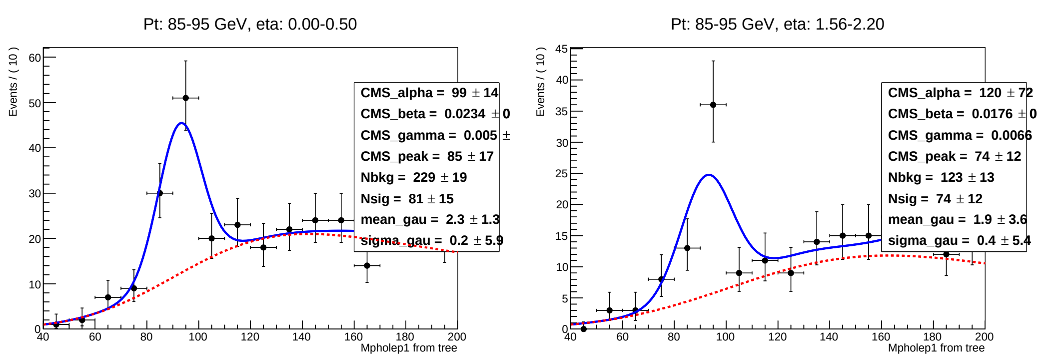

Figure J.10: $M_{e\gamma}$ fits, $W\gamma$, electron channel, underflow bin (85-95 GeV), 2 η^{γ} bins.

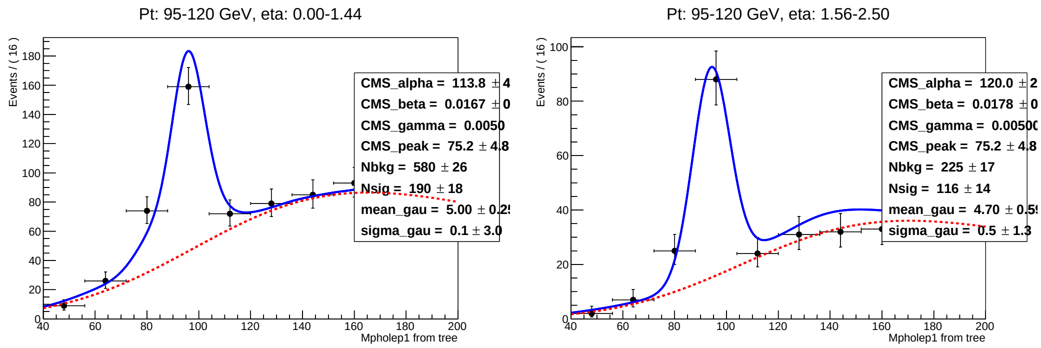

Figure J.11: $M_{e\gamma}$ fits, $W\gamma$, electron channel, underflow bin (95-120 GeV), 2 η^{γ} bins.

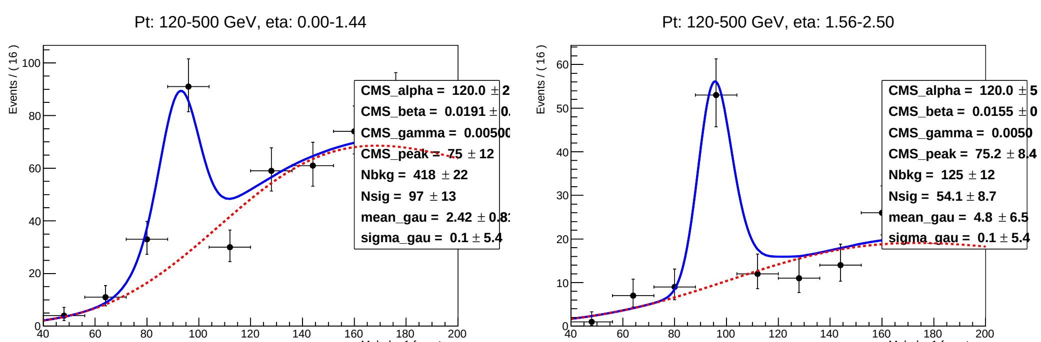

Figure J.12: $M_{e\gamma}$ fits, $W\gamma$, electron channel, underflow bin (120-500 GeV), 2 η^{γ} bins.

Bibliography

[1] K. A. Olive et al. Review of Particle Physics. *Chin. Phys.*, C38:090001, 2014. Available at: pdg.lbl.gov.

[2] S. Duric. *Measurement of associated Wgamma production and search for anomalous WWgamma couplings with the CMS detector*. PhD thesis, University of Zagreb, 2013.

[3] CMS collaboration. Limits on anomalous triple and quartic gauge couplings. Available at: https://twiki.cern.ch/twiki/bin/view/CMSPublic/ PhysicsResultsSMPaTGC#Figure_1_Limits_on_WWgamma_aTGC.

[4] CMS collaboration. Measurement of the Wgamma and Zgamma inclusive cross sections in pp collisions at sqrt(s) = 7 TeV and limits on anomalous triple gauge boson couplings. *Phys. Rev. D*, 89(092005), 2014. Available at: https://arxiv.org/abs/1308.6832.

[5] ATLAS Collaboration. Measurements of Wgamma and Zgamma production in pp collisions at sqrt(s)= 7 TeV with the ATLAS detector at the LHC. *Phys. Rev. D*, 87(112003), 2013. Available at: https://arxiv.org/abs/1302.1283.

[6] Figure available at: http://cds.cern.ch/record/1621583/files/.

[7] Figure available at: https://muon.files.wordpress.com/2014/01/cms-sigma-vs-e.png.

[8] Figure available at: https://twiki.cern.ch/twiki/bin/view/CMSPublic/ LumiPublicResults.

[9] Figure available at: https://inspirehep.net/record/837874/plots.

[10] Figure available at: https://cms-docdb.cern.ch/cgi-bin/PublicDocDB/ShowDocument?docid=4172.

[11] F. Meier Aeschbacher. *Measurement of the Λ_b^0 baryon lifetime using the Compact Muon Solenoid experiment at CERN's Large Hadron Collider*. PhD thesis, ETH Zurich, 2013.

[12] *CERN LHC brochure*. Available at: http://cds.cern.ch/record/1165534/files/CERN-Brochure-2009-003-Eng.pdf.

[13] CMS Collaboration. Observation of a new boson at a mass of 125 GeV with CMS experiment at the LHC. *Phys. Lett. B*, 716(1):30–61, 2012. Available at: https://arxiv.org/abs/1207.7235.

[14] ATLAS Collaboration. Observation of a new particle in the search for the standard model Higgs boson with the ATLAS detector at the LHC. *Phys. Lett. B*, 716(1):1–29, 2012. Available at: https://arxiv.org/abs/1207.7214.

[15] NASA website. Available at: https://science.nasa.gov/astrophysics/focus-areas/what-is-dark-energy.

[16] A. Pich. *The Standard Model of Electroweak Interactions*, 2007. Updated version of the lectures given at the 2006 European School of High Energy Physics (Aronsborg, Sweden, 18 June - 1 July 2006) and at the 4th CERN - CLAF School of High Energy Physics (Vina del Mar, Chile, 18 February - 3 March 2007). Available at: https://arxiv.org/abs/0705.4264.

[17] D. Griffiths. *Introduction to Elementary Particles*. WILEY-VCH, 2008.

[18] S. Snyder. Of luminosities and cross sections. Available at: https://www-do.fnal.gov/results/publications_talks/thesis/snyder/html/node17.html.

[19] Martin Halzen. *Quarks and leptons*. John Wiles Sons Inc., 1984.

[20] W. Stirling J. Campbell, J. Huston. Hard interactions of quarks and gluons: a primer for LHC physics. *Progress in Physics*, 70, 2006. Available at: http://iopscience.iop.org/article/10.1088/0034-4885/70/1/R02.

[21] D. Sahdev R. Brown, K. Mikaelian. $W^{\pm}Z^0$ and $W^{\pm}\gamma$ pair production in νe, pp, and $\bar{p}p$ collisions. *Physical Review D*, 20(5), 1979.

[22] J. Ohnemus. Order-α_s calculations of hadronic $W^{\pm}\gamma$ and $Z\gamma$ production. *Physical Review D*, 47(3), 1993. Available at: https://journals.aps.org/prd/pdf/10.1103/PhysRevD.47.940.

[23] D. Rathev M. Grazzini, S. Kallweit. $W\gamma$ and $Z\gamma$ production at the LHC in NNLO QCD. *JHEP*, 201(85), 2015. Available at: https://arxiv.org/pdf/1504.01330.pdf.

[24] D. Zeppenfeld et. al. G. Gounaris, J.-L. Kneur. Triple gauge boson couplings. *High Energy Physics - Phenomenology*, 1996. Available at: https://arxiv.org/abs/hep-ph/9601233.

[25] D0 collaboration. Limits on anomalous trilinear gauge boson couplings from WW, WZ and Wgamma production in pp-bar collisions at sqrt(s)=1.96 TeV. *Phys. Lett. B*, 718:451–459, 2012. Available at: https://arxiv.org/abs/1208.5458.

[26] L3 Collaboration et. al. ALEPH Collaboration, DELPHI Collaboration. Electroweak measurements in electron-positron collisions at W-boson-pair energies at LEP. *Physics Reports*, 2013. Available at: https://arxiv.org/abs/1302.3415.

[27] ATLAS collaboration. Measurement of total and differential w+w production cross sections in proton-proton collisions at s= 8 tev with the atlas detector and limits on anomalous triple-gauge-boson couplings. *JHEP*, 09(029), 2016. Available at: https://arxiv.org/abs/1603.01702.

[28] CMS collaboration. Measurement of the W+W- cross section in pp collisions at sqrt(s) = 7 TeV and limits on anomalous WWgamma and WWZ couplings. *Eur. Phys. J. C*, 73(2610), 2013. Available at: https://arxiv.org/abs/1306.1126.

[29] CMS collaboration. Measurement of the W+W- cross section in pp collisions at sqrt(s) = 8 TeV and limits on anomalous gauge couplings. *Eur. Phys. J. C*, 76(401), 2016. Available at: https://arxiv.org/abs/1507.03268.

[30] ATLAS collaboration. Measurement of the WW+WZ cross section and limits on anomalous triple gauge couplings using final states with one lepton, missing transverse momentum, and two jets with the ATLAS detector at sqrt(s)=7 TeV. *JHEP*, 01(049), 2015. Available at: https://arxiv.org/abs/1410.7238.

[31] CMS collaboration. Measurement of the sum of WW and WZ production with W+dijet events in pp collisions at sqrt(s) = 7 TeV. *Eur. Phys. J. C*, 73(2283), 2013. Available at: https://arxiv.org/abs/1210.7544.

[32] W. Giele et. al. J. Campbell, K. Ellis. MCFM calculator. Available at: https://mcfm.fnal.gov/.

[33] P. Collier et. al. O. Brüning. *LHC Design Report*, 2004. Available at: https://cds.cern.ch/record/782076.

[34] The Large Hadron Collider. Available at: http://home.cern/topics/large-hadron-collider.

[35] Figure available at: https://twiki.cern.ch/twiki/bin/view/CMSPublic/ LumiPublicResults.

[36] CMS collaboration. *CMS Physics Technical Design Report*, 2006. Available at: https://cdsweb.cern.ch/record/922757/files/lhcc-2006-001.pdf.

[37] G. Passardi et. al. D. Delikaris, J. Dauvergne. *The cryogenic system for the superconducting solenoid magnet of the CMS experiment*, 1998. Available at: https://cds.cern.ch/record/345832/files/lhc-project-report-165.pdf.

[38] CMS collaboration. Description and performance of track and primary-vertex reconstruction with the CMS tracker. *JINST*, 9, 2014. Available at: https://arxiv.org/abs/1405.6569.

[39] CMS collaboration. Alignment of the CMS tracker with LHC and cosmic ray data. *JINST*, 9, 2014. Available at: https://arxiv.org/abs/1403.2286.

[40] CMS collaboration. Energy calibration and resolution of the CMS electromagnetic calorimeter in pp collisions at sqrt(s)=7 TeV. *JINST*, 8(P09009), 2013. Available at: https://arxiv.org/abs/1306.2016.

[41] CMS collaboration. The performance of the cms muon detector in proton-proton collisions at sqrt(s)=7 TeV at the LHC. *JINST*, 8, 2013. Available at: https://arxiv.org/abs/1306.6905.

[42] CMS collaboration. The CMS trigger system. *JINST*, 12, 2017. Available at: https://arxiv.org/abs/1609.02366.

[43] CMS collaboration. *Particle-Flow Event Reconstruction in CMS and Performance for Jets, Taus, and E_T^{miss}*, 2009. https://inspirehep.net/record/925379/files/PFT-09-001-pas.pdf.

[44] Lampen et. al. Karimäki, Veikko. *The HIP Algorithm for Track Based Alignment and its Application to the CMS Pixel Detector*, 2006. Available at: http://cds.cern.ch/record/926537.

[45] Millepede-II. Available at: http://www.desy.de/~kleinwrt/MP2/doc/html/index.html.

[46] CMS tracker detector performance results 2015: Alignment. Available at: https://twiki.cern.ch/twiki/bin/view/CMSPublic/TkAlignmentPerformance2015.

[47] CMS collaboration. Measurement of the Zgamma production cross section in pp collisions at 8 TeV and search for anomalous triple gauge boson couplings. *JHEP*, 04(164), 2015. Available at: https://arxiv.org/abs/1502.05664.

[48] Madgraph generator. Available at: http://madgraph.physics.illinois.edu/.

[49] Pythia generator. Available at: http://home.thep.lu.se/~torbjorn/Pythia.html.

[50] Cteq6l1 pdf set. Available at: http://hep.pa.msu.edu/cteq/public/cteq6.html.

[51] Geant. Available at: http://geant.cern.ch/.

[52] Fewz calculator. Available at: http://gate.hep.anl.gov/fpetriello/FEWZ.html.

[53] CMS collaboration. Measurements of the pp to Wgammagamma and pp to Zgammagamma cross sections and limits on anomalous quartic

gauge couplings at sqrt(s)=8 TeV. *submitted to JHEP*, 2017. Available at: https://arxiv.org/abs/1704.00366.

[54] RooFit. Available at: https://root.cern.ch/roofit.

[55] RooCMSShape. Available at: https://github.com/cms-sw/cmssw/blob/master/PhysicsTools/TagAndProbe/interface/RooCMSShape.h.

[56] G. D'Agostini. A multidimensional unfolding method based on Bayes' theorem. *Nuclear Instruments and Methods in Physics Research A*, 362:487–498, 1995.

[57] RooUnfold. Available at: http://hepunx.rl.ac.uk/∼adye/software/unfold/RooUnfold.html.

[58] ROOT. Available at: https://root.cern.ch/.

[59] CMS software. Available at: http://cms-sw.github.io/index.html.

[60] github. Available at: https://github.com/.

[61] Code that makes ggNtuples. Available at: https://github.com/cmkuo/ggAnalysis/tree/V05-03-12-04/ggNtuplizer.

[62] Michael E. Peskin and Daniel V. Schroeder. *An Introduction to quantum field theory*. Addison-Wesley, Reading, USA, 1995.

[63] L. Gray. *A measurement of the $Z\gamma$ Cross Section and Limits on Anomalous Gauge Couplings at $\sqrt{s}$ =7 TeV Using CMS*. PhD thesis, University of Wisconsin - Madison, 8 2012.

[64] Wikipedia article. cross section (physics). Available at: https://en.wikipedia.org/wiki/Cross_section_%28physics%29.

[65] CMS collaboration. Search for anomalous couplings in semileptonic WW/WZ to l nu qqbar production in proton-proton collisions at sqrt(s)=8 TeV. *Submitted to Phys. Lett. B*, 2017. Available at: https://arxiv.org/abs/1703.06095.

[66] CMS collaboration. Measurement of the production cross section for Zgamma to nu nu gamma in pp collisions at sqrt(s) = 7 TeV and limits on ZZgamma and Zgammagamma triple gauge boson couplings. *JHEP*, 10(164), 2013. Available at: https://arxiv.org/abs/1309.1117.

[67] Figure available at: https://inspirehep.net/record/1235541/files/LHC_all.png.

[68] Figure available at: http://cds.cern.ch/journal/CERNBulletin/2014/24/News%20Articles/1706606.

[69] CMS collaboration. Measurements of differential cross sections for associated production of a W boson and jets in proton-proton collisions at sqrt(s)=8 TeV. *Phys. Rev. D*, 95, 2017. Available at: https://arxiv.org/abs/1610.04222.

[70] Code that performs the cross section measurement. Available at: https://github.com/eavdeeva/usercode.